13
Rising bubbles

13.1 The dissipation approximation and viscous potential flow

Dissipation approximations have been used to calculate the drag on bubbles and drops; VCVPF can be used for the same purpose. The viscous pressure correction on the interface can be expressed by a harmonic series. The principal mode of this series is matched to the velocity potential and its coefficient is explicitly determined. The other modes do not enter into the expression for the drag on bubbles and drops.

13.1.1 Pressure correction formulas

We consider separable solutions of $\nabla^2\phi = 0$. For simplicity, we consider axisymmetric or planar problems and use the orthogonal coordinate system (α, β); the gas-liquid interface is given by α=const. The solution of the potential flow equations may be written as

$$\phi = h_k(\alpha) f_k(\beta), \tag{13.1.1}$$

where $f_k(\beta)$ is the kth mode of the surface harmonics. A pressure correction function which is periodic or finite at the gas-liquid interface may be expanded as a series of surface harmonics of integral orders:

$$-p_{\mathrm{v}} = C_k f_k(\beta) + \sum_{j\neq k} C_j f_j(\beta), \tag{13.1.2}$$

where $f_j(\beta)$'s are surface harmonics and C_j's are constant coefficients.

Substitution of (13.1.2) into (12.6.1) leads to

$$C_k \int_A \mathbf{u}\cdot\mathbf{n} f_k(\beta)\, dA + \sum_{j\neq k} C_j \int_A \mathbf{u}\cdot\mathbf{n} f_j(\beta)\, dA = \mathcal{P}_{\mathrm{s}}, \tag{13.1.3}$$

where $\mathcal{P}_{\mathrm{s}}$ is defined as $\mathcal{P}_{\mathrm{s}} = \int_A \mathbf{u}\cdot\mathbf{t}\tau_{\mathrm{s}}\, dA$. We assume that the normal velocity is orthogonal to $f_j(\beta), j \neq k$:

$$\int_A \mathbf{u}\cdot\mathbf{n} f_j(\beta)\, dA = 0 \quad \text{when} \quad j \neq k \tag{13.1.4}$$

which is a verifiable condition and is confirmed in each example we consider here. Now equation (13.1.3) gives the coefficient C_k

$$C_k = \frac{\mathcal{P}_{\mathrm{s}}}{\int_A \mathbf{u}\cdot\mathbf{n} f_k(\beta)\, dA}. \tag{13.1.5}$$

Using (13.1.5) for VCVPF we may write

$$-p = -p_{\mathrm{i}} + \frac{\mathcal{P}_{\mathrm{s}} f_k(\beta)}{\int_A \mathbf{u}\cdot\mathbf{n} f_k(\beta)\, dA} + \sum_{j\neq k} C_j f_j(\beta). \tag{13.1.6}$$

The term $\mathcal{P}_{\mathrm{s}} f_k(\beta)/\int_A \mathbf{u}\cdot\mathbf{n} f_k(\beta)\, dA$ may be called the principal part of the viscous pressure correction; it is proportional to the power integral of the uncompensated irrotational shear stress. It is the only term in the pressure correction to enter into the power of traction integral, and into the direct calculation of the drag on rising bubbles or drops. The principal part of the pressure correction is explicitly computable as we shall see in the examples to follow. In general, the values of $C_j, j \neq k$ are not known, but for the special case of a rising spherical gas bubble, Kang & Leal (1988a) presented computable expressions for these coefficients.

The expression (13.1.6) completes the formulation of the pressure correction in VCVPF up to the principal part of the harmonic series.

We may compare the dissipation calculation and direct calculation of the drag using VPF and VCVPF. Let D_1 be the drag calculated by the dissipation method

$$D_1 = \mathcal{D}/U, \tag{13.1.7}$$

and D_2 be the drag by direct calculation

$$D_2 = \int_A \mathbf{e}_x \cdot \mathbf{T} \cdot \mathbf{n}\, dA = \int_A [\mathbf{e}_x \cdot \mathbf{n}(-p + \tau_{\rm n}) + \mathbf{e}_x \cdot \mathbf{t}\tau_{\rm s}]\, dA, \tag{13.1.8}$$

where x is the direction of translation. The direct calculation using VPF leads to $D_2 = 0$ even though the dissipation is not zero, which is a known result (see, for example, Zierep 1984, Joseph & Liao 1994). The dissipation approach involves a volume integral and the direct calculation involves a surface integral. The solution to the Navier-Stokes equations in these nearly irrotational flows involves a leading order term (the irrotational solution) and a viscous correction at the boundary. When using the dissipation approach, the leading order calculation only involves the irrotational result. However, the viscous correction has to be considered to obtain the leading order result when using the direct calculation. We shall focus on the direct calculation using VCVPF in the following examples (Section 13.2 - 13.4) and show that D_2 computed using VCVPF here is equal to D_1 obtained by dissipation method in the literature.

13.2 Rising spherical gas bubble

Consider now a spherical gas bubble rising with a constant velocity $U\mathbf{e}_x$ in a viscous fluid, for which

$$\phi = -\frac{1}{2}Ua^3\frac{\cos\theta}{r^2}. \tag{13.2.1}$$

At the surface of the bubble, where $r = a$, we have

$$\begin{aligned} u_r = U\cos\theta, \quad u_\theta = U\sin\theta/2; \\ \tau_{rr} = -6\mu U\cos\theta/a, \quad \tau_{r\theta} = -3\mu U\sin\theta/a; \\ p_{\rm i} = p_\infty + \frac{\rho}{2}U^2(1 - \frac{9}{4}\sin^2\theta). \end{aligned} \tag{13.2.2}$$

The dissipation is given by $\mathcal{D} = 12\pi\mu aU^2$ and $\mathcal{P}_{\rm s} = 4\pi\mu aU^2$.

The pressure correction may be expanded as a spherical surface harmonic series $\sum_{j=0}^{\infty} C_j P_j(\cos\theta)$. Substitution of u_r and $p_{\rm v}$ into (12.6.1) gives

$$-\int_{-1}^{1} UP_1(\cos\theta)\left[C_1P_1(\cos\theta) + \sum_{j\neq 1} C_jP_j(\cos\theta)\right] 2\pi a^2\, d(\cos\theta) = \mathcal{P}_{\rm s}. \tag{13.2.3}$$

The coefficient C_1 is then determined and the pressure correction is

$$-p_{\rm v} = -3\mu UP_1(\cos\theta)/a + \sum_{j\neq 1} C_jP_j(\cos\theta), \tag{13.2.4}$$

which is the same as the pressure correction by Kang & Leal (1988a) who obtained it by means of a general relationship between the viscous pressure correction and the vorticity distribution for a spherical bubble in an arbitrary axisymmetric flow. Kang and Leal demonstrated that the drag from direct calculation using the pressure correction (13.2.4) is $12\pi\mu aU$, the same as the drag by dissipation calculation.

13.3 Rising oblate ellipsoidal bubble (Moore 1965) ADD TO REFERENCE LIST

The equation of the ellipsoid is

$$\frac{x^2 + y^2}{b^2} + \frac{z^2}{a^2} = 1$$

where $b \geq a$. Orthogonal ellipsoidal coordinates (α, β, ω) are related to (x, y, z) by

$$\begin{cases} x = \kappa[(1+\alpha^2)(1-\beta^2)]^{\frac{1}{2}}\cos\omega, \\ y = \kappa[(1+\alpha^2)(1-\beta^2)]^{\frac{1}{2}}\sin\omega, \\ z = \kappa\alpha\beta. \end{cases}$$

The ellipsoid is given by $\alpha = \alpha_0$ provided that

$$\kappa(1+\alpha_0^2)^{\frac{1}{2}} = b, \quad \kappa\alpha_0 = a.$$

The potential for an oblate ellipsoid rising with a constant velocity $U\mathbf{e}_z$ is

$$\phi = -U\kappa q\beta(1 - \alpha\cot^{-1}\alpha), \tag{13.3.1}$$

where $q(\alpha_0) = (\cot^{-1}\alpha_0 - \frac{\alpha_0}{1+\alpha_0^2})^{-1}$. The velocity components in the ellipsoidal coordinates are $(u_\alpha, u_\beta, 0)$, and at the surface of the ellipsoid, we have

$$u_\alpha = U\beta\sqrt{\frac{1+\alpha_0^2}{\alpha_0^2+\beta^2}}, \quad u_\beta = -Uq\sqrt{\frac{1-\beta^2}{\alpha_0^2+\beta^2}}(1 - \alpha_0\cot^{-1}\alpha_0). \tag{13.3.2}$$

The normal stress $\tau_{\alpha\alpha}$ and shear stress $\tau_{\beta\alpha}$ are calculated using the potential flow, and their values at the surface of the ellipsoid are

$$\tau_{\alpha\alpha} = -2\mu\frac{U\beta q(1+2\alpha_0^2+\beta^2)}{(\alpha_0^2+\beta^2)^2\kappa(1+\alpha_0^2)}, \quad \tau_{\beta\alpha} = 2\mu\frac{Uq\alpha_0}{\kappa(\alpha_0^2+\beta^2)^2}\sqrt{\frac{1-\beta^2}{1+\alpha_0^2}}. \tag{13.3.3}$$

Then the power of the shear stress can be evaluated

$$\mathcal{P}_\mathrm{s} = -\int_A u_\beta\tau_{\beta\alpha}\,dA = 4\mu\pi U^2\kappa q^2(1-\alpha_0\cot^{-1}\alpha_0)[\alpha_0 + (1-\alpha_0^2)\cot^{-1}\alpha_0]/\alpha_0^2. \tag{13.3.4}$$

Now we calculate the pressure correction p_v. Noting that ellipsoidal harmonics $P_j(\beta)$ (see Lamb 1932) are appropriate in this case and the potential (13.3.1) is proportional to $P_1(\beta) = \beta$, we write the pressure correction as

$$-p_\mathrm{v} = C_1P_1(\beta) + \sum_{j\neq 1} C_jP_j(\beta). \tag{13.3.5}$$

Inserting (13.3.5) into (12.6.1) and using $dA = 2\pi\kappa^2(1+\alpha_0^2)^{\frac{1}{2}}(\alpha_0^2+\beta^2)^{\frac{1}{2}}d\beta$, we obtain

$$-\int_A u_\alpha(-p_\mathrm{v})\,dA = -2\pi\kappa^2U(1+\alpha_0^2)\int_{-1}^{1} P_1(\beta)\left[C_1P_1(\beta) + \sum_{j\neq 1} C_jP_j(\beta)\right]d\beta = \mathcal{P}_\mathrm{s}. \tag{13.3.6}$$

The terms P_j $(j \neq 1)$ do not contribute the integral; the coefficient C_1 is determined. Then the pressure correction is

$$-p_\mathrm{v} = \frac{-3\mu Uq^2}{\kappa(1+\alpha_0^2)\alpha_0^2}(1-\alpha_0\cot^{-1}\alpha_0)\left[\alpha_0 + (1-\alpha_0^2)\cot^{-1}\alpha_0\right]P_1(\beta) + \sum_{j\neq 1} C_jP_j(\beta). \tag{13.3.7}$$

At the limit $\alpha_0 \to \infty$ where the ellipsoid becomes a sphere, the pressure correction (13.3.7) reduces to

$$\lim_{\alpha_0\to\infty} -p_\mathrm{v} = -3\mu U\cos\theta/a + \sum_{j\neq 1} C_jP_j(\cos\theta) \tag{13.3.8}$$

with $\beta = \cos\theta$ at this limit being understood. This is in agreement with the pressure correction (13.2.4) for the spherical gas bubble.

We calculate the drag by direct integration:

$$D_2 = \int_A \mathbf{e}_z\cdot\mathbf{e}_\alpha(-p_\mathrm{v} + \tau_{\alpha\alpha})\,dA = \frac{4\mu\pi U\kappa q^2}{1+\alpha_0^2}\left(\frac{1}{\alpha_0} + \frac{1-\alpha_0^2}{\alpha_0^2}\cot^{-1}\alpha_0\right), \tag{13.3.9}$$

which is in agreement with the dissipation calculation of Moore (1965).

13.4 A liquid drop rising in another liquid (Harper & Moore 1968)

The steady flow of a spherical liquid drop in another immiscible liquid can be approximated by Hill's spherical vortex inside, and potential flow outside. We use the superscript "^{o}" for quantities outside the drop and "^{i}" for quantities inside. The stream and potential functions of the outer flow are

$$\psi^o = \frac{1}{2}U\sin^2\theta\frac{a^3}{r} \quad \text{and} \quad \phi = -\frac{1}{2}Ua^3\frac{\cos\theta}{r^2}, \tag{13.4.1}$$

respectively. The stream function for a Hill's vortex moving at a constant velocity relative to fixed coordinate system is

$$\psi^i = \frac{3Ur^2}{4}\sin^2\theta(1-\frac{r^2}{a^2}) + \frac{1}{2}Ur^2\sin^2\theta = \frac{Ur^2}{4}\sin^2\theta(5-\frac{3r^2}{a^2}). \tag{13.4.2}$$

At the surface of the drop, where $r=a$, we have

$$u_r = u_r^o = u_r^i = U\cos\theta, \quad u_\theta = u_\theta^o = u_\theta^i = U\sin\theta/2, \tag{13.4.3}$$

$$\tau_{rr}^o = -6\mu^o U\cos\theta/a, \quad \tau_{r\theta}^o = -3\mu^o U\sin\theta/a, \tag{13.4.4}$$

$$\tau_{rr}^i = -6\mu^i U\cos\theta/a, \quad \tau_{r\theta}^i = 9\mu^i U\sin\theta/(2a). \tag{13.4.5}$$

This Hill's vortex problem fits in the general framework discussed in this section in the sense that there is a shear stress discontinuity at the interface which needs to be resolved by adding a pressure correction to the irrotational pressure. However, it is somewhat different than gas-liquid interface problems because the shear stress inside the drop is not zero but is determined by the Hill's vortex. Again we seek the expression for the pressure correction by comparing the VPF solution and the VCVPF solution. We proceed by calculating the total dissipation of the system, which is equal to the sum of the power of traction on the outer and inner liquids $\mathcal{P}^o + \mathcal{P}^i$. There is only one way to calculate $\mathcal{P}^i$, but $\mathcal{P}^o$ may be evaluated on VPF or VCVPF. For VPF, τ_{rr}^o and $\tau_{r\theta}^o$ given by (13.4.4) are used to calculate $\mathcal{P}^o$ and

$$\mathcal{D} = \mathcal{P}^o + \mathcal{P}^i = -\int_A [u_r(-p_\mathrm{i} + \tau_{rr}^o) + u_\theta\tau_{r\theta}^o]\,dA + \mathcal{P}^i. \tag{13.4.6}$$

For VCVPF, a pressure correction is added to resolve the discontinuity between $\tau_{r\theta}^o$ and $\tau_{r\theta}^i$. Then the value of the shear stress at the interface is $\tau_{r\theta}^i$, not $\tau_{r\theta}^o$. The dissipation for VCVPF is

$$\mathcal{D} = \mathcal{P}^o + \mathcal{P}^i = -\int_A [u_r(-p_\mathrm{i} - p_\mathrm{v} + \tau_{rr}^o) + u_\theta\tau_{r\theta}^i]\,dA + \mathcal{P}^i. \tag{13.4.7}$$

Since $\mathcal{D}$, $\mathcal{P}^i$, p_i, τ_{rr}^o and $\mathbf{u}$ are the same in both cases, we find that

$$\int_A u_r(-p_\mathrm{v})\,dA = \int_A u_\theta(\tau_{r\theta}^o - \tau_{r\theta}^i)\,dA. \tag{13.4.8}$$

Now we expand the pressure correction as a spherical surface harmonic series and equation (13.4.8) becomes

$$\int_{-1}^{1} U\cos\theta\left[C_1\cos\theta + \sum_{j\neq 1} C_j P_j(\cos\theta)\right] 2\pi a^2\,d(\cos\theta) = -4\pi aU^2(\mu^o + 3\mu^i/2). \tag{13.4.9}$$

The coefficient C_1 is then obtained and the pressure correction is

$$-p_\mathrm{v} = \frac{-3U}{a}(\mu^o + \frac{3\mu^i}{2})\cos\theta + \sum_{j\neq 1} C_j P_j(\cos\theta). \tag{13.4.10}$$

If the inside liquid is gas, $\mu^i = 0$ and the first term of (13.4.10) becomes $-3\mu^o U\cos\theta/a$, which agrees with the first term of the pressure correction (13.2.4) for a gas bubble. The pressure correction (13.4.10) can also be tested by direct calculation of the drag D_2 on the drop:

$$D_2 = \int_A \mathbf{e}_x\cdot\mathbf{T}\cdot(-\mathbf{e_r})\,dA = -\int_A [\cos\theta(-p_\mathrm{v} + \tau_{rr}^o) - \sin\theta\tau_{r\theta}^i]\,dA = 12\pi aU(\mu^o + \frac{3\mu^i}{2}) \tag{13.4.11}$$

which is the same as the result from the dissipation approximation by Harper & Moore (1968).

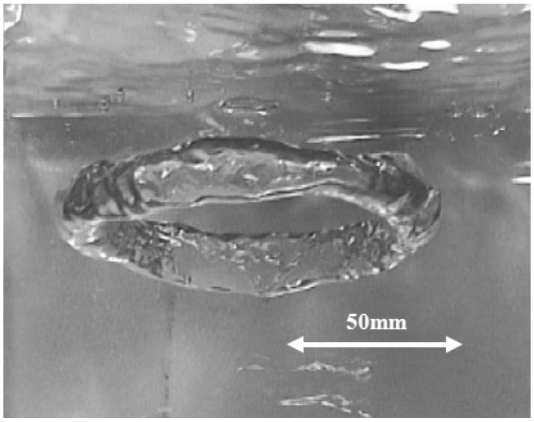

Fig. 13.1. (Matsumoto *et al.* 1999 ADD TO REFERENCE LIST) Photograph of a toroidal gas bubble in water.

13.5 Purely irrotational analysis of the toroidal bubble in a viscous fluid

Here we consider the problem of the rise of a toroidal gas bubble in a viscous liquid (figure 13.1) assuming that the motion is purely irrotational. Earlier, this same problem was studied by Pedley (1968) who considered the generation and diffusion of vorticity and more recently by Lundgren and Mansour (1991) for the case in which the liquid is inviscid.

13.5.1 Prior work, experiments

Pedley rejected the purely irrotational analysis in which the viscous drag is computed from the viscous dissipation of the irrotational flow. The purely irrotational method works well for the study of drag on other bubbles considered in this chapter. Pedley argues that the toroidal bubble is an exception because of the way that vorticity is generated and diffused by the toroidal bubble. He calls attention to a difference between the equations of energy on which the irrotational theory is based and the equations of impulse in which he says the irrotational viscous drag does not appear. He says that "... It is also shown that if the flow is assumed to remain approximately irrotational in a viscous fluid, so that Lamb's formulae may again be used almost as they stand, the equations of impulse and energy yield conflicting results." The equations of impulse are not often used today but similar conclusions follow from the Kutta-Joukowski approach used by Lundgren and Mansour (1991) (see the discussion following equation (13.5.49)).

Pedley argues that the dissipation argument, which works well for other bubbles, fails for the toroidal bubble because the vorticity is contained as it diffuses and, following arguments presented by Moore (1963), there can be no drag until the vorticity diffuses outward from the bubble surface and forms a wake. The toroidal bubble may become unstable before this happens. Pedley gave an analysis of stability for an inviscid fluid. His analysis is extended to the case of irrotational flow of a viscous fluid.

Pedley showed that in a viscous fluid, vorticity will continuously diffuse out from the bubble surface, with irrotational flow outside. Pedley's rotational solution does not differ greatly from the irrotational solution for an inviscid liquid (see figure 13.2)

Here we are going to do the irrotational analysis of the toroidal gas bubble in the case in which an irrotational viscous drag is added to force wrench in the impulse equation. In this case, the impulse equation and the energy equation governing the rise of the bubble are the same. The solution of this equation is computed; after a transient state the system evolves to a steady state in which the diameter, toroidal radius and rise velocity are constant.

Experiments on vortex ring bubbles are sparse and inconclusive. All the experiments are for gas bubbles in water. These experiments suggest that gas bubbles rising in a large expanse of water do not reach a steady state before breaking up due to capillary instability.

Turner (1957) developed a theory for the motion of a buoyant ring in an inviscid liquid. The theory shows that the buoyant force acts to increase the impulse of a ring. The ring diameter increases as the ring rises. He also carried out experiments to verify the theory with small vortex rings formed in water, using methylated spirits and salt to produce the density differences.

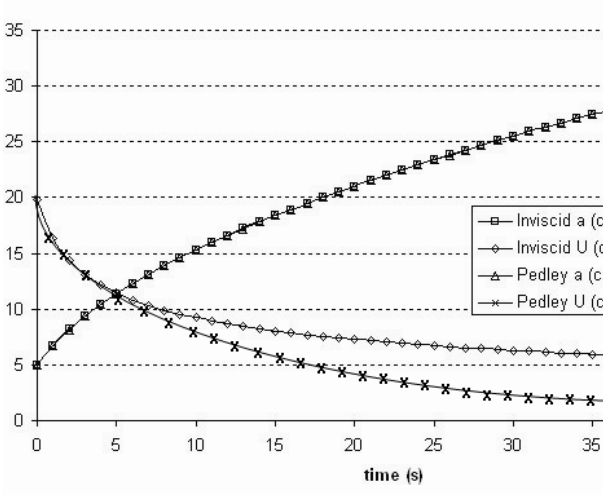

Fig. 13.2. Evolution of the ring radius a and velocity U with time t, according to Pedley. The data for Pedley's solution for U are extracted from figure 3 in Pedley (1968). —□— inviscid solution for a, —◇— Pedley's viscous solution for a, —△— inviscid solution for U, —×— Pedley's viscous solution for U. FIGURE CROPPED NEED NEW FIGURE

Walters & Davidson (1963) observed that a rising toroidal bubble could be produced by release of a mass of gas in water. The form of the bubble is a vortex ring with a buoyant air core. They created vortex rings by rapidly opening and closing an air jet in the bottom of a water tank obtaining ring bubbles from 6 to 110 cm^3. These were observed to spread as they rise as Turner predicted, but there were no measurement of the rate of spreading.

Matsumoto, Kunugi and Serizawa (1999) ADD TO REFERENCE LIST reported results for the numerical simulation of ring-typed bubbles and they also presented results for experiments on ring bubbles of air in water in a swimming pool of about 5 meters in depth and in a small acrylics box. In a private communication Prof. Serizawa noted that in the ring bubbles in the acrylics box grew to ten centimeter and were stable. However, the bubbles in the swimming pool grew to a few tens of cm in diameter expanding outwards and eventually broke into air bubbles.

Lundgren and Mansour (1991) describe the ring bubbles as air vortex rings, with approximately constant core volumes perhaps as large as a half a litre, which expand to be rings of the order of two feet in diameters as they rise towards the free surface.

Experiments which give rise to reliable data to which various theories can be compared are not available. It would be particularly valuable if experiments could be carried out in a highly viscous liquids, not only water. The effects of lateral boundaries on the rise velocity could also be considered.

13.5.2 The energy equation

We will use the notation introduced by Pedley and summarized in figure 13.3. The radius of the ring is a and the plane of this ring is horizontal. The center of this ring is instantaneously at the point O and the axis Oz is the upward vertical. The cross section of the air core is assumed to be a circle with radius b. The circulation around the air core is $2\pi\Gamma$. (s, χ) are polar coordinates in a meridional plane, centered at the point A. The bubble is rising vertically with velocity U and the radius a can be expanding at the same time. The volume of the bubble V is given by $2\pi^2 ab^2$.

Pedley analyzed the motion of a toroidal bubble by two methods, the impulse equation and the energy equation. The rate of change of the vertical impulse is

$$\mathrm{d}P/\mathrm{d}t = F, \tag{13.5.1}$$

where F is the resultant force on the bubble in the vertical direction. Pedley argued that in this case, F is due to the buoyancy of the bubble and there is no viscous drag. The energy equation is

$$\frac{\mathrm{d}}{\mathrm{d}t}(T + \Omega) = -\mathcal{D}, \tag{13.5.2}$$

where T and Ω are the kinetic and potential energies of the system and $\mathcal{D}$ is the dissipation. Pedley wrote the

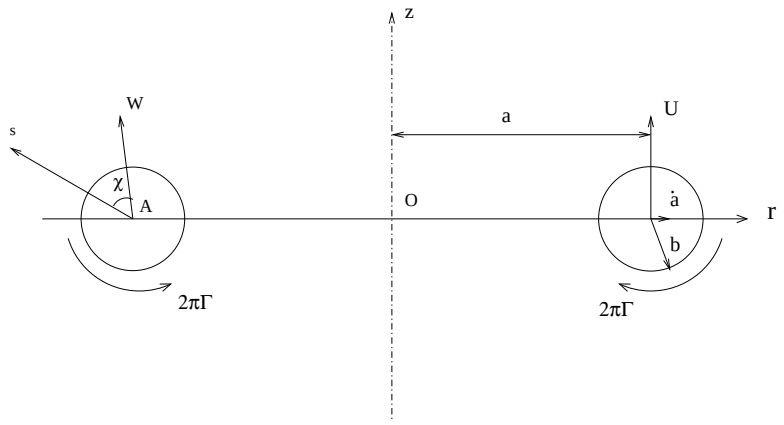

Fig. 13.3. Meridional section of the toroidal bubble.

rate of change of potential energy as

$$\frac{\mathrm{d}\Omega}{\mathrm{d}t} = \frac{\mathrm{d}}{\mathrm{d}t}(\rho g V h) = -\rho g V U, \tag{13.5.3}$$

where ρ is the density of the ambient fluid, and h is the depth of the bubble beneath a fixed reference level.

Pedley first considered the ambient fluid to be inviscid and the motion to be irrotational. Under these assumptions, the impulse and energy equations give rise to the same expressions for a and U as functions of t: a ultimately increases as $t^{1/2}$, and U decreases as $t^{-1/2}\ln t$. Pedley then considered viscous fluid and assumed that the flow remained approximately irrotational. He argued that the impulse equation would be the same as for the inviscid fluid; however, the energy equation would be changed due to the viscous dissipation. Thus the two methods yielded conflicting results, which led Pedley to conclude that the flow could not remain approximately irrotational. Pedley then investigated the diffusion of vorticity from the bubble surface and showed that the vorticity distribution became approximately Gaussian, with an effective radius b' which also increased as $t^{1/2}$. The solution for a as a function of t turned out to be the same as in inviscid case, while U decreased as $t^{-1/2}$. Other results produced by Pedley's analysis include an evaluation of the effect of a hydrostatic variation in bubble volume, and a prediction of the time when the bubble becomes unstable under the action of surface tension.

We consider the toroidal bubble under the assumption that the flow remains approximately irrotational and the ambient fluid is viscous. Our analysis is purely irrotational and it is different than the one given by Pedley because we include the viscous drag on the bubble in the impulse equation (13.5.1). This viscous drag can be computed using the dissipation method, as was done by Levich (1949) in his calculation of the drag on a spherical gas bubble in the irrotational flow of a viscous fluid. When the drag is added, the inconsistency between the impulse equation and energy equation disappears. Our equations predict that initially the bubble expands and rises in the fluid. The rise velocity U decreases as the ring radius a increases. Ultimately the viscous drag balances the buoyant force and a steady solution is achieved, for which a and U become constants.

In our calculation, we assume that the circulation Γ and the bubble volume V are constant, and the ratio $b/a << 1$. The same assumptions were adopted by Pedley (1968).

The flow around the toroidal bubble is approximated by the irrotational flow around a cylindrical bubble of radius b. The translational velocities of the bubble include the vertical velocity U and horizontal velocity $\dot{a}$ (figure 13.3). We denote the resultant velocity as

$$W = \sqrt{U^2 + \dot{a}^2}. \tag{13.5.4}$$

The rise velocity U may be calculated from the condition that there is no normal velocity across the bubble surface. If the core cross-section is taken to be circular and the quantity ω/r uniform inside, where ω is the vorticity, Lamb (1932, §163) gives

$$U = \frac{\Gamma}{2a}\left[\ln\frac{8a}{b} - n\right], \tag{13.5.5}$$

where $n = 1/4$. Hicks (1884) gives the value $n = 1/2$ for his hollow vortex-ring in which the core cross-section

is not circular and ω/r is not uniform. The irrotational flow around a cylindrical bubble of radius b is given by the velocity potential

$$\phi = -W\frac{b^2}{s}\cos\chi + \Gamma\chi, \tag{13.5.6}$$

where the coordinates s and χ are shown in figure 13.3. The velocities can be obtained from the potential

$$u_s = \frac{\partial\phi}{\partial s}, \quad u_\chi = \frac{1}{s}\frac{\partial\phi}{\partial\chi}. \tag{13.5.7}$$

The kinetic energy for a 2D section is

$$T' = \frac{1}{2}\rho\int_b^{C_0 a}\int_0^{2\pi}\left(u_s^2 + u_\chi^2\right) s\,\mathrm{d}s\mathrm{d}\chi \tag{13.5.8}$$

$$= \rho\pi\left[\frac{1}{2}W^2b^2\left(1 - \frac{b^2}{C_0^2a^2}\right) + \Gamma^2\ln\frac{C_0a}{b}\right], \tag{13.5.9}$$

where the integration is from b to C_0a rather than b to ∞ because of the logarithmic singularity. Multiply by $2\pi a$, the circumference of the bubble, and obtain the total kinetic energy

$$T = \rho\pi^2aW^2b^2\left(1 - \frac{b^2}{C_0^2a^2}\right) + 2\rho\pi^2a\Gamma^2\ln\frac{C_0a}{b}. \tag{13.5.10}$$

The value of C_0 may be determined by comparing (13.5.10) to the kinetic energy given by Pedley (1968). Pedley used Lamb's (1932) formula for the kinetic energy of an arbitrary axisymmetric distribution of azimuthal vorticity and obtained

$$T = 2\pi^2\rho a\Gamma^2\left[\ln\frac{8a}{b} - 2 + O\left(\frac{b^2}{a^2}\ln\frac{8a}{b}\right)\right] \approx 2\pi^2\rho a\Gamma^2\ln\left(\frac{8a}{b}\mathrm{e}^{-2}\right). \tag{13.5.11}$$

The kinetic energy given by Pedley neglected the energy associated with the translation of the bubble. Comparing this with the energy associated with the circulation in (13.5.10), we obtain

$$C_0 = 8\mathrm{e}^{-2} \approx 1.0827. \tag{13.5.12}$$

Since $b << a$, the energy (13.5.10) is approximately

$$T = \rho\pi^2a\left(W^2b^2 + 2\Gamma^2\ln\frac{C_0a}{b}\right). \tag{13.5.13}$$

The dissipation of the potential flow (13.5.6) can be evaluated as

$$\mathcal{D}' = \int_0^{2\pi}\int_b^{\infty} 2\mu\mathbf{D}:\mathbf{D}\,s\,\mathrm{d}s\mathrm{d}\chi = 8\pi\mu W^2 + \frac{4\pi\mu\Gamma^2}{b^2}, \tag{13.5.14}$$

where $\mathbf{D}$ is the rate of strain tensor. The same dissipation was obtained by Ackeret (1952). After multiplying $2\pi a$, we obtain the total dissipation

$$\mathcal{D} = 8\pi^2\mu a\left(2W^2 + \Gamma^2/b^2\right). \tag{13.5.15}$$

The part of the dissipation associated with the circulation Γ in (13.5.15) is the same as that given by Pedley(1968). Pedley did not consider the dissipation associated with the translation W.

After inserting the kinetic energy (13.5.13), potential energy (13.5.3) and the dissipation (13.5.15) into the energy equation (13.5.2), we obtain

$$\frac{1}{2}V\frac{\mathrm{d}W^2}{\mathrm{d}t} + \left(2\pi^2\Gamma^2\dot{a} - \frac{gV\Gamma}{2a}\right)\left(\ln\frac{8a}{b} - \frac{1}{2}\right) = -16\pi^2\nu a\left(W^2 + \pi^2a\Gamma^2/V\right), \tag{13.5.16}$$

where we have used $n = 1/2$ in the expression for U (13.5.5). Since b can be eliminated from $V = 2\pi^2ab^2$, a is the only unknown in equation (13.5.16). If the fluid is inviscid and the kinetic energy associated with translation is neglected, (13.5.16) reduces to

$$2\pi^2\Gamma^2\dot{a} - \frac{gV\Gamma}{2a} = 0 \quad \Rightarrow \quad a^2 = a_0^2 + \frac{gV}{2\pi^2\Gamma}t, \tag{13.5.17}$$

where a_0 is the value of a at $t = 0$. This equation is the same as the formula given by Pedley (1968) for both inviscid and viscous fluids.

The translational velocity W has the following form

$$W^2 = \frac{\Gamma^2}{4a^2}\left(\ln\frac{8a}{b} - \frac{1}{2}\right)^2 + \dot{a}^2. \tag{13.5.18}$$

The derivative of W^2 with respect to time in (13.5.16) leads to a second order ordinary differential equation for a. We specify two initial conditions for a at $t = 0$. The first condition is

$$a = a_0 \quad \text{at} \quad t = 0. \tag{13.5.19}$$

The second condition is derived from (13.5.17)

$$\dot{a}(t = 0) = \frac{gV}{4\pi^2\Gamma a_0}. \tag{13.5.20}$$

This condition is justified if the energy and dissipation associated with the translation of the bubble is much smaller than those associated with the circulation, and the viscous effects are small at $t = 0$. We will verify these conditions in §13.5.4 when we insert the parameters taken from the experiments of Walters & Davidson into our equations and compute the numerical results.

If the part of the energy and dissipation associated with W is relatively small at all times, (13.5.16) becomes

$$\left(2\pi^2\Gamma\dot{a} - \frac{gV}{2a}\right)\left(\ln\frac{8a}{b} - \frac{1}{2}\right) = -16\pi^4\nu a^2\frac{\Gamma}{V}. \tag{13.5.21}$$

This is the same energy equations considered by Pedley (1968) under the assumption that the flow remains approximately irrotational in a viscous fluid. Equation (13.5.21) is a first order ordinary differential equation for a and the condition (13.5.19) will suffice. In §13.5.4 we will show that the solutions of (13.5.16) and (13.5.21) are nearly the same when using the parameters taken from the experiments of Walters & Davidson.

13.5.3 The impulse equation

Pedley used Lamb's formula for the impulse of an arbitrary axisymmetric distribution of azimuthal vorticity and obtained

$$P = 2\pi^2\rho a^2\Gamma\left[1 + O\left(\frac{b^2}{a^2}\ln\frac{8a}{b}\right)\right]. \tag{13.5.22}$$

Pedley included the buoyant force in the impulse equation and argued that the drag does not enter into this problem even when the fluid is viscous. We propose to include the viscous drag on the bubble in the impulse equation; then the inconsistency between the impulse equation and the energy equation disappears.

The viscous drag on a bubble may be computed using the dissipation method, which equates the power of the drag to the dissipation. Levich (1949) used the dissipation method to calculate the drag on a spherical gas bubble rising in the irrotational flow of a viscous fluid. Ackeret (1952) used the dissipation method to compute the drag on a rotating cylinder in a uniform stream. If the flow around the toroidal bubble is approximated by the irrotational flow around a cylindrical bubble with circulation, the velocity potential (13.5.6) is the same as that used by Ackeret (1952). The irrotational dissipation is given by (13.5.15). In §13.5.4 we will show that the dissipation associated with the translation W is small and $\dot{a}$ is much smaller than U when using the parameters taken from the experiments of Walters & Davidson. Therefore the drag in the vertical direction from the dissipation method is approximately

$$D = \frac{\mathcal{D}}{U} = 8\pi^2\mu a\frac{\Gamma^2}{b^2U}. \tag{13.5.23}$$

With this viscous drag, the impulse equation (13.5.1) becomes

$$2\pi^2\rho\Gamma\frac{\mathrm{d}a^2}{\mathrm{d}t} = \rho gV - 8\pi^2\mu a\frac{\Gamma^2}{b^2U}. \tag{13.5.24}$$

After using the expression for U (13.5.5), we obtain

$$\left(2\pi^2\Gamma\dot{a} - \frac{gV}{2a}\right)\left(\ln\frac{8a}{b} - \frac{1}{2}\right) = -16\pi^4\nu a^2\frac{\Gamma}{V}, \tag{13.5.25}$$

which is the same as the energy equation (13.5.21). Thus the impulse equation with the viscous drag included is the same as the energy equation with the viscous dissipation.

13.5.4 Comparison of irrotational solutions for inviscid and viscous fluids

We solve the equations (13.5.16) and (13.5.21) using the physical constants

$$g = 980\text{cm}\,\text{s}^{-2}, \quad \nu = 0.011\text{cm}^2\text{s}^{-1}, \tag{13.5.26}$$

and the parameters taken from the experiments of Walters & Davidson

$$\Gamma = 50\text{cm}^2\text{s}^{-1}, \quad V = 21\text{cm}^3, \quad a_0 = 2.5\text{cm}, \quad b_0 = 0.65\text{cm}. \tag{13.5.27}$$

These parameters, except a_0 and b_0, are the same as those used by Pedley (1968); Pedley estimated $a_0 = 5$ cm. Our estimate of a_0 is based on figure 7 of Walters & Davidson (1963) which shows the photos of the toroidal bubble rising close to the free surface at the top of the tank. The caption in their figure 7 indicates that the ring radius is about 4 cm. Because the ring expands as it rises, the initial ring radius should be less than 4 cm. We estimate a_0 to be 2.5 cm and $b_0/a_0 \approx 0.26$.

We solve equation (13.5.16) with the initial conditions (13.5.19) and (13.5.20), and equation (13.5.21) with (13.5.19). To highlight the viscous effects, we also solve (13.5.16) with $\nu = 0$; the initial conditions for the inviscid equation are still (13.5.19) and (13.5.20). The solutions for a as a function of time are plotted in figure 13.4. The rise velocity U is then computed from (13.5.5) and plotted in figure 13.5. Integration of U gives rise to the height $h - h_0$ of rise, where h_0 is the initial position of the bubble. The plots for $h - h_0$ against a are given in figure 13.6.

The solution of the inviscid equation shows that a increases and U decreases with time. These solutions are similar to those obtained by Pedley (1968) using irrotational flow of a inviscid fluid. The plot for $h - h_0$ against a from the inviscid solution demonstrates that the bubble rises and expands conically, which is consistent with the solutions of Turner (1957) and Pedley (1968). Figure 13.4 shows that the two viscous equations (13.5.16) and (13.5.21) lead to almost the same solution. This demonstrates that the energy and dissipation associated with the translation W is relatively small, and that the choice of the initial condition (13.5.20) does not have substantial effects on the solution. Figure 13.7 shows the ratio between the ring expansion velocity $\dot{a}$ and the rise velocity U obtained from the solution of (13.5.16). This plot demonstrates that $\dot{a}$ is much smaller than U. Initially the viscous solution is similar to the inviscid solution; $\dot{a}$ increases and U decreases with time. As a/b^2 increases, the viscous drag (13.5.23) increases and finally balances the buoyant force. Then a steady state is reached, in which the toroidal bubble keeps its shape and rises at a constant velocity. Our viscous solutions give $a = 10.9$ cm and $U = 11.8$ cm/s at the steady state. This steady state solution is consistent with the classical description of the motion of a vortex ring. For example, Milne-Thomson (1968) says in § 19.41

"We may, however, observe that for points in the plane of the ring (considered as of infinitesimal cross-section) there is no radial velocity. This follows at once from the Biot and Savart principle, explained in 19.23. It therefore follows that the radius of the ring remains constant, and the ring moves forward with a velocity which must be constant since the motion must be steady relatively to the ring."

The comparison of our solutions to the experiments of Walters & Davidson (1963) is inconclusive. Walters & Davidson did not provide data for the ring radius or the rise velocity as a function of time. The tank used in their experiments is only 3 ft (91.44 cm) tall. Their figure 8 shows the computed circulation vs. time for only 0.6 second. For such a short time, we cannot even tell the difference between the viscous and inviscid solutions in figures 13.4 and 13.5. It is not known whether the bubble will ultimately reach a steady state as predicted by our viscous solution, or the ring radius will keep growing until instability occurs as in Pedley's solution.

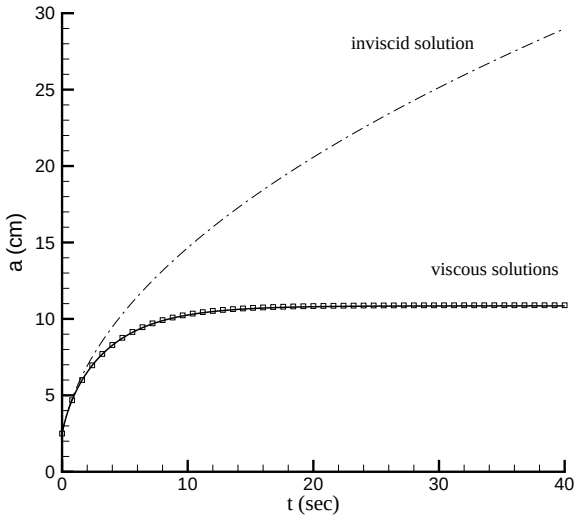

Fig. 13.4. Evolution of the ring radius a with time. The dash-dotted line represents the inviscid solution obtained by putting $\nu = 0$ in (13.5.16). The solid line represents the viscous solution of (13.5.16) with the initial conditions (13.5.19) and (13.5.20). The symbol □ represents the viscous solution of (13.5.21) with the initial condition (13.5.19).

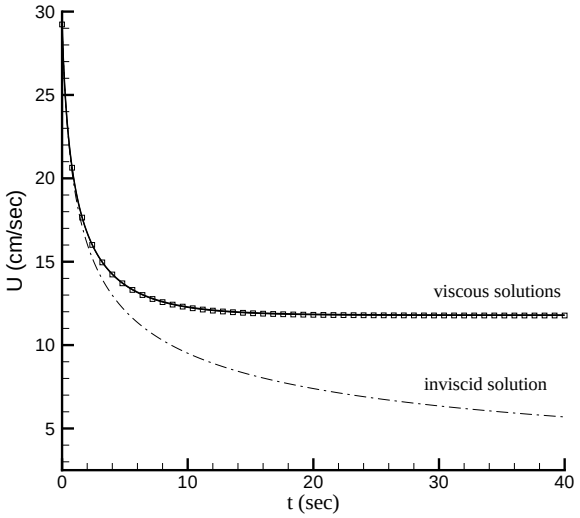

Fig. 13.5. Evolution of the rise velocity U computed from (13.5.5) with time. The dash-dotted line represents the inviscid solution obtained by putting $\nu = 0$ in (13.5.16). The solid line represents the viscous solution of (13.5.16) with the initial conditions (13.5.19) and (13.5.20). The symbol □ represents the viscous solution of (13.5.21) with the initial condition (13.5.19).

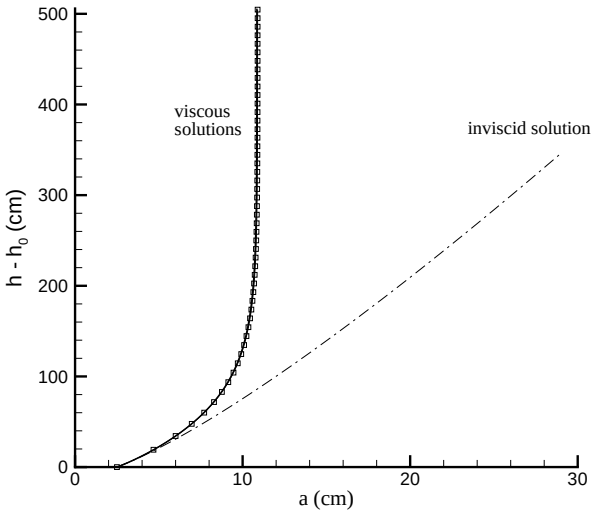

Fig. 13.6. The height of rise $h-h_0$ against the ring radius a. The dash-dotted line represents the inviscid solution obtained by putting $\nu = 0$ in (13.5.16). The solid line represents the viscous solution of (13.5.16) with the initial conditions (13.5.19) and (13.5.20). The symbol □ represents the viscous solution of (13.5.21) with the initial condition (13.5.19).

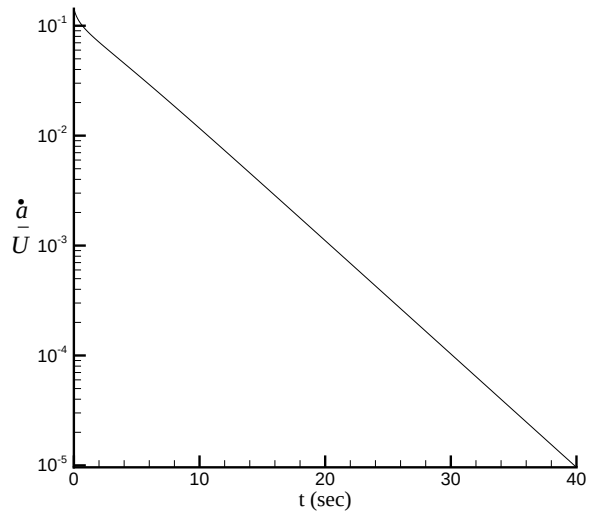

Fig. 13.7. The ratio between the ring expansion velocity $\dot{a}$ and the rise velocity U obtained from the solution of (13.5.16).

13.5.5 Stability of the toroidal vortex

Ponstein (1959) and Pedley (1967) studied capillary stability of a vortex core with core curvature neglected. This was the problem studied by Rayleigh (1892) with viscosity neglected and in chapter 16 with viscosity included, in which a strong stabilizing of circulation is demonstrated. The swirl velocity $v_\theta = \Gamma_*/2\pi r$ for $r \gg a$, is irrotational. For axially symmetric disturbances of the form $\exp[\mathrm{i}(kz - \omega t)]$, the dispersion relation is given by

$$\omega^2 = -\frac{kaK_1(ka)}{K_0(ka)}\left[\left(1-k^2a^2\right)\frac{\gamma}{\rho a^3} - \frac{\Gamma_*^2}{4\pi^2 a^4}\right]. \tag{13.5.28}$$

The flow is stable when ω^2 is positive and it is stable for all k when

$$\Gamma_*^2 \geq 4\pi^2 a\gamma/\rho. \tag{13.5.29}$$

Pedley obtained the same result and concluded that the vortex core would eventually become unstable because Γ_* decreases due to the action of viscosity and b decreases in his dynamic solution.

Pedley notes that his stability analysis ignores viscosity, and "... is therefore likely to be valid only if disturbance time scales are much shorter than the viscous diffusion time $36^2/8\nu$." Here we construct a purely irrotational analysis of the effects of viscosity on the stability of the same basic state using VPF. A viscous diffusion time does not enter into this analysis. †

13.5.5.1 Basic flow

We are considering the stability of a potential vortex with circulation $\Gamma_* = 2\pi\Gamma$. The velocity is purely azimuthal $\boldsymbol{u} = \boldsymbol{e}_\theta V_\theta$

$$V_\theta = \frac{\Gamma_*}{2\pi r} = \frac{\Gamma}{r}. \tag{13.5.30}$$

The pressure P is given by Bernoulli's equation

$$\frac{P}{\rho} = \frac{P_\infty}{\rho} - \frac{1}{2}V_\theta^2 = \frac{P_\infty}{\rho} - \frac{1}{2}\frac{\Gamma_*^2}{4\pi^2 r^2}, \tag{13.5.31}$$

where P_∞ is a constant. The normal stress balance at $r = a$ is

$$P(a) - P_0 = -\frac{\gamma}{a}, \tag{13.5.32}$$

where P_0 is the uniform pressure in the vortex $r < a$.

13.5.5.2 Small disturbances

The velocity potential for a small disturbance of the basic flow satisfies Laplace's equation

$$\frac{\partial^2\phi}{\partial r^2} + \frac{1}{r}\frac{\partial\phi}{\partial r} + \frac{1}{r^2}\frac{\partial^2\phi}{\partial\theta^2} + \frac{\partial^2\phi}{\partial z^2} = 0. \tag{13.5.33}$$

The free surface at $r = a$ is disturbed

$$r = a + \delta(\theta, z, t). \tag{13.5.34}$$

The disturbed surface satisfies

$$\frac{\partial\phi}{\partial r} = \frac{\partial\delta}{\partial t} + \frac{V_\theta}{r}\frac{\partial\delta}{\partial\theta}. \tag{13.5.35}$$

The disturbed normal stress balance on $r = a$ is

$$\frac{\Gamma_*^2}{4\pi^2 a^2}\frac{\delta}{a} + p - 2\nu\frac{\partial^2\phi}{\partial r^2} - 4\nu\frac{\Gamma}{a^3}\frac{\partial\delta}{\partial\theta} = \frac{\gamma}{\rho}\left(\frac{\delta}{a^2} + \frac{\partial^2\delta}{\partial z^2} + \frac{1}{a^2}\frac{\partial^2\delta}{\partial\theta^2}\right). \tag{13.5.36}$$

We seek a solution of (13.5.33)-(13.5.36) in normal modes

$$\phi = \phi_0(r)\exp(\imath kz - \imath\omega t + \imath n\theta) + c.c., \tag{13.5.37}$$

$$\delta = \delta_0\exp(\imath kz - \imath\omega t + \imath n\theta) + c.c. \tag{13.5.38}$$

† T.Funada, J.C.Padrino and D.D. Joseph, 2006 Purely irrotational theories of capillary instability of viscous liquids. Under preparation (see http://www.aem.umn.edu/people/faculty/joseph/ViscousPotentialFlow/.)

We find that $\phi_0 = AI_n(kr) + BK_n(kr)$. Since $I_n(kr)$ is unbounded as $r \to \infty$,

$$\phi_0 = BK_n(kr). \tag{13.5.39}$$

Then

$$p = -\frac{\partial \phi}{\partial t} - \frac{\Gamma}{r^2}\frac{\partial \phi}{\partial \theta} = \left(\imath\omega - \imath n\frac{\Gamma}{r^2}\right) BK_n(kr)\exp(\imath kz - \imath\omega t + \imath n\theta) + c.c. \tag{13.5.40}$$

and (13.5.35) implies that

$$\left(-\imath\omega + \imath n\frac{\Gamma}{a^2}\right)\delta_0 = BkK_n'(ka). \tag{13.5.41}$$

Hence

$$\phi = \left(-\imath\omega + \imath n\frac{\Gamma}{a^2}\right)\delta_0 \frac{K_n(kr)}{kK_n'(ka)}\exp(\imath kz - \imath\omega t + \imath n\theta) + c.c. \tag{13.5.42}$$

The normal stress condition (13.5.36) becomes

$$\begin{aligned}\left(\omega - n\frac{\Gamma}{a^2}\right)^2 \frac{K_n(ka)}{kaK_n'(ka)} + 2\imath\left(\omega - n\frac{\Gamma}{a^2}\right)\nu k^2 \frac{K_n''(ka)}{kaK_n'(ka)} \\ = \frac{\gamma}{\rho a^3}\left(1 - k^2a^2 - n^2\right) - \frac{\Gamma_*^2}{4\pi^2 a^4} + 4\nu\frac{\imath n\Gamma}{a^4}.\end{aligned} \tag{13.5.43}$$

which is a relation for the eigenvalue ω. By taking $n = 0$ in (13.5.43), VPF dispersion relation for axisymmetric disturbances is obtained

$$-\omega^2 \frac{K_0(ka)}{kaK_1(ka)} - 2\imath\omega\nu k^2\left(\frac{K_0(ka)}{kaK_1(ka)} + \frac{1}{k^2a^2}\right) = \frac{\gamma}{\rho a^3}\left(1 - k^2a^2\right) - \frac{\Gamma^2}{a^4}, \tag{13.5.44}$$

where standard formulae for the modified Bessel functions have been used. The dispersion relation (13.5.44) gives the irrotational effects of viscosity on the stability of the basic flow. With $\nu = 0$, (13.5.44) reduces to the Ponstein/Pedley result (13.5.28) for inviscid fluids. Introducing the following dimensionless parameters

$$k = \hat{k}/a, \qquad \omega = \imath\hat{\sigma}\sqrt{\frac{\gamma}{\rho a^3}}, \qquad \Gamma = \hat{\Gamma}\sqrt{\frac{\gamma a}{\rho}}, \tag{13.5.45}$$

and letting

$$\alpha = \frac{K_0(\hat{k})}{K_1(\hat{k})}, \tag{13.5.46}$$

expression (13.5.44) can be written as

$$\alpha\hat{\sigma}^2 + \frac{2}{\sqrt{J}}\hat{k}\left(1 + \hat{k}\alpha\right)\hat{\sigma} = \hat{k}\left(1 - \hat{k}^2 - \hat{\Gamma}^2\right), \tag{13.5.47}$$

where $J = Oh^2 = \rho\gamma a/\mu^2$ and Oh is the Ohnesorge number. Relation (13.5.47) is a quadratic equation for the eigenvalue $\hat{\sigma}$ with roots

$$\hat{\sigma} = -\frac{\hat{k}\left(1 + \hat{k}\alpha\right)}{\alpha\sqrt{J}} \pm \sqrt{\left[\frac{\hat{k}\left(1 + \hat{k}\alpha\right)}{\alpha\sqrt{J}}\right]^2 + \frac{\hat{k}}{\alpha}\left(1 - \hat{k}^2 - \hat{\Gamma}^2\right)}. \tag{13.5.48}$$

The motion is unstable to axisymmetric disturbances when $\mathrm{Re}[\hat{\sigma}] > 0$, which occurs if, and only if, $\hat{\Gamma}^2 < 1 - \hat{k}^2$ for which $\hat{\sigma}$ is real. Hence, when $\hat{\Gamma}^2 \geq 1$ the motion is stable for all $\hat{k}$ and when $\hat{k} \geq 1$ it is stable for all $\hat{\Gamma}$. When $\sqrt{J} \to \infty$, (13.5.47) goes to the inviscid result. Figure 13.8 shows the growth rate $\hat{\sigma}$ versus the wave-number $\hat{k}$ according to VPF relation (13.5.48) compared to the inviscid result for four values of J= 10^{-3}, 1, 100 and 10^6 and three values of the circulation $\hat{\Gamma}^2$= 0, 0.5 and 0.75. For small J (e.g., large viscosity) the difference between VPF and the inviscid theory is significant and viscosity diminishes the growth rate. As J increases, VPF results tend to the inviscid ones. For instance, for $J = 10^6$ no difference is discernible. Moreover, for J fixed, the growth rate decreases and the minimum wavelength of the unstable waves increases with decreasing $\hat{\Gamma}^2$ until instabilities totally vanish ($\hat{\Gamma}^2 \geq 1$).

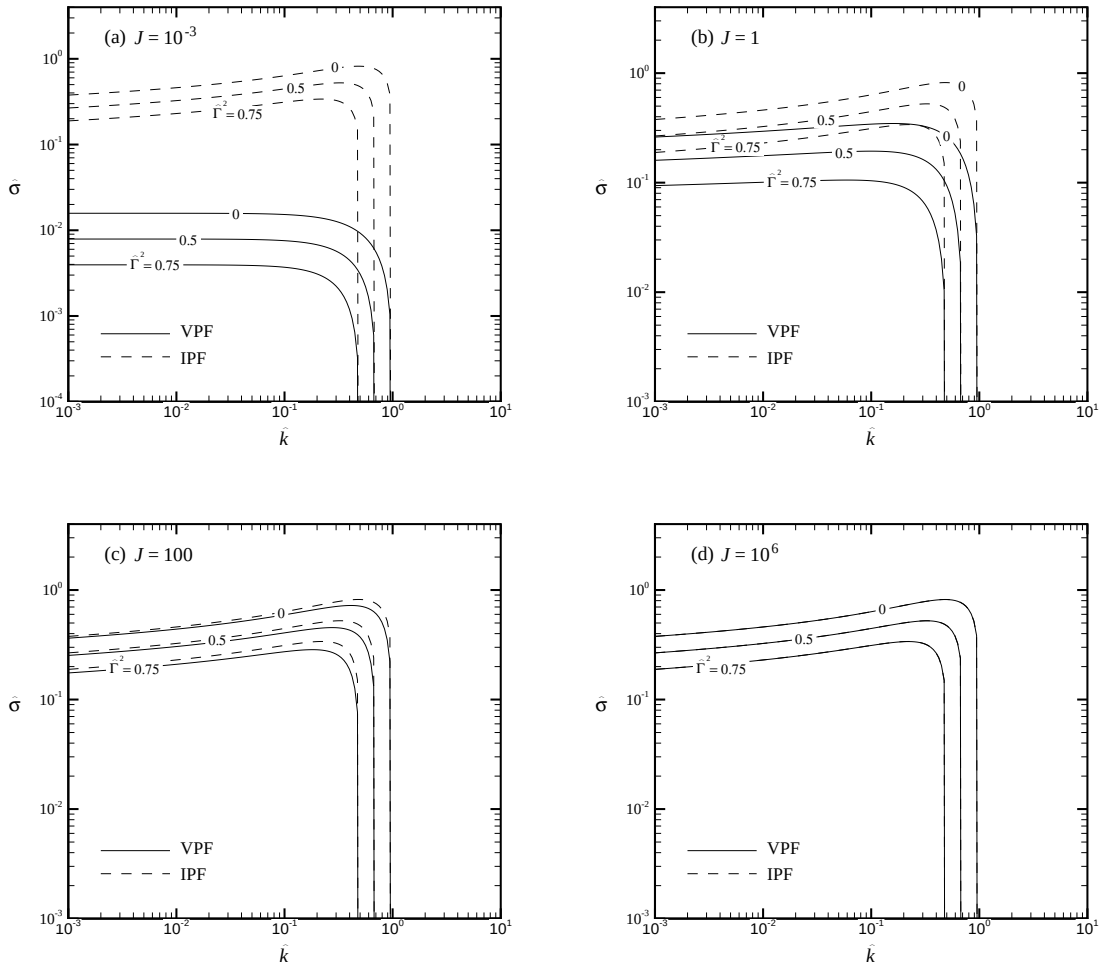

Fig. 13.8. Growth rate $\hat{\sigma}$ as a function of the wavenumber $\hat{k}$ for a cylindrical bubble with circulation $\hat{\Gamma}^2$. Instability takes place for the results shown. Four values of the parameter J are selected. The definition of the dimensionless quantities $\hat{\sigma}$, $\hat{k}$ and $\hat{\Gamma}$ is given in (13.5.45) and $J = \rho\gamma a/\mu^2$.

13.5.6 Boundary integral study of vortex ring bubbles in a viscous liquid

Lundgren and Mansour (1991) studied toroidal bubbles with circulation by a boundary integral method and by a physically motivated model equation (13.5.49). The numerical calculations were the first to reveal the deformations of the bubble shape in a fully nonlinear context. Two series of computations were performed;

"... one set shows the starting motion of an initially spherical bubble as a gravitationally driven liquid jet penetrates through the bubble from below causing a toroidal geometry to develop. The jet becomes broader as surface tension increases and fails to penetrate if surface tension is too large. The dimensionless circulation that develops is not very dependent on the surface tension. The second series of computations starts from a toroidal geometry, with circulation determined from the earlier series, and follows the motion of the rising and spreading vortex ring. Some modifications to the boundary-integral formulation were devised to handle the multiply connected geometry."

The irrotational effects of viscosity were not studied but they can be obtained by boundary integral methods following the work of Miksis *et al.* (1982), Georgescu *et al.* (2002) and Canot *et al.* (2003).

The physically motivated model of vortex ring bubbles proposed by Lundgren and Mansour is based on the force-momentum balance on a section of a slender ring, treated as locally two-dimensional, given by

$$\rho A \frac{\mathrm{d}\boldsymbol{u}}{\mathrm{d}t} = \rho \Gamma_* \boldsymbol{t} \times \boldsymbol{u} + \rho A g \boldsymbol{e}_z. \tag{13.5.49}$$

The term on the left is the apparent mass per unit length times acceleration. The first term on the right is the Kutta-Joukowski lift per unit length on a vortex in cross flow. It acts perpendicularly to the relative velocity

$\boldsymbol{u}$. The unit vector $\boldsymbol{t}$ is along the centerline of the vortex, in the direction of the vorticity. The last term is the buoyancy force per unit length acting in the upward direction.

Lundgren and Mansour consider the case in which the acceleration $\dfrac{\mathrm{d}\boldsymbol{u}}{\mathrm{d}t} = 0$ but the dimensionless ring radius $R = a/r_0$ changes with time. After expressing

$$\boldsymbol{u} = \boldsymbol{e}_r u + \boldsymbol{e}_z v$$

in dimensionless form with $\dot{u},\ \dot{v} = 0$, they find that $v = 0$,

$$u = \frac{2}{3\Gamma R}, \quad R = \left\{ R_0^2 + \frac{4t}{3\Gamma} \right\}^{1/2} \tag{13.5.50}$$

where Γ is a dimensionless circulation. They note "... that equation (13.5.50) is Turner's result for a constant volume buoyant vortex ring. Our interpretation is that the ring spreads radially at a velocity that gives just enough downward cross flow lift to balance the upward buoyancy force. This is the direct physical reason for the radial growth of the ring."

As in the case of impulse, the addition of an irrotational viscous drag per unit length

$$-\mu \tilde{D} \boldsymbol{e}_z$$

to equation (13.5.49) alters the dynamics in a fundamental way. In this case the system evolves to steady state in which the viscous drag balances the buoyant lift

$$\mu \tilde{D} = \rho g A$$

with no further increase of the radius of the core or ring.

13.5.7 Irrotational motion of a massless cylinder under the combined action of Kutta-Joukowski lift, acceleration of added mass and viscous drag

Consider the irrotational motion of a cylinder of radius a in a viscous fluid with circulation Γ. Our analysis follows that given by Lundgren and Mansour (1991) for the same problem in an inviscid fluid. Let

$$\boldsymbol{R}(t) = X(t)\boldsymbol{i} + Y(t)\boldsymbol{j} \tag{13.5.51}$$

be the instantaneous position of the center of the cylinder. The velocity is then

$$\dot{\boldsymbol{R}} = U\boldsymbol{i} + V\boldsymbol{j}. \tag{13.5.52}$$

The direction of the velocity $\boldsymbol{n}$ is

$$\boldsymbol{n} = \frac{U}{W}\boldsymbol{i} + \frac{V}{W}\boldsymbol{j} \text{ with } W = \sqrt{U^2 + V^2}. \tag{13.5.53}$$

The motion is approximated by a potential flow. The dissipation per unit length for a cylinder moving with a speed W and a circulation Γ evaluated using the potential flow is (Wang and Joseph 2006a)

$$D = 8\pi\mu W^2 + \frac{\mu\Gamma^2}{\pi a^2}. \tag{13.5.54}$$

The dissipation should be equal to the power of the drag and torque on the cylinder. Ackeret (1952) did not consider the torque and used this dissipation to compute the drag on the cylinder:

$$\mathcal{D} = D/W = 8\pi\mu W + \frac{\mu\Gamma^2}{\pi a^2 W}. \tag{13.5.55}$$

Here we use this drag for the purpose of illustration of the viscous effect on the dynamics of the cylinder.

Lundgren and Mansour (1991) derived an equation (their Equation A7) governing the motion of the cylinder based on the assumption that the cylinder is a massless bubble and has no applied force. If the drag force (13.5.55) is added, the governing equation for the motion becomes

$$\rho\pi a^2 \ddot{\boldsymbol{R}} = \rho\Gamma \boldsymbol{k} \times \boldsymbol{R} - \mathcal{D}\boldsymbol{n}, \tag{13.5.56}$$

that is, the apparent mass times acceleration is balanced by the Kutta-Joukowski lift and the viscous drag. To make (13.5.56) dimensionless, we introduce the following scales

$$[\text{length}, \text{velocity}, \text{time}] \sim \left[a,\ \frac{\Gamma}{a\pi},\ \frac{a^2\pi}{\Gamma}\right]. \tag{13.5.57}$$

In this analysis, we assume that the circulation Γ is a constant and does not depend on time. The dimensionless equations are written in the scalar form as follows

$$\dot{\tilde{U}} = -\tilde{V} - \frac{1}{R_e}\left(8\tilde{W} + \frac{1}{\tilde{W}}\right)\frac{\tilde{U}}{\tilde{W}}, \tag{13.5.58}$$

$$\dot{\tilde{V}} = \tilde{U} - \frac{1}{R_e}\left(8\tilde{W} + \frac{1}{\tilde{W}}\right)\frac{\tilde{V}}{\tilde{W}}, \tag{13.5.59}$$

where "$\sim$" indicates dimensionless parameters and the Reynolds number is defined as

$$R_e = \frac{\rho\Gamma}{\mu\pi}. \tag{13.5.60}$$

We set the initial conditions for (13.5.58) and (13.5.59) arbitrarily to be

$$\tilde{U}(t=0) = 10, \text{ and } \tilde{V}(t=0) = 0. \tag{13.5.61}$$

The set of equations (13.5.58), (13.5.59) and (13.5.61) can be solved analytically. First we assume

$$\tilde{U} = \tilde{W}\cos\theta, \quad \tilde{V} = \tilde{W}\sin\theta, \tag{13.5.62}$$

thus we have a set of equations:

$$\left.\begin{aligned}
&\frac{\mathrm{d}\tilde{U}}{\mathrm{d}t} = \frac{\mathrm{d}\tilde{W}}{\mathrm{d}t}\cos\theta - \tilde{W}\sin\theta\frac{\mathrm{d}\theta}{\mathrm{d}t} = -\tilde{V} - \frac{1}{R_e}\left(8\tilde{W} + \frac{1}{\tilde{W}}\right)\frac{\tilde{U}}{\tilde{W}} \\
&= -\tilde{W}\sin\theta - \frac{1}{R_e}\left(8\tilde{W} + \frac{1}{\tilde{W}}\right)\cos\theta, \\
&\frac{\mathrm{d}\tilde{V}}{\mathrm{d}t} = \frac{\mathrm{d}\tilde{W}}{\mathrm{d}t}\sin\theta + \tilde{W}\cos\theta\frac{\mathrm{d}\theta}{\mathrm{d}t} = \tilde{U} - \frac{1}{R_e}\left(8\tilde{W} + \frac{1}{\tilde{W}}\right)\frac{\tilde{V}}{\tilde{W}} \\
&= \tilde{W}\cos\theta - \frac{1}{R_e}\left(8\tilde{W} + \frac{1}{\tilde{W}}\right)\sin\theta.
\end{aligned}\right\} \tag{13.5.63}$$

Multiply the first of (13.5.63) by $\cos\theta$ and the second by $\sin\theta$, then the sum gives

$$\frac{\mathrm{d}\tilde{W}}{\mathrm{d}t} = -\frac{1}{R_e}\left(8\tilde{W} + \frac{1}{\tilde{W}}\right) \ \rightarrow\ \frac{\mathrm{d}}{\mathrm{d}t}\left(\frac{1}{2}\tilde{W}^2\right) = -\frac{1}{R_e}\left(8\tilde{W}^2 + 1\right) \tag{13.5.64}$$

$$\tilde{W}^2 + \frac{1}{8} = C_1\exp\left(-16t/R_e\right). \tag{13.5.65}$$

Multiply the first by $\sin\theta$ and the second by $\cos\theta$, then the subtraction gives

$$\tilde{W}\frac{\mathrm{d}\theta}{\mathrm{d}t} = \tilde{W} \ \rightarrow\ \frac{\mathrm{d}\theta}{\mathrm{d}t} = 1 \ \rightarrow\ \theta = t + C_2. \tag{13.5.66}$$

The integration constants C_1 and C_2 are to be determined by initial conditions; $C_1 = 10^2 + \frac{1}{8}$ and $C_2 = 0$. When $R_e \rightarrow \infty$, $\tilde{W}$=constant and $\theta = t + C_2$. $\tilde{U}$ and $\tilde{V}$ are integrated to obtain the position of the cylinder. The calculation results are shown in figure 13.9.

When $R_e \rightarrow \infty$, the results tend to be the same as the inviscid solution given by Lundgren and Mansour (1991); the cylinder moves with a constant speed along a circular path. When the Reynolds number is finite, the cylinder moves in a spiral fashion. The speed decreased continuously because of the viscous effect and the cylinder eventually stops. The dimensionless stopping time is about 8.36 for R_e =20 and 41.79 for R_e =100. The paths from the start to the end of the motion are shown for R_e =20 and 100 in figure 13.9.

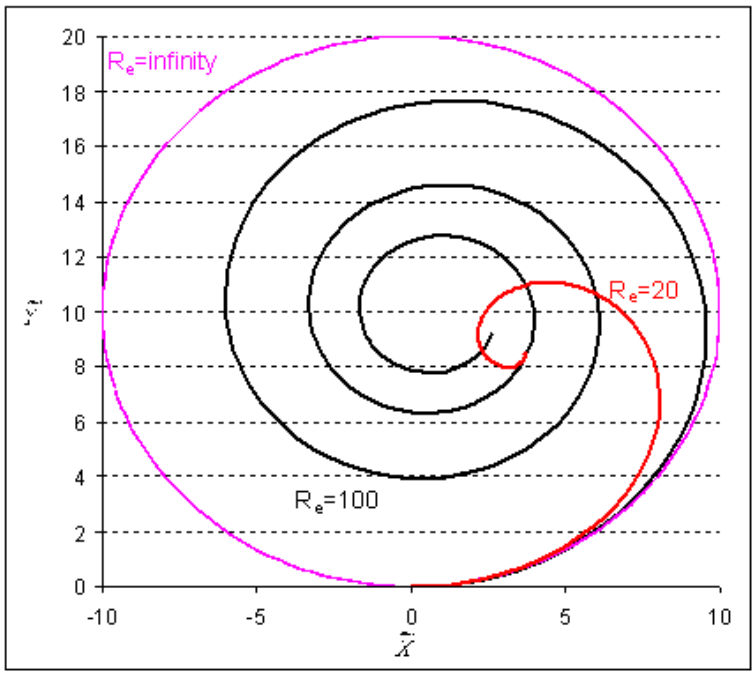

Fig. 13.9. The path of the cylinder at different Reynolds numbers. —: $R_e \to \infty$; —: R_e=100; —: R_e=20.

13.6 The motion of a spherical gas bubble in viscous potential flow

A spherical gas bubble accelerates to steady motion in an irrotational flow of a viscous liquid induced by a balance of the acceleration of the added mass of the liquid with the Levich drag. The equation of rectilinear motion is linear and may be integrated giving rise to exponential decay with a decay constant $18\nu t/a^2$ where ν is the kinematic viscosity of the liquid and a is the bubble radius. The problem of decay to rest of a bubble moving initially when the forces maintaining motion are inactivated and the acceleration of a bubble initially at rest to terminal velocity are considered. The equation of motion follows from the assumption that the motion of the viscous liquid is irrotational. It is an elementary example of how potential flows can be used to study the unsteady motions of a viscous liquid suitable for the instruction of undergraduate students.

We consider a body moving with the velocity U in an unbounded viscous potential flow. Let M be the mass of the body and M' be the added mass, then the total kinetic energy of the fluid and body is

$$T = \frac{1}{2}(M + M')U^2. \tag{13.6.1}$$

Let D be the drag and F be the external force in the direction of motion, then the power of D and F should be equal to the rate of the total kinetic energy,

$$(F + D)U = \frac{\mathrm{d}T}{\mathrm{d}t} = (M + M')U\frac{\mathrm{d}U}{\mathrm{d}t}. \tag{13.6.2}$$

We next consider a spherical gas bubble, for which $M = 0$ and $M' = \frac{2}{3}\pi a^3\rho_f$. The drag can be obtained by direct integration using the irrotational viscous normal stress and a viscous pressure correction: $D = -12\pi\mu aU$ (see Joseph and Wang 2004). Suppose the external force just balances the drag, then the bubble moves with a constant velocity $U = U_0$. Imagine that the external force suddenly disappears, then (13.6.2) gives rise to

$$-12\pi\mu aU = \frac{2}{3}\pi a^3\rho_f\frac{\mathrm{d}U}{\mathrm{d}t}. \tag{13.6.3}$$

The solution is

$$U = U_0\mathrm{e}^{-\frac{18\nu}{a^2}t}, \tag{13.6.4}$$

which shows that the velocity of the bubble approaches zero exponentially.

If gravity is considered, then $F = \frac{4}{3}\pi a^3\rho_f g$. Suppose the bubble is at rest at $t = 0$ and starts to move due to

the buoyant force. Equation (13.6.2) can be written as

$$\frac{4}{3}\pi a^3\rho_f g - 12\pi\mu a U = \frac{2}{3}\pi a^3\rho_f \frac{\mathrm{d}U}{\mathrm{d}t}. \tag{13.6.5}$$

The solution is

$$U = \frac{a^2 g}{9\nu}\left(1 - \mathrm{e}^{-\frac{18\nu}{a^2}t}\right), \tag{13.6.6}$$

which indicates the bubble velocity approaches the steady state velocity

$$U = \frac{a^2 g}{9\nu} \tag{13.6.7}$$

exponentially.

Another way to obtain the equation of motion is to argue following Lamb (1932) and Levich (1949) that the work done by the external force F is equal to the rate of the total kinetic energy and the dissipation:

$$FU = (M + M')U\frac{\mathrm{d}U}{\mathrm{d}t} + \mathcal{D}. \tag{13.6.8}$$

Since $\mathcal{D} = -DU$, (13.6.8) is the same as (13.6.2).

The motion of a single spherical gas bubble in a viscous liquid has been considered by some authors. Typically, these authors assemble terms arising in various situations, like Stokes flow (Hadamard-Rybczynski drag, Basset memory integral) and high Reynolds number flow (Levich drag, boundary layer drag, induced mass) and other terms into a single equation. Such general equations have been presented by Yang and Leal (1991) and by Park, Klausner and Mei (1995) and they have been discussed in the review paper of Magnaudet and Eams (2000, see their section 4). Yang and Leal's equation has Stokes drag and no Levich drag. Our equation is not embedded in their equation. Park *et al.* listed five terms for the force on a gas bubble; our equation may be obtained from theirs if the free stream velocity U is put to zero, the memory term is dropped, and the boundary layer contribution to the drag given by Moore (1963) is neglected. Park *et al.* did not write down the same equation as our equation (13.6.5) and did not obtain the exponential decay.

It is generally believed that the added mass contribution, derived for potential flow is independent of viscosity. Magnaudet and Eames say that "... results all indicate that the added mass coefficient is independent of the Reynolds, strength of acceleration and ... boundary conditions." This independence of added mass on viscosity follows from the assumption that the motion of viscous fluids can be irrotational. The results cited by Magnaudet and Eams seem to suggest that induced mass is also independent of vorticity.

Chen (1974) did a boundary layer analysis of the impulsive motion of a spherical gas bubble which shows that the Levich drag $48/R_e$ at short times evolves to the drag $\frac{48}{R_e}\left(1 - \frac{2.21}{\sqrt{R_e}}\right)$ obtained in a boundary layer analysis by Moore (1963). The Moore drag cannot be distinguished from the Levich drag when R_e is large. The boundary layer contribution is vortical and is neglected in our potential flow analysis.

13.7 Steady motion of a deforming gas bubble in a viscous potential flow

Miksis, Vanden-Broeck and Keller (MVK, 1982) computed the shape of an axisymmetric rising bubble, or a falling drop, in an incompressible fluid assuming that the flow in the liquid is irrotational but viscous. The boundary condition for the normal stress including surface tension is satisfied but as in other problems of VPF, the tangential stress is neglected. The shape function is obtained from the gravitational potential evaluated on the free surface; two shape functions are computed, one on the top and one on the bottom of the bubble. The shape is single valued on each function. The potential function is obtained from the values of the potential on the free surface, using a Green's function approach following ideas introduced by Longuet-Higgins and Cokelet (1976), Vanden-Broeck and Keller (1980) and Miksis, Vanden-Broeck and Keller (1981). The system of differential and integral equations are solved in a frame in which the bubble is stationary and the velocity at infinity is U which is calculated by a drag balance in two ways. The first calculation is like that of Moore (1959) in which the drag comes from the normal irrotational viscous stress leading to $32/R$. This direct method should not be used because of the additional contribution due to the irrotational viscous pressure.

This pressure is not easy to calculate in general, but the correct drag leading to $48/R$ can be obtained, and was obtained by MVK in a second calculation using the dissipation method.

The solution of the system of governing equations was obtained as a power series in the Weber number and

R^{-1} and is therefore restricted to low Weber numbers (large surface tension) and high Reynolds numbers (small viscosity).

13.8 Dynamic simulations of the rise of many bubbles in a viscous potential flow

This problem was considered by Sangani and Didwania (1993). They placed N bubbles initially randomly within a unit cell and assumed that the entire space is filled with copies of this cell. They determined the potential flow around many bubbles exactly by using a multiple expansion. They computed a drag force on the bubbles by two different methods: (1) compute the gradient of the total viscous energy based on the relative velocity of individual bubbles (2) compute the bounce of colliding bubbles assuming that the collision time is short compared to the timescale for the inertial motion and that the momentum and kinetic energy is conserved in the motion (Sangani 1991). These are apparently quite different mechanisms; one depends on viscosity, the other on inertia.

They did simulations in which they include buoyancy and viscous forces. They find that the state of uniform bubbly liquids is unstable under the aforementioned conditions and that the bubbles form large aggregates by arranging themselves in planes perpendicular to gravity. These aggregates form even when a swarm of gas bubbles rises through a liquid at rest.

We think that the aggregates which form are due to the same inertial forces which turn long bodies broadside-on and cause aircraft to stall. Colliding bubbles are unstable long bodies which look for a stable configuration with line of centers across the stream. The dynamic scenario underway is called "drafting, kissing and tumbling." This scenario is discussed in §20.7.1 and §20.7.2.

14

Purely irrotational theories of the effect of the viscosity on the decay of waves

14.1 Decay of free gravity waves

It is generally believed that the major effects of viscosity are associated with vorticity. This belief is not always well founded; major effects of viscosity cachap14-sep11-nocup.n be obtained from purely irrotational analysis of flows of viscous fluids. Here we illustrate this point by a comparing irrotational solutions with Lamb's 1932 exact solution of the problem of the decay of free gravity waves. Excellent agreements, even in fluids 10^7 more viscous than water, are achieved for the decay rates $n(k)$ for all wave numbers k excluding a small interval around a critical value k_c where progressive waves change to monotonic decay.

14.1.1 Introduction

Lamb (1932, §348, §349) performed an analysis of the effect of viscosity on free gravity waves. He computed the decay rate by a dissipation method using the irrotational flow only. He also constructed an exact solution for this problem, which satisfies both the normal and shear stress conditions at the interface.

Joseph & Wang (2004) studied Lamb's problem using the theory of viscous potential flow (VPF) and obtained a dispersion relation which gives rise to both the decay rate and wave-velocity. They also used VCVPF to obtain another dispersion relation. Since VCVPF is an irrotational theory the shear stress cannot be made to vanish. However, the shear stress in the energy balance can be eliminated in the mean by the selection of an irrotational pressure which depends on viscosity.

Here we find that the viscous pressure correction gives rise to a higher order irrotational correction to the velocity which is proportional to the viscosity and does not have a boundary layer structure. The corrected velocity depends strongly on viscosity and is not related to vorticity. The corrected irrotational flow gives rise to a dispersion relation which is in splendid agreement with Lamb's exact solution, which has no explicit viscous pressure. The agreement with the exact solution holds for fluids even 10^7 times more viscous than water and for all wave numbers away from the cutoff wave number k_c which marks the place where progressive waves change to monotonic decay. We find that VCVPF gives rise to the same decay rate as in Lamb's exact solution and in his dissipation calculation when $k < k_c$. The exact solution agrees with VPF when $k > k_c$. The effects of vorticity are evident only in a small interval centered on the cutoff wave number. We present a comprehensive comparison for the decay rate and wave-velocity given by Lamb's exact solution and Joseph and Wang's VPF and VCVPF theories.

14.1.2 Irrotational viscous corrections for the potential flow solution

The gravity wave problem is governed by the linearized Navier-Stokes equation and the continuity equation

$$\frac{\partial \mathbf{u}}{\partial t} = -\frac{1}{\rho}\nabla p - g\mathbf{e}_y + \nu\nabla^2\mathbf{u}, \tag{14.1.1}$$

$$\nabla \cdot \mathbf{u} = 0, \tag{14.1.2}$$

subject to the boundary conditions at the free surface ($y \approx 0$)

$$T_{xy} = 0, \quad T_{yy} = 0, \tag{14.1.3}$$

where T_{xy} and T_{yy} are components of the stress tensor and the surface tension is neglected. Surface tension is important at high wavenumbers but, for simplicity, is neglected in the analyses given here. We divide the velocity and pressure field into two parts

$$\mathbf{u} = \mathbf{u}_{\mathrm{p}} + \mathbf{u}_{\mathrm{v}}, \quad p = p_{\mathrm{p}} + p_{\mathrm{v}}, \tag{14.1.4}$$

where the subscript p denotes potential solutions and v denotes viscous corrections. The potential solutions satisfy

$$\mathbf{u}_{\mathrm{p}} = \nabla\phi, \quad \nabla^2\phi = 0, \tag{14.1.5}$$

and

$$\frac{\partial \mathbf{u}_{\mathrm{p}}}{\partial t} = -\frac{1}{\rho}\nabla p_{\mathrm{p}} - g\mathbf{e}_y. \tag{14.1.6}$$

The viscous corrections are governed by

$$\nabla \cdot \mathbf{u}_{\mathrm{v}} = 0, \tag{14.1.7}$$

$$\frac{\partial \mathbf{u}_{\mathrm{v}}}{\partial t} = -\frac{1}{\rho}\nabla p_{\mathrm{v}} + \nu\nabla^2\mathbf{u}_{\mathrm{v}}. \tag{14.1.8}$$

We take the divergence of (14.1.8) and obtain

$$\nabla^2 p_{\mathrm{v}} = 0, \tag{14.1.9}$$

which shows that the pressure correction must be harmonic. Next we introduce a stream function ψ so that (14.1.7) is satisfied identically:

$$u_{\mathrm{v}} = -\frac{\partial\psi}{\partial y}, \quad v_{\mathrm{v}} = \frac{\partial\psi}{\partial x}. \tag{14.1.10}$$

We eliminate p_{v} from (14.1.8) by cross differentiation and obtain following equation for the stream function

$$\frac{\partial}{\partial t}\nabla^2\psi = \nu\nabla^4\psi. \tag{14.1.11}$$

To determine the normal modes which are periodic in respect of x with a prescribed wave-length $\lambda = 2\pi/k$, we assume that

$$\psi = B\mathrm{e}^{nt+\imath kx}\mathrm{e}^{my}, \tag{14.1.12}$$

where m is to be determined from (14.1.11). Inserting (14.1.12) into (14.1.11), we obtain

$$(m^2 - k^2)\left[n - \nu(m^2 - k^2)\right] = 0. \tag{14.1.13}$$

The root $m^2 = k^2$ gives rise to irrotational flow; the root $m^2 = k^2 + n/\nu$ leads to the rotational component of the flow. The rotational component cannot give rise to a harmonic pressure satisfying (14.1.9) because

$$\nabla^2\mathrm{e}^{nt+\mathrm{i}kx}\mathrm{e}^{my} = (m^2 - k^2)\mathrm{e}^{nt+\mathrm{i}kx}\mathrm{e}^{my} \tag{14.1.14}$$

does not vanish if $m^2 \neq k^2$. Thus, the governing equation for the rotational part of the flow can be written as

$$\frac{\partial\psi}{\partial t} = \nu\nabla^2\psi. \tag{14.1.15}$$

This is the equation used by Lamb (1932) for the rotational part of his exact solution.

The effect of viscosity on the decay of a free gravity wave can be approximated by a purely irrotational theory in which the explicit appearance of the irrotational shear stress in the mechanical energy equation is eliminated by a viscous contribution p_{v} to the irrotational pressure. In this theory $\mathbf{u}{=}\nabla\phi$ and a stream function, which is associated with vorticity, is not introduced. The kinetic energy, potential energy and dissipation of the flow can be computed using the potential flow solution

$$\phi = A\mathrm{e}^{nt+ky+\mathrm{i}kx}. \tag{14.1.16}$$

We insert the potential flow solution into the mechanical energy equation (12.5.14)

$$\int_{S_{\mathrm{f}}} u_{\mathrm{n}}\left[\rho\left(\frac{\partial\phi}{\partial t} + \frac{|\nabla\phi|^2}{2} + g\eta\right) + 2\mu\frac{\partial^2\phi}{\partial n^2} + \gamma\nabla_{\mathrm{II}}\cdot\mathbf{n}\right]\mathrm{d}S_{\mathrm{f}} = -\int_{S_{\mathrm{f}}}\tau_{\mathrm{s}}u_{\mathrm{s}}\mathrm{d}S_{\mathrm{f}}, \tag{14.1.17}$$

where η is the elevation of the surface and $\mathbf{D}$ is the rate of strain tensor. The pressure correction $p_{\rm v}$ satisfies

$$\int_0^\lambda v(-p_{\rm v})\mathrm{d}x = \int_0^\lambda u\tau_{xy}\mathrm{d}x. \tag{14.1.18}$$

But in our problem here, there is no explicit viscous pressure function in the exact solution [see (14.1.23) and (14.1.24)]. It turns out that the pressure correction defined here in the purely irrotational flow is related to quantities in the exact solution in a complicated way which requires further analysis [see (14.1.30)].

Joseph & Wang (2004) solved for the harmonic pressure correction from (14.1.9), then determined the constant in the expression of $p_{\rm v}$ using (14.1.18), and obtained

$$p_{\rm v} = -2\mu k^2 A\mathrm{e}^{nt+ky+\mathrm{i}kx}. \tag{14.1.19}$$

The velocity correction associated with this pressure correction can be obtained from (14.1.8). We seek normal modes solution $\mathbf{u}_{\rm v} \sim \mathrm{e}^{nt+ky+\imath kx}$ and equation (14.1.8) becomes

$$\rho n\mathbf{u}_{\rm v} = -\nabla p_{\rm v}. \tag{14.1.20}$$

Hence, $\mathrm{curl}(\mathbf{u}_{\rm v}) = 0$ and $\mathbf{u}_{\rm v}$ is irrotational. After assuming $\mathbf{u}_{\rm v} = \nabla\phi_1$ and $\phi_1 = A_1\mathrm{e}^{nt+ky+\mathrm{i}kx}$, we obtain

$$\rho n\phi_1 = -p_{\rm v} \quad \Rightarrow \quad \phi_1 = \frac{2\mu k^2}{\rho n}A\mathrm{e}^{nt+ky+\mathrm{i}kx}. \tag{14.1.21}$$

Given ϕ_1, the correction η_1 of η can be computed from the equation $n\eta = \partial\phi_1/\partial y$.

This calculation shows that the velocity $\mathbf{u}_{\rm v}$ associated with the pressure correction is irrotational. The pressure correction (14.1.19) is proportional to μ and it induces a correction ϕ_1 given by (14.1.21), which is also proportional to μ. The shear stress computed from $\mathbf{u}_{\rm v} = \nabla\phi_1$ is then proportional to μ^2. To balance this non-physical shear stress, one can add a pressure correction proportional to μ^2, which will in turn induce a correction for the velocity potential proportional to μ^2. One can continue to build higher order corrections and they will all be irrotational. The final velocity potential has the following form

$$\phi = (A + A_1 + A_2 + \cdots)\mathrm{e}^{nt+ky+\mathrm{i}kx}, \tag{14.1.22}$$

where $A_1 \sim \mu$, $A_2 \sim \mu^2$... Thus the VCVPF theory is an approximation to the exact solution based on solely potential flow solutions, but the normal stress condition and n are not corrected.

Prosperetti (1976) considered viscous effects on standing free gravity waves using the same governing equations (14.1.7) and (14.1.8) for the viscous correction terms. If we adapt our VCPVF method to treat standing waves represented by the potential $\phi = k^{-1}(\mathrm{d}a/\mathrm{d}t)\mathrm{e}^{ky}\cos kx$, we can obtain $-p_{\rm v} = 2\mu k(\mathrm{d}a/\mathrm{d}t)\mathrm{e}^{ky}\cos kx$, which is exactly the same pressure correction obtained by Prosperetti (1976) using a different method.

14.1.3 Relation between the pressure correction and Lamb's exact solution

It has been conjectured and is widely believed (Moore 1963; Harper and Moore 1968; Joseph and Wang 2004) that a viscous pressure correction arises in the vortical boundary layer at the free surface which is neglected in the irrotational analysis. However, no viscous pressure correction arises in Lamb's exact solution. His solution is given by a potential ϕ and a stream function ψ:

$$u = \frac{\partial\phi}{\partial x} - \frac{\partial\psi}{\partial y}, \quad v = \frac{\partial\phi}{\partial y} + \frac{\partial\psi}{\partial x}, \quad \frac{p}{\rho} = -\frac{\partial\phi}{\partial t} - gy, \tag{14.1.23}$$

satisfying

$$\nabla^2\phi = 0, \quad \partial\psi/\partial t = \nu\nabla^2\psi. \tag{14.1.24}$$

The stream function gives rise to the rotational part of the flow. No pressure term enters into the stream function equation, as we have shown in the previous section that the only harmonic pressure for the rotational part is zero. The pressure p comes from Bernoulli's equation in (14.1.23) and no explicit viscous pressure exists, though p depends on the viscosity through the velocity potential. Lamb shows that (14.1.24) can be solved with normal modes

$$\phi = A\mathrm{e}^{ky}\mathrm{e}^{\mathrm{i}kx+nt}, \quad \psi = C\mathrm{e}^{my}\mathrm{e}^{\mathrm{i}kx+nt}, \quad m^2 = k^2 + n/\nu, \tag{14.1.25}$$

where A and C are constants.

k	$p_{\rm v}/\rho$	term1	term2	term 3	term 4
0.01	-2.063×10^{-6}	$-1.325\times10^{-9}+$ $\imath 2.01\times10^{-4}$	$-2.063\times10^{-6}-$ $\imath 2.01\times10^{-4}$	-1.325×10^{-9}	$5.300\times10^{-9}+$ $\imath 5.300\times10^{-9}$
0.1	-2.057×10^{-4}	$-7.441\times10^{-7}+$ $\imath 0.00358$	$-2.071\times10^{-4}-$ $\imath 0.00358$	-7.461×10^{-7}	$2.980\times10^{-6}+$ $\imath 2.980\times10^{-6}$
1	-0.02022	$-4.207\times10^{-4}+$ $\imath 0.06272$	$-0.02106-$ $\imath 0.06440$	-4.186×10^{-4}	$0.001679+$ $\imath 0.001679$
10	-1.881	$-0.3131+\imath 0.6303$	$-2.423-\imath 1.513$	-0.1829	$1.038+\imath 0.8830$

Table 14.1. *The value of each term in (14.1.30) normalized by A^E for SO10000 oil at different wave numbers; term1 = $\partial\left(\phi^J-\phi^E\right)/\partial t$, term2 = $g(\eta^J-\eta^E)$, term3 =$2\nu\partial^2\left(\phi^J-\phi^E\right)/\partial y^2$, and term4 = $2\nu\partial^2\psi^E/\partial x\partial y$.*

It is therefore of interest to derive the connection between the viscous pressure correction $p_{\rm v}$ in our VCVPF theory and Lamb's exact solution; superscript E represents Lamb's exact solution and J represent Joseph and Wang's VCVPF theory. The irrotational pressure in the two solutions are

$$p^E=-\rho\frac{\partial\phi^E}{\partial t}-\rho g\eta^E,\quad p_{\rm i}^J=-\rho\frac{\partial\phi^J}{\partial t}-\rho g\eta^J. \tag{14.1.26}$$

The elevation η is obtained from the kinematic condition at $y\approx 0$

$$\frac{\partial\eta}{\partial t}^E=\frac{\partial\phi^E}{\partial y}+\frac{\partial\psi^E}{\partial x},\quad \frac{\partial\eta}{\partial t}^J=\frac{\partial\phi^J}{\partial y}. \tag{14.1.27}$$

The normal stress balance for the two solutions is

$$T_{yy}^E=-p^E+2\mu\frac{\partial^2\phi^E}{\partial^2 y}+2\mu\frac{\partial^2\psi^E}{\partial x\partial y}=0, \tag{14.1.28}$$

$$T_{yy}^J=-p_{\rm i}^J-p_{\rm v}+2\mu\frac{\partial^2\phi^J}{\partial^2 y}=0. \tag{14.1.29}$$

Therefore $T_{yy}^E-T_{yy}^J=0$ and we can obtain

$$\frac{p_{\rm v}}{\rho}=\frac{\partial\left(\phi^J-\phi^E\right)}{\partial t}+g(\eta^J-\eta^E)+2\nu\frac{\partial^2\left(\phi^J-\phi^E\right)}{\partial y^2}-2\nu\frac{\partial^2\psi^E}{\partial x\partial y}. \tag{14.1.30}$$

The amplitude A for the potential is different in Lamb's exact solution and in VCPVF:

$$\phi^E=A^E{\rm e}^{nt+ky+{\rm i}kx},\quad \phi^J=A^J{\rm e}^{nt+ky+{\rm i}kx},\quad A^E\neq A^J. \tag{14.1.31}$$

To make the two solutions comparable, we compute the relation between A^E and A^J by equating the dissipation evaluated using Lamb's exact solution and evaluated using VCVPF. In Table 14.1 we list the values of each term in (14.1.30) normalized by A^E. It seems that the term $g(\eta^J-\eta^E)$ gives the most important contribution to p_v, but the other terms are not negligible.

14.1.4 Comparison of the decay rate and wave-velocity given by the exact solution, VPF and VCVPF

When the surface tension is ignored, Lamb's exact solution gives rise to the following dispersion relation:

$$n^2+4\nu k^2 n+4\nu^2k^4+gk=4\nu^2k^3\sqrt{k^2+n/\nu}. \tag{14.1.32}$$

Lamb considered the solution of (14.1.32) in the limits of small k and large k. When $k\ll k_c=({\rm g}/\nu^2)^{1/3}$, he obtained approximately

$$n=-2\nu k^2\pm{\rm i}k\sqrt{g/k}, \tag{14.1.33}$$

which gives rise to the decay rate $-2\nu k^2$, in agreement with the dissipation result, and the wave-velocity $\sqrt{g/k}$, which is the same as the wave-velocity for inviscid potential flow. When $k\gg k_c=({\rm g}/\nu^2)^{1/3}$, Lamb noted that the two roots of (14.1.32) are both real. One of them is

$$n_1=-\frac{g}{2\nu k}, \tag{14.1.34}$$

and the other one is

$$n_2 = -0.91\nu k^2. \tag{14.1.35}$$

Lamb pointed out n_1 is the more important root because the motion corresponding to n_2 dies out very rapidly.

14.1.4.1 VPF results

Joseph & Wang (2004) treated this problem using VPF and obtained the following dispersion relation

$$n^2 + 2\nu k^2 n + gk = 0. \tag{14.1.36}$$

When $k < k_c = (\mathrm{g}/\nu^2)^{1/3}$, the solution of (14.1.36) is

$$n = -\nu k^2 \pm \mathrm{i}k\sqrt{g/k - \nu^2 k^2}. \tag{14.1.37}$$

We note that the decay rate $-\nu k^2$ is half of that in (14.1.33) and the wave-velocity $\sqrt{g/k - \nu^2 k^2}$ is slower than the inviscid wave-velocity. When $k > k_c = (\mathrm{g}/\nu^2)^{1/3}$, the two roots of (14.1.36) are both real and they are

$$n = -\nu k^2 \pm \sqrt{\nu^2 k^4 - gk}. \tag{14.1.38}$$

If $k \gg k_c = (\mathrm{g}/\nu^2)^{1/3}$, the above two roots are approximately

$$n_1 = -\frac{g}{2\nu k}, \tag{14.1.39}$$

and

$$n_2 = -2\nu k^2 + \frac{g}{2\nu k}. \tag{14.1.40}$$

We note that (14.1.39) is the same as (14.1.34), and the magnitude of (14.1.40) is approximately twice of (14.1.35).

14.1.4.2 VCVPF results

Joseph & Wang (2004) computed a pressure correction and added it to the normal stress balance to obtain

$$n^2 + 4\nu k^2 n + gk = 0, \tag{14.1.41}$$

which is the dispersion relation for VCVPF theory. When $k < k_c' = (\mathrm{g}/4\nu^2)^{1/3}$, the solution of (14.1.41) is

$$n = -2\nu k^2 \pm \mathrm{i}k\sqrt{g/k - 4\nu^2 k^2}. \tag{14.1.42}$$

We note that the decay rate $-2\nu k^2$ is the same as in (14.1.33) and the wave-velocity $\sqrt{g/k - 4\nu^2 k^2}$ is slower than the inviscid wave-velocity. When $k > k_c' = (\mathrm{g}/4\nu^2)^{1/3}$, the two roots of (14.1.41) are both real and they are

$$n = -2\nu k^2 \pm \sqrt{4\nu^2 k^4 - gk}. \tag{14.1.43}$$

If $k \gg k_c' = (\mathrm{g}/4\nu^2)^{1/3}$, the above two roots are approximately

$$n_1 = -\frac{g}{4\nu k}, \tag{14.1.44}$$

and

$$n_2 = -4\nu k^2 + \frac{g}{4\nu k}. \tag{14.1.45}$$

We note that (14.1.44) is half of (14.1.34), and the magnitude of (14.1.45) is approximately four times of (14.1.35).

Fluid	water	glycerin	SO10000	–
$\nu(\mathrm{m}^2/\mathrm{s})$	10^{-6}	6.21×10^{-4}	1.03×10^{-2}	10
$k_c(1/\mathrm{m})$	21399.7	294.1	45.2	0.461

Table 14.2. *The values for the cutoff wave number k_c for water, glycerin, SO10000 oil and the liquid with ν= 10 m^2/s. k_c decreases as the viscosity increases.*

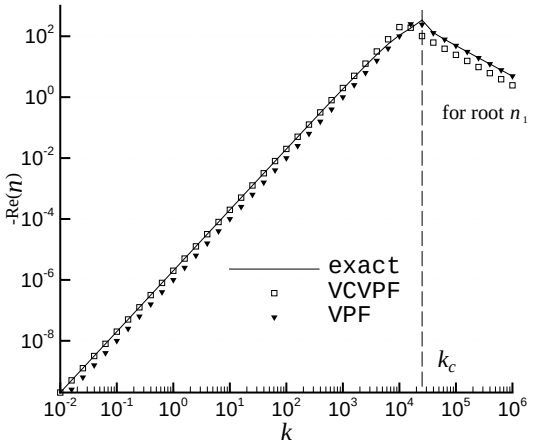

Fig. 14.1. Decay rate $-\mathrm{Re}(n)$ vs. wave number k for water, $\nu = 10^{-6}$ m^2/s. $\mathrm{Re}(n)$ is computed for the exact solution from (14.1.32), for VPF from (14.1.36) and for VCVPF from (14.1.41). When $k < k_c$, the decay rate $-2\nu k^2$ for VCVPF is in good agreement with the exact solution, whereas the decay rate $-\nu k^2$ for VPF is only half of the exact solution. When $k > k_c$, n has two real solutions in each theory. In this figure, we plot the decay rate n_1 corresponding to (14.1.34), (14.1.39) and (14.1.44). The exact solution can be approximated by $-g/(2\nu k)$; the decay rate $-g/(2\nu k)$ for VPF is in agreement with the exact solution, whereas the decay rate $-g/(4\nu k)$ for VCVPF is only half of the exact solution.

14.1.4.3 Comparison of the exact and purely irrotational solutions

We compute the solution of (14.1.32) and compare the real and imaginary part of n with those obtained by solving (14.1.36) and (14.1.41). Water, glycerin and SO10000 oil, for which the kinematic viscosity is 10^{-6}, 6.21×10^{-4}, and 1.03×10^{-2} m^2/s, respectively, are chosen as examples. Figures 14.1 and 14.2 show the decay rate $-\mathrm{Re}(n)$ for water; the root n_1 when $k > k_c$ is shown in figure 14.1 and the root n_2 in figure 14.2. The imaginary part of n, i.e. the wave-velocity multiplied by k, is plotted in figure 14.3 for water. For glycerin and SO10000 oil (figures 14.4 and 14.5), we only plot the decay rate corresponding to the more important root n_1; the plots for the root n_2 and the wave-velocity are omitted. Figure 14.6 shows the decay rate corresponding to the root n_1 for $\nu = 10$ m^2/s, which is 1000 times more viscous than SO10000 oil; the comparison between the exact solution and VPF, VCVPF is still excellent. The cutoff wave number $k_c = (g/\nu^2)^{1/3}$ decreases as the viscosity increases. In Table 14.2 we list the values of k_c for water, glycerin, SO10000 oil and the liquid with ν= 10 m^2/s. In practice waves associated with different wave numbers may exist simultaneously. For very viscous fluids, k_c is small and the majority of the wave numbers are above k_c, therefore the motion of monotonic decay dominates; for less viscous fluids, the motion of progressive waves may dominate.

14.1.5 Why does the exact solution agree with VCVPF when $k < k_c$ and with VPF when $k > k_c$?

Our VCVPF solution and Lamb's dissipation calculation are based on the assumption that the energy equation (14.1.17) for the exact solution is well approximated by an irrotational solution. To verify this, we computed and compared the rates of change of the kinetic energy, the potential energy and dissipation terms in (14.1.17) for Lamb's exact solution and for the purely irrotational part of his solution. The agreement is excellent when $k < k_c$. This shows that the vorticity may be neglected in the computation of terms in the energy balance when $k < k_c$, and is consistent with results given in §14.1.4 which demonstrate that the decay rates from VCVPF and the dissipation calculation agree with the exact solution when k is small. The agreement is poor for k in

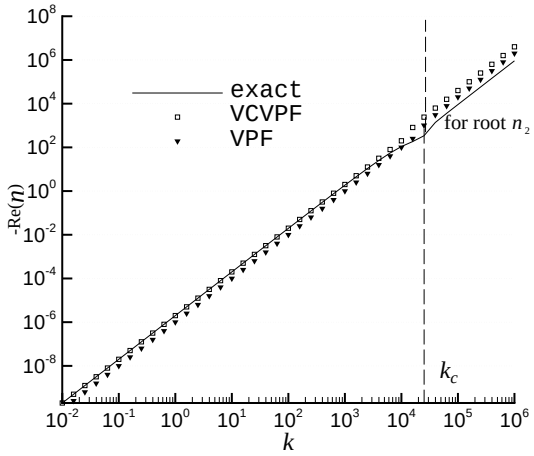

Fig. 14.2. Decay rate $-\mathrm{Re}(n)$ vs. wave number k for water, $\nu = 10^{-6}$ m^2/s. $\mathrm{Re}(n)$ is computed for the exact solution from (14.1.32), for VPF from (14.1.36) and for VCVPF from (14.1.41). When $k > k_c$, n has two real solutions in each theory. In this figure, we plot the decay rate n_2 corresponding to (14.1.35), (14.1.40) and (14.1.45). The decay rate for the exact solution can be approximated by $-0.91\nu k^2$; the decay rate $\approx -2\nu k^2$ for VPF is closer to the exact solution than the decay rate $\approx -4\nu k^2$ for VCVPF.

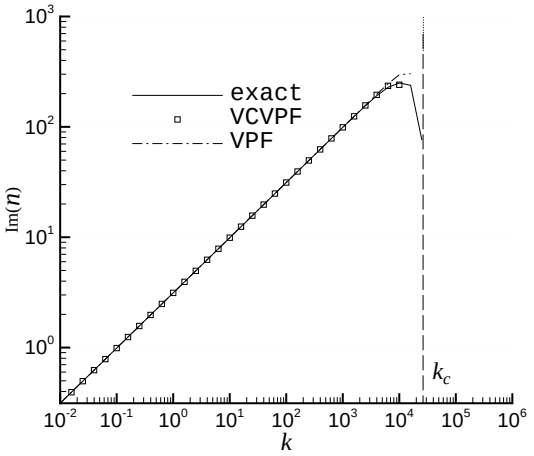

Fig. 14.3. $\mathrm{Im}(n)$, i.e. the wave-velocity multiplied by k, vs. wave number k for water, ν=10^{-6}m^2/s. $\mathrm{Im}(n)$ is computed for the exact solution from (14.1.32), for VPF from (14.1.36) and for VCVPF from (14.1.41). When $k < k_c$, the three theories give almost the same wave-velocity. When $k > k_c$, all the three theories give zero imaginary part of n.

the vicinity of k_c, therefore the decay rates from VCVPF deviate from the exact solution near k_c as shown in figures 14.1-14.6.

When k is much larger than k_c, the energy equation is not well approximated by the irrotational part of the exact solution. However, this result does not mean that the vorticity is important. Lamb pointed out $m \approx k$ when k is large, which is confirmed in our calculation. It follows that the vorticity of the exact solution is

$$\nabla^2\psi = \left(m^2 - k^2\right) C\mathrm{e}^{my+\mathrm{i}kx+nt} \approx 0; \tag{14.1.46}$$

the vorticity is negligible when k is large. The result that the wave is nearly irrotational for large k was also pointed out by Tait (1890). Consequently, the decay rate $-g/(2\nu k)$ from VPF is in good agreement with the exact solution and no pressure correction is needed.

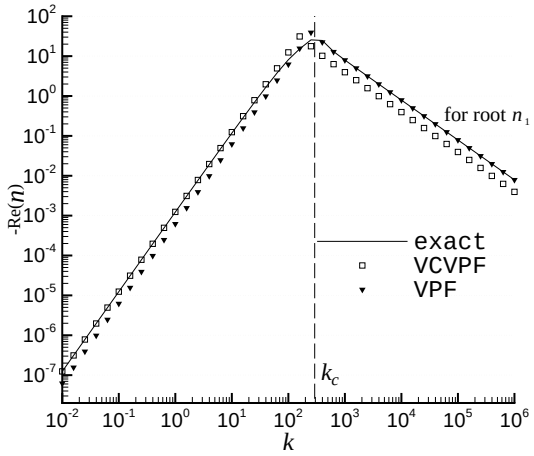

Fig. 14.4. Decay rate $-\mathrm{Re}(n)$ vs. wave number k for glycerin, $\nu = 6.21 \times 10^{-4}\mathrm{m}^2/\mathrm{s}$. $\mathrm{Re}(n)$ is computed for the exact solution from (14.1.32), for VPF from (14.1.36) and for VCVPF from (14.1.41). When $k < k_c$, the decay rate $-2\nu k^2$ for VCVPF is in good agreement with the exact solution, whereas the decay rate $-\nu k^2$ for VPF is only half of the exact solution. When $k > k_c$, n has two real solutions in each theory. In this figure, we plot the decay rate n_1 corresponding to (14.1.34), (14.1.39) and (14.1.44). The decay rate for the exact solution can be approximated by $-g/(2\nu k)$; the decay rate $-g/(2\nu k)$ for VPF is in agreement with the exact solution, whereas the decay rate $-g/(4\nu k)$ for VCVPF is only half of the exact solution.

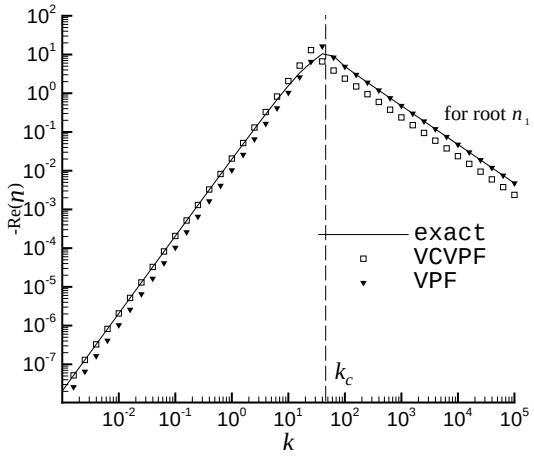

Fig. 14.5. Decay rate $-\mathrm{Re}(n)$ vs. wave number k for SO10000 oil, $\nu = 1.03 \times 10^{-2}\ \mathrm{m}^2/\mathrm{s}$. $\mathrm{Re}(n)$ is computed for the exact solution from (14.1.32), for VPF from (14.1.36) and for VCVPF from (14.1.41). When $k < k_c$, the decay rate $-2\nu k^2$ for VCVPF is in good agreement with the exact solution, whereas the decay rate $-\nu k^2$ for VPF is only half of the exact solution. When $k > k_c$, n has two real solutions in each theory. In this figure, we plot the decay rate n_1 corresponding to (14.1.34), (14.1.39) and (14.1.44). The decay rate for the exact solution can be approximated by $-g/(2\nu k)$; the decay rate $-g/(2\nu k)$ for VPF is in agreement with the exact solution, whereas the decay rate $-g/(4\nu k)$ for VCVPF is only half of the exact solution.

14.1.6 Conclusion and discussion

The problem of decay of free gravity waves due to viscosity was analyzed using two different theories of viscous potential flow, VPF and VCVPF. The pressure correction leads to a hierarchy of potential flows in powers of viscosity. These higher order contributions vanish more rapidly than the principal correction which is proportional to μ. The higher order corrections do not have a boundary layer structure and may not have a physical significance.

The irrotational theory is in splendid agreement with Lamb's exact solution for all wave numbers k except for those in a small interval around k_c where progressive waves change to monotonic decay. VCVPF agrees with Lamb's solution when $k < k_c$ (progressive waves) and VPF agrees with Lamb's exact solution when $k > k_c$ (monotonic decay). The cutoff wave number $k_c = (g/\nu^2)^{1/3}$ decreases as the viscosity increases. In practice

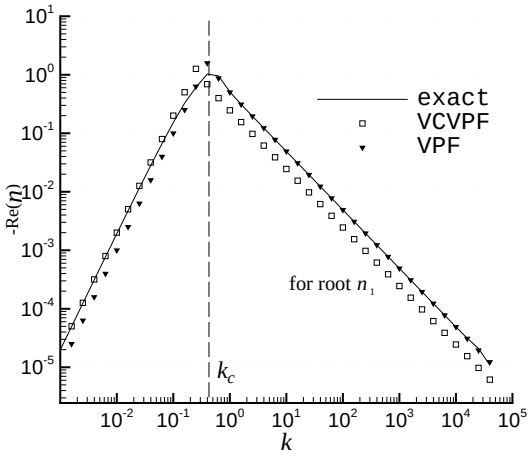

Fig. 14.6. Decay rate $-\mathrm{Re}(n)$ vs. wave number k for ν=10 m^2/s. $\mathrm{Re}(n)$ is computed for the exact solution from (14.1.32), for VPF from (14.1.36) and for VCVPF from (14.1.41). When $k < k_c$, the decay rate $-2\nu k^2$ for VCVPF is in good agreement with the exact solution, whereas the decay rate $-\nu k^2$ for VPF is only half of the exact solution. When $k > k_c$, n has two real solutions in each theory. In this figure, we plot the decay rate n_1 corresponding to (14.1.34), (14.1.39) and (14.1.44). The decay rate for the exact solution can be approximated by $-g/(2\nu k)$; the decay rate $-g/(2\nu k)$ for VPF is in agreement with the exact solution, whereas the decay rate $-g/(4\nu k)$ for VCVPF is only half of the exact solution.

waves associated with different wave numbers may exist simultaneously. For very viscous fluids, k_c is small and the majority of the wave numbers are above k_c, therefore the motion of monotonic decay dominates; for less viscous fluids, the motion of progressive waves may dominate.

There is a boundary layer of vorticity associated with the back and forth motion of the progressive waves. The confined vorticity layer has almost no effect on the solution except for k near k_c. There is no explicit pressure correction in the exact solution. The vortical part of the exact solution does not generate a pressure correction; the pressure depends on the viscosity through the velocity potential and the surface elevation; it is related to the potential and vortical parts of the exact solution in a complicated way. The vortical part is not dominant and the pressure correction is not primarily associated with a boundary layer [see (14.1.30) and Table 14.1].

The analysis of capillary instability of liquid in gas (Wang, Joseph & Funada 2005) is very much like the analysis of the decay of free gravity waves. The purely potential flow analysis is in splendid agreement with Tomotika's (1935) exact solution which has no explicit dependence on viscous pressure. In the case of capillary instability, the best result is based on VCVPF because the short waves which give rise to a sluggish decay in Lamb's problem are stabilized by surface tension.

14.1.7 Quasipotential approximation – vorticity layers

A tractable theory for weakly damped, nonlinear Stokes waves was formulated by Ruvinsky and Freidman (1985a, b; 1987). This theory has come to known as the quasi-potential approximation. The approximation is based on a Helmholtz decomposition

$$\boldsymbol{u} = \nabla\phi + \boldsymbol{v} \tag{14.1.47}$$

where $\boldsymbol{v}$ is the rotational part. They apply a boundary-layer approximation to $\boldsymbol{v}$ and obtain the following system of coupled equations

$$\nabla^2\phi = 0, \quad \frac{\partial\phi}{\partial z} \to 0, \text{ as } z \to \infty \tag{14.1.48}$$

and, on $z = \eta$

$$\frac{\partial\phi}{\partial t} + \frac{1}{2}\left|\nabla\phi\right|^2 + g\eta - \frac{\gamma}{\rho}\kappa + 2\nu\frac{\partial^2\phi}{\partial z^2} = 0, \tag{14.1.49}$$

$$\frac{\partial\eta}{\partial t} + \frac{\partial\eta}{\partial x}\frac{\partial\phi}{\partial x} = \frac{\partial\phi}{\partial z} + v_z \tag{14.1.50}$$

where $\kappa = \left(\partial^2\eta/\partial x^2\right) / \left(1 + (\partial\eta/\partial x)^2\right)^{3/2}$ and v_z is the vertical component of the rotational velocity satisfying

$$\frac{\partial v_z}{\partial t} = 2\nu \frac{\partial^3 \phi}{\partial x^2 \partial z}. \tag{14.1.51}$$

These are three equations in ϕ, η and v_z. The derivation of these is such that v_z is assumed small. This is one reason why the quasipotential approximation is said to model weak effects of viscosity.

Spivak *et al.* 2002 applied the quasi-potential methodology, for a slightly viscous fluid and small surface elasticity, to numerically compute typical free surface profiles induced by a moving pressure distribution under the combined effects of gravity, viscosity, surface tension and film elasticity.

Ruvinsky, Feldstein and Freidman 1991 carried out simulations of ripple excitation by steep gravity capillary waves. They note that when describing the capillary-gravity excitation phenomenon, dissipative processes must be taken into account. "In an exact formulation, this problem has not yet been solved even with a computer." To solve their problem they used the quasi-potential methodology.

Longuet-Higgins 1992 gave a simplified derivation of the quasi-potential methodology in an application to the theory of weakly damped Stokes waves. He gave a simpler form of the equations by applying the boundary conditions on a slightly displaced surface.

Are the principal effects of viscosity associated with vorticity or are they purely irrotational? In his 1992 paper Longuet-Higgins says that "... Lamb 1932 ... showed that for most wavelengths of interest the effects of viscosity on linear, deep-water waves are confined to a thin vortex layer near the free surface, of thickness $D_0 = (2\nu/\gamma)^{1/2}$ (where ν denotes the kinematic viscosity and σ the radian frequency). When $kD_0 \ll 1$ (k the wavenumber) we may say that the waves are weakly damped."

The foregoing statement by Longuet-Higgins is not correct. The effects of viscosity are not confined to a thin vortex layer; the main effects of viscosity on the decay of waves are irrotational. Typically the effects of viscosity arising from the boundary layer at a gas-liquid surface are small because the rates of strain in these layers are no larger than in the irrotational flow and the layer thickness is small. In a later work, Longuet-Higgins 1997 (§14.3.2) calculated the decay of nonlinear capillary-gravity waves by computing the viscous dissipation of the irrotational flow without vorticity or vorticity layers.

14.2 Viscous decay of capillary waves on drops and bubbles

Now we consider the problem of decay of capillary waves on free surfaces of spherical form. Free-surfaces are gas-liquid surfaces in which the dynamical effects of the gas is neglected. A drop is a liquid sphere with gas outside; a bubble is a gas sphere with liquid outside.

We may consider two types of waves on a spherical surface, capillary waves and gravity waves. Capillary waves are driven by surface tension. Gravity waves are driven by gravity; in the case of spheres some form of central gravity law must be adopted.

In the limit of a large radius of the spherical surface we obtain a plane problem such as the problem of free gravity waves considered in the previous section. The problem of decay of capillary waves or capillary-gravity waves on plane or spherical surfaces can be considered.

In the last section we studied the decay of gravity waves on a plane free surface. The short waves decay monotonically and are well approximated by VPF. The long waves are progressive and the decay of these progressive waves are well approximates by VCVPF. Here we shall show that the same result holds for capillary waves and hence may be expected for capillary-gravity waves.

In the sequel, we shall confine our attention to capillary waves on a spherical surface. The problem of the viscous decay of gravity waves on a globe was considered by Lamb 1932.

The following citation from Lamb §355 makes the point about viscosity and irrotationality in oscillations of a liquid globe. He gives the formula for decay constant τ for $\exp(-t/\tau)$ from the dissipation analysis $\tau = a^2/(n-1)(2n+1)\nu$ and says that

> the most remarkable feature of this result is the excessively minute extent to which the oscillations of a globe of moderate dimensions are affected by such a degree of viscosity as is ordinarily met in nature. For a globe of the size of the earth, and of the same kinematic viscosity as water, we have, on the cgs system, $a = 6.37 \times 10^8$, $\nu = 0.0178$ and the value of τ for the gravitational oscillation of longest period ($n = 2$) is therefore
>
> $$\tau = 1.44 \times 10^{11} \text{ years.}$$

Even with the value found by Darwin (1878) for the viscosity of pitch near the freezing temperature, viz $\mu = 1.3 \times 10^8 \times g$, we find, taking $g = 980$, the value

$$\tau = 180 \text{ h}$$

for the modules of decay of the slowest oscillation of a globe the size of the earth, having the density of water and the viscosity of pitch. Since this is still large compared with the period of 1 h 34 min found in Art 262, it appears that such a globe would oscillate almost like a perfect fluid.

Padrino *et al.* 2006 have shown how to improve Lamb's 1932 analysis of dissipation (DM). Lamb's analysis predicts the effects of viscosity on the rate of decay of the waves but not on the frequency. The effects of viscosity on the frequency of irrotational waves were obtained using VCVPF. Furthermore, it was shown that DM and VCVPF give the same dispersion relation. This result goes farther than Lamb's, since the effects of viscosity on the wave frequency can be obtained from DM.

The analysis in this chapter is developed for the problem of decay of irrotational waves on an interface between two liquids. This kind of problem is not perfectly suited to analysis based on purely irrotational flow; the analysis is in §16.1 16.1 of capillary instability of one liquid in another shows that vorticity is important for long waves but less important for short waves. The results we need for the free surface problems in which purely irrotational theories give excellent results will be obtained as limits of two fluid case.

14.2.1 Introduction

A viscous liquid drop surrounded by a quiescent gas or a gas bubble immersed in a viscous liquid tends to an equilibrium spherical shape if the effects of surface tension are significantly large in comparison with gravitational effects. When the spherical interface of the bubble or drop is slightly perturbed by an external agent, the bubble or drop will recover their original spherical configuration through an oscillatory motion of decreasing amplitude. In the case of the drop, depending upon its size and physical properties, the return to the spherical shape may consist of monotonically decaying standing waves. For a drop immersed in another viscous liquid, decaying oscillatory waves always occur at the liquid-liquid interface.

Early studies on the subject for inviscid liquids are due to Kelvin (1890) and Rayleigh (1896). The former obtained an expression for the frequencies of small oscillations of an inviscid liquid globe that tends to the spherical shape by the existence of an internal gravitational potential in the absence of surface tension. The latter included surface tension instead of gravitation. Lamb (1881, 1932) considered the effect of viscosity on the rate of decay of the oscillations of a liquid globe assuming an irrotational velocity field using the dissipation method. Lamb's result is independent of the nature of the forces that drive the interface to the spherical shape. Chandrasekhar (1959) studied fully viscous effects on the small oscillations of a liquid globe with self-gravitation forces neglecting surface tension. The same form of the solution was also obtained by Reid (1960) when surface tension instead of self-gravitation is the force that tends to maintain the spherical shape. A good account of both solutions is presented in the treatise by Chandrasekhar (1961). Following Lamb's reasoning, Valentine, Sather & Heideger (1965) applied the dissipation method to the case of a drop surrounded by another viscous liquid.

A comprehensive analysis of viscous effects in a drop embeded in liquid was presented by Miller & Scriven (1968) who also included rheological properties of the interface. The limiting cases of a drop in a vacuum or a bubble surrounded by a liquid were considered. However, no numerical results were given. Prosperetti (1980a) presented numerical results for the eigenvalue problem for modes $\ell = 2$ to $\ell = 6$. He showed that the spectrum is continuous when the liquid outside is unbounded. Previous studies relied on normal-modes. Prosperetti (1977, 1980b) considered the initial-value fully-viscous problem posed by small perturbations about the spherical shape of a drop or a bubble in which no 'a priori' form of the time dependence is assumed. The solution showed that the normal-mode results are recovered for large times.

Finite size disturbances have received some attention. Tsamopoulus & Brown (1983) considered the small-to-moderate-amplitude inviscid oscillations using perturbations methods. Lundgren & Mansour (1988) and Patzek *et al.* (1991) studied the inviscid problem posed by large oscillations applying the boundary-integral and the finite-element methods, respectively. Lundgren & Mansour also investigated the effect of a 'small' viscosity on drop oscillations. Basaran (1992) carried out the numerical analysis of moderate-to-large-amplitude axisymmetric oscillations of a viscous liquid drop.

In this section, approximate solutions of the linearized problem for small departures from the spherical shape

for a drop surrounded by a gas of negligible density and viscosity or a bubble embedded in a liquid are sought using VPF and VCVPF. These solutions are compared with each other, with IPF, and with exact solutions.

14.2.2 VPF analysis of a single spherical drop immersed in another fluid

Consider a single spherical drop of radius a filled with a fluid with density ρ_l and viscosity μ_l immersed in another fluid with density ρ_a and viscosity μ_a. The coefficient of interfacial tension is denoted as γ. Both fluids are incompressible and Newtonian with gravity neglected. At the basic or undisturbed state both fluids are at rest and the pressure jump across the spherical interface is balanced by surface tension.

When the basic state is disturbed with small irrotational perturbations, the resulting velocity field can be written as the gradient of a potential. The disturbance of the spherical interface is denoted by $\zeta \equiv \zeta(t, \theta, \varphi)$; the interface position is $r = a + \zeta$.

For irrotational flow the incompressible Navier–Stokes equations reduce to the Bernoulli equation. The resulting pressure field can be decomposed into the undisturbed pressure plus a 'small' disturbance.

After subtracting the basic state from the disturbed fluid motion and performing standard linearization of the resulting expressions by neglecting products of the small fluctuations and products of their derivatives, one obtains, for the interior motion ($0 \le r < a$),

$$\nabla^2 \phi_l = 0, \tag{14.2.1}$$

$$p_l = -\rho_l \frac{\partial \phi_l}{\partial t}, \tag{14.2.2}$$

and, for the exterior motion ($a < r < \infty$),

$$\nabla^2 \phi_a = 0, \tag{14.2.3}$$

$$p_a = -\rho_a \frac{\partial \phi_a}{\partial t}. \tag{14.2.4}$$

where ϕ is the velocity potential and p is the pressure disturbance. For irrotational motion, the boundary conditions at the interface require the continuity of the radial velocity and the balance of the normal stresses by interfacial tension. For small departures about the spherical shape, $a >> \zeta$ and the boundary conditions can be written as

$$u_r^l = u_r^a, \tag{14.2.5}$$

for the continuity of the radial velocity at $r = a$ and

$$\left[\left[-p + 2\mu \frac{\partial u_r}{\partial r} \right]\right] = \frac{\gamma}{a^2}(L^2 - 2)\zeta, \tag{14.2.6}$$

for the balance of normal stresses across the interface $r = a$, written in linearized form, accounting for the pressure balance in the undisturbed state. The notation $[\![\cdot]\!] = (\cdot)_{r=b^+} - (\cdot)_{r=b^-}$ is being used to denote the jump across the interface located at $r = a$. The linearized kinematic condition is

$$u_r = \frac{\partial \zeta}{\partial t}, \tag{14.2.7}$$

at $r = a$ with, $u_r = \partial\phi/\partial r$. The R.H.S. of (14.2.6) is obtained from the linearized form of the divergence of the outward unit normal vector to the disturbed interface for the interior fluid. The operator L^2 is also known as the spherical Laplacian and emerges, for instance, in the solution of the Laplace equation using spherical coordinates by applying the method of separation of variables. It is defined as

$$-L^2\zeta = \frac{1}{\sin\theta}\frac{\partial}{\partial\theta}\left(\sin\theta \frac{\partial \zeta}{\partial \theta}\right) + \frac{1}{\sin^2\theta}\frac{\partial^2 \zeta}{\partial \varphi^2}. \tag{14.2.8}$$

Solutions of (14.2.1) and (14.2.3) for the interior and exterior of a sphere, respectively, can be sought in the form

$$\phi_l(r, \theta, \varphi, t) = \sum_{\ell=0}^{\infty} A_\ell \left(\frac{r}{a}\right)^\ell e^{-\sigma_\ell t} S_\ell(\theta, \varphi) + \text{c.c.} \qquad 0 \le r < a, \tag{14.2.9}$$

$$\phi_a(r,\theta,\varphi,t) = \sum_{\ell=0}^{\infty} C_\ell \left(\frac{r}{a}\right)^{-\ell-1} e^{-\sigma_\ell t} S_\ell(\theta,\varphi) + \text{c.c.} \qquad a < r < \infty, \tag{14.2.10}$$

such that ϕ_l is finite at $r = 0$ and ϕ_a remains bounded as $r \to \infty$; σ_ℓ is an eigenvalue to be determined. It will be shown that σ_ℓ does not depend upon the index m. The symbol c.c. designates the complex conjugate of the previous term. The functions S_ℓ are the surface harmonics of integral order

$$S_\ell(\theta,\varphi) = \sum_{m=-\ell}^{\ell} B_{\ell m} Y_\ell^m(\theta,\varphi), \tag{14.2.11}$$

which, with the choice $\bar{B}_{\ell m} = B_{\ell,-m}$, are real functions. The functions $Y_\ell^m(\theta,\varphi)$ are known as the spherical harmonics (Strauss 1992)

$$Y_\ell^m(\theta,\varphi) = P_\ell^{|m|}(\cos\theta) e^{im\varphi}, \tag{14.2.12}$$

where $P_\ell^{|m|}$ are the associated Legendre functions. The spherical harmonics satisfy

$$L^2 Y_\ell^m(\theta,\varphi) = \ell(\ell+1) Y_\ell^m(\theta,\varphi), \tag{14.2.13}$$

for $\ell = 0, 1, 2, \ldots$ and $m = -\ell, \ldots, -1, 0, 1, \ldots, \ell$. The operator L^2 has been defined in (14.2.8). Expressions for the radial components of the velocity can be obtained from (14.2.9) and (14.2.10) by applying $u_r = \partial\phi/\partial r$. Then, the pressure disturbances p_l and p_a can be obtained from (14.2.2) and (14.2.4).

Let us write the disturbance of the spherical shape of the interface as a series expansion,

$$\zeta(\theta,\varphi,t) = \sum_{\ell=0}^{\infty} \zeta_\ell(\theta,\varphi) \mathrm{e}^{-\sigma_\ell t} + \text{c.c.}. \tag{14.2.14}$$

By considering $\zeta_\ell(\theta,\varphi) = \zeta_{0\ell} S_\ell(\theta,\varphi)$, where $\zeta_{0\ell}$ is a constant, and using conditions (14.2.5) and (14.2.7) one obtains

$$-\sigma_\ell \zeta_{0\ell} = \left(\frac{\ell}{a}\right) A_\ell, \qquad \sigma_\ell \zeta_{0\ell} = \left(\frac{\ell+1}{a}\right) C_\ell. \tag{14.2.15}$$

In addition, we have

$$(L^2 - 2)\zeta = \sum_{\ell=0}^{\infty} \{\ell(\ell+1) - 2\} \zeta_{0\ell} \mathrm{e}^{-\sigma_\ell t} S_\ell + \text{c.c.} = \sum_{\ell=0}^{\infty} (\ell+2)(\ell-1) \zeta_{0\ell} \mathrm{e}^{-\sigma_\ell t} S_\ell + \text{c.c.}, \tag{14.2.16}$$

by virtue of (14.2.13) and (14.2.14). Substituting normal-mode expressions for u_r and p, obtained using (14.2.9) and (14.2.10), into the L.H.S. of (14.2.6), applying the result (14.2.16) and replacing A_ℓ and C_ℓ with (14.2.15) yields the dispersion relation for the eigenvalue σ_ℓ, which, after some manipulation, may be written as

$$\begin{aligned} \left(\rho_l(\ell+1) + \rho_a \ell\right)\sigma^2 \quad &- \quad \left(\frac{2\mu_l}{a^2}(\ell+1)\ell(\ell-1) + \frac{2\mu_a}{a^2}(\ell+2)(\ell+1)\ell\right)\sigma \\ &+ \quad \frac{\gamma}{a^3}(\ell+2)(\ell+1)\ell(\ell-1) = 0, \end{aligned} \tag{14.2.17}$$

for $\ell = 0, 1, 2, \ldots$, where the subscript ℓ has been dropped from σ for convenience. Expression (14.2.17) may be written in dimensionless form with the following choices of dimensionless parameters (Funada & Joseph 2002),

$$\hat{l} = \frac{\rho_a}{\rho_l}, \quad \hat{m} = \frac{\mu_a}{\mu_l}, \quad \hat{\sigma} = \sigma\frac{a}{U} \qquad \text{with} \qquad U = \sqrt{\frac{\gamma}{\rho_l a}}, \tag{14.2.18}$$

In dimensionless form, expression (14.2.17) becomes,

$$\begin{aligned} &\left((\ell+1) + \hat{l}\ell\right)\hat{\sigma}_\ell^2 - \frac{2}{\sqrt{J}}\left((\ell+1)\ell(\ell-1) + \hat{m}(\ell+2)(\ell+1)\ell\right)\hat{\sigma} \\ &+(\ell+2)(\ell+1)\ell(\ell-1) = 0 \end{aligned} \tag{14.2.19}$$

with a Reynolds number

$$J = \frac{\rho_l V a}{\mu_l} = Oh^2 \qquad \text{with} \qquad V = \frac{\gamma}{\mu_l}, \tag{14.2.20}$$

where Oh is the Ohnesorge number. Therefore, the eigenvalue $\hat{\sigma}$ for viscous potential flow (VPF) can be computed from

$$\hat{\sigma} = \frac{(\ell+1)\ell(\ell-1)+\hat{m}(\ell+2)(\ell+1)\ell}{\sqrt{J}\left((\ell+1)+\hat{l}\ell\right)} \pm \sqrt{\left[\frac{(\ell+1)\ell(\ell-1)+\hat{m}(\ell+2)(\ell+1)\ell}{\sqrt{J}((\ell+1)+\hat{l}\ell)}\right]^2 - \frac{(\ell+2)(\ell+1)\ell(\ell-1)}{(\ell+1)+\hat{l}\ell}}, \tag{14.2.21}$$

which has two different real roots or two complex roots. In the former case, the interface does not oscillate and the disturbances are damped. In the latter case, $\hat{\sigma} = \hat{\sigma}_R \pm i\hat{\sigma}_I$ where the real part represents the damping coefficient while the imaginary part corresponds to the frequency of the damped oscillations.

When both fluids are considered inviscid (IPF), expression (14.2.21) simplifies to ($\hat{m} \to 0$ and $\sqrt{J} \to \infty$)

$$\hat{\sigma} = \pm i\sqrt{\frac{(\ell+2)(\ell+1)\ell(\ell-1)}{(\ell+1)+\hat{l}\ell}}. \tag{14.2.22}$$

The same expression found by Lamb (1932).

Drop: If the external fluid has negligible density and viscosity ($\hat{l} \to 0$ and $\hat{m} \to 0$), a drop surrounded by a dynamically inactive ambient fluid is obtained, in which case expression (14.2.21) becomes,

$$\hat{\sigma} = \frac{\ell(\ell-1)}{\sqrt{J}} \pm \sqrt{\left[\frac{\ell(\ell-1)}{\sqrt{J}}\right]^2 - (\ell+2)\ell(\ell-1)}. \tag{14.2.23}$$

Moreover, for an inviscid drop $\sqrt{J} \to \infty$ and (14.2.23) reduces to

$$\hat{\sigma}_D = \pm i\sqrt{(\ell+2)\ell(\ell-1)} = \pm i\hat{\sigma}_D^*, \tag{14.2.24}$$

and the drop oscillates about the spherical form. This result was also obtained by Lamb (1932), p. 475.

Using the expression obtained from VPF in (14.2.23), one can readily find two roots for the rate of decay as $J \to 0$ in the drop (e.g., high viscosity). The relevant root on physical grounds is given by

$$\hat{\sigma} = \hat{\sigma}_D^{*2}\sqrt{J}\frac{1}{2\ell(\ell-1)}. \tag{14.2.25}$$

In the case $J \to \infty$ (low viscosity, say), the eigenvalues are complex, and then one encounters progressive decaying waves. These eigenvalues behave as

$$\hat{\sigma} = \frac{\ell(\ell-1)}{\sqrt{J}} \pm i\hat{\sigma}_D^*. \tag{14.2.26}$$

Bubble: By taking $\rho_l \to 0$ and $\mu_l \to 0$ in (14.2.17), the eigenvalue relation for a bubble of negligible density and viscosity embedded in a liquid is obtained for VPF

$$\hat{\sigma} = \frac{(\ell+2)(\ell+1)}{\sqrt{J}} \pm \sqrt{\left[\frac{(\ell+2)(\ell+1)}{\sqrt{J}}\right]^2 - (\ell+2)(\ell+1)(\ell-1)}, \tag{14.2.27}$$

where J is defined in terms of the liquid properties. In the limit of an inviscid external fluid $\sqrt{J} \to \infty$ in (14.2.27) and we obtain

$$\hat{\sigma}_B = \pm i\sqrt{(\ell+2)(\ell+1)(\ell-1)} = \pm i\hat{\sigma}_B^*, \tag{14.2.28}$$

and the bubble oscillates about the spherical shape without damping. This expression was obtained by Lamb (1932).

The dispersion relation obtained from VPF in (14.2.27) can be used to study the trend followed by the disturbances when $J \to 0$ in the case of the bubble. For this case, monotonically decaying waves are predicted with decay rate

$$\hat{\sigma} = \hat{\sigma}_B^{*2}\sqrt{J}\frac{1}{2(\ell+2)(\ell+1)}. \tag{14.2.29}$$

In the case of $J \to \infty$, VPF analysis for the bubble yields

$$\hat{\sigma} = \frac{(\ell+2)(\ell+1)}{\sqrt{J}} \pm i\hat{\sigma}_B^*. \tag{14.2.30}$$

Therefore, progressive decaying waves are found.

14.2.3 VCVPF analysis of a single spherical drop immersed in another fluid

For irrotational motion, continuity of shear stress at the drop's interface is not satisfied. Following Wang *et al* (2005b), a pressure correction p^v can be added to the irrotational pressure p^i in order to compensate for this discontinuity. They showed that the power of the viscous pressure correction p^v equals the power of the irrotational shear stress

$$\int_A (-p_l^v + p_a^v) u_n \mathrm{d}A = \int_A (\tau_l^s u_l^s - \tau_a^s u_a^s) \mathrm{d}A \tag{14.2.31}$$

where the continuity of the normal velocity $u_n = \boldsymbol{u} \cdot \boldsymbol{n}_1$ at the interface A is considered. We use the notation

$$\tau^S u^S \equiv \boldsymbol{n}_1 \cdot \mathbf{T} \cdot (\boldsymbol{u} - u_n \boldsymbol{n}_1),$$

where $\boldsymbol{n}_1$ is the outward unit normal vector at the interface for the interior fluid and $\mathbf{T}$ is the stress tensor.

For small disturbances, after linearization, the pressure corrections p_l^v and p_a^v are harmonic functions, such that

$$\nabla^2 p_l^v = 0 \qquad \text{and} \qquad \nabla^2 p_a^v = 0 \tag{14.2.32}$$

For the interior and exterior of a sphere of radius a, respectively, the following expressions solve (14.2.32)

$$-p_l^v = \sum_{k=0}^{\infty} D_k \left(\frac{r}{a}\right)^k e^{-\sigma_k t} S_k(\theta, \varphi) + \text{c.c.}, \tag{14.2.33}$$

and

$$-p_a^v = \sum_{k=0}^{\infty} G_k \left(\frac{r}{a}\right)^{-k-1} e^{-\sigma_k t} S_k(\theta, \varphi) + \text{c.c.}, \tag{14.2.34}$$

where D_k and G_k are constants. The balance of the normal stress at the sphere's interface $r = a$ is modified by adding the extra-pressures p_l^v and p_a^v

$$-p_a^i - p_a^v + p_l^i + p_l^v + 2\mu_a \frac{\partial^2 \phi_a}{\partial r^2} - 2\mu_l \frac{\partial^2 \phi_l}{\partial r^2} = \frac{\gamma}{a^2}\left(L^2 - 2\right)\zeta. \tag{14.2.35}$$

Substitution into (14.2.35) of the solutions for p_l^v (14.2.33) and p_a^v (14.2.34) and using (14.2.9), (14.2.10), (14.2.16) and the normal-mode expression for the irrotational pressure disturbance as in §2 yields,

$$\begin{aligned} &\Big(\rho_l(\ell+1) + \rho_a \ell\Big) A_\ell \sigma_\ell^2 - (\ell+1)(D_\ell - G_\ell)\sigma_\ell \\ &-\left(\frac{2\mu_l}{a^2}(\ell+1)\ell(\ell-1) + \frac{2\mu_a}{a^2}(\ell+2)\ell(\ell+1)\right) A_\ell \sigma_\ell + \frac{\gamma}{a^3}(\ell+2)(\ell+1)\ell(\ell-1) A_\ell = 0, \end{aligned} \tag{14.2.36}$$

where the relation $\ell A_\ell = -(\ell+1)C_\ell$, readily obtained from (14.2.15), has been used. For a sphere of radius a, the integrals in (14.2.31) can be written in terms of the velocity and shear stress components in spherical coordinates

$$\int_A (-p_l^v + p_a^v) u_r \mathrm{d}A = \int_A \left(\tau_{r\theta}^l u_\theta^l + \tau_{r\varphi}^l u_\varphi^l - \tau_{r\theta}^a u_\theta^a - \tau_{r\varphi}^a u_\varphi^a\right) \mathrm{d}A, \tag{14.2.37}$$

with $u_r^a = u_r^l = u_r$ by continuity of normal velocities at $r = a$. The velocity components in spherical coordinates can be computed from well-known formulas for the gradient of a scalar field. Then, the shear stress components

in spherical coordinates are found from standard expressions for a Newtonian fluid. By applying this procedure, the L.H.S. of (14.2.37) becomes,

$$\begin{aligned}\int_A(-p_l^v+p_a^v)u_r\mathrm{d}A &= 2\,\mathrm{Re}\Bigg[\sum_{\ell=0}^{\infty}\sum_{k=0}^{\infty}a^2(D_\ell-G_\ell)e^{-\sigma_\ell t}\left(\frac{k}{a}\right)\Bigg(A_k e^{-\sigma_k t}\\ &+ \bar{A}_k e^{-\bar{\sigma}_k t}\Bigg)\int_0^{2\pi}\int_0^{\pi}S_\ell S_k\sin\theta\mathrm{d}\theta\mathrm{d}\varphi\Bigg], \end{aligned} \tag{14.2.38}$$

where $\mathrm{Re}[z]$ delivers the real part of a complex number z. The equality in (14.2.38) follows from the formula

$$\int_A\left(B+\bar{B}\right)\left(C+\bar{C}\right)\mathrm{d}A = 2\int_A\mathrm{Re}\left[BC+B\bar{C}\right]\mathrm{d}A = 2\mathrm{Re}\left[\int_A\left(BC+B\bar{C}\right)\mathrm{d}A\right] \tag{14.2.39}$$

where A represents the domain of integration (e.g., volume) and B and C are complex fields. This formula is also used in the integration of the right-hand side of (14.2.37). Using the definition of S_ℓ in (14.2.11), the double integral in (14.2.38) can be written as

$$\int_0^{2\pi}\int_0^{\pi}S_\ell S_k\sin\theta\mathrm{d}\theta\mathrm{d}\varphi = \sum_{m=-\ell}^{\ell}\sum_{j=-k}^{k}B_{\ell m}\bar{B}_{kj}\int_0^{2\pi}\int_0^{\pi}P_\ell^{|m|}(\cos\theta)P_k^{|j|}(\cos\theta)e^{i(m-j)\varphi}\sin\theta\mathrm{d}\theta\mathrm{d}\varphi, \tag{14.2.40}$$

since S_k is real (i.e. $S_k=\bar{S}_k$). This integral is zero for all the different duplets $(\ell,m)\neq(k,j)$. Then, we have

$$\begin{aligned}\int_0^{2\pi}\int_0^{\pi}[S_\ell(\theta,\varphi)]^2\sin\theta\mathrm{d}\theta\mathrm{d}\varphi &= \sum_{m=0}^{\ell}2\pi F_{\ell m}\int_0^{\pi}\left[P_\ell^m(\cos\theta)\right]^2\sin\theta\mathrm{d}\theta\\ &= \sum_{m=0}^{\ell}F_{\ell m}\left[\frac{4\pi}{(2\ell+1)}\frac{(\ell+m)!}{(\ell-m)!}\right], \end{aligned} \tag{14.2.41}$$

using a standard result for the integral in the second term. Here, $F_{\ell m}$ represent real constants. Then, from (14.2.38) the power of the pressure correction can be expressed as

$$\begin{aligned}\int_A(-p_l^v+p_a^v)u_r\mathrm{d}A &= 2\,\mathrm{Re}\Bigg[\sum_{\ell=0}^{\infty}\sum_{m=0}^{\ell}F_{\ell m}4\pi a(D_\ell-G_\ell)e^{-\sigma_\ell t}(A_\ell e^{-\sigma_\ell t}\\ &+ \bar{A}_\ell e^{-\bar{\sigma}_\ell t})\frac{\ell}{(2\ell+1)}\frac{(\ell+m)!}{(\ell-m)!}\Bigg]. \end{aligned} \tag{14.2.42}$$

Similarly, the right-hand side of (14.2.37) yields,

$$\begin{aligned}\int_A\left(\tau_{r\theta}^l u_\theta^l+\tau_{r\varphi}^l u_\varphi^l-\tau_{r\theta}^a u_\theta^a-\tau_{r\varphi}^a u_\varphi^a\right)\mathrm{d}A = 2\mathrm{Re}\Bigg[\sum_{\ell=0}^{\infty}\sum_{k=0}^{\infty}\frac{2}{a}A_\ell e^{-\sigma_\ell t}\Bigg(\mu_l(\ell-1)\\ +\mu_a\frac{\ell(\ell+2)}{(\ell+1)}\frac{k}{(k+1)}\Bigg)(A_k e^{-\sigma_k t}+\bar{A}_k e^{-\bar{\sigma}_k t})\int_0^{2\pi}\int_0^{\pi}\left(\sin\theta\frac{\partial S_\ell}{\partial\theta}\frac{\partial S_k}{\partial\theta}+\frac{1}{\sin\theta}\frac{\partial S_\ell}{\partial\varphi}\frac{\partial S_k}{\partial\varphi}\right)\mathrm{d}\theta\mathrm{d}\varphi\Bigg]. \end{aligned} \tag{14.2.43}$$

Using standard formulae (Bowman, Senior & Uslenghi 1987) for the double integral in the right-hand side of (14.2.43), we find that the power of the shear stress can be expressed as

$$\begin{aligned}\int_A(\tau_{r\theta}^l u_\theta^l+\tau_{r\varphi}^l u_\varphi^l-\tau_{r\theta}^a u_\theta^a-\tau_{r\varphi}^a u_\varphi^a)\mathrm{d}A = 2\,\mathrm{Re}\Bigg[\sum_{\ell=0}^{\infty}\sum_{m=0}^{\ell}F_{\ell m}\frac{8\pi}{a}A_\ell e^{-\sigma_\ell t}(A_\ell e^{-\sigma_\ell t}+\\ +\quad\bar{A}_\ell e^{-\bar{\sigma}_\ell t})\Bigg(\mu_l(\ell+1)(\ell-1)+\mu_a\frac{\ell^2(\ell+2)}{\ell+1}\Bigg)\frac{\ell}{(2\ell+1)}\frac{(\ell+m)!}{(\ell-m)!}\Bigg]. \end{aligned} \tag{14.2.44}$$

By virtue of (14.2.37), equating (14.2.42) and (14.2.44) yields the relation

$$D_\ell-G_\ell = 2\frac{A_\ell}{a^2}\Bigg(\mu_l(\ell+1)(\ell-1)+\mu_a\frac{\ell^2(\ell+2)}{\ell+1}\Bigg). \tag{14.2.45}$$

Replacing $D_\ell-G_\ell$ from (14.2.45) in (14.2.36) yields the dispersion relation for the complex eigenvalue σ_ℓ arising

from VCVPF (again we drop the subscript ℓ for convenience),

$$\begin{aligned}\Big(\rho_l(\ell+1)+\rho_a\ell\Big)\sigma^2 &- \frac{2\mu_l}{a^2}(2\ell+1)(\ell+1)(\ell-1)\sigma \\ &- \frac{2\mu_a}{a^2}(2\ell+1)(\ell+2)\ell\sigma+\frac{\gamma}{a^3}(\ell+2)(\ell+1)\ell(\ell-1)=0. \end{aligned} \tag{14.2.46}$$

In dimensionless form, expression (14.2.46) becomes,

$$\begin{aligned}\Big((\ell+1)+\hat{l}\ell\Big)\hat{\sigma}^2 &- \frac{2}{\sqrt{J}}(2\ell+1)(\ell+1)(\ell-1)\hat{\sigma} \\ &- \frac{2\hat{m}}{\sqrt{J}}(2\ell+1)(\ell+2)\ell\hat{\sigma}+(\ell+2)(\ell+1)\ell(\ell-1)=0. \end{aligned} \tag{14.2.47}$$

with eigenvalues

$$\begin{aligned}\hat{\sigma} &= \frac{(2\ell+1)(\ell+1)(\ell-1)+\hat{m}(2\ell+1)(\ell+2)\ell}{\sqrt{J}\Big((\ell+1)+\hat{l}\ell\Big)} \\ &\pm\sqrt{\left[\frac{(2\ell+1)(\ell+1)(\ell-1)+\hat{m}(2\ell+1)(\ell+2)\ell}{\sqrt{J}((\ell+1)+\hat{l}\ell)}\right]^2-\frac{(\ell+2)(\ell+1)\ell(\ell-1)}{(\ell+1)+\hat{l}\ell}}, \end{aligned} \tag{14.2.48}$$

which has two different real roots or a complex-conjugate pair of roots. The former case corresponds to monotonically decaying waves while the latter implies progressive decaying waves.

Drop: In the case of a drop surrounded by a gas of negligible density and viscosity, we have $\hat{l}\to 0$ and $\hat{m}\to 0$ in (14.2.48) and the eigenvalues become,

$$\hat{\sigma}=\frac{(2\ell+1)(\ell-1)}{\sqrt{J}}\pm\sqrt{\left[\frac{(2\ell+1)(\ell-1)}{\sqrt{J}}\right]^2-(\ell+2)\ell(\ell-1)}, \tag{14.2.49}$$

where the dimensionless parameter $\hat{\sigma}$ and the Reynolds number J have been defined in (14.2.18) and (14.2.20), respectively. In the case of progressive waves, the rate of decay $(2\ell+1)(\ell-1)/\sqrt{J}$ was obtained by Lamb (1932) in §355 through the dissipation method. In the present calculations, the relation (14.2.49) gives the decay rate of progressive waves ($\mathrm{Im}(\hat{\sigma})\neq 0$) as well as the wave velocity. For $\mathrm{Im}(\hat{\sigma})=0$, the monotonically decay rate for standing waves including the effect of surface tension is obtained. Expression (14.2.49) can be compared with (14.2.23) from VPF and (14.2.24) from IPF.

As $J\to 0$, VCVPF produces two roots for the rate of decay from (**??**); the following gives the lowest rate of decay,

$$\hat{\sigma}=\hat{\sigma}_D^{*2}\sqrt{J}\frac{1}{2(2\ell+1)(\ell-1)}. \tag{14.2.50}$$

In the case of $J\to\infty$ the eigenvalues are complex,

$$\hat{\sigma}=\frac{(2\ell+1)(\ell-1)}{\sqrt{J}}\pm i\hat{\sigma}_D^{*}. \tag{14.2.51}$$

Hence, one finds progressive–decaying waves. The definition of $\hat{\sigma}_D^*$ is given in (14.2.24).

Prosperetti (1977) studied the initial value problem posed by small departures from the spherical shape of a viscous drop surrounded by another viscous liquid. In the limiting case of a drop in a vacuum, he found (14.2.49) in the limit $t\to 0$ if an irrotational initial condition is assumed. We remark that (14.2.49) was obtained here by a different method. Similarly, in the limiting case of a bubble, Prosperetti's initial-value-problem analysis with an irrotational initial condition yields, for $t\to 0$, the same dispersion relation as the one obtained from VCVPF in (**??**).

Bubble: The dispersion relation from VCVPF for a bubble of negligible density and viscosity immersed in a viscous liquid can be determined from (14.2.46) taking $\rho_l\to 0$ and $\mu_l\to 0$, which gives rise to the following expression for the eigenvalues,

$$\hat{\sigma}=\frac{(2\ell+1)(\ell+2)}{\sqrt{J}}\pm\sqrt{\left[\frac{(2\ell+1)(\ell+2)}{\sqrt{J}}\right]^2-(\ell+2)(\ell+1)(\ell-1)}, \tag{14.2.52}$$

with J determined from the liquid properties. In the case of small oscillations, the rate of decay given in (14.2.52) as $(2\ell+1)(\ell+2)/\sqrt{J}$ is the same as the rate computed by Lamb (1932) using the dissipation method without the explicit inclusion of the surface tension effects in the formulation.

VCVPF expression (14.2.52) yields the following result as $J \to 0$ ($\nu \to \infty$, say) for the bubble,

$$\hat{\sigma} = \hat{\sigma}_B^{*2}\sqrt{J}\frac{1}{2(2\ell+1)(\ell+2)}, \tag{14.2.53}$$

and thus monotonically decaying waves with $\hat{\sigma}_B^*$ defined in (14.2.28).

In the case of $J \to \infty$ ($\nu \to 0$, say), VCVPF predicts progressive-decaying waves with eigenvalues

$$\hat{\sigma} = \frac{(2\ell+1)(\ell+2)}{\sqrt{J}} \pm i\hat{\sigma}_B^*. \tag{14.2.54}$$

14.2.4 Dissipation approximation (DM)

Lamb (1932) applied a dissipation approximation to compute the decay rate for small progressive waves in the free surface of a liquid spherical drop immersed in gas and a spherical bubble surrounded by liquid. Lamb's approach was extended to a drop surrounded by another viscous liquid by Valentine, Sather & Heideger (1965). We showed in Chapter 12 that in gas-liquid flows VCVPF gives rise to the same results as DM. The construction of VCVPF theories for progressive waves gives rise to a frequency which depends on viscosity. This dependence of frequency on viscosity was not obtained either by Lamb or Valentine *et al.*, who assumed the frequency of an inviscid fluid in his dissipation calculation. In §14.3.1 the correction of frequency due to viscosity using the dissipation method is calculated for capillary-gravity waves. The same kind of analysis can be applied in the case of two fluids.

In the case of a viscous liquid drop surrounded by another viscous liquid, addition of the mechanical energy equations for the interior and exterior domains gives rise to the expression

$$\begin{aligned} &\frac{d}{dt}\int_{V_a}\rho_a\frac{|\boldsymbol{u}_a|^2}{2}\mathrm{d}V + \frac{d}{dt}\int_{V_l}\rho_l\frac{|\boldsymbol{u}_l|^2}{2}\mathrm{d}V \\ = \;& -\int_A \boldsymbol{n}_1\cdot\boldsymbol{T}_a\cdot\boldsymbol{u}_a\mathrm{d}A + \int_A \boldsymbol{n}_1\cdot\boldsymbol{T}_l\cdot\boldsymbol{u}_l\mathrm{d}A - \int_{V_a} 2\mu_a\boldsymbol{D}_a:\boldsymbol{D}_a\mathrm{d}V - \int_{V_l} 2\mu_l\boldsymbol{D}_l:\boldsymbol{D}_l\mathrm{d}V. \end{aligned} \tag{14.2.55}$$

where V_a and V_l are the volumes occupied by the exterior and interior fluid, respectively; $\boldsymbol{D}$ is the strain-rate tensor and $\boldsymbol{n}_1$ denotes the outward unit normal for the interior fluid. The last two terms in (14.2.55) represent the viscous dissipation. The first two integrals in the R.H.S of (14.2.55) can be expanded in terms of the pressure and viscous-stress components. Then,we assume that continuity of normal velocity and stress and continuity of tangential velocity and stress are satisfied at the interface $r = a$ and (14.2.55) reduces to

$$\begin{aligned} &\frac{d}{dt}\int_{V_a}\rho_a\frac{|\boldsymbol{u}_a|^2}{2}\mathrm{d}V + \frac{d}{dt}\int_{V_l}\rho_l\frac{|\boldsymbol{u}_l|^2}{2}\mathrm{d}V \\ = \;& -\int_A \frac{\gamma}{a^2}(L^2-2)\zeta u_r\mathrm{d}A + \int_A \boldsymbol{n}_1\cdot 2\mu_a\boldsymbol{D}_a\cdot\boldsymbol{u}_a\mathrm{d}A - \int_A \boldsymbol{n}_1\cdot 2\mu_l\boldsymbol{D}_l\cdot\boldsymbol{u}_l\mathrm{d}A, \end{aligned} \tag{14.2.56}$$

where potential flow is assumed for the entire fluid domain, such that the dissipation volume integrals give rise to the last to terms in (14.2.56). With $|\boldsymbol{u}|^2 = u_r^2 + u_\theta^2 + u_\varphi^2$ and the components of $\boldsymbol{D}$ expressed in spherical coordinates, such that $\boldsymbol{n}_1\cdot 2\mu\boldsymbol{D}\cdot\boldsymbol{u} = \tau_{rr}u_r + \tau_{r\theta}u_\theta + \tau_{r\varphi}u_\varphi$ computed from potential flow, the integrals in (14.2.56) can be evaluated (we use the standard results for the double integrals as presented in the VCVPF calculation). This calculation, which is omitted for brevity, yields the same dispersion relation (14.2.46) obtained from VCVPF.

14.2.5 Exact solution of the linearized free surface problem

In this section we present the dispersion relation for the effect of viscosity on small oscillations of a drop immersed in a vacuum and a bubble of negligible density and viscosity embedded in a viscous liquid obtained from the solution of the linearized equations of motion without the assumption of irrotational flow. The result for the drop was presented by Reid (1960) whereas the solution for the bubble can be obtained following a similar path. In both cases, the dispersion relation shall coincide with the corresponding limiting results presented by Miller and Scriven (1968) and Prosperetti (1980a), who posed and solved the most general two-fluid problem.

The linearized Navier-Stokes equations govern this problem

$$\rho\frac{\partial \boldsymbol{u}}{\partial t} = -\nabla p + \mu\nabla^2\boldsymbol{u}, \tag{14.2.57}$$

with $\nabla\cdot\boldsymbol{u} = 0$ in $0 \le r < a$ for the drop and in $a < r < \infty$ for the bubble. Continuity of velocity and shear stresses at $r = a$ are satisfied.

14.2.5.1 Spherical drop

Reid (1960) obtained the dispersion relation for the eigenvalue σ

$$\alpha^4 = 2q^2\,(\ell-1)\left[\ell + (\ell+1)\,\frac{q - 2\ell Q^J_{\ell+1/2}}{q - 2Q^J_{\ell+1/2}}\right] - q^4, \tag{14.2.58}$$

with

$$Q^J_{\ell+1/2}(q) = J_{\ell+3/2}(q)/J_{\ell+1/2}(q), \qquad \alpha^2 = \frac{\sigma^*_D a^2}{\nu} = \hat\sigma^*_D\sqrt{J}, \qquad \frac{q^2}{\alpha^2} = \frac{\sigma}{\sigma^*_D} = \frac{\hat\sigma}{\hat\sigma^*_D}, \tag{14.2.59}$$

where σ^*_D is the frequency of oscillations from inviscid potential flow (IPF) given in (14.2.24). A thorough discussion on the solution of (14.2.58) is presented by Chandrasekhar (1959, 1961) when q is real. Considering ℓ fixed, the R.H.S. of (14.2.58) is a function of q, $\Phi(q)$ say. The graph of this function on the axis of positive q reveals that there is an infinite number of intervals where $\Phi(q)$ is positive. The first of these intervals, which contains $q = 0$, encloses a maximum ($\alpha^2_{\max}$). For $\alpha^2 < \alpha^2_{\max}$ this first interval gives two real roots of (14.2.58), which determine the slowest rates of decay. Since $\alpha^2 = \hat\sigma^*_D\sqrt{J}$, for every mode ℓ, the magnitude of the Reynolds number J defines the roots. In the other intervals, one has $0 \le \Phi(q) < \infty$. When $\alpha^2 > \alpha^2_{\max}$, (14.2.58) admits complex-conjugate eigenvalues with positive real parts which give the lowest rate of decay; these waves oscillate as they decay. Results from this dispersion relation are presented and discussed in §14.2.7.

As $J \to 0$, the rate of decay from the exact solution of a drop surrounded by gas behaves as

$$\hat\sigma = \hat\sigma^{*2}_D\sqrt{J}\frac{2\ell+1}{2(\ell-1)(2\ell^2+4\ell+3)}. \tag{14.2.60}$$

From the exact solution given above the behavior of the complex eigenvalue σ for the drop as $J \to \infty$ is

$$\hat\sigma = \frac{(2\ell+1)(\ell-1)}{\sqrt{J}} \pm i\hat\sigma^*_D. \tag{14.2.61}$$

These expressions were also obtained by Chandrasekhar (1959, 1961) and Miller & Scriven (1968). The result given in (14.2.51) from VCVPF is the same as the expression obtained in (14.2.61) from the exact solution.

14.2.5.2 Spherical bubble

A procedure similar to the one applied to the drop gives rise to the following dispersion relation for the bubble

$$\alpha^4 = (\ell+2)\,q^2\frac{(2\ell+1)\,q^2 - 2\,(\ell+1)\,(\ell-1)\left[(2\ell+1) - qQ^H_{\ell+1/2}\right]}{(2\ell+1) + q^2/2 - qQ^H_{\ell+1/2}} - q^4, \tag{14.2.62}$$

with

$$Q^H_{\ell+1/2} = H^{(1)}_{\ell+3/2}(q)/H^{(1)}_{\ell+1/2}(q), \tag{14.2.63}$$

and using the relations (**??**). In these relations, σ^*_B from IPF given in (14.2.28) for a bubble is used instead of σ^*_D.

Expression (14.2.62) is the same dispersion relation found by Miller & Scriven (1968). Prosperetti (1980a) indicates that this dispersion relation only admits complex roots as a consequence of the character of the Hankel functions. Therefore, for a bubble, only progressive–decaying waves are predicted. For a drop, we recall that real eigenvalues can be found. Another feature of the dispersion relation is that the solutions occur in conjugate pairs, as in the drop case, since, for $\mathrm{Im}(\sigma) < 0$, one can choose the Hankel function of the second kind in (**??**), and (14.2.62) is satisfied.

For a gas bubble in a viscous liquid, a real σ can be approximated as $J \to 0$,

$$\hat\sigma = \hat\sigma^{*2}_B\sqrt{J}\frac{2\ell+1}{2(2\ell^2+1)(\ell+2)}, \tag{14.2.64}$$

For $J \to \infty$, damped-progressive waves take place with eigenvalues

$$\hat{\sigma} = \frac{(2\ell+1)(\ell+2)}{\sqrt{J}} \pm i\hat{\sigma}_B^*. \tag{14.2.65}$$

Both results presented by Miller & Scriven (1968). As in the case of the drop, the result obtained from VCVPF in (14.2.54) is the same as the expression given in (14.2.65) from the exact solution.

14.2.6 VPF and VCVPF analyses for waves acting on a plane interface considering surface tension – comparison with Lamb's solution

The problem of the viscous effects on free gravity waves was solved exactly by Lamb (1932). In his analysis, surface tension effects were included. Joseph & Wang (2004) gave a solution to this problem using viscous potential flow (VPF). They also added a viscous correction to the irrotational pressure and obtained another dispersion relation for the complex eigenvalue σ. In their analysis they neglected the surface tension effects and considered gravity effects. Here we find the rate of decay and wave velocity for free waves on an otherwise plane interface neglecting gravity effects and including surface tension. These expressions are found as limiting results from our VPF and VCVPF analyses of waves on the surface of a liquid drop surrounded by gas presented at the end of §14.2.3 and §14.2.4, respectively. This procedure considers taking the limits $\ell \to \infty$ and $a \to \infty$ such that $\ell/a \to k$ in the expressions for the complex eigenvalue σ (Miller & Scriven 1968).

For VPF, in the case of $k > k_c = \gamma/\rho\nu^2$, the decay rate is

$$\sigma = \nu k^2 \pm \sqrt{(\nu k^2)^2 - \gamma k^3/\rho}. \tag{14.2.66}$$

If $k < k_c = \gamma/\rho\nu^2$ then we have

$$\sigma = \nu k^2 \pm ik\sqrt{\gamma k/\rho - \nu^2 k^2}, \tag{14.2.67}$$

such that the wave-velocity is $c = \sqrt{\gamma k/\rho - \nu^2 k^2}$ and the rate of decay is νk^2.

Studying the asymptotic behavior for $k >> k_c = \gamma/\rho\nu^2$, the rate of decay goes as

$$\sigma_1 = \frac{\gamma k}{2\rho\nu} \qquad \text{and} \qquad \sigma_2 = 2\nu k^2. \tag{14.2.68}$$

Then, σ_1 gives the slowest rate of decay for large k.

On the other hand, the asymptotic behavior as $k << k_c = \gamma/\rho\nu^2$ can be expressed as

$$\sigma = \nu k^2 \pm ik\sqrt{\gamma k/\rho}, \tag{14.2.69}$$

such that the wave velocity is given by $c = \sqrt{\gamma k/\rho}$; this is the same result from IPF as shown below. The rate of decay goes as νk^2.

For VCVPF, in the case of $k > k_c = \gamma/4\rho\nu^2$, the rate of decay is

$$\sigma = 2\nu k^2 \pm \sqrt{(2\nu k^2)^2 - \gamma k^3/\rho}. \tag{14.2.70}$$

If $k < k_c = \gamma/4\rho\nu^2$ then we have

$$\sigma = 2\nu k^2 \pm ik\sqrt{\gamma k/\rho - 4\nu^2 k^2}, \tag{14.2.71}$$

such that the wave-velocity is $c = \sqrt{\gamma k/\rho - 4\nu^2 k^2}$ and the rate of decay is $2\nu k^2$.

Studying the asymptotic behavior for $k >> k_c = \gamma/4\rho\nu^2$ the rate of decay goes as

$$\sigma_1 = \frac{\gamma k}{4\rho\nu} \qquad \text{and} \qquad \sigma_2 = 4\nu k^2. \tag{14.2.72}$$

Hence, σ_1 gives the slowest rate of decay for large k.

On the other hand, the asymptotic behavior as $k << k_c = \gamma/4\rho\nu^2$ can be expressed as

$$\sigma = 2\nu k^2 \pm ik\sqrt{\gamma k/\rho}, \tag{14.2.73}$$

such that the wave velocity is given by $c = \sqrt{\gamma k/\rho}$, which is the same result from inviscid potential flow (IPF) as shown below. In this case the rate of decay goes as $2\nu k^2$. It can be verified that the same results are found if one starts from the VPF and VCVPF solutions obtained for a bubble surrounded by a viscous liquid.

Lamb (1932) solved the problem of free gravity waves exactly considering the effects of surface tension (art. 349, pp. 625). Lamb's dispersion relation, neglecting gravitational effects, is

$$\left(\sigma - 2\nu k^2\right)^2 + \frac{\gamma}{\rho}k^3 = 4\nu^2 k^3 m, \tag{14.2.74}$$

with

$$m^2 = k^2 - \sigma/\nu.$$

Therefore, the dispersion relation is biquadratic. As the viscosity goes to zero, Lamb found that the complex eigenvalue σ behaves as

$$\sigma = 2\nu k^2 \pm ik\sqrt{\gamma k/\rho}, \tag{14.2.75}$$

which is exactly the result from VCVPF in the case of $k << k_c = \gamma/4\rho\nu^2$ as shown in (14.2.73). In the limit $\nu \to 0$ Lamb's exact solution reduces to

$$\sigma_P^2 = \gamma k^3/\rho, \tag{14.2.76}$$

corresponding to IPF analysis. Then, the wave-velocity for inviscid flow is $c = \sqrt{\gamma k/\rho}$, as mentioned above.

For the case of $\nu \to \infty$, Lamb (1932) found two real roots from his exact solution neglecting surface tension. Following the same procedure but neglecting gravity effects and keeping surface tension, we find that the relevant root on physical grounds is

$$\sigma = \frac{\gamma k}{2\rho\nu}, \tag{14.2.77}$$

which is the same result obtained from VPF in (14.2.68). Using asymptotic formulas for Bessel functions of large order and large variable such that $a \to \infty$ and $\ell \to \infty$ for fixed k, Prosperetti (1980a) showed that the dispersion relation for the bubble (14.2.62) reduces to Lamb's result (14.2.74). Prosperetti (1976) posed and solved the initial-value problem for small disturbances of the infinite plane without assuming an exponential decay with time. For an irrotational initial condition and neglecting gravity, in the limit $t \to 0$, his dispersion relation is the same as (14.2.71), obtained here by a different method.

14.2.7 Results and discussion

In this section, a detailed comparison of the results for the decay rate and frequency of the waves according to VPF and VCVPF with the exact solutions of the fully viscous linear problem are presented for a drop and a bubble. A wide interval is selected for the mode number ℓ ranging from $\ell = 2$ up to $\ell = 100$. The smallest value of $\ell = 2$ is chosen since lower values yield compressive or expansive motions of the drop interface which are not compatible with the incompressibility assumption or a non-physical static disturbed interface. For higher values of ℓ, the exact fully viscous solution for the drop predicts oscillations that decay faster (Miller & Scriven 1968). The same lowest value of $\ell = 2$ is selected for the bubble case.

Figure 14.7(a) shows the critical Reynolds number J_c as a function of ℓ for a drop. The critical Reynolds number is defined as the value of J at a given ℓ for which transition from monotonically decaying waves (standing waves) to progressive waves (oscillations) occurs. For $J \leq J_c$ the eigenvalues $\hat{\sigma}$ are real and monotonically decaying waves take place, whereas for $J > J_c$ the eigenvalues are complex and the waves decay through oscillations. Figure 14.7 (b) presents the trends of J_c with ℓ for VPF and VCVPF for a bubble. Recall that the exact solution always predicts decaying oscillations (i.e. complex eigenvalues) in the bubble case. Therefore, the exact solution does not give rise to a critical J. If VCVPF predicts progressive decaying waves, then VPF gives the same prediction. If VPF predicts standing waves, then the same behavior is obtained from VCVPF.

For a drop, the decay rate and wave frequency as a function of the Reynolds number J are presented in Figures 14.8 (a) and (b), respectively, for $\ell = 2$ as predicted by VPF, VCVPF and the exact solution. The wave frequency given by IPF is also included for comparison. For large J, VCVPF and the exact solution show excellent agreement, whereas VPF is off the mark. The wave frequencies from the three viscous theories tend to the inviscid solution for large J. As J decreases (below $J = 10$, say), transition from the progressive waves regime to the standing waves regime occurs. In the point of transition, the frequency becomes identically zero and the curve of $\mathrm{Re}(\hat{\sigma})$ bifurcates yielding two real and different roots. In Figure 14.8 (a), the lowest root, representing the least damped mode of decay, is presented.

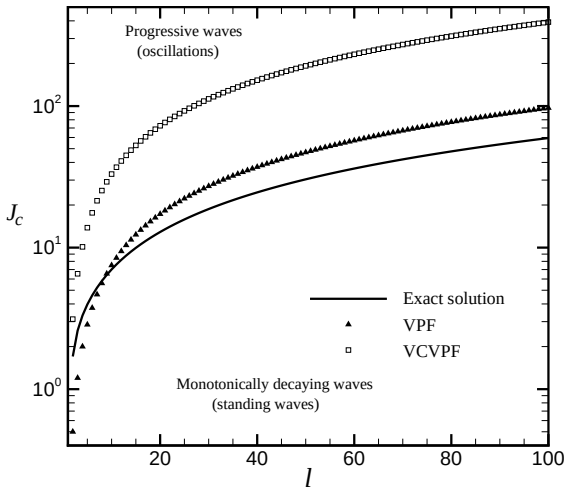

(a) drop

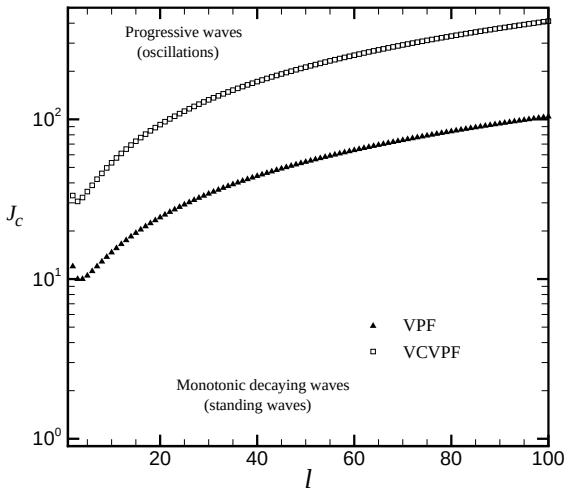

(b) bubble

Fig. 14.7. Critical Reynolds number J_c as a function of the mode number ℓ for a *drop* and a *bubble*. At a given ℓ, for $J > J_c$ progressive decaying waves (oscillations) are predicted (i.e. the eigenvalues $\hat{\sigma}$ are complex), whereas for $J \leq J_c$ monotonically decaying waves are obtained (i.e. the eigenvalues $\hat{\sigma}$ are real). The results are presented for VPF, VCVPF and the exact solution. Notice that the exact solution does not provide a crossover value, since the imaginary part is never identically zero.

For a bubble, the rate of decay and wave frequency are presented in Figures 14.9 (a) and (b), respectively for $\ell = 2$. Notice that the results follow similar trends as those described above for the drop. An important difference, however, is that the exact solution does not predict transition to the aperiodic standing waves regime, but the wave frequency tends smoothly to zero as J decreases (the viscosity increases, say). On the other hand, the irrotational viscous theories, VPF and VCVPF do render a cross-over J_c for which transition to monotonically decaying waves occurs.

For large values of J, if one of the fluids has negligible density and viscosity, a thin boundary layer results (Miller & Scriven 1968). Thus, an irrotational velocity field works as a good approximation with a pressure correction arising within the boundary layer and resolving the discrepancy between the non-zero irrotational shear stress and the actual zero shear stress at the interface. These considerations explain the excellent agreement of VCVPF and the exact solution for large J. In terms of the dissipation approximation, such a thin boundary layer yields a negligible contribution to the total viscous dissipation, which is thus determined by the irrotational flow. By contrast, as J decreases (e.g., the liquid viscosity increases), the boundary layer becomes thicker and

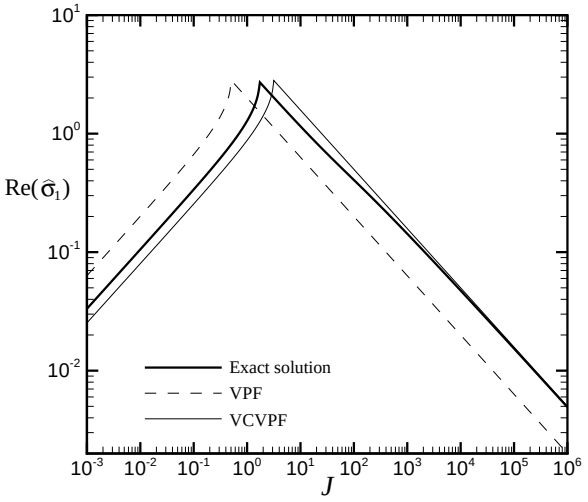

(a) Decay rate

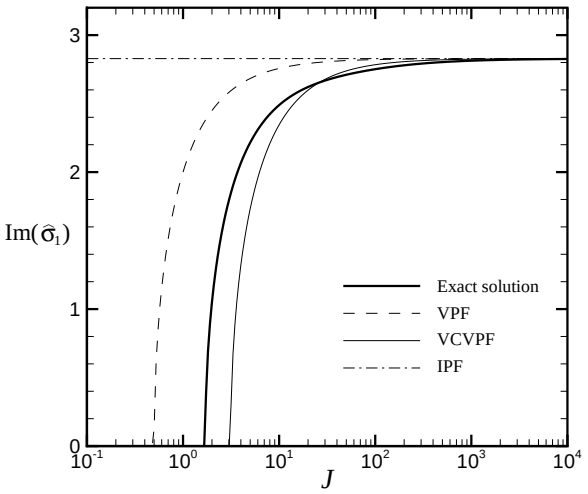

(b) Wave frequency

Fig. 14.8. Decay rate and wave frequency for the fundamental mode $\ell = 2$ as function of the Reynolds number J for a *drop* from the exact solution, VPF, VCVPF and IPF. The decay rate predicted by IPF is identically zero for all ℓ.

the performance of the irrotational approximations (VPF and VCVPF) deteriorates. A non-negligible boundary layer flow contributes substantially to the rate of viscous dissipation. The motion for small J, as discussed by Prosperetti (1980a), is restrained in such a drastic way that the energy dissipation per unit time, and thus the decay rate, decrease with the Reynolds number J.

The sharp cross-over from the progressive waves regime to the standing waves regime can be readily obtained from the dispersion relations (Figure 14.8). For a bubble, oscillatory decaying waves are always predicted by the exact linearized theory yet the smooth region where the decay-rate graph reaches a maximum as a function of the Reynolds number J suggests a transition in the structure of the flow (Figure 14.9). This was associated by Prosperetti (1980a) with the two length scales characteristic of the problem, namely, the sphere's radius a and the vorticity diffusion length of order $(\nu/\omega_B)^{1/2}$, where ω_B is the frequency of the oscillations for the inviscid case given in (14.2.28). When $a >> (\nu/\omega_B)^{1/2}$, which represents the right branch of the exact solution in Figure 14.9 (a), a thin vorticity layer at the interface occurs, having a minute effect on the rate of viscous dissipation. On the other hand, the left branch in Figure 14.9 (a), for which the rate of decay is reduced with decreasing J, as explained above, is associated with a relatively thicker vorticity layer such that $a << (\nu/\omega_B)^{1/2}$.

Computations carried out for several higher modes ($\ell = 3$, 4 and 10) have shown that the features commented

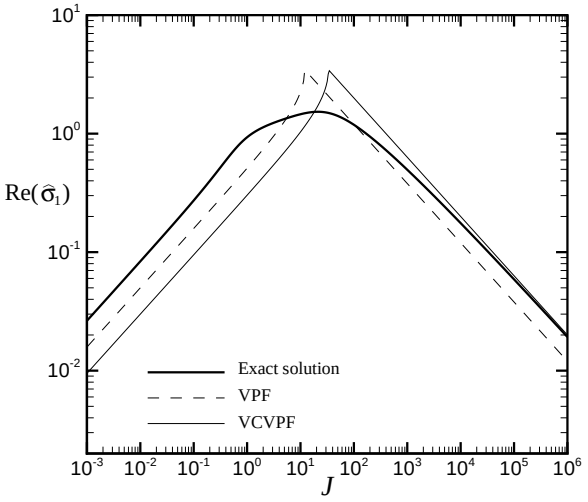

(a) Decay rate

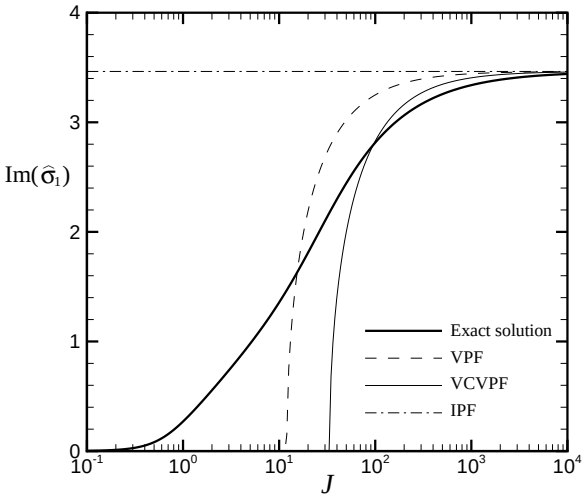

(b) Wave frequency

Fig. 14.9. Decay rate and wave frequency for the fundamental mode $\ell = 2$ as function of the Reynolds number J for a *bubble* from the exact solution, VPF, VCVPF and IPF. The decay rate predicted by IPF is identically zero for all ℓ.

for the fundamental mode are also observed for these other modes. The general trend is that the rate of decay increases with increasing ℓ. The analysis of the predictions from the exact solution indicates that the change-over from progressive waves to standing waves takes place for a larger critical J as ℓ increases for a drop. Even though no transition to standing waves occur, a somewhat similar behavior occurs for the bubble. The viscous irrotational theories follow these tendencies. These results show that viscosity damps the motion more effectively for shorter waves.

For a drop, Figures 14.10 through 14.12 show predictions from VPF, VCVPF and the exact solution for the rate of decay and frequency of the oscillations for several values of the Reynolds number J, namely, $J = 10^{-3}$, 40 and 10^6 as a function of ℓ. Results from IPF are only presented for the frequency. When J is small, in the standing waves regime, VCVPF gives a better approximation to the exact solution than VPF for the fundamental mode $\ell = 2$, as can be observed in Figure 14.10 for $J = 10^{-3}$. By contrast, for larger ℓ (i.e. shorter waves), VPF shows a better performance. As J increases, the waves start to oscillate. For instance, in the case of $J = 40$, the cross-over values of ℓ according to every viscous theory enters the analysis (see Figure 14.11). In this case, progressive waves are fully inhibited according to the viscous theories for $\ell < \ell_{\mathrm{VCVPF}}$, whereas these theories agree and predict standing waves for $\ell > \ell_{\mathrm{exact}}$. According to Figure 14.7 (a), this trend seems to hold for $J \geq 6$.

In Figure 14.12 for $J = 10^6$, the cross-over ℓ_c obtained from each viscous theory is larger than 100 and lie out of the figure. For large J, in the regime of progressive waves, the region of good agreement between VCVPF and the exact solution extends to higher values of ℓ (e.g., $2 \leq \ell \leq 100$ for $J = 10^6$ in Figure 14.12), while VPF shows poor agreement in comparison. At least for values of $\ell << \ell_{\text{exact}}$ in the neighborhood of $\ell = 2$, VCVPF provides the better approximation of the decay rate.

For very small values of J, as in the case of $J = 10^{-3}$, the exact solution, VPF and VCVPF predict zero frequency, while IPF is off the mark giving rise to a non-zero frequency for non-decaying waves (see Figure 14.10 b). For moderate to large values of J, the oscillatory regime appears for a certain ℓ interval starting with $\ell = 2$. This interval becomes wider with increasing J. The cross-over ℓ_c moves to the right as J increases and the agreement in terms of the frequency becomes much better in particular for low values of ℓ (Figure 14.11 b). On the other hand, since the cross over value ℓ_{VPF} is larger than ℓ_{VCVPF}, VPF follows the trend of the exact solution in the oscillatory regime for a wider interval. For very large values of J, the three approximations for the frequency cannot be distinguished from the predictions given by the exact solution for a wide ℓ interval (e.g., $2 \leq \ell \leq 100$ for $J = 10^6$ in Figure 14.12 b).

To some extend, similar trends as those described for the drop are observed for the bubble. However, a noteworthy difference is that, for low to moderate J (from 10^{-3} to 500, say), VPF predicts decay rates closer to the values from the exact solution than VCVPF. This trend is reversed for large J.

Kojo and Ueno (2006) present experimental results for oscillatory bubbles under ultrasonic vibration. Figure 14.13 shows the time series of shape oscillations for an air bubble in water under ultrasonic vibration of 20 kHz and the predicted shape with spherical harmonics. Several other figures showing the trends described above are included in the work by Padrino *et al.* (2006) available from the URL: http://www.aem.umn.edu/people/faculty/joseph/Visco

Concluding remarks

The results obtained from the viscous purely irrotational approximations for the decay rate and frequency of the oscillations for a drop and a bubble are in good to reasonable agreement with the exact solution of the linearized problem. The damping role of viscosity in the dynamics of the waves is adequately described by the viscous irrotational theories through the modeling of the decay rate and frequency of the oscillations, whereas the classical inviscid theory predicts undamped oscillations, and thus, an identically-zero decay rate. Some features are noteworthy from the comparison carried out in this study for the drop and the bubble:

- In the limit of short waves (i.e., large mode number ℓ), VPF gives a very good approximation of the decay rate for standing waves for both the drop and the bubble. On the other hand, VCVPF gives rise to values of the decay rate in closer agreement with the exact solution within a certain ℓ interval, including $\ell = 2$, in the progressive waves regime (i.e. long waves) for large values of the Reynolds number J. This trend resembles the tendencies obtained for free gravity waves perturbing a plane interface by Wang & Joseph (2006) presented in §14.1.4. Nonetheless, a notable difference between their results and those given here is that surface tension has a stronger regularizing effect on short waves than gravity.
- VPF also follows the trend described by the exact solution for the frequency of the oscillations, since the transition from progressive to standing waves predicted by this irrotational theory occurs at a higher critical value of ℓ than the threshold given by VCVPF.
- The viscous irrotational approximations predict effects of viscosity on the frequency of the oscillations. For every mode, there is a Reynolds number J for which transition from progressive waves to monotonically decaying waves occurs for either the drop or the bubble. Whereas a transitional value of J is predicted by the exact solution for a drop, only progressive waves are found by this theory for a bubble. In this case, very small frequencies are obtained as $J \to 0$ (e.g., $\nu \to \infty$).
- The viscous irrotational theories do not give rise to a continuos spectrum of eigenvalues for the bubble as has been found for the exact solution by Prosperetti (1980a).
- After carrying out the calculations, it is verified that the dissipation approximation yields the same dispersion relation as VCVPF. A general proof of this equivalence was shown in chapter 12.

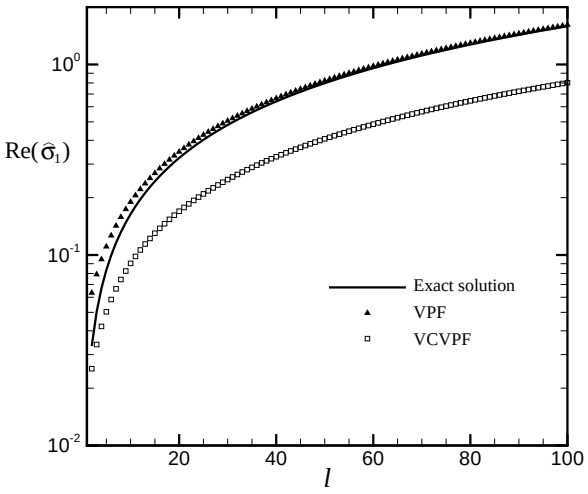

(a) Decay rate

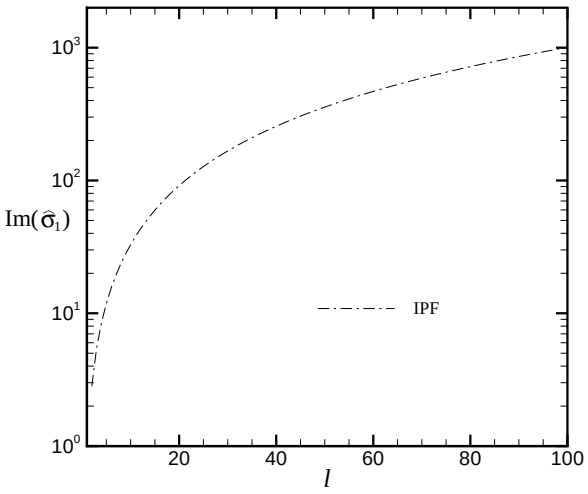

(b) Wave frequency

Fig. 14.10. Decay rate $\mathrm{Re}(\hat{\sigma}_1)$ and wave frequency $\mathrm{Im}(\hat{\sigma}_1)$ for $J = 10^{-3}$ versus the mode number ℓ for a *drop*. For the interval of ℓ shown, the eigenvalues from the viscous theories are real and different. The lowest decay rate is plotted in (a) and the trend exhibited by $\mathrm{Im}(\hat{\sigma}_1)$ is shown in (b) for IPF, which predicts oscillatory waves with constant amplitude.

14.3 Irrotational dissipation of capillary-gravity waves

In §14.1 we considered irrotational theories of the effect of viscosity on the decay of free gravity waves. In §14.2 we considered the same problem for capillary waves on a spherical surface. Capillary-gravity waves combine these two mechanisms of propagation and decay. The dissipation of irrotational waves was considered by Stokes 1851 and applied extensively by Lamb 1932. Here we consider extensions of Lamb's dissipation method to obtain the effect of viscosity on frequency and to nonlinear effects.

14.3.1 Correction of the wave frequency assumed by Lamb

The dissipation method stems from the mechanical energy equation. To apply the dissipation approximation to capillary-gravity waves, the working equation is obtained after subtracting the basic state of rest from the incompressible Navier-Stokes equation and then taking the scalar ('dot') product with the velocity vector. Integration

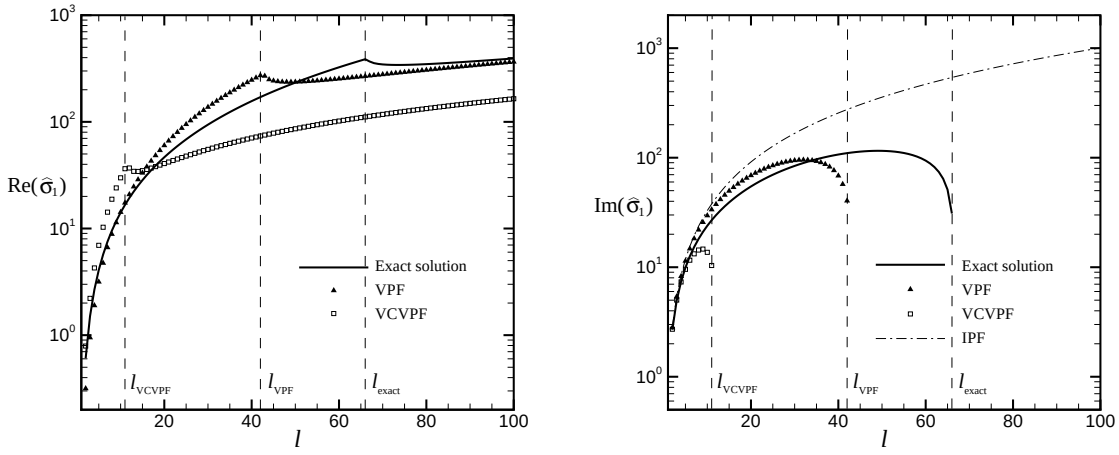

(a) Decay rate

(b) Wave frequency

Fig. 14.11. Decay rate $\mathrm{Re}(\hat{\sigma}_1)$ and wave frequency $\mathrm{Im}(\hat{\sigma}_1)$ for $J = 40$ versus the mode number ℓ for a *drop*. In this case, the eigenvalues are a pair of complex conjugates for the interval of $\ell < \ell_c$ and they are real and different for $\ell \geq \ell_c$. For the latter case, the lowest decay rate is plotted in (a). The symbol ℓ_c stands for the highest value of ℓ for which a non-zero imaginary part is obtained, i.e. progressive waves occur. For instance, $\ell_{\mathrm{exact}} = \ell_c$ from fully viscous flow theory (exact solution); analogous definitions can be set for VPF (ℓ_{VPF}) and VCVPF (ℓ_{VCVPF}).

over the region of interest yields the mechanical energy equation for the flow disturbances in integral form. Next, it is assumed that the zero-shear-stress condition at the interface is satisfied. After some manipulation, this equation can be written as

$$\frac{\mathrm{d}}{\mathrm{d}t}\left(\int_V \rho\,|\mathbf{u}|^2/2\;\mathrm{d}V + \int_0^\lambda \rho g\eta^2/2\;\mathrm{d}x\right) = \int_0^\lambda v\gamma\frac{\partial^2\eta}{\partial x^2}\;\mathrm{d}x - \int_V 2\mu\mathbf{D}:\mathbf{D}\;\mathrm{d}V, \tag{14.3.1}$$

where γ is the surface tension. Setting $\gamma = 0$ yields expression (14.1.17). The last term in (14.3.1) gives the viscous dissipation. This term is computed assuming that the fluid motion is irrotational, neglecting the thickness of the vorticity layer at the free surface. For irrotational flow, the following identity holds,

$$\int_V 2\mu\mathbf{D}:\mathbf{D}\mathrm{d}V = \int_A \mathbf{n}\cdot 2\mu\mathbf{D}\cdot\mathbf{u}\mathrm{d}A. \tag{14.3.2}$$

which is used in the calculation of the viscous dissipation; in (14.3.2), $\mathbf{n}$ is the outward normal. The integration of (14.3.1) is carried out with the velocity potential given in (14.1.16) over the region defined by $0 \leq x \leq \lambda$ and $-\infty < y \leq 0$. Periodic boundary conditions at $x = 0$ and $x = \lambda$ and vanishingly small disturbances (both velocity and pressure) as $y \to -\infty$ are taken into account in (14.3.1). Therefore, the surface integrals are evaluated at $y = 0$. As a result, the following expression is obtained for the eigenvalues

$$n = -2\nu k^2 \pm \mathrm{i}k\sqrt{(g/k + \gamma' k) - 4\nu^2 k^2}, \tag{14.3.3}$$

with $\gamma' = \gamma/\rho$. For $2\nu k^2 \geq \sqrt{gk + \gamma' k^3}$, the eigenvalues are real and monotonically decaying waves occur. On the other hand, for $2\nu k^2 \leq \sqrt{gk + \gamma' k^3}$ we find progressive decaying waves with rate of decay $-2\nu k^2$. This is the same value computed by Lamb (1932) via the dissipation method. However, Lamb's approach did not account for the effects of viscosity in the wave speed of traveling decaying waves. For this type of waves, the wave speed is extracted from (14.3.3) as

$$c = \sqrt{(g/k + \gamma' k) - 4\nu^2 k^2} \tag{14.3.4}$$

which is slower than the inviscid result $\sqrt{g/k + \gamma' k}$ used by Lamb (1932, §348) . Therefore, these calculations indicate that effects of viscosity, considered through the viscous dissipation of the mechanical energy, decrease the traveling speed of capillary-gravity waves. This trend also holds for either zero gravity or zero surface tension, as can be deduced from (14.3.4).

It turns out that the result given in (14.3.3) is exactly the same obtained from VCVPF according to Padrino

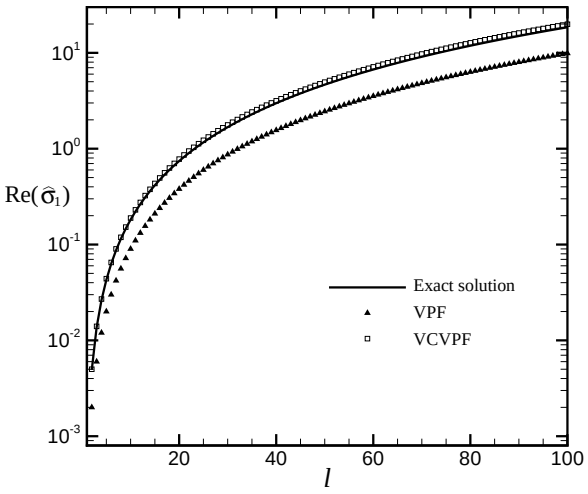

(a) Decay rate

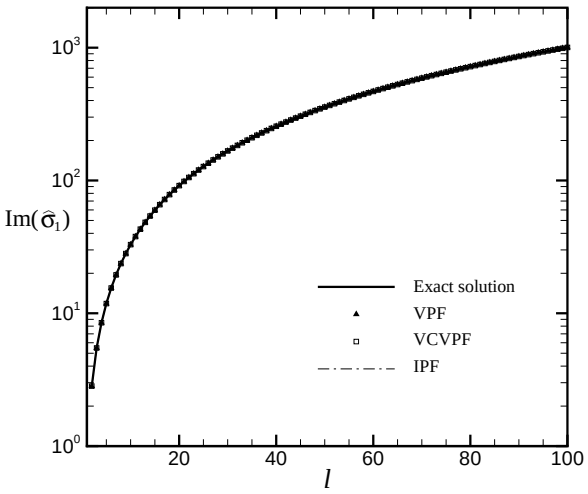

(b) Wave frequency

Fig. 14.12. Decay rate $\mathrm{Re}(\hat{\sigma}_1)$ and wave frequency $\mathrm{Im}(\hat{\sigma}_1)$ for $J = 10^6$ versus the mode number ℓ for a *drop*. In this case, the eigenvalues are a pair of complex conjugates for the interval of ℓ considered in this study.

et al. (2006). More details on the various aspects of the VPF, VCVPF and DM analyses for capillary-gravity waves are presented there.

14.3.2 Irrotational dissipation of nonlinear capillary-gravity waves

Many studies of nonlinear irrotational waves can be found in the literature but the only study of the effects of viscosity on the decay of these waves known to us is due to Longuet-Higgins (1997) who used the dissipation method to determine the decay due to viscosity of irrotational steep capillary-gravity waves in deep water. He finds that the limiting rate of decay for small amplitude solitary waves are twice those for linear periodic waves computed by the dissipation method. The dissipation of very steep waves can be more than ten times more than linear waves due to the sharply increased curvature in wave troughs. He assumes that the nonlinear wave maintains its steady form while decaying under the action of viscosity. The wave shape could change radically from its steady shape in very steep waves.

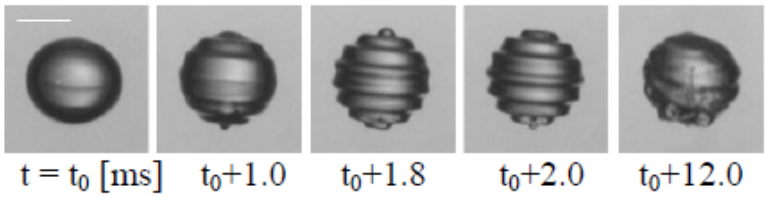

(a) Experiments.

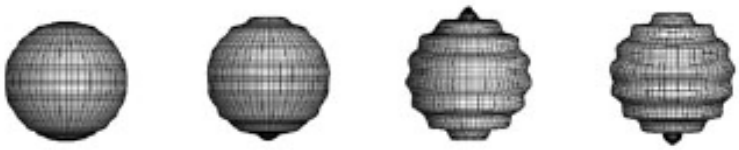

(b) Predictions.

Fig. 14.13. Experimental and theoretical time evolution of shape oscillations of an air bubble in water with oscillation mode $(\ell,m) = (15,0)$ under ultrasonic vibration of 20 kHz. The bar at the top of the left frame in (a) corresponds to 1.0 mm (Kojo and Ueno 2006).

15

Irrotational Faraday waves on a viscous fluid

When a vessel containing liquid is made to vibrate vertically with constant frequency and amplitude a pattern of standing waves on the gas-liquid surface can appear. For some combinations of frequency and amplitude waves appear, for other combinations the free surface remains flat. These waves were first studied in the experiments of Faraday (1831), who noticed that the frequency of the liquid vibrations was only half that of the vessel. Nowadays, this would be described as a symmetry breaking vibration of a type that characterized the motion of a simple pendulum subjected to a vertical oscillation of its purpose.

The first mathematical study of Faraday waves are due to Rayleigh (1883a, b) but the first definitive study is due to Benjamin and Ursell (1954) who remark that "... The present work has been made possible by the development of the theory of Mathieu functions."

Faraday's problem is a rich source of problems in pattern formation, bifurcation, chaos and other topics in the frame of fluid mechanics applications in the modern theory of dynamical system. Under the excitation of different parameters governing the Faraday system different patterns, stripes, squares, hexagons and time dependent states can be observed. These features have spawned a large recent literature on Faraday waves. The experiments of Ciliberto and Gollub (1985) and Simonelli and Gollub (1989) on chaos, symmetry and mode interactions are often cited. Theoretical approaches are restricted to "weak nonlinearities;" practically, some forms of expansion truncated at low order are used. The theoretical studies of Miles (1967), Ockendon and Ockendon (1973), Gu and Sethna (1987) and Feng and Sethna (1989) are weakly nonlinear studies of the Faraday instability for an inviscid fluid. Vega *et al.* (2001) and Higuera *et al.* (2005, 2006) studied weakly nonlinear and nearly inviscid Faraday waves with weak viscous effect, driven from boundary layers at the bottom of the containers and at the free surface.

Here we study the effects of viscosity of Faraday waves. There are two kinds of effects, those associated with vorticity and purely irrotational effects. The purely irrotational effects have not been considered before and they are studied here.

Effects associated with boundary layers at which vorticity is generated have been discussed by Miles (1967) who notes that

> "... the damping of surface waves in closed basins appears to be due to (a) viscous dissipation at the boundary of the surrounding basin, (b) viscous dissipation at the surface in consequence of surface contamination, and (c) capillary hysteresis associated with the meniscus surrounding the free surface."

Free surfaces are a source for the generation of vorticity due to the fact that the shear stress vanishes there but the shear stress computed on irrotational flow does not vanish. Vorticity generation does not have a strong effect on damping even for progressive waves (§14.1), much less for Rayleigh-Taylor waves which are closely related to the Faraday waves studied here.

Miles (1984) used a Lagrangina/Hamiltonian approach and included weak linear damping in treating the

Faraday wave problem while retaining the inviscid approximation. Miles (1984) and Miles and Henderson (1990) advocate an empirical approach to these damping effects. Miles and Henderson note that

"Weak linear damping may be incorporated ... by introducing the dissipation function $D = \frac{1}{2}\alpha_n \left(p_n^2 + q_n^2\right)$ where $\alpha_n \equiv \delta_n/\epsilon$ and δ_n is the ratio of actual to critical damping for free oscillations in the n-th mode [δ_n is best determined experimentally, although theoretical estimates are available (Miles 1967)] ..."

The possibility that viscous damping can be rigorously calculated from purely irrotational theories without boundary layers has not been considered. Here we show that this possibility can be realized in the linearized case. The same kind of techniques can be used to calculate damping in nonlinear problems based on the equations of potential flow of an inviscid fluid. Of particular interest are the bifurcation studies on nonlinear Faraday waves on an inviscid fluid by Feng and Sethna (1989) and Gu and Sethna (1987) which are discussed in §15.8.

15.1 Introduction

The seminal paper of Benjamin & Ursell (1954) (referred to as BU hereafter) on the stability of the plane free surface of a liquid in vertical periodic motion has spawned a huge literature which extends their analysis to include effects of viscosity, two liquids, side wall, bottom and free surface boundary layers and nonlinear effects associated with bifurcation and pattern formation. Review papers emphasizing different aspects of this problem have been prepared by Miles & Henderson (1990), Dias & Kharif (1999), and Perlin & Schultz (2000). This paper focuses of the effects of viscosity using viscous potential flow for exactly the same problem, in exactly the same formulation as Benjamin & Ursell (1954).

We have derived the following two damped Mathieu equations from systematic analysis of the irrotational motion of viscous fluids in the formulation and using the notations introduced by BU. Thus

$$\ddot{a}_m + N\nu\dot{a}_m k_m^2 + k_m \tanh\left(k_m h\right)\left[\frac{\gamma}{\rho}k_m^2 + \left(g - f\cos\left(\omega t\right)\right)\right] a_m = 0 \tag{15.1.1}$$

where k_m is an eigenvalue of the vibrating membrane equation

$$\frac{\partial^2 S_m}{\partial x^2} + \frac{\partial^2 S_m}{\partial y^2} + k_m^2 S_m = 0 \tag{15.1.2}$$

and

$$N = 2 \text{ (VPF)}, \quad N = 4 \text{ (VCVPF)}.$$

The number $N = 4$ also appears in the approximation called phenomenological by Kumar and Tuckerman (KT) (1994) who incorporated damping using a damping coefficient given by Landau and Lifshitz (1987), §25. They say that "... for small damping (*i.e.* for $\lambda^2\omega \gg \nu$) and for small deformation of the interface ..., the flow can be considered to be irrotational except for a thin layer around the interface. The restriction to small deformations of the interface is required for linearization, but the restriction to small damping, to small viscosities is not implied by any mathematical argument and, in fact, is erroneous. The damping coefficient of Landau and Lifshitz (1987) is correct for gas-liquid flow but the application of this damping coefficient by KT (1994) to waves on the interface between two liquids is less justified and will lead to large errors for the long waves (§16.1.8) which occur in the Faraday problem. We find that the damped Mathieu equation (15.1.1) with $N = 2$ gives a better approximation to small amplitude Faraday dynamics than $N = 4$ for which the waves are "overdamped."

15.2 Energy equation

The energy equation is the basis of our VCVPF theory. We derive the mechanical energy equation from Navier-Stokes equations

$$\rho\frac{\mathrm{d}\boldsymbol{u}}{\mathrm{d}t}=\nabla\cdot\mathbf{T}+\rho\left(g-f\cos(\omega t)\right)\ \boldsymbol{e}_z \tag{15.2.1}$$

in the usual way; scalar multiply (15.2.1) by $\boldsymbol{u}$, integrate over the fluid domain V, apply Reynolds' transport theorem and Gauss' theorem, to find

$$\frac{\mathrm{d}}{\mathrm{d}t}\int_V\frac{1}{2}\rho\left|\boldsymbol{u}\right|^2\mathrm{d}V=\int_{A_f}\boldsymbol{u}\cdot\mathbf{T}\cdot\boldsymbol{n}\mathrm{d}A+\int_{A_w}\boldsymbol{u}\cdot\mathbf{T}\cdot\boldsymbol{n}\mathrm{d}A-\int_V 2\mu\mathbf{D}:\mathbf{D}\mathrm{d}V+(g-f\cos(\omega t))\int_V\rho\frac{\mathrm{d}z}{\mathrm{d}t}\mathrm{d}V, \tag{15.2.2}$$

where A_f is the free surface, A_w represents both the side walls and the bottom wall, and $\boldsymbol{n}$ is the outward normal of V on A. The integrals $\displaystyle\int_{A_f}\boldsymbol{u}\cdot\mathbf{T}\cdot\boldsymbol{n}\mathrm{d}A$ and $\displaystyle\int_{A_w}\boldsymbol{u}\cdot\mathbf{T}\cdot\boldsymbol{n}\mathrm{d}A$ are the power of traction. On the free surface $\boldsymbol{n}\approx-\boldsymbol{e}_z$ and we can show readily that

$$\boldsymbol{u}\cdot\mathbf{T}\cdot\boldsymbol{n}=-\left(u_xT_{xz}+u_yT_{yz}+u_zT_{zz}\right). \tag{15.2.3}$$

We shall be considering the potential flow of viscous fluids called VPF. For these flows, the no-slip conditions usually cannot be satisfied and they are replaced with (15.3.1) below. The stresses on the free surface are evaluated using potential flow

$$\left.\begin{aligned}T_{xz}&=\tau^i_{xz}=\mu\left(\frac{\partial u_x}{\partial z}+\frac{\partial u_z}{\partial x}\right),\\T_{yz}&=\tau^i_{yz}=\mu\left(\frac{\partial u_y}{\partial z}+\frac{\partial u_z}{\partial y}\right),\\T_{zz}&=-p_i+\tau^i_{zz}=-p_i+2\mu\frac{\partial u_z}{\partial z},\end{aligned}\right\} \tag{15.2.4}$$

where p_i is the irrotational pressure computed from the Bernoulli equation. Then the mechanical energy equation for VPF may be written as

$$\begin{aligned}\frac{\mathrm{d}}{\mathrm{d}t}\int_V\frac{1}{2}\rho\left|\boldsymbol{u}\right|^2\mathrm{d}V=&\int_{A_f}-\left[u_x\tau^i_{xz}+u_y\tau^i_{yz}+u_z\left(-p_i+\tau^i_{zz}\right)\right]\mathrm{d}A+\int_{A_w}\boldsymbol{u}\cdot\mathbf{T}\cdot\boldsymbol{n}\mathrm{d}A\\&-\int_V 2\mu\mathbf{D}:\mathbf{D}\mathrm{d}V+(g-f\cos(\omega t))\int_V\rho\frac{\mathrm{d}z}{\mathrm{d}t}\mathrm{d}V.\end{aligned} \tag{15.2.5}$$

The shear stresses τ^i_{xz} and τ^i_{yz} from the potential flow are not zero at the free surface. However, the shear stresses should be zero physically. T_{xz} and T_{yz} cannot be made zero in irrotational flows, but we can remove the power by the shear stress $\displaystyle\int_{A_f}\left(u_x\tau^i_{xz}+u_y\tau^i_{yz}\right)\mathrm{d}A$ from the mechanical energy equation. At the same time, a pressure correction p_v is added to p_i to compensate for the shear stresses. The mechanical energy equation for VCVPF is then written as

$$\begin{aligned}\frac{\mathrm{d}}{\mathrm{d}t}\int_V\frac{1}{2}\rho\left|\boldsymbol{u}\right|^2\mathrm{d}V=&\int_{A_f}-\left[u_z\left(-p_i-p_v+\tau^i_{zz}\right)\right]\mathrm{d}A+\int_{A_w}\boldsymbol{u}\cdot\mathbf{T}\cdot\boldsymbol{n}\mathrm{d}A\\&-\int_V 2\mu\mathbf{D}:\mathbf{D}\mathrm{d}V+(g-f\cos(\omega t))\int_V\rho\frac{\mathrm{d}z}{\mathrm{d}t}\mathrm{d}V.\end{aligned} \tag{15.2.6}$$

A comparison of (15.2.5) and (15.2.6) gives rise to the relation between the pressure correction and the irrotational shear stresses

$$\int_{A_f}\left[u_x\tau^i_{xz}+u_y\tau^i_{yz}\right]\mathrm{d}A=\int_{A_f}\left(-p_vu_z\right)\mathrm{d}A. \tag{15.2.7}$$

15.3 VPF & VCVPF

The two theories VPF and VCVPF give rise to different results. Our experience with other problems is such as to suggest that VCVPF is closer to exact results for progressive waves, and VPF is closer to exact results when

waves do not propagate, more precisely, in this case the eigenvalues are real. This second case, in which VPF is better, applies here to irrotational Faraday waves on viscous fluids.

15.3.1 Potential flow

The velocity $\boldsymbol{u} = \nabla\phi = (u_x, u_y, u_z)$ is expressed in terms of a harmonic potential $\nabla^2\phi = 0$ in a coordinate system moving with the container. Boundary conditions at the container walls are given by

$$\left.\begin{aligned} \frac{\partial\phi}{\partial n} &= 0 \ \text{ on the side walls,} \\ \frac{\partial\phi}{\partial z} &= 0 \ \text{ on the bottom wall at } z = h. \end{aligned}\right\} \tag{15.3.1}$$

A harmonic solution satisfying (15.3.1) can be written as

$$\phi(x, y, z, t) = \sum_{m=0}^{\infty} f_m(t) \cosh\left[k_m\left(h - z\right)\right] S_m(x, y), \tag{15.3.2}$$

where the eigenfunctions $S_m(x, y)$ satisfy

$$\frac{\partial S_m}{\partial n} = 0, \tag{15.3.3}$$

on the side wall. The condition at the bottom wall gives

$$\left(\frac{\partial\phi}{\partial z}\right)_{z=h} = \sum_{m=0}^{\infty} f_m(t)\left(-k_m\right)\sinh\left[k_m\left(h - z\right)\right] S_m(x, y)\Big|_{z=h} = 0. \tag{15.3.4}$$

The normal stress balance at the free surface

$$z = \zeta(x, y, t), \tag{15.3.5}$$

in the linearized approximation, is

$$\left(p - 2\mu\frac{\partial u_z}{\partial z}\right)_{z=0} = \gamma\left(\frac{\partial^2\zeta}{\partial x^2} + \frac{\partial^2\zeta}{\partial y^2}\right). \tag{15.3.6}$$

For VPF, $p = p_i$ where p_i is given by the Bernoulli equation. For VCVPF, $p = p_i + p_v$ where p_v is a viscous correction of the irrotational pressure p_i.

15.3.2 Amplitude equations for the elevation of the free surface

Now consider the kinematic condition at $z = 0$

$$\frac{\partial\zeta}{\partial t} = u_z = \frac{\partial\phi}{\partial z} \quad \text{at} \quad z = 0 \tag{15.3.7}$$

where

$$\left(\frac{\partial\phi}{\partial z}\right)_{z=0} = \sum_{m=0}^{\infty} f_m(t)\left(-k_m\right)\sinh\left(k_m h\right) S_m(x, y). \tag{15.3.8}$$

If we write the surface elevation as

$$\zeta = \sum_{m=0}^{\infty} a_m(t) S_m(x, y), \tag{15.3.9}$$

then

$$\frac{\partial\zeta}{\partial t} = \sum_{m=0}^{\infty} \frac{\mathrm{d}a_m}{\mathrm{d}t} S_m(x, y). \tag{15.3.10}$$

Since the total volume of fluid is constant, $a_0(t)$ is constant

$$\frac{\mathrm{d}a_0}{\mathrm{d}t} = 0$$

and

$$\frac{\gamma}{\rho}\left(\frac{\partial^2\zeta}{\partial x^2} + \frac{\partial^2\zeta}{\partial y^2}\right) = -\frac{\gamma}{\rho}\sum_{m=1}^{\infty} k_m^2 a_m(t) S_m(x,y). \tag{15.3.11}$$

Since $k_0 = 0$, (15.3.11) and (15.3.8) show that $f_0(t)$ is undetermined. BU showed that $a_0(t)$ can be put to zero.

For $m \geq 1$, (15.3.7), (15.3.8) and (15.3.10) give

$$\frac{\mathrm{d}a_m}{\mathrm{d}t} S_m(x,y) = f_m(t)\,(-k_m)\sinh(k_m h)\,S_m(x,y), \quad \text{hence } f_m(t) = -\frac{\mathrm{d}a_m}{\mathrm{d}t}\frac{1}{k_m \sinh(k_m h)},$$

so that the potential is given by

$$\phi(x,y,z,t) = -\sum_{m=1}^{\infty} \frac{\mathrm{d}a_m}{\mathrm{d}t}\frac{\cosh\left[k_m\,(h-z)\right]}{k_m \sinh(k_m h)} S_m(x,y). \tag{15.3.12}$$

The Bernoulli's equation is

$$\frac{p_i}{\rho} + \frac{\partial\phi}{\partial t} - (g - f\cos(\omega t))\,z = 0. \tag{15.3.13}$$

The normal stress balance (15.3.6) is

$$\left(p_i + p_v - 2\mu\frac{\partial u_z}{\partial z}\right)_{z=0} = \gamma\left(\frac{\partial^2\zeta}{\partial x^2} + \frac{\partial^2\zeta}{\partial y^2}\right). \tag{15.3.14}$$

Linearized governing equations for the viscous corrections are

$$\rho\frac{\partial \boldsymbol{u}_v}{\partial t} = -\nabla p_v + \mu\nabla^2\boldsymbol{u}_v, \quad \nabla\cdot\boldsymbol{u}_v = 0. \tag{15.3.15}$$

Hence,

$$\nabla^2 p_v = 0. \tag{15.3.16}$$

The solution of (15.3.16) may be written as

$$-p_v = \sum_{m=0}^{\infty} C_m \hat{r}_m(t)\theta_m(z) S_m(x,y), \quad \theta_m = c_{m1}\mathrm{e}^{k_m z} + c_{m2}\mathrm{e}^{-k_m z}. \tag{15.3.17}$$

At $z = 0$,

$$-p_v(z=0) = \sum_{m=0}^{\infty} C_m r_m(t) S_m(x,y), \tag{15.3.18}$$

where $r_m = \hat{r}_m(t)\,(c_{m1} + c_{m2})$.

We may eliminate p_i from (15.3.14) using (15.3.13)

$$\left[p_v + \rho\,(g - f\cos(\omega t))\,\zeta - \rho\frac{\partial\phi}{\partial t} - 2\mu\frac{\partial^2\phi}{\partial z^2}\right]_{x=0} = \gamma\left(\frac{\partial^2\zeta}{\partial x^2} + \frac{\partial^2\zeta}{\partial y^2}\right). \tag{15.3.19}$$

Equation (15.3.19) may be evaluated on modal functions using (15.3.9), (15.3.11),

$$2\mu\frac{\partial^2\phi}{\partial z^2} = -2\mu\sum_{m=1}^{\infty}\frac{\mathrm{d}a_m}{\mathrm{d}t} k_m \frac{\cosh\left[k_m\,(h-z)\right]}{\sinh(k_m h)} S_m(x,y) \tag{15.3.20}$$

and

$$\frac{\partial\phi}{\partial t} = -\sum_{m=1}^{\infty}\frac{\mathrm{d}^2 a_m}{\mathrm{d}t^2}\frac{\coth\left[k_m\,(h-z)\right]}{k_m \sinh(k_m h)} S_m(x,y). \tag{15.3.21}$$

Hence

$$\sum_{m=1}^{\infty}\left[-C_m r_m(t)+\rho\left(g-f\cos\left(\omega t\right)\right)a_m(t)+\rho\frac{\mathrm{d}^2a_m}{\mathrm{d}t^2}\frac{\coth\left(k_m h\right)}{k_m}\right.$$
$$\left.+2\mu\frac{\mathrm{d}a_m}{\mathrm{d}t}k_m\coth\left(k_m h\right)+\gamma k_m^2 a_m(t)\right]S_m(x,y)=0. \tag{15.3.22}$$

The coefficients of the linearly independent functions $S_m(x,y)$ vanish. Hence the amplitude equation for VCVPF is

$$\frac{\mathrm{d}^2a_m}{\mathrm{d}t^2}+2\nu k_m^2\frac{\mathrm{d}a_m}{\mathrm{d}t}+k_m\tanh\left(k_m h\right)\left[\frac{\gamma}{\rho}k_m^2+g-f\cos(\omega t)\right]a_m$$
$$-\frac{k_m}{\rho}\tanh\left(k_m h\right)C_m r_m(t)=0. \tag{15.3.23}$$

To evaluate $C_m r_m(t)$ in (15.3.23) we need to work only with mode m. To simplify the writing we shall suppress the subscript m and write

$$u_x = -\frac{\mathrm{d}a}{\mathrm{d}t}\frac{\coth\left(kh\right)}{k}\frac{\partial S}{\partial x}, \tag{15.3.24}$$
$$\tau_{xz} = 2\mu\frac{\mathrm{d}a}{\mathrm{d}t}\frac{\partial S}{\partial x}, \tag{15.3.25}$$
$$u_y = -\frac{\mathrm{d}a}{\mathrm{d}t}\frac{\coth\left(kh\right)}{k}\frac{\partial S}{\partial y}, \tag{15.3.26}$$
$$\tau_{yz} = 2\mu\frac{\mathrm{d}a}{\mathrm{d}t}\frac{\partial S}{\partial y}, \tag{15.3.27}$$
$$u_z = \frac{\mathrm{d}a}{\mathrm{d}t}S, \tag{15.3.28}$$
$$p_v = -Cr(t)S, \tag{15.3.29}$$
$$\tau_{zz} = -2\mu\frac{\mathrm{d}a}{\mathrm{d}t}k\coth\left(kh\right)S, \tag{15.3.30}$$

$$\int_A\left[u_x\tau_{xz}+u_y\tau_{yz}+p_v u_z\right]\mathrm{d}A=\int_A\left\{-2\mu\left(\frac{\mathrm{d}a}{\mathrm{d}t}\right)^2\frac{\coth\left(kh\right)}{k}\left[\left(\frac{\partial S}{\partial x}\right)^2+\left(\frac{\partial S}{\partial y}\right)^2\right]-Cr(t)\frac{\mathrm{d}a}{\mathrm{d}t}S^2\right\}\mathrm{d}A=0.$$

Using Gauss' theorem and the boundary condition on the side wall (15.3.3), we obtain

$$\int_A\left[\frac{\partial}{\partial x}\left(S\frac{\partial S}{\partial x}\right)+\frac{\partial}{\partial y}\left(S\frac{\partial S}{\partial y}\right)\right]\mathrm{d}A=\int_L\left[S\frac{\partial S}{\partial n}\right]\mathrm{d}L=0,$$

where L is the boundary of the free surface A and L is on the side wall. With the condition $\nabla_2^2 S=-k^2S$, we can show that

$$\int_A\left[\left(\frac{\partial S}{\partial x}\right)^2+\left(\frac{\partial S}{\partial y}\right)^2\right]\mathrm{d}A=-\int_A S\nabla_2^2 S\mathrm{d}A=k^2\int_A S^2\mathrm{d}A. \tag{15.3.31}$$

We find that

$$\left(2\mu\left(\frac{\mathrm{d}a}{\mathrm{d}t}\right)^2k\coth\left(kh\right)+Cr(t)\frac{\mathrm{d}a}{\mathrm{d}t}\right)\int S^2\mathrm{d}A=0 \tag{15.3.32}$$

and

$$C_m r_m(t)=Cr(t)=-2\mu k\frac{\mathrm{d}a}{\mathrm{d}t}\coth\left(kh\right). \tag{15.3.33}$$

Inserting (15.3.33) into (15.3.23) we find the amplitude equation for VCVPF

$$\frac{\mathrm{d}^2a}{\mathrm{d}t^2}+4\nu k^2\frac{\mathrm{d}a}{\mathrm{d}t}+k\tanh\left(kh\right)\left[\frac{\gamma}{\rho}k^2+g-f\cos(\omega t)\right]a=0. \tag{15.3.34}$$

Viscous potential flow VPF is the same as VCVPF without the pressure correction p_v. If p_v is set to zero, we find that

$$\frac{\mathrm{d}^2 a}{\mathrm{d}t^2} + 2\nu k^2 \frac{\mathrm{d}a}{\mathrm{d}t} + k\tanh(kh)\left[\frac{\gamma}{\rho}k^2 + g - f\cos(\omega t)\right] a = 0. \tag{15.3.35}$$

The damping term can be written as

$$N\nu k^2 \frac{\mathrm{d}a}{\mathrm{d}t} \tag{15.3.36}$$

with $N = 2$ for VPF and $N = 4$ for VCVPF.

15.4 Dissipation method

The dissipation method leads to the same amplitude equation (15.3.34) which we derived for VCVPF. The two theories are equivalent, but no pressure, whatever is required to implement the dissipation method. In the dissipation calculation, the power of the pressure correction is replaced with the power of shear tractions (see (12.6.1)).

The dissipation calculation gives the same results as VCVPF. (15.3.34) is also in agreement with (4.21) of Kumar & Tuckerman(1994).

15.5 Stability analysis

The amplitude equations are

$$\ddot{a} + N\nu\dot{a}k^2 + k\tanh(kh)\left[\frac{\gamma}{\rho}k^2 + (g - f\cos(\omega t))\right] a = 0 \tag{15.5.1}$$

where

$$N = 2 \text{ (VPF)}, \quad N = 4 \text{ (VCVPF)}. \tag{15.5.2}$$

In the fourth order RK integration, we may take time difference $\Delta t = \pi/2^{12} = \pi/4096$ for which time at n steps is given by $t = n \times \Delta t$ and periodic time T may be defined as

$$T = \left[\frac{t}{2\pi}\right] \tag{15.5.3}$$

with Gauss' symbol [ ]. According to Floquet theory, we may represent the solutions of (15.5.1) in the unstable region as

$$\ln(a(t)) = \sigma t + \beta = \sigma 2\pi T + \beta \tag{15.5.4}$$

where $\exp(\beta(t)) = b(t)$ is periodic in t but constant in T, and the growth rate σ is positive; $\sigma = 0$ at the marginal state. To check $\exp(\beta(t)) = b(t)$, we may use Fourier series expressed as

$$b(t) = \sum_{n=-\infty}^{\infty} A_n \exp(\mathrm{i}nt) \tag{15.5.5}$$

where the Fourier coefficient A_{-n} is the complex conjugate of A_n. The coefficient is evaluated as

$$A_m = \frac{1}{2\pi}\int_t^{t+2\pi} b(t)\exp(-\mathrm{i}mt)\mathrm{d}t = \frac{1}{2\pi}\sum_{j=1}^{8192}\left[b(t_j)\exp(-\mathrm{i}mt_j) + b(t_{j-1})\exp(-\mathrm{i}mt_{j-1})\right]\frac{\Delta t}{2} \tag{15.5.6}$$

with the trapezoidal rule; $t_j = t + j \times \Delta t$.

The solution of (15.5.1) can be written in Floquet form.

$$a(t) = \mathrm{e}^{\sigma t} b(t) \tag{15.5.7}$$

where σ is the growth rate and $b(t)$ is a bounded oscillatory function which is periodic when

$$\sigma = 0 \quad \text{(marginal state)} \tag{15.5.8}$$

or

$$\sigma > 0 \quad \text{(unstable state)}. \tag{15.5.9}$$

A growth rate curve is given by

$$\sigma = \sigma(k) = \sigma(-k) \tag{15.5.10}$$

which is an even function of k.

The maximum growth rate is

$$\sigma_m = \overset{\text{Max}}{k} > 0 \, [\sigma(k)] = \sigma(k_m). \tag{15.5.11}$$

The flow is stable when $k > k_c$

$$\sigma(k) < 0, \quad k > k_c \tag{15.5.12}$$

where k_c is called the cut off wave number. This says that short waves are stable.

The governing equation (15.5.1) for the oscillation amplitude in a deep liquid $h \to \infty$ is

$$\ddot{a} + N\nu\dot{a}k^2 + k\left[\frac{\gamma}{\rho}k^2 + (g - f\cos(\omega t))\right]a = 0 \tag{15.5.13}$$

where $N = 2$ (VPF) or $N = 4$ (VCVPF). The main goal of this calculation is to show that for any value of the kinematic viscosity ν, the other parameters being constant, $N = 2$ has a larger maximum growth rate than $N = 4$. Hence, the irrotational theory associated with the direct effects of the viscous normal stress (VPF) on the motion of the waves will give a better description of the effects of viscosity on the waves, than the value $N = 4$ (VCVPF) which has been universally used by researchers in this subject since the study of Kumar & Tuckerman(1994).

Cerda & Tirapegui (1998) considered Faraday's instability in a viscous fluid and found a Mathieu equation based on lubrication theory rather than potential flow. They interpret the irrotational theory leading to $N = 4$ as appropriate to weak dissipation. Our irrotational theories are not restricted to small viscosity, but they do not account for vorticity generated by the no-slip condition on the container side walls or bottom. For periodic disturbances on deep water the irrotational theories are valid for all values of ν.

Our results apply to silicon oils with kinematic viscoucities ranging from zero to 10 cm^2/sec, the density of 0.97 g/cm^3 and surface tension of $\gamma = 21$ dyne/cm. The frequency $\omega = 15.87 \times 2\pi$ sec^{-1} is fixed and $(g,\ f) = (981,\ 981)$ cm/sec^2.

In figure 15.1 and 15.2 we present graphs and tables for the Floquet representation $a = \text{e}^{\sigma t}b(t)$ for the stability of Faraday waves on an inviscid and a viscous fluid.

In figure 15.3 we have plotted σ_m vs ν for Faraday waves on an inviscid fluid ($N = 0$) and on a viscous fluid using VPF ($N = 2$) and VCVPF ($N = 4$). These theories are all irrotational. VCVPF gives the same results as the dissipation method as shown here in section 15.4. Previously, the dissipation theory with $N = 4$, was proposed by Kumar & Tuckerman(1994) from heurestic considerations. In figure 15.4 we plot the critical wave number k_m vs ν. The growth rates and critical wave number are largest for $N = 0$ and are larger for VPF than for VCVPF at each fixed ν.

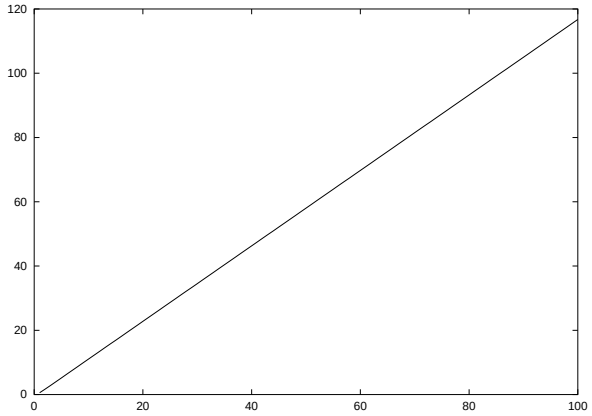

(a) $\ln(a)$ versus $t/(2\pi)$, $k = 1.974$ cm^{-1}.

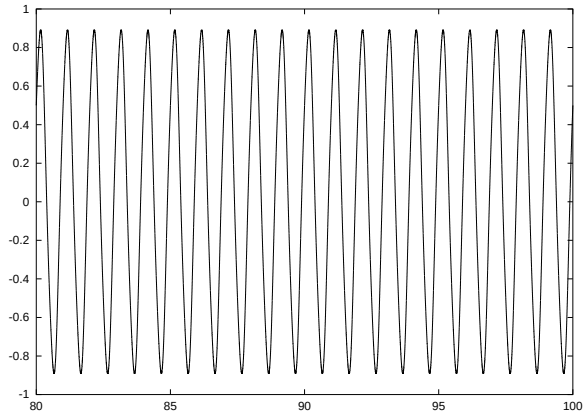

(b) $ae^{-\sigma t}$ versus $t/(2\pi)$, $k = 1.974$ cm^{-1}.

Spectrum of $ae^{-\sigma t}$ for $k = 1.974$ cm^{-1}.

n	$\Re\{A_n\}$	$\Im\{A_n\}$
0	-6.9334e-09	0.0000e+00
1	2.6445e-01	-3.4452e-01
2	2.5204e-09	3.7177e-09
3	-1.4703e-02	1.4509e-02
4	3.3942e-10	1.2655e-09
5	2.5412e-04	-2.1465e-04

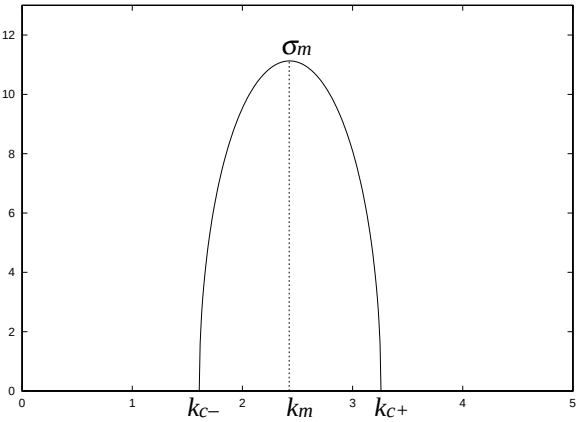

(c) σ versus k.

Fig. 15.1. Floquet theory $a = e^{\sigma t} b(t)$ for Faraday waves on an inviscid fluid ($N = 0$); $\rho = 0.97$ g/cm^3, $\gamma = 21$ dyne/cm, $g = 981$ cm/sec^2, $\omega = 2\pi \times 15.87$ sec^{-1}, $f = g$ cm/sec^2. (a) $\ln(a)$ vs $t/(2\pi)$, (b) $ae^{-\sigma t} = b(t) = b(t + 2\pi)$ vs $t/(2\pi)$, (c) $\sigma(N\nu)$ vs k. $\sigma_m = 11.1274$ sec^{-1} at $k_m = 2.4246$ cm^{-1}.

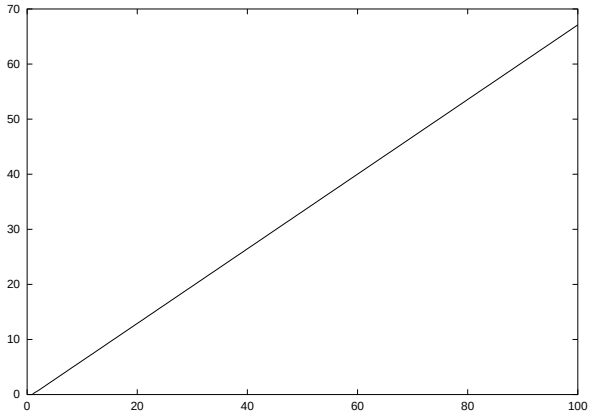

(a) $\ln(a)$ versus $t/(2\pi)$, $k = 1.974$ cm^{-1}.

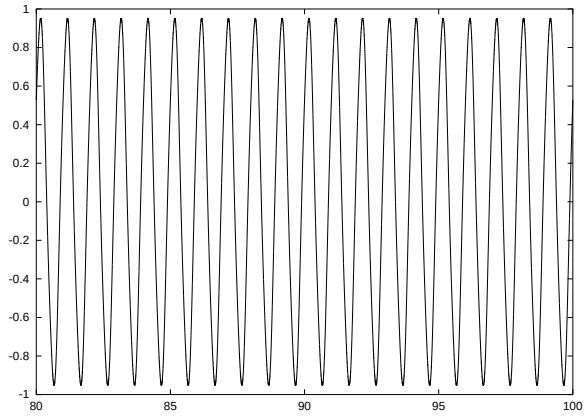

(b) $ae^{-\sigma t}$ versus $t/(2\pi)$, $k = 1.974$ cm^{-1}.

Spectrum of $ae^{-\sigma t}$ for $k = 1.974$ cm^{-1}.

n	$\Re\{A_n\}$	$\Im\{A_n\}$
0	-7.2599e-09	0.0000e+00
1	2.7907e-01	-3.7011e-01
2	2.6395e-09	3.8242e-09
3	-1.5536e-02	1.5620e-02
4	3.5512e-10	1.3015e-09
5	2.6873e-04	-2.3150e-04

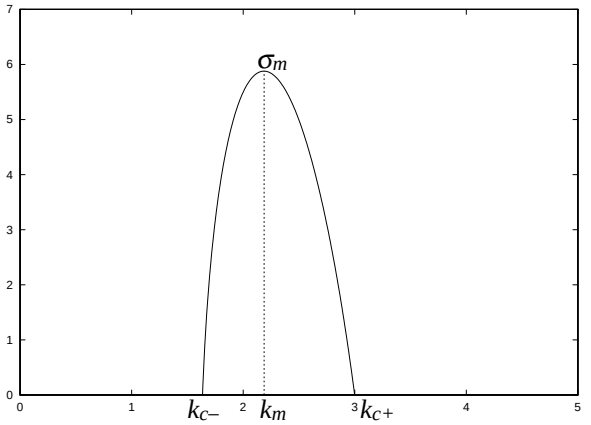

(c) σ versus k.

Fig. 15.2. Floquet theory $a = e^{\sigma t} b(t)$ for Faraday waves on a viscous liquid $\nu = 1$ cm^2/sec with $N = 2$ (VPF); $\rho = 0.97$ g/cm^3, $\gamma = 21$ dyne/cm, $g = 981$ cm/sec^2, $\omega = 2\pi \times 15.87$ sec^{-1}, $f = g$ cm/sec^2. (a) $\ln(a)$ vs $t/(2\pi)$, (b) $ae^{-\sigma t} = b(t) = b(t + 2\pi)$, (c) σ vs k. $\sigma_m = 5.8790$ sec^{-1} at $k_m = 2.1874$ cm^{-1}. The dissipation theory with $N = 4$ (VCVPF) is stable $\Re\{\sigma\} < 0$.

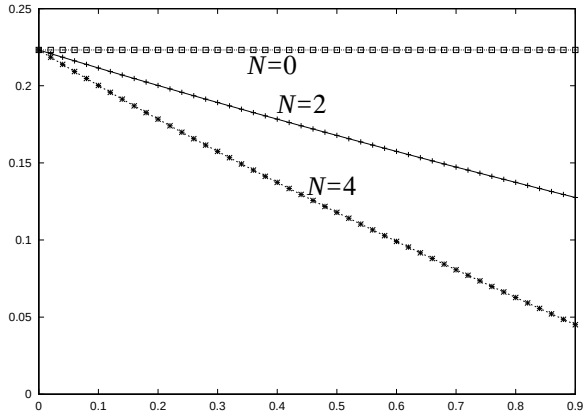

Fig. 15.3. σ_m versus ν cm^2/sec.

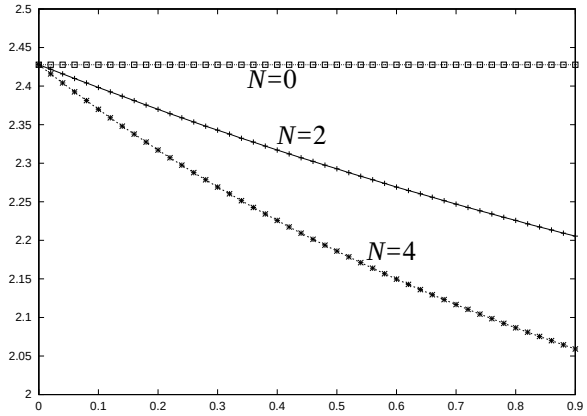

Fig. 15.4. k_m versus ν cm^2/sec.

15.6 Rayleigh-Taylor instability and Faraday waves

This section follows the work of Kumar (2000) who compared wave number selection in Rayleigh-Taylor (RT) instability and Faraday instability on deep and highly viscous liquids. He used the dissipation theory (VCVPF) of Faraday instability with $N = 4$, first proposed by Kumar & Tuckerman(1994). Our main goal is to introduce VPF with $N = 2$ into this comparison. We shall also revise slightly the comparisons made by Kumar (2000) so that a direct comparison of maximum growth rates in the two problems can be made.

Kumar (2000) compared a critical $k_c = k_m$ at $f = f_c$ (where $\sigma(k_m) = 0$, $\sigma < 0$ for $k \neq k_m = k_c$) for Faraday waves with the maximum growth rate of RT waves when the gravitational acceleration is replaced with

$$\bar{a}_c = \frac{\omega}{\pi}\int_{3\pi/2\omega}^{5\pi/2\omega} [f_c \cos(\omega t) - g]\,\mathrm{d}t = \frac{2}{\pi} f_c - g. \tag{15.6.1}$$

This value of $\bar{a}_c$ is an average upward acceleration in the Faraday problem. He used (15.6.1) with $N = 4$ in his calculation.

The maximum growth rate for RT instability can be computed from the exact linear theory given by equation (18) in Joseph, Belanger & Beavers (1999) or more easily and with good accuracy by the purely irrotational theory by equation (28) with $\nu = \mu_2/\rho_2$ and g replaced by $\bar{a}_c$. In this case, their (28) gives

$$\sigma = -k^2\nu \pm \sqrt{k\bar{a}_c - \frac{k^3\gamma}{\rho} + k^4\nu^2}. \tag{15.6.2}$$

The function $k_m(\bar{a}_c)$ is given by maximizing σ given by (15.6.2) with respect to k.

$$\frac{\mathrm{d}\sigma}{\mathrm{d}k} = -2\nu k + \frac{1}{2}\frac{\bar{a} - 3\frac{\gamma}{\rho}k^2 + 4k^3\nu^2}{\sqrt{\bar{a}k - \frac{\gamma}{\rho}k^3 + k^4\nu^2}} = 0 \tag{15.6.3}$$

which can be arranged as

$$8\nu^2 k^3\left(\bar{a} + \frac{\gamma}{\rho}k^2\right) = \left(\bar{a} - 3\frac{\gamma}{\rho}k^2\right)^2. \tag{15.6.4}$$

This is a fifth order algebraic equation for $k = k_m$. When $\bar{a}$ is large, we have

$$8\nu^2 k^3\bar{a} = (\bar{a})^2. \tag{15.6.5}$$

Hence

$$k_m = \left(\frac{\bar{a}}{8\nu^2}\right)^{1/3} \tag{15.6.6}$$

gives the maximum growth rate for large $\bar{a}$.

The maximum growth rate $\sigma_m = \sigma(k_m)$ and the wave number $k = k_m$ of maximum growth rate for RT instability and dissipative Faraday waves are compared in figures 15.5, 15.6 and 15.7. These figures show that the dissipative theory with $N = 4$ introduced by Kumar & Tuckerman(1994) and used by Kumar (2000) are more damped than the dissipative potential flow solution VPF with $N = 2$; damped solutions with $\sigma_m < 0$ at small values of f/g are shown in figures 15.6 and 15.7. We can say that the demonstration that damped Faraday waves at large viscosities are driven by the same acceleration mechanism which produce RT waves is better demonstrated by VPF with $N = 2$ than by the dissipative theory which is equivalent to our irrotational VCVPF with $N = 4$.

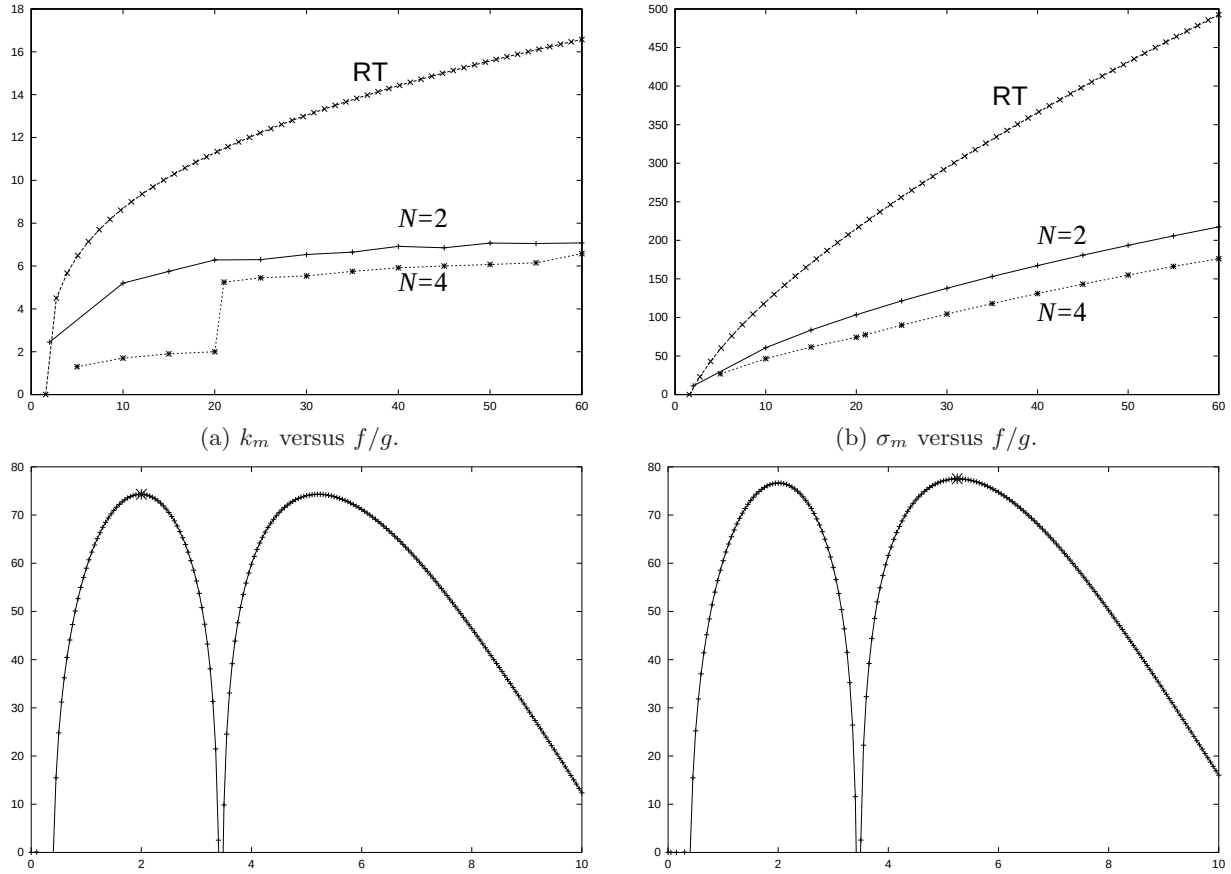

(a) k_m versus f/g.

(b) σ_m versus f/g.

(c) σ versus k for $N = 4$ and $f/g = 20$.

(d) σ versus k for $N = 4$ and $f/g = 21$.

Fig. 15.5. (a) k_m versus f/g and (b) σ_m versus f/g, for $\nu = 1$ cm^2/sec. (c), (d) σ versus k for $N = 4$ in a transition region, in which the mark $*$ denotes the maximum growth rate.

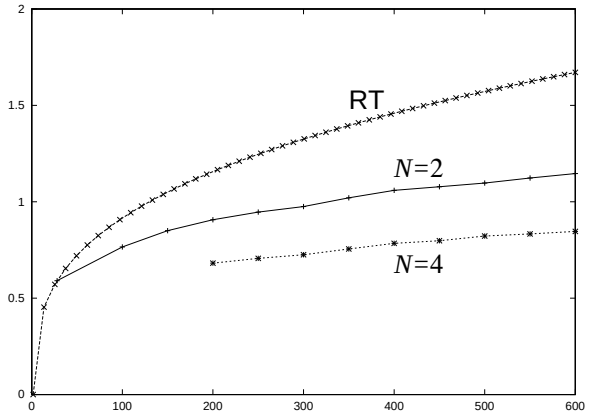

(a) k_m versus f/g for $\nu = 100$ cm^2/sec.

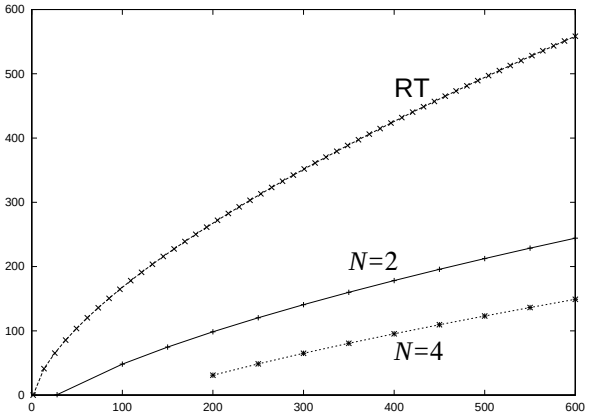

(b) σ_m versus f/g for $\nu = 100$ cm^2/sec.

Fig. 15.6. (a) k_m versus f/g and (b) σ_m versus f/g, for $\nu = 100$ cm^2/sec.

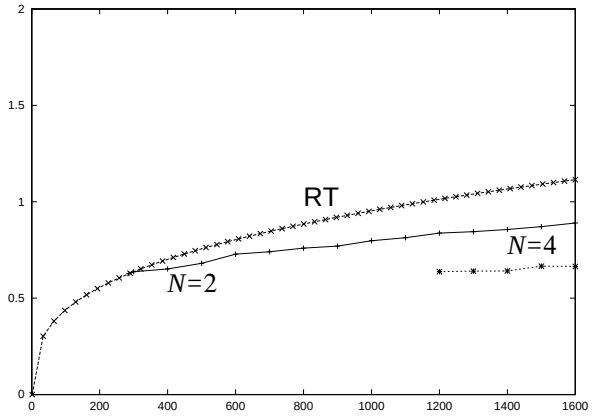

(a) k_m versus f/g for $\nu = 300$ cm^2/sec.

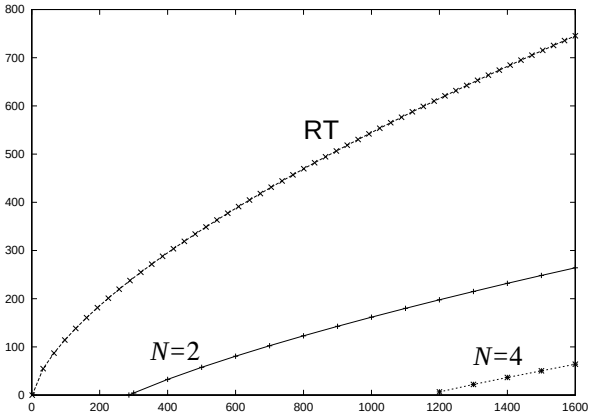

(b) σ_m versus f/g for $\nu = 300$ cm^2/sec.

Fig. 15.7. (a) k_m versus f/g and (b) σ_m versus f/g, for $\nu = 300$ cm^2/sec. For small values of f/g the potential flow solutions for Faraday waves are stable, $\sigma_m < 0$ but $N = 2$ is less stable and more like RT waves than $N = 4$.

15.7 Comparison of purely irrotational solutions with exact solutions

Kumar & Tuckerman(1994) presented a linear stability analysis of the interface between two viscous fluids. Starting from the Navier-Stokes equations, they derived the relevant equations describing the hydrodynamic system in the presence of parametric forcing and carried out a Floquet analysis to solve the stability problem. The viscous problem does not reduce to a system of Mathieu equations with a linear damping term, which is traditionally considered to represent the effect of viscosity. The traditional approach ignores the viscous boundary conditions at the interface of two fluids. To determine the effect of neglecting these, they compared their exact viscous fluid results with those derived from the traditional phenomenological approach. They call the exact theory FHS (fully hydrodynamic system). The traditional phenomenological approach is an application of the dissipation method; it is called a model. When applied to an air/liquid system the model is the same as the dissipation method which is the same as our irrotational theory VCVPF with damping proportional to 4ν.

They compared the results of the FHS and of the model to experimental results obtained in a viscous glycerine-water mixture (Edwards & Fauve 1993) in contact with air. They considered the glycerine-water nixture to be a layer of finite height $h = 0.29$ cm, in contact with a layer of air of infinite height. In their figure 3 (our 15.8) they plotted the experimental data for the critical wavelength λ_c and amplitude f_c as a function of forcing frequency. The solid and dashed curves are obtained from the FHS and from the model with finite depth corrections, respectively. They noted, however, that the values for the surface tension γ and the viscosity ν were chosen so as to best fit the FHS to the experimental data. This led to values $\gamma = 67.6 \times 10^{-3}$ N/m and $\nu = 1.02 \times 10^{-4}$ m^2/sec, which are in good agreement with the corresponding values given in the literature for the mixture composed of 88% (by weight) glycerol and 12% water, at temperature 23 °C. With these values, both the model and the FHS agree reasonably well with the experimentally measured wavelengths. They noted that "... the experimentally measured amplitudes agree quite well with the FHS over the entire frequency range, and not at all with the model. It is impossible to improve the fit of the critical amplitudes to the model by varying γ and ν."

The model results shown in the inset for f_c/g in figure 15.8 are for the dissipative approximation VCVPF ($N = 4$).

In figure 15.9 we have compared the exact solution with the irrotational approximation for $N = 4$ and $N = 2$. It is apparent that the fit of the critical amplitudes to the model with $N = 2$ is rather good.

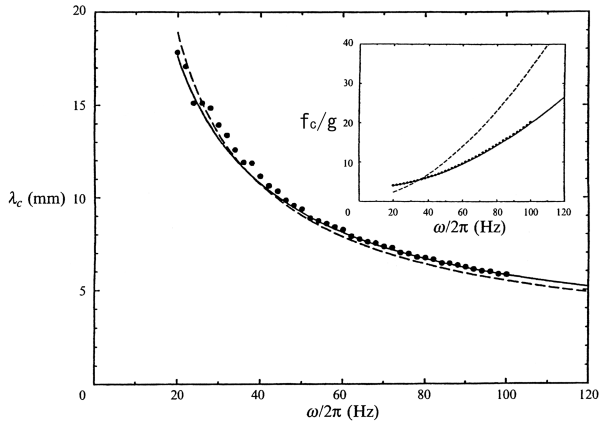

Fig. 15.8. Dispersion relation for glycerine-water mixture in contact with air at atmospheric pressure. Fitting the experimental data (Edwards & Fauve 1993) with the results of the FHS (solid lines) leads to $\gamma = 67.6 \times 10^{-3}$ N/m. Inset: Fitting of the experimental data for the stability threshold leads to $\nu = 1.02 \times 10^{-4}$ m^2/sec.

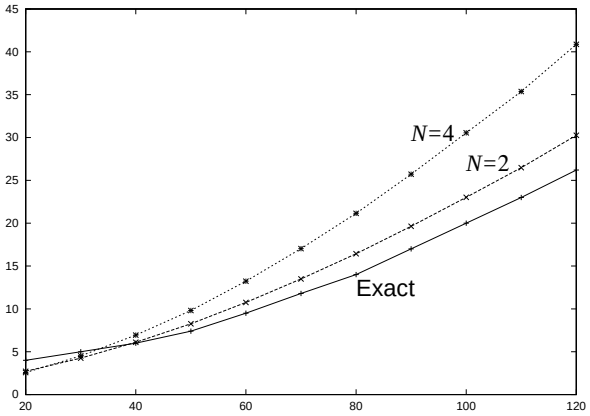

Fig. 15.9. f_C/g versus $\omega/(2\pi)$. Based on the data of $\lambda_C = \lambda_C(\omega/(2\pi))$ for their exact solution in figure 15.8 of Kumar & Tuckerman(1994), the critical value f_C/g is estimated for VCVPF and VPF. VPF is closer to the eact solution than VCVPF. $\rho = 1.1848$ g/cm^3, $h = 0.29$ cm, $\nu = 1.02$ cm^2/sec, $\gamma = 67.6$ dnye/cm.

15.8 Bifurcation of Faraday waves in a nearly square container

This problem has been studied using techniques of the theory of dynamical systems by Feng and Sethna (1989). Their study is of interest here since it is based on the nonlinear equations governing the potential flow of an inviscid fluid and can be updated to include the irrotational effects of viscosity. Their equations are the same as those given by BU. They look for a harmonic potential ϕ satisfying $\boldsymbol{n} \cdot \nabla\phi = 0$ on side walls and the container bottom, such that

$$\frac{\partial \phi}{\partial z} = \frac{\partial \eta}{\partial t} + \frac{\partial \phi}{\partial x}\frac{\partial \eta}{\partial x} + \frac{\partial \phi}{\partial y}\frac{\partial \eta}{\partial y}, \tag{15.8.1}$$

and

$$\frac{\gamma}{\rho}(\kappa_1 + \kappa_2) + \frac{\partial \phi}{\partial t} + \frac{1}{2}|\nabla\phi|^2 - (g - f\cos\omega t)\,\eta = 0. \tag{15.8.2}$$

Surface tension $\gamma = 0$ in the analysis of Feng and Sethna (1989). In our studies of purely irrotational effects of viscosity in the linear problem, we found the less damped of the irrotational studies gave better results; VPF was closer to experiments and exact analysis than VCVPF and the dissipation method. To implement VPF in the nonlinear problem, we add $2\mu\boldsymbol{n} \cdot (\nabla \otimes \nabla\phi) \cdot \boldsymbol{n}$ to the left side (15.8.2)

It would be of interest to see how the addition of surface tension and viscosity alter the agreements between theory and experiment reported by Miles and Henderson (1990) cited below.

"Feng & Sethna (1989) and Simonelli & Gollub (1989) have measured the stability boundaries for square and almost square cylinders. Feng & Sethna's experiments confirm some, and do not qualitatively contradict any, of their theoretical predictions. Simonelli & Gollub's experiments in square containers are in qualitative accord with Feng & Sethna's theory for $|\beta_1 - \beta_2| \ll 1$. However, their experiments reveal a much richer structure than those of either Ciliberto & Gollub (1985) or Feng & Sethna. In particular, they find that the transition between the various states may be hysteretic and associate this with a subcritical bifurcation. For an almost square container, their experiments appear to be compatible with Feng & Sethna's theory, although direct comparison is difficult owing to different choices of control parameters. In particular, they find that the parameter space includes a region of time-dependent behavior but no region of a stable superposition of the two modes. Feng & Sethna do find the stable coexistence of the pure modes. In addition, they report slow rotational (about a vertical axis) motions not observed by Simonelli & Gollub. Experiments on standing waves in square cylinders also have been reported by Douady & Fauve (1988)."

15.9 Conclusion

We developed two purely irrotational theories for the effects of viscosity on Faraday waves. In both theories the velocity is computed from the potential and the viscous term in the normal stress balance at the free surface is evaluated on potential flow. In one theory, called VPF, the pressure is given by the Bernoulli equation; it is the same pressure as would be computed for an inviscid fluid. The second irrotational theory, called VCVPF, is the same as the first except for the introduction of an additional pressure generated to remove the unphysical irrotational shear stress from the energy balance. The first theory leads to an amplitude equation with a damping coefficient proportional to 2ν. The second theory leads to the same amplitude equation except that the damping coefficient is proportional 4ν. We show that the VCVPF theory with damping coefficcient 4ν is identical to the well known dissipation theory in which no pressure, inviscid or viscous, appears. We show then that the dissipation theory is identical to the damped theory which was introduced by Kumar & Tuckerman(1994) following a heuristic argument. This theory, equivalent to VCVPF, with damping 4ν has been universally regarded as the correct irrotational approximation for viscous damping for small ν. Here, we show that both these ideas are not correct; the VPF theory with damping equal to 2ν is a better approximation and the approximation is not restricted to small viscosities.

16

Stability of a liquid jet into incompressible gases and liquids

In this chapter we carry out an analysis of the stability of a liquid jet into a gas or another fluid using viscous potential flow. This instability may be driven by Kelvin-Helmholtz KH instability due to a velocity difference and a neckdown due to capillary instability. KH instabilities are driven by pressures generated by a dynamically active ambient flow, gas or liquid. On the other hand, capillary instability can occur in a vacuum; the ambient can be neglected. KH instability is included by a discontinuity of the velocity at a two-fluid interface. This discontinuity is inconsistent with the no-slip condition for Navier-Stokes studies of viscous fluids, but is consistent with the theory of potential flow of a viscous fluid. We shall start our study with an analysis of capillary instability.

16.1 Capillary instability of a liquid cylinder in another fluid

The studty of this problem is especially valuable because it can be solved exactly and was solved by Tomotika 1935. This solution allows one to compute the effects of vorticity generated by the no-slip condition. The exact solution can be compared with irrotational solutions of the same problem. One effect of viscosity on the irrotational motion may be introduced by evaluating the viscous normal stress at the liquid-liquid interface on the irrotational motions. In a second approximation, the explicit effects of the discontinuity of the shear stress and tangential component of velocity which cannot be resolved pointwise in irrotational flows, can be removed in the mean from the energy equation by the selection of two viscous corrections of the irrotational pressure. We include the irrotational stress and pressure correction in the normal stress balance and compare the computed growth rates to the growth rates of the exact viscous flow solution. The agreement is excellent when one of the liquids is a gas; for two viscous liquids, the agreement is good to reasonable for the maximum growth rates but poor for long waves. Calculations show that good agreement is obtained when the vorticity is relatively small or the irrotational part is dominant in the exact viscous solution. We show that the irrotational viscous flow with pressure corrections gives rise to exactly the same dispersion relation as the dissipation method in which no pressure at all is required and the viscous effect is accounted for by evaluating the viscous dissipation using the irrotational flow.

16.1.1 Introduction

A liquid thread of mean radius R immersed in another liquid is subject to capillary instability. The capillary collapse can be described as a neck-down due to the surface tension γ in which the liquid is ejected from the throat of the neck, as seen in Fig. 16.1. Capillary instability is responsible for drop formation in applications such as ink-jet printing, fiber spinning and silicon chip technology.

The dynamical theory of instability of a long cylindrical column of liquid of radius R under the action of capillary force was given by Rayleigh (1879) following earlier work by Plateau (1873) who showed that a long cylinder of liquid is unstable to disturbances with wavelengths greater than $2\pi R$. Rayleigh showed that the effect of inertia is such that the wavelength λ corresponding to the mode of maximum instability is $\lambda = 4.51 \times 2R$, exceeding considerably the circumference of the cylinder. The idea that the wavelength associated with fastest

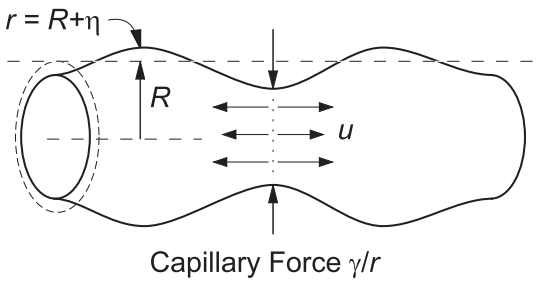

Fig. 16.1. Capillary instability. The force γ/r drives fluid away from the throat, leading to collapse.

growing growth rate would become dominant and be observed in practice was first put forward by Rayleigh (1879). The analysis of Rayleigh is based on potential flow of an inviscid liquid neglecting the effect of the outside fluid. An attempt to account for viscous effects was made by Rayleigh (1892) again neglecting the effect of the surrounding fluid. One of the effects considered is meant to account for the forward motion of an inviscid fluid with a resistance proportional to velocity. The effect of viscosity is treated in the special case in which the viscosity is so great that inertia may be neglected. He showed that the wavelength for maximum growth is very large, strictly infinite. Weber (1931) extended Rayleigh's theory by considering an effect of viscosity and that of surrounding air on the stability of a columnar jet. The effect of viscosity on the stability of a liquid cylinder when the surrounding fluid is neglected and on a hollow (dynamically passive) cylinder in a viscous liquid was treated briefly by Chandrasekhar (1961). Eggers (1997) has given a comprehensive review of nonlinear dynamics and breakup of free surface flows.

Tomotika (1935) studied capillary instability and gave an exact normal mode solution of the linearized Navier-Stokes equations. Funada and Joseph (2002) analyzed the same problem using VPF. Wang, Joseph and Funada (2004) considered capillary instability in cases in which one liquid is viscous and the other is a gas of negligible density and viscosity. They included the pressure correction in the normal stress balance at the free surface and showed that the growth rates computed using VCVPF are almost indistinguishable from the exact solution.

Here, we extend the VCVPF analysis to cases involving the interface of two viscous fluids. The formulation for the pressure correction is derived and used to compute growth rates for capillary instability of two viscous fluids. The computed values of the maximum growth rate and the associated wave-number computed from VCVPF are close to those from the exact solution; but the growth rates at small wave-numbers are not in good agreement.

16.1.2 Linearized equations governing capillary instability

Consider the stability of a liquid cylinder of radius R with viscosity μ_l and density ρ_l surrounded by another fluid with viscosity μ_a and density ρ_a under capillary forces generated by interfacial tension γ. Note that we use the subscript "l" for the inside fluid and "a" for the outside fluid. The analysis is done in cylindrical coordinates (r, θ, z) and only axisymmetric disturbances independent of θ are considered. The linearized Navier-Stokes equations and interfacial conditions are made dimensionless with the following scales:

$$[\text{length, velocity, time, pressure}] = [D,\ U,\ D/U,\ p_0]$$

where D is the diameter of the liquid cylinder, $U = \sqrt{\gamma/(\rho_l D)}$, $p_0 = \rho_l U^2 = \gamma/D$. The three dimensionless parameters controlling the solution are $m = \mu_a/\mu_l$, $l = \rho_a/\rho_l$ and a Reynolds number $J = VD\rho_l/\mu_l = Oh^2$ where $V = \gamma/\mu_l$ and Oh is the Ohnesorge number. The governing equations are

$$\frac{\partial u_l}{\partial r} + \frac{u_l}{r} + \frac{\partial w_l}{\partial z} = 0, \tag{16.1.1}$$

$$\frac{\partial u_l}{\partial t} = -\frac{\partial p_l}{\partial r} + \frac{1}{\sqrt{J}}\left(\nabla^2 u_l - \frac{u_l}{r^2}\right), \quad \frac{\partial w_l}{\partial t} = -\frac{\partial p_l}{\partial z} + \frac{1}{\sqrt{J}}\nabla^2 w_l, \tag{16.1.2}$$

$$\frac{\partial u_a}{\partial r} + \frac{u_a}{r} + \frac{\partial w_a}{\partial z} = 0, \tag{16.1.3}$$

$$l\frac{\partial u_a}{\partial t} = -\frac{\partial p_a}{\partial r} + \frac{m}{\sqrt{J}}\left(\nabla^2 u_a - \frac{u_a}{r^2}\right), \quad l\frac{\partial w_a}{\partial t} = -\frac{\partial p_a}{\partial z} + \frac{m}{\sqrt{J}}\nabla^2 w_a, \tag{16.1.4}$$

with $\nabla^2 = \dfrac{\partial^2}{\partial r^2} + \dfrac{1}{r}\dfrac{\partial}{\partial r} + \dfrac{\partial^2}{\partial z^2}$. The kinematic condition at the interface $r = 1/2 + \eta$ (where η is the varicose displacement) is given by

$$\frac{\partial \eta}{\partial t} = u_l, \quad \frac{\partial \eta}{\partial t} = u_a. \tag{16.1.5}$$

The normal stress balance at the interface is given by

$$p_a - p_l + \frac{2}{\sqrt{J}}\frac{\partial u_l}{\partial r} - \frac{2m}{\sqrt{J}}\frac{\partial u_a}{\partial r} = \frac{\partial^2 \eta}{\partial z^2} + \frac{\eta}{R^2}. \tag{16.1.6}$$

The tangential stress balance at the interface is given by

$$\left(\frac{\partial u_l}{\partial z} + \frac{\partial w_l}{\partial r}\right) = m\left(\frac{\partial u_a}{\partial z} + \frac{\partial w_a}{\partial r}\right). \tag{16.1.7}$$

The continuity of the velocity at the interface requires

$$u_l = u_a, \tag{16.1.8}$$

$$w_l = w_a. \tag{16.1.9}$$

16.1.3 Fully viscous flow analysis (Tomotika 1935)

Tomotika (1935) gave a normal mode solution to the linearized governing equations. This is an exact solution which satisfies all the four interfacial conditions in (16.1.6)–(16.1.9). He expressed the velocities with a stream function $\psi(r, z, t)$:

$$u = \frac{1}{r}\frac{\partial \psi}{\partial z}, \quad w = -\frac{1}{r}\frac{\partial \psi}{\partial r}, \tag{16.1.10}$$

and the basic variables are expressed in normal modes:

$$\psi_l = [A_1 r I_1(kr) + A_2 r I_1(k_l r)]\exp(\sigma t + \mathrm{i}kz), \tag{16.1.11}$$

$$\psi_a = [B_1 r K_1(kr) + B_2 r K_1(k_a r)]\exp(\sigma t + \mathrm{i}kz), \tag{16.1.12}$$

$$\eta = H\exp(\sigma t + \mathrm{i}kz), \tag{16.1.13}$$

where σ is the complex growth rate and k is the wave-number; the modified Bessel functions of the first order are denoted by I_1 for the first kind and K_1 for the second kind. Substitution of (16.1.11)–(16.1.13) to (16.1.6)–(16.1.9) leads to the solvability condition, which is given as the dispersion relation:

$$\begin{vmatrix} I_1(kR) & I_1(k_l R) & K_1(kR) & K_1(k_a R) \\ kI_0(kR) & k_l I_0(k_l R) & -kK_0(kR) & -k_a K_0(k_a R) \\ 2k^2 I_1(kR) & \left(k^2 + k_l^2\right) I_1(k_l R) & 2mk^2 K_1(kR) & m\left(k^2 + k_a^2\right) K_1(k_a R) \\ F_1 & F_2 & F_3 & F_4 \end{vmatrix} = 0, \tag{16.1.14}$$

where

$$F_1 = \mathrm{i}\sigma I_0(kR) + 2\mathrm{i}\frac{k^2}{\sqrt{J}}\left(\frac{\mathrm{d}I_1(kR)}{\mathrm{d}(kR)}\right) - \left(\frac{1}{R^2} - k^2\right)\mathrm{i}\frac{k}{\sigma}I_1(kR), \tag{16.1.15}$$

$$F_2 = 2\mathrm{i}\frac{kk_l}{\sqrt{J}}\left(\frac{\mathrm{d}I_1(k_lR)}{\mathrm{d}(k_lR)}\right) - \left(\frac{1}{R^2} - k^2\right)\mathrm{i}\frac{k}{\sigma}I_1(k_lR), \tag{16.1.16}$$

$$F_3 = -\mathrm{i}l\sigma K_0(kR) + 2\mathrm{i}\frac{mk^2}{\sqrt{J}}\left(\frac{\mathrm{d}K_1(kR)}{\mathrm{d}(kR)}\right), \quad F_4 = 2\mathrm{i}\frac{mkk_a}{\sqrt{J}}\left(\frac{\mathrm{d}K_1(k_aR)}{\mathrm{d}(k_aR)}\right), \tag{16.1.17}$$

with

$$k_l = \sqrt{k^2 + \sqrt{J}\sigma}, \quad k_a = \sqrt{k^2 + \frac{l}{m}\sqrt{J}\sigma}. \tag{16.1.18}$$

16.1.4 Viscous potential flow analysis (Funada and Joseph 2002)

The potential flow solution is given by $\boldsymbol{u} = \nabla\phi$, $\nabla^2\phi = 0$, where ϕ is the velocity potential. The normal stress balance (16.1.6) and normal velocity continuity (16.1.8) are satisfied; the shear stress and tangential velocity conditions (16.1.7) and (16.1.9) cannot be enforced. The potential solution can be expressed as

$$\psi_l = A_1 r I_1(kr)\exp(\sigma t + \mathrm{i}kz), \tag{16.1.19}$$

$$\psi_a = B_1 r K_1(kr)\exp(\sigma t + \mathrm{i}kz), \tag{16.1.20}$$

$$\eta = H\exp(\sigma t + \mathrm{i}kz), \tag{16.1.21}$$

for which the dispersion relation is given by

$$(\alpha_l + l\alpha_a)\sigma^2 + \frac{2k^2}{\sqrt{J}}(\beta_l + m\beta_a)\sigma = \left(\frac{1}{R^2} - k^2\right)k, \tag{16.1.22}$$

with

$$\alpha_l = \frac{I_0(kR)}{I_1(kR)}, \quad \alpha_a = \frac{K_0(kR)}{K_1(kR)}, \quad \beta_l = \alpha_l - \frac{1}{kR}, \quad \text{and} \quad \beta_a = \alpha_a + \frac{1}{kR}. \tag{16.1.23}$$

Solving (16.1.22), we obtain

$$\sigma = -\frac{k^2(\beta_l + m\beta_a)}{\sqrt{J}(\alpha_l + l\alpha_a)} \pm \sqrt{\left[\frac{k^2(\beta_l + m\beta_a)}{\sqrt{J}(\alpha_l + l\alpha_a)}\right]^2 + \left(\frac{1}{R^2} - k^2\right)\frac{k}{\alpha_l + l\alpha_a}}. \tag{16.1.24}$$

Thus instability arises in $0 < kR < 1$, for which the dimensionless critical wave-number $k_c = 1/R = 2$. When $\sqrt{J} \to \infty$, (16.1.24) reduces to

$$\sigma = \pm\sqrt{\left(\frac{1}{R^2} - k^2\right)\frac{k}{\alpha_l + l\alpha_a}}, \tag{16.1.25}$$

which is just the dispersion relation in inviscid potential flow (IPF); the same dispersion relation was obtained by Christiansen and Hixson (1957).

16.1.5 Pressure correction for viscous potential flow

Joseph and Wang (2004) derived a viscous correction for the irrotational pressure at free surfaces of steady flows, which is induced by the discrepancy between the non-zero irrotational shear stress and the zero-shear-stress condition at free surfaces. In the VPF analysis of capillary instability, the interface between two viscous fluids is involved and the two potential flows are unsteady. We will derive the pressure correction for capillary instability from the basic mechanical energy equation.

If we ignore the small deformation η in the linear problem, we have $\boldsymbol{n}_1 = \boldsymbol{e}_r$ as the outward normal at the interface for the inside fluid; $\boldsymbol{n}_2 = -\boldsymbol{n}_1$ is the outward normal for the outside fluid; $\boldsymbol{t} = \boldsymbol{e}_z$ is the unit tangential vector. We use the superscript "i" for "irrotational" and "v" for "viscous." The normal and shear parts of the viscous stress are represented by τ^n and τ^s, respectively.

The velocities and stresses are evaluated using the potentials, which are expressed by stream functions (16.1.19) and (16.1.20). The mechanical energy equations for the outside and inside fluids are respectively

$$\begin{aligned}&\frac{\mathrm{d}}{\mathrm{d}t}\int_{V_a}\frac{\rho_a}{2}\left|\boldsymbol{u}_a\right|^2\mathrm{d}V=\int_A\left[\boldsymbol{u}_a\cdot\mathbf{T}_a\cdot\boldsymbol{n}_2\right]\mathrm{d}A-\int_{V_a}2\mu_a\mathbf{D}_a:\mathbf{D}_a\mathrm{d}V\\&=-\int_A\left[\boldsymbol{u}_a\cdot\boldsymbol{n}_1\left(-p_a^i+\tau_a^n\right)+\boldsymbol{u}_a\cdot\boldsymbol{t}\tau_a^s\right]\mathrm{d}A-\int_{V_a}2\mu_a\mathbf{D}_a:\mathbf{D}_a\mathrm{d}V,\end{aligned}\tag{16.1.26}$$

$$\begin{aligned}&\frac{\mathrm{d}}{\mathrm{d}t}\int_{V_l}\frac{\rho_l}{2}\left|\boldsymbol{u}_l\right|^2\mathrm{d}V=\int_A\left[\boldsymbol{u}_l\cdot\mathbf{T}_l\cdot\boldsymbol{n}_1\right]\mathrm{d}A-\int_{V_l}2\mu_l\mathbf{D}_l:\mathbf{D}_l\mathrm{d}V\\&=\int_A\left[\boldsymbol{u}_l\cdot\boldsymbol{n}_1\left(-p_l^i+\tau_l^n\right)+\boldsymbol{u}_l\cdot\boldsymbol{t}\tau_l^s\right]\mathrm{d}A-\int_{V_l}2\mu_l\mathbf{D}_l:\mathbf{D}_l\mathrm{d}V.\end{aligned}\tag{16.1.27}$$

With the continuity of the normal velocity

$$\boldsymbol{u}_a\cdot\boldsymbol{n}_1=\boldsymbol{u}_l\cdot\boldsymbol{n}_1=u_n,\tag{16.1.28}$$

the sum of (16.1.26) and (16.1.27) can be written as

$$\begin{aligned}&\frac{\mathrm{d}}{\mathrm{d}t}\int_{V_a}\frac{\rho_a}{2}\left|\boldsymbol{u}_a\right|^2\mathrm{d}V+\frac{\mathrm{d}}{\mathrm{d}t}\int_{V_l}\frac{\rho_l}{2}\left|\boldsymbol{u}_l\right|^2\mathrm{d}V=\int_A\left[u_n\left(-p_l^i+\tau_l^n+p_a^i-\tau_a^n\right)\right.\\&\left.+\boldsymbol{u}_l\cdot\boldsymbol{t}\tau_l^s-\boldsymbol{u}_a\cdot\boldsymbol{t}\tau_a^s\right]\mathrm{d}A-\int_{V_a}2\mu_a\mathbf{D}_a:\mathbf{D}_a\mathrm{d}V-\int_{V_l}2\mu_l\mathbf{D}_l:\mathbf{D}_l\mathrm{d}V.\end{aligned}\tag{16.1.29}$$

Now consider the boundary layer approximation of viscous potential flow. We propose two pressure corrections, p_l^v and p_a^v, for the inside and outside potential flows respectively, together with the continuity conditions

$$\tau_a^s=\tau_l^s=\tau^s,\quad\text{and}\quad\boldsymbol{u}_a\cdot\boldsymbol{t}=\boldsymbol{u}_l\cdot\boldsymbol{t}=u_s.\tag{16.1.30}$$

We assume that the boundary layer approximation has a negligible effect on the flow in the bulk liquid but it changes the pressure and continuity conditions at the interface. Hence, the mechanical energy equations become

$$\frac{\mathrm{d}}{\mathrm{d}t}\int_{V_l}\frac{\rho_l}{2}\left|\boldsymbol{u}_l\right|^2\mathrm{d}V=\int_A\left[u_n\left(-p_l^i-p_l^v+\tau_l^n\right)+u_s\tau^s\right]\mathrm{d}A-\int_{V_l}2\mu_l\mathbf{D}_l:\mathbf{D}_l\mathrm{d}V,\tag{16.1.31}$$

$$\frac{\mathrm{d}}{\mathrm{d}t}\int_{V_a}\frac{\rho_a}{2}\left|\boldsymbol{u}_a\right|^2\mathrm{d}V=-\int_A\left[u_n\left(-p_a^i-p_a^v+\tau_a^n\right)+u_s\tau^s\right]\mathrm{d}A-\int_{V_a}2\mu_a\mathbf{D}_a:\mathbf{D}_a\mathrm{d}V.\tag{16.1.32}$$

The sum of (16.1.31) and (16.1.32) can be written as

$$\begin{aligned}&\frac{\mathrm{d}}{\mathrm{d}t}\int_{V_a}\frac{\rho_a}{2}\left|\boldsymbol{u}_a\right|^2\mathrm{d}V+\frac{\mathrm{d}}{\mathrm{d}t}\int_{V_l}\frac{\rho_l}{2}\left|\boldsymbol{u}_l\right|^2\mathrm{d}V=\int_A\left[u_n\left(-p_l^i-p_l^v+\tau_l^n+p_a^i+p_a^v-\tau_a^n\right)\right]\mathrm{d}A\\&-\int_{V_a}2\mu_a\mathbf{D}_a:\mathbf{D}_a\mathrm{d}V-\int_{V_l}2\mu_l\mathbf{D}_l:\mathbf{D}_l\mathrm{d}V.\end{aligned}\tag{16.1.33}$$

Comparing (16.1.29) and (16.1.33), we obtain an equation which relates the pressure corrections to the uncompensated irrotational shear stresses

$$\int_A u_n\left(-p_l^v+p_a^v\right)\mathrm{d}A=\int_A\left(\mathbf{u}_l\cdot\boldsymbol{t}\tau_l^s-\boldsymbol{u}_a\cdot\boldsymbol{t}\tau_a^s\right)\mathrm{d}A.\tag{16.1.34}$$

Joseph and Wang (2004) showed that in linearized problems, the governing equation for the pressure corrections is

$$\nabla^2p^v=0.\tag{16.1.35}$$

Solving equation (16.1.35), we obtain the two pressure corrections

$$-p_l^v=\sum_{j=0}^{\infty}C_j'\mathrm{i}I_0\left(\frac{2\pi}{\lambda}jr\right)\exp\left(\sigma t+\mathrm{i}\frac{2\pi}{\lambda}jz\right),\tag{16.1.36}$$

$$-p_a^v = \sum_{j=0}^{\infty} D_j' \mathrm{i} K_0\left(\frac{2\pi}{\lambda} jr\right) \exp\left(\sigma t + \mathrm{i}\frac{2\pi}{\lambda} jz\right), \tag{16.1.37}$$

where C_j' and D_j' are constants to be determined, j is an integer and λ is the period in z direction. Suppose $2\pi j_0/\lambda = k$, $C_{j_0}' = C_k$ and $D_{j_0}' = D_k$, then the two pressure corrections can be written as

$$-p_l^v = C_k \mathrm{i} I_0(kr)\exp(\sigma t + \mathrm{i}kz) + \sum_{j\neq j_0} C_j' \mathrm{i} I_0\left(\frac{2\pi}{\lambda} jr\right)\exp\left(\sigma t + \mathrm{i}\frac{2\pi}{\lambda} jz\right), \tag{16.1.38}$$

$$-p_a^v = D_k \mathrm{i} K_0(kr)\exp(\sigma t + \mathrm{i}kz) + \sum_{j\neq j_0} D_j' \mathrm{i} K_0\left(\frac{2\pi}{\lambda} jr\right)\exp\left(\sigma t + \mathrm{i}\frac{2\pi}{\lambda} jz\right). \tag{16.1.39}$$

With the pressure corrections, the normal stress balance has the following form

$$p_a^i + p_a^v - p_l^i - p_l^v + \frac{2}{\sqrt{J}}\frac{\partial u_l}{\partial r} - \frac{2m}{\sqrt{J}}\frac{\partial u_a}{\partial r} = \frac{\partial^2 \eta}{\partial z^2} + \frac{\eta}{R^2}, \tag{16.1.40}$$

which gives rise to

$$\begin{aligned}
&\left\{\begin{array}{l} lB_1 K_0(kR)\sigma - D_k K_0(kR) + A_1\sigma I_0(kR) + C_k I_0(kR) \\ +\dfrac{2k^2}{\sqrt{J}} A_1\left[I_0(kR) - \dfrac{I_1(kR)}{kR}\right] + \dfrac{2mk^2}{\sqrt{J}} B_1\left[K_0(kR) + \dfrac{K_1(kR)}{kR}\right] \end{array}\right\}\exp(\sigma t + \mathrm{i}kz) \\
&+ \sum_{j\neq j_0}\left[C_j' I_0\left(\frac{2\pi}{\lambda} jR\right) - D_j' K_0\left(\frac{2\pi}{\lambda} jR\right)\right]\exp\left(\sigma t + \mathrm{i}\frac{2\pi}{\lambda} jz\right) \\
&= A_1\frac{k}{\sigma} I_1(kR)\left(\frac{1}{R^2} - k^2\right)\exp(\sigma t + \mathrm{i}kz).
\end{aligned} \tag{16.1.41}$$

By orthogonality of the Fourier series, we obtain

$$\begin{aligned}
&lB_1 K_0(kR)\sigma - D_k K_0(kR) + A_1\sigma I_0(kR) + C_k I_0(kR) + \frac{2k^2}{\sqrt{J}} A_1\left[I_0(kR) - \frac{I_1(kR)}{kR}\right] \\
&+\frac{2mk^2}{\sqrt{J}} B_1\left[K_0(kR) + \frac{K_1(kR)}{kR}\right] = A_1\frac{k}{\sigma} I_1(kR)\left(\frac{1}{R^2} - k^2\right),
\end{aligned} \tag{16.1.42}$$

and

$$C_j' I_0\left(\frac{2\pi}{\lambda} jR\right) - D_j' K_0\left(\frac{2\pi}{\lambda} jR\right) = 0 \quad \text{when} \quad j \neq j_0. \tag{16.1.43}$$

Equation (16.1.42) replaces the normal stress balance and can be solved for the growth rate σ. However, the undetermined part $C_k I_0(kR) - D_k K_0(kR)$ has to be computed from (16.1.34) before we can solve (16.1.42). Substitution of (16.1.38), (16.1.39) and (16.1.43) into the left hand side of (16.1.34) gives rise to

$$\begin{aligned}
&\int_A \bar{u}_n\left(-p_l^v + p_a^v\right)\mathrm{d}A = \int_0^{2\pi} R\mathrm{d}\theta \int_z^{z+\lambda} \bar{u}_n\left(-p_l^v + p_a^v\right)\mathrm{d}z \\
&= 2\pi R\lambda\left[\bar{A}_1 C_k I_0(kR) I_1(kR) - \bar{B}_1 D_k K_0(kR) K_1(kR)\right] k\exp(\sigma + \bar{\sigma})t,
\end{aligned} \tag{16.1.44}$$

where $\bar{u}_n$ is the conjugate of u_n. The right hand side of (16.1.34) can be evaluated

$$\begin{aligned}
&\int_A \left[\left(\overline{\boldsymbol{u}_l \cdot \boldsymbol{t}}\right)\tau_l^s - \left(\overline{\boldsymbol{u}_a \cdot \boldsymbol{t}}\right)\tau_a^s\right]\mathrm{d}A \\
&= \frac{4\pi R\lambda}{\sqrt{J}}\left[\bar{A}_1 A_1 I_0(kR) I_1(kR) + m\bar{B}_1 B_1 K_0(kR) K_1(kR)\right] k^3\exp(\sigma + \bar{\sigma})t.
\end{aligned} \tag{16.1.45}$$

Combining (16.1.44) and (16.1.45), we obtain

$$\begin{aligned}
&\bar{A}_1 C_k I_0(kR) I_1(kR) - \bar{B}_1 D_k K_0(kR) K_1(kR) \\
&= \frac{2}{\sqrt{J}}\bar{A}_1 A_1 k^2 I_0(kR) I_1(kR) + \frac{2m}{\sqrt{J}}\bar{B}_1 B_1 k^2 K_0(kR) K_1(kR).
\end{aligned} \tag{16.1.46}$$

Table 16.1. *The properties of the five pairs of fluids used to study capillary instability and the controlling dimensionless parameters l, m and J.*

case	1	2	3	4	5
Fluids	Mercury-water	Water-benzene	Glycerin-mercury	Goldensyrup-paraffin	Goldensyrup-BBoil
ρ_l(kg m^{-3})	13500	1000	1257	1400	1400
ρ_a(kg m^{-3})	1000	0.001	13500	1600	900
μ_l(kg/m s)	0.00156	860	0.782	11.0	11.0
μ_a(kg/m s)	0.001	0.00065	0.00156	0.0034	6.0
γ(N/m)	0.375	0.0328	0.375	0.023	0.017
$l=\rho_a/\rho_l$	0.07407	0.86	10.74	1.143	0.6429
$m=\mu_a/\mu_l$	0.6410	0.65	1.995×10^{-3}	3.091×10^{-4}	0.5455
$J=\rho_l\gamma D/\mu_l^2$	2.080×10^{7}	3.280×10^{5}	7.708	2.661×10^{-3}	1.967×10^{-3}

The normal velocity continuity condition (16.1.28) leads to

$$B_1 = A_1 \frac{I_1(kR)}{K_1(kR)}. \tag{16.1.47}$$

Substitution of (16.1.47) into (16.1.46) leads to

$$C_k I_0(kR) - D_k K_0(kR) = \frac{2}{\sqrt{J}} A_1 k^2 I_0(kR) + \frac{2m}{\sqrt{J}} A_1 k^2 I_1(kR) K_0(kR)/K_1(kR). \tag{16.1.48}$$

Inserting (16.1.47) and (16.1.48) into (16.1.42), we obtain the dispersion relation

$$(\alpha_l + l\alpha_a)\,\sigma^2 + \frac{2k^2}{\sqrt{J}}\left[(\alpha_l + \beta_l) + m\,(\alpha_a + \beta_a)\right]\sigma = \left(\frac{1}{R^2} - k^2\right)k, \tag{16.1.49}$$

where α_l, α_a, β_a and β_l are defined in (16.1.23). Solving (16.1.49), we obtain the growth rate

$$\sigma = -\frac{k^2\left[(\alpha_l + \beta_l) + m\,(\alpha_a + \beta_a)\right]}{\sqrt{J}\,(\alpha_l + l\alpha_a)} \pm \sqrt{\left[\frac{k^2\left[(\alpha_l + \beta_l) + m\,(\alpha_a + \beta_a)\right]}{\sqrt{J}\,(\alpha_l + l\alpha_a)}\right]^2 + \left(\frac{1}{R^2} - k^2\right)\frac{k}{\alpha_l + l\alpha_a}}. \tag{16.1.50}$$

16.1.6 Comparison of growth rates

We calculate the growth rate σ using IPF (16.1.25), VPF (16.1.24) and VCVPF (16.1.50) and compare these results with the exact solution (16.1.14). We choose five pairs of fluids to study capillary instability and the properties of the fluids and controlling dimensionless parameters are listed in Table 16.1.

We are essentially comparing solutions assuming irrotational flows to the exact solution. To better understand the potential flow approximation to the fully viscous flow, we may evaluate the vorticity

$$\omega = \frac{\partial u_r}{\partial z} - \frac{\partial u_z}{\partial r} = \frac{\partial u}{\partial z} - \frac{\partial w}{\partial r} \tag{16.1.51}$$

in the interior and exterior fluids from the exact solution. When the vorticity is great, the potential flow cannot give a satisfactory approximation.

The vorticity is

$$\omega_l = A_2 I_1(k_l r)\left(k_l^2 - k^2\right)\exp(\sigma t + \mathrm{i}kz) = A_2 I_1(k_l r)\sqrt{J}\sigma\exp(\sigma t + \mathrm{i}kz) \tag{16.1.52}$$

in the interior fluid and is

$$\omega_a = B_2 K_1(k_a r)\left(k_a^2 - k^2\right)\exp(\sigma t + \mathrm{i}kz) = B_2 K_1(k_a r)\frac{l}{m}\sqrt{J}\sigma\exp(\sigma t + \mathrm{i}kz) \tag{16.1.53}$$

in the exterior fluid. The magnitudes of ω_l and ω_a are proportional to A_2 and B_2, respectively. We normalize them by B_2 so that the two magnitudes are measured by the same scale and can be compared. The normalized magnitudes of the vorticities at the interface ($r \approx R$) are

$$\omega_l^* = -\frac{A_2}{B_2} I_1(k_l R)\sqrt{J}\sigma \quad \text{and} \quad \omega_a^* = K_1(k_a R)\frac{l}{m}\sqrt{J}\sigma. \tag{16.1.54}$$

Note that we add a minus sign for ω_l^*. The reason is that the vorticity vectors in the interior and exterior fluids are in opposite directions, leading to vorticities of opposite signs. By adding a minus sign for ω_l^*, we obtain the absolute value of the vorticity in the interior fluid. To compute (16.1.54), we need to know the value of A_2/B_2. This can be achieved by manipulation of the dispersion relation (16.1.14)

$$\begin{bmatrix} I_1(kR) & I_1(k_l R) & K_1(kR) \\ kI_0(kR) & k_l I_0(k_l R) & -kK_0(kR) \\ 2k^2 I_1(kR) & (k^2 + k_l^2) I_1(k_l R) & 2mk^2 K_1(kR) \end{bmatrix} \begin{bmatrix} A_1/B_2 \\ A_2/B_2 \\ B_1/B_2 \end{bmatrix} = \begin{bmatrix} -K_1(k_a R) \\ k_a K_0(k_a R) \\ -m(k^2 + k_a^2) K_1(k_a R) \end{bmatrix}, \tag{16.1.55}$$

from which we can solve for A_1/B_2, A_2/B_2 and B_1/B_2.

We note that the stream functions (16.1.11) and (16.1.12) in the exact solution can be divided into the irrotational part and rotational part:

$$\psi_l^i = A_1 r I_1(kr)\exp(\sigma t + \mathrm{i}kz), \quad \psi_l^r = A_2 r I_1(k_l r)\exp(\sigma t + \mathrm{i}kz); \tag{16.1.56}$$

$$\psi_a^i = B_1 r K_1(kr)\exp(\sigma t + \mathrm{i}kz), \quad \psi_a^r = B_2 r K_1(k_a r)\exp(\sigma t + \mathrm{i}kz). \tag{16.1.57}$$

The irrotational parts are exactly the potential flow solution, whereas the vorticities are solely determined by the rotational parts. When the irrotational parts dominate, potential flows can give good approximation to the exact solution; when the rotational parts are important, the approximation cannot be satisfactory. We define two ratios of the irrotational part to the rotational part:

$$f_l = \left|\frac{\psi_l^i(r = R)}{\psi_l^r(r = R)}\right| = \left|\frac{A_1 I_1(kR)}{A_2 I_1(k_l R)}\right|, \tag{16.1.58}$$

$$f_a = \left|\frac{\psi_a^i(r = R)}{\psi_a^r(r = R)}\right| = \left|\frac{B_1 K_1(kR)}{B_2 K_1(k_a R)}\right|. \tag{16.1.59}$$

These two ratios characterize the relative importance of the irrotational and rotational parts at the interface. When the Reynolds number is large, we expect the values of the ratios to be high.

We present the comparison of the growth rates computed from IPF, VPF, VCVPF and the exact solution in Figs. 16.2–16.6 for the five pairs of fluids listed in Table 16.1. In each case, a growth rate vs. wave-number plot, a vorticity vs. wave-number plot, and a plot for the two ratios f_l and f_a vs. wave-number are shown. The vorticity plot and the plot for the two ratios can help to understand the agreement and disagreement between the growth rates from potential-based solutions and from the exact solution.

When the Reynolds number is high (Figs. 16.2 and 16.3), the three potential flow based solutions are essentially the same; they are in good agreement with the exact solution in the maximum growth region (see Table 16.2) but deviate from the exact solution when $k \ll 1$. When the Reynolds number is lower (Figs. 16.4 and 16.5), IPF and VPF deviate from the exact solution in the maximum growth region whereas VCVPF can give almost the same maximum growth rate σ_m and the associated wave-number k_m as the exact solution. However, VCVPF dose not differ greatly from IPF or VPF when $k \ll 1$. Figure 16.6 shows the results for case 5 in which the Reynolds number is low and the viscosity ratio $m \sim O(1)$; VCVPF does not give the correct values of σ_m and k_m in this case.

The vorticity as a function of the wave-number k helps to understand the non-uniform agreement between the VCVPF results and the exact results. In cases 1, 2 and 3 (Figs. 16.2, 16.3 and 16.4), the magnitude of the

Table 16.2. *Data of the maximum growth rate and the associated wave-number.*

case	IPF		EXACT	
	k_m	σ_m	k_m	σ_m
1	1.3909616e+00	9.6377400e-01	1.3893986e+00	9.5517399e-01
2	1.3585050e+00	8.9589722e-01	1.3508895e+00	8.4918585e-01
3	1.1897181e+00	5.5734616e-01	9.9496394e-01	3.4140194e-01
4	1.3493716e+00	8.7507633e-01	2.7032697e-01	1.6552208e-02
5	1.3661634e+00	9.1303869e-01	1.0632024e+00	4.3484116e-03

case	VPF		VCVPF	
	k_m	σ_m	k_m	σ_m
1	1.3909616e+00	9.6337186e-01	1.3893986e+00	9.6289992e-01
2	1.3569785e+00	8.9325293e-01	1.3539306e+00	8.9017625e-01
3	1.0716030e+00	4.7575270e-01	9.1862735e-01	3.6760629e-01
4	2.9643429e-01	4.8733702e-02	1.7693239e-01	1.6878141e-02
5	2.0203403e-01	2.7575187e-02	1.3433168e-01	1.2291103e-02

vorticity is large when $k \ll 1$ and small in the maximum growth region. This could explain the good agreement in the maximum growth region and poor agreement when $k \ll 1$. In cases 4 and 5 (Figs. 16.5 and 16.6), the magnitude of the vorticity is large at almost all the values of k except when k is very close to $k_c = 2$. The distribution of the vorticity is helpful for understanding the growth rate calculation but a clear explanation for the non-uniform agreement is not obtained in cases 4 and 5.

We find that the values of the two ratios f_l and f_a are close to 1 when $k \ll 1$ in all the cases, indicating that the rotational parts are important for long waves even at high Reynolds number. This is consistent with our growth rate calculation, which shows that the agreement between VCVPF and the exact solution is poor for long waves. In the maximum growth region (k close to 1), the values of f_l and f_a are larger than for long waves. When the Reynolds number is large, the maximum value of f_l and f_a is large, indicating that the irrotational parts dominate the solution; at the same time, we observe good agreement between VCVPF and the exact solution for wave numbers near k_m. When the Reynolds number is small, the values of f_l and f_a are close to 1 in the whole range of k; at the same time, we observe that the agreement between VCVPF and the exact solution is poor at almost all the values of k.

16.1.7 Dissipation calculation for capillary instability

We have shown in Chapter 12 that the dissipation method gives the same result as VCVPF for gas-liquid flows. This is also true for the two-fluid problem considered in §16.1.5 as the following calculation shows. Here we extend the dissipation calculation to capillary instability of two viscous fluids.

The sum of the mechanical energy equations of the interior and exterior fluids can be written as

$$\begin{aligned}&\frac{\mathrm{d}}{\mathrm{d}t}\int_{V_a}\frac{\rho_a}{2}\left|\boldsymbol{u}_a\right|^2\mathrm{d}V+\frac{\mathrm{d}}{\mathrm{d}t}\int_{V_l}\frac{\rho_l}{2}\left|\boldsymbol{u}_l\right|^2\mathrm{d}V=\int\limits_A\left[u_n\left(-p_l+\tau_l^n+p_a-\tau_a^n\right)\right.\\&\left.+\boldsymbol{u}_l\cdot\boldsymbol{t}\tau_l^s-\boldsymbol{u}_a\cdot\boldsymbol{t}\tau_a^s\right]\mathrm{d}A-\int_{V_a}2\mu_a\mathbf{D}_a:\mathbf{D}_a\mathrm{d}V-\int\limits_{V_l}2\mu_l\mathbf{D}_l:\mathbf{D}_l\mathrm{d}V.\end{aligned}\tag{16.1.60}$$

We assume that the normal stress balance

$$p_a-\tau_a^n-p_l+\tau_l^n=\frac{\partial^2\eta}{\partial z^2}+\frac{\eta}{R^2},\tag{16.1.61}$$

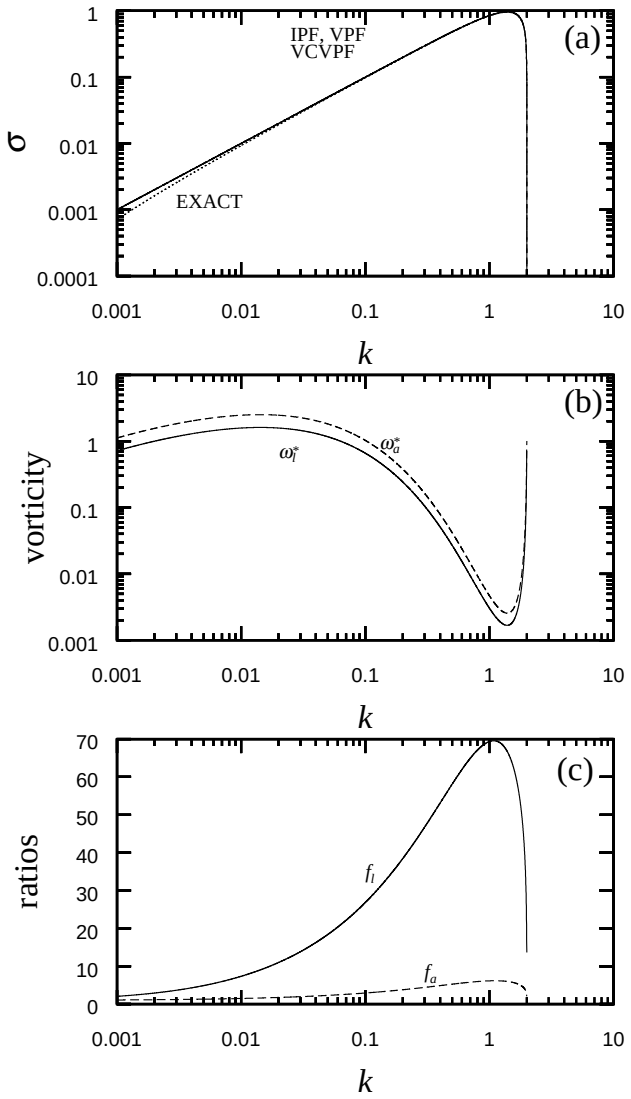

Fig. 16.2. (a) The growth rate σ vs. k for case 1, mercury in water. The three potential flow based analyses agree with the exact solution well but deviate from it slightly when $k \ll 1$. (b) The vorticities ω_l^* and ω_a^* vs. k for case 1. The magnitude of the vorticity is large when $k \ll 1$ and small when k is about 1. (c) The two ratios f_l and f_a vs. k for case 1. The irrotational parts dominate when k is close to 1; the irrotational and rotational parts are comparable when $k \ll 1$ or $k \approx 2$. The dominance of the irrotational part in the maximum growth region is understandable because the Reynolds number is very high, 2.080×10^7. Both the vorticities and the two ratios could help to understand the deviation of the potential based analyses from the exact solution when $k \ll 1$.

and the continuity of the tangential velocity and stress

$$\tau_a^s = \tau_l^s = \tau^s, \quad \text{and} \quad \boldsymbol{u}_a \cdot \boldsymbol{t} = \boldsymbol{u}_l \cdot \boldsymbol{t} = u_s, \tag{16.1.62}$$

are all satisfied at the interface. At the same time, the flow in the bulk of the fluids are approximated by potential flow, for which the following identity can be easily proved

$$\int_V 2\mu \mathbf{D} : \mathbf{D} \mathrm{d}V = \int_A \boldsymbol{n} \cdot 2\mu \mathbf{D} \cdot \boldsymbol{u} \mathrm{d}A, \tag{16.1.63}$$

where A is the surface of V and $\boldsymbol{n}$ is the unit normal pointing outward. Inserting (16.1.61), (16.1.62) and

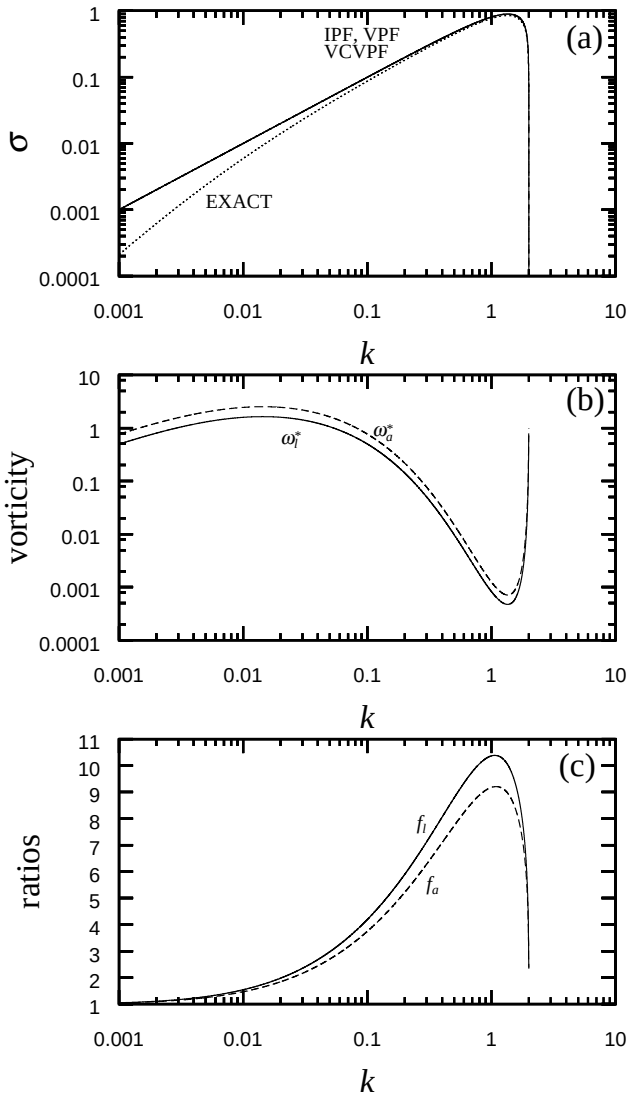

Fig. 16.3. (a) The growth rate σ vs. k for case 2, water in benzene. The three potential flow based analyses agree with the exact solution in the maximum growth region but deviate from it considerably when k is small. (b) The vorticities ω_l^* and ω_a^* vs. k for case 2. The magnitude of the vorticity is large when $k \ll 1$ and small in the maximum growth region. (c) The two ratios f_l and f_a vs. k for case 2. The ratios are high when k is close to 1 but close to 1 when $k \ll 1$ or $k \approx 2$. The maximum value of f_l is 10.37 here, smaller than the value 66.82 in case 1. The reason is that the Reynolds number in case 2 is smaller than in case 1. Both the vorticities and the two ratios could help to understand the good agreement in the maximum growth region and poor agreement when $k \ll 1$ as shown in (a).

(16.1.63) into (16.1.60), we obtain

$$\begin{aligned}&\frac{\mathrm{d}}{\mathrm{d}t}\int_{V_a}\frac{\rho_a}{2}\left|\boldsymbol{u}_a\right|^2\mathrm{d}V+\frac{\mathrm{d}}{\mathrm{d}t}\int_{V_l}\frac{\rho_l}{2}\left|\boldsymbol{u}_l\right|^2\mathrm{d}V=\int_A u_n\gamma\left(\frac{\partial^2\eta}{\partial z^2}+\frac{\eta}{R^2}\right)\mathrm{d}A\\&+\int_A\boldsymbol{n}_1\cdot 2\mu_a\mathbf{D}_a\cdot\boldsymbol{u}_a\mathrm{d}V-\int_A\boldsymbol{n}_1\cdot 2\mu_l\mathbf{D}_l\cdot\boldsymbol{u}_l\mathrm{d}V.\end{aligned}\tag{16.1.64}$$

The dimensionless form of (16.1.64) is

$$\begin{aligned}&l\frac{\mathrm{d}}{\mathrm{d}t}\int_{V_a}\frac{1}{2}\left|\boldsymbol{u}_a\right|^2\mathrm{d}V+\frac{\mathrm{d}}{\mathrm{d}t}\int_{V_l}\frac{1}{2}\left|\boldsymbol{u}_l\right|^2\mathrm{d}V=\int_A u_n\left(\frac{\partial^2\eta}{\partial z^2}+\frac{\eta}{R^2}\right)\mathrm{d}A\\&+\frac{m}{\sqrt{J}}\int_A\boldsymbol{n}_1\cdot 2\mathbf{D}_a\cdot\boldsymbol{u}_a\mathrm{d}A-\frac{1}{\sqrt{J}}\int_A\boldsymbol{n}_1\cdot 2\mathbf{D}_l\cdot\boldsymbol{u}_l\mathrm{d}A.\end{aligned}\tag{16.1.65}$$

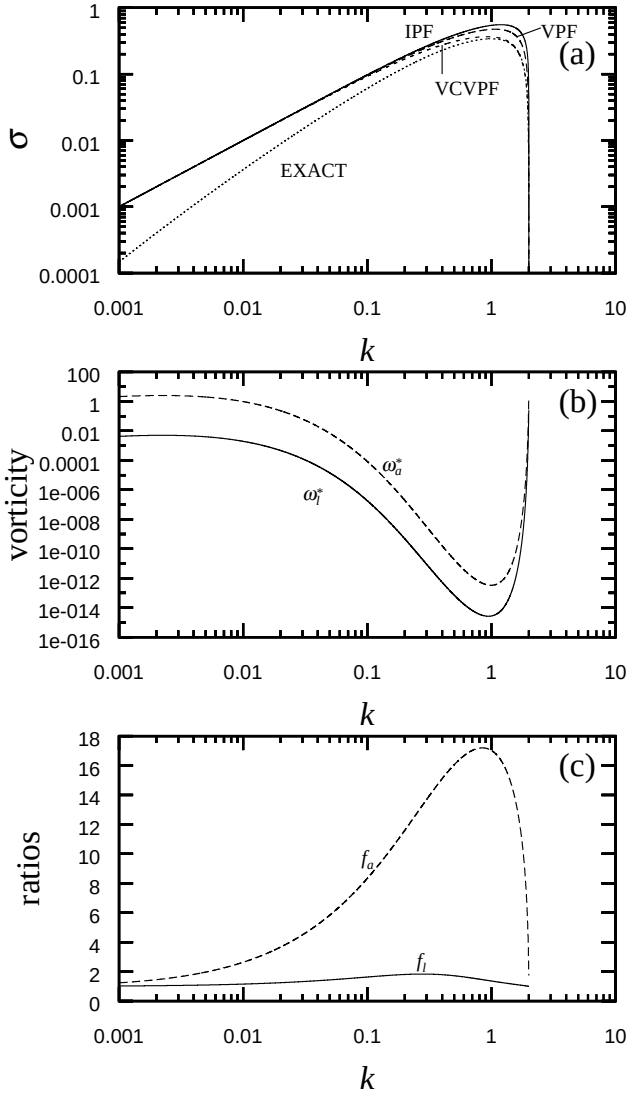

Fig. 16.4. (a) The growth rate σ vs. k for case 3, glycerin in mercury. In the maximum region, IPF and VPF overestimate the growth rate whereas VCVPF gives almost the same value as EXACT. IPF, VPF and VCVPF deviate from the exact solution considerably when $k \ll 1$. (b) The vorticities ω_l^* and ω_a^* vs. k for case 3. The magnitude of the vorticity is large when $k \ll 1$ and small in the maximum growth region. (c) The two ratios f_l and f_a vs. k for case 3. The ratios are high when k is close to 1 but close to 1 when $k \ll 1$ or $k \approx 2$. The maximum value of f_l is 1.83, much smaller than in case 1 and case 2. At the same time the Reynolds number is also much smaller than in case 1 and case 2. It is noted that the maximum value of f_a is 17.19, much larger than f_l. The reason is that the value of f_a should correspond to the Reynolds number based on ρ_a and μ_a, which is 2.08×10^7 in case 3. Both the vorticities and the two ratios could help to understand the good agreement in the maximum growth region and poor agreement when $k \ll 1$ as shown in (a).

The integrals in (16.1.65) are evaluated

$$\frac{\mathrm{d}}{\mathrm{d}t}\int_{V_l}\frac{|\boldsymbol{u}_l|^2}{2}\mathrm{d}V = \frac{\mathrm{d}}{\mathrm{d}t}\int_0^{2\pi}\mathrm{d}\theta\int_z^{z+\lambda}\int_0^R\frac{|\boldsymbol{u}_l|^2}{2}\,r\,\mathrm{d}r\mathrm{d}z$$
$$= |A_1|^2\,\pi\lambda R^2 k I_0(kR)I_1(kR)(\sigma+\bar{\sigma})\exp(\sigma+\bar{\sigma})t, \tag{16.1.66}$$

$$l\frac{\mathrm{d}}{\mathrm{d}t}\int_{V_a}\frac{|\boldsymbol{u}_a|^2}{2}\mathrm{d}V = l\frac{\mathrm{d}}{\mathrm{d}t}\int_0^{2\pi}\mathrm{d}\theta\int_z^{z+\lambda}\int_R^\infty\frac{|\boldsymbol{u}_a|^2}{2}\,r\,\mathrm{d}r\mathrm{d}z$$
$$= l\,|B_1|^2\,\pi\lambda R^2 k K_0(kR)K_1(kR)(\sigma+\bar{\sigma})\exp(\sigma+\bar{\sigma})t, \tag{16.1.67}$$

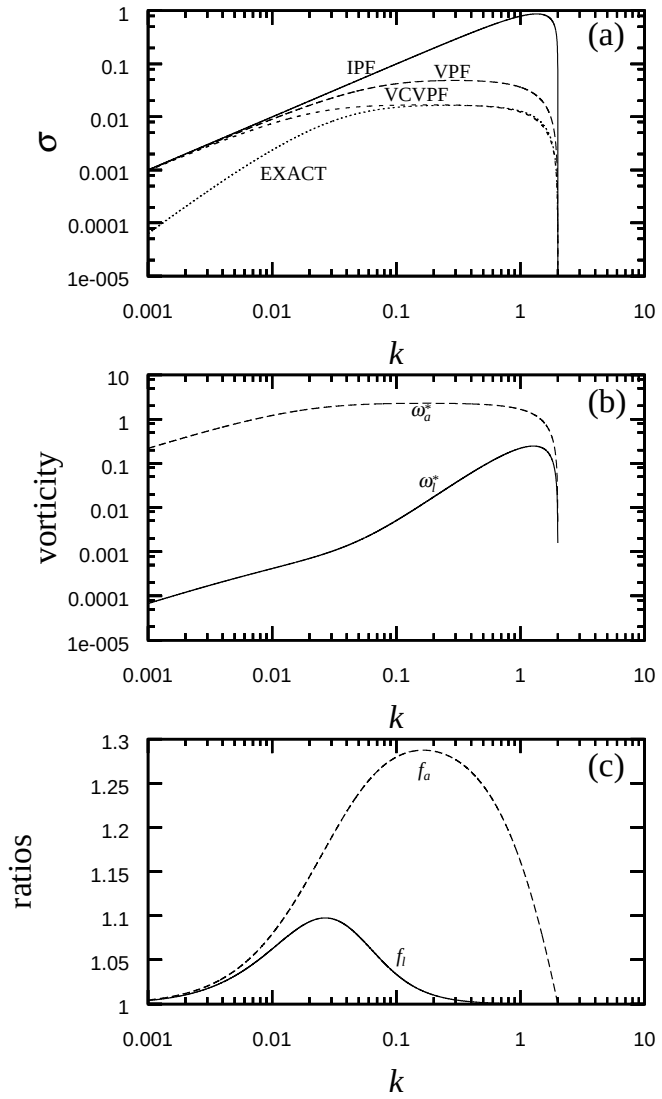

Fig. 16.5. (a) The growth rate σ vs. k for case 4, goldensyrup in paraffin. IPF and VPF deviate from the exact solution considerably in the whole range of $k \leq k_c = 2$. VCVPF is still in good agreement with the exact solution in the maximum growth region. (b) The vorticities ω_l^* and ω_a^* vs. k for case 4. The magnitude of the vorticity is large at almost all the values of k except when k is very close to $k_c = 2$. (c) The two ratios f_l and f_a vs. k for case 4. The maximum value of f_l and f_a does not exceed 1.3, indicating that the rotational parts are important in the whole range of k. This could explain the deviation of IPF and VPF from the exact solution in the whole range. At the same time, the curve for f_a shows that the ratio is higher in the maximum growth region than in the region where $k \ll 1$ or $k \approx 2$. This may help to understand the good agreement between VCVPF and the exact solution in the neighborhood of the maximum growth rate.

$$\int_A \left(\frac{\partial^2 \eta}{\partial z^2} + \frac{\eta}{R^2}\right) u_l \mathrm{d}A = 2\left|A_1\right|^2 \pi\lambda R \frac{k^2}{\sigma} I_1^2(kR) \left(\frac{1}{R^2} - k^2\right) \exp(\sigma + \bar{\sigma})t, \tag{16.1.68}$$

$$\frac{1}{\sqrt{J}} \int_A \boldsymbol{n}_1 \cdot 2\mathbf{D}_l \cdot \boldsymbol{u}_l \mathrm{d}A = \frac{4}{\sqrt{J}} \left|A_1\right|^2 \pi\lambda R k^3 I_1(kR) \left[2I_0(kR) - \frac{I_1(kR)}{kR}\right] \exp(\sigma + \bar{\sigma})t, \tag{16.1.69}$$

$$\frac{m}{\sqrt{J}} \int_A \boldsymbol{n}_1 \cdot 2\mathbf{D}_a \cdot \boldsymbol{u}_a \mathrm{d}A = \frac{4m}{\sqrt{J}} \left|A_1\right|^2 \pi\lambda R k^3 K_1(kR) \left[2K_0(kR) + \frac{K_1(kR)}{kR}\right] \exp(\sigma + \bar{\sigma})t. \tag{16.1.70}$$

Inserting (16.1.66)–(16.1.70) into (16.1.65), we obtain

$$(\alpha_l + l\alpha_a)\frac{\sigma + \bar{\sigma}}{2} + \frac{2k^2}{\sqrt{J}} \left[(\alpha_l + \beta_l) + m(\alpha_a + \beta_a)\right] = \left(\frac{1}{R^2} - k^2\right) \frac{k}{\sigma}, \tag{16.1.71}$$

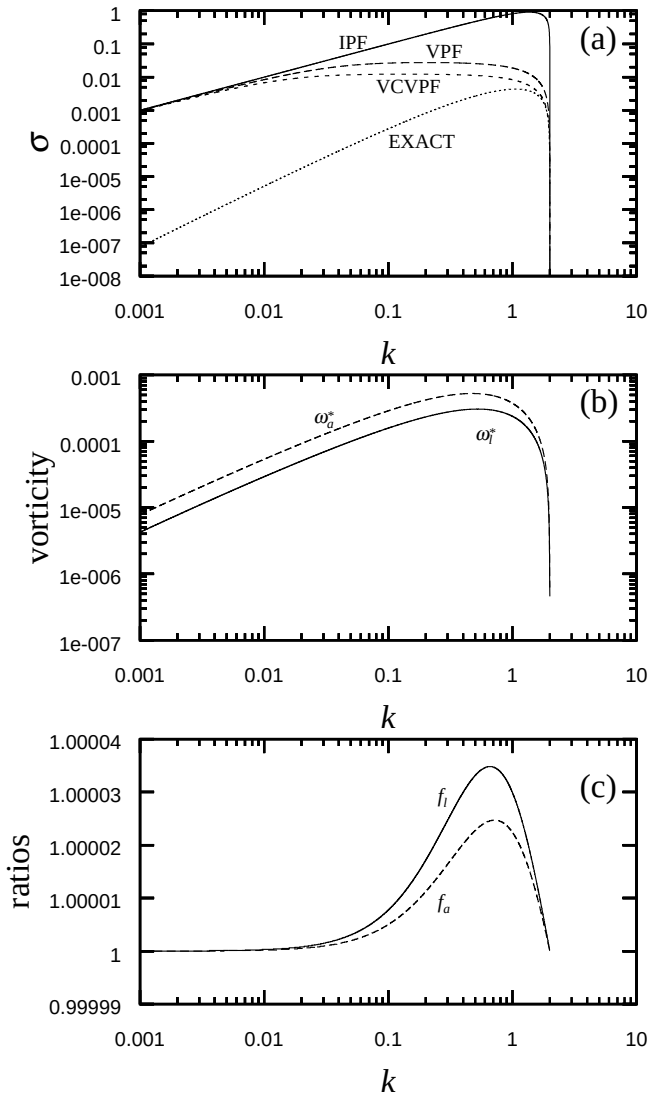

Fig. 16.6. (a) The growth rate σ vs. k for case 5, goldensyrup in BBoil. The agreement between IPF, VPF and VCVPF with the exact solution is poor at almost all the values of k. (b) The vorticities ω_l^* and ω_a^* vs. k for case 5. The magnitude of the vorticity is relatively large at almost all the values of k, and becomes small only when k is very close to $k_c = 2$. (c) The two ratios f_l and f_a vs. k for case 5. The maximum value of f_l and f_a does not exceed 1.000035, indicating that the irrotational and rotational parts are almost equally important in the whole range of k. Both the vorticities and the two ratios could help to understand the poor agreement between IPF, VPF and VCVPF with the exact solution shown in (a).

where α_l, α_a, β_a and β_l are defined in (16.1.23). If we assume that σ is real, (16.1.71) is the same as the dispersion relation (16.1.49) from the VCVPF solution. The solution of the dispersion relation is given in (16.1.50). In the range $0 < k \leq 1/R = 2$, σ is real and our assumption is satisfied. Therefore, the growth rate computed by the dissipation calculation is the same as that computed by the VCVPF.

16.1.8 Discussion of the pressure corrections at the interface of two viscous fluids

Our pressure corrections arise in a boundary layer induced by the discontinuity of the tangential velocity and shear stress at the interface evaluated using the potential solution. We assume that the boundary layer is thin and when the boundary layer is considered, the tangential velocity and shear stress are continuous at the interface. This assumption leads to good agreements between the exact solution and VCVPF for the liquid-gas

cases and less good agreements, better than what might be expected, in the cases of two fluids for which the boundary layer assumptions do not hold uniformly and will be discussed in this section. In the boundary layer near the interface, we divide the velocity and pressure into irrotational part and viscous correction part

$$u = u^i + u^v, \quad w = w^i + w^v, \quad p = p^i + p^v. \tag{16.1.72}$$

The irrotational tangential velocities at the interface are

$$w_l^i = -A_1 k I_0(kR) \exp(\sigma t + \mathrm{i}kz), \tag{16.1.73}$$

$$w_a^i = A_1 k \frac{I_1(kR)}{K_1(kR)} K_0(kR) \exp(\sigma t + \mathrm{i}kz). \tag{16.1.74}$$

The tangential stresses at the interface evaluated using the potential flows are

$$\tau_l^s = -\left(2/\sqrt{J}\right) A_1 k^2 I_1(kR) \exp(\sigma t + \mathrm{i}kz), \tag{16.1.75}$$

$$\tau_a^s = -\left(2m/\sqrt{J}\right) A_1 k^2 I_1(kR) \exp(\sigma t + \mathrm{i}kz). \tag{16.1.76}$$

The continuity of the tangential velocity requires

$$w_l^i + w_l^v = w_a^i + w_a^v, \tag{16.1.77}$$

which gives rise to

$$w_l^v - A_1 k I_0(kR) \exp(\sigma t + \mathrm{i}kz) = w_a^v + A_1 k \frac{I_1(kR)}{K_1(kR)} K_0(kR) \exp(\sigma t + \mathrm{i}kz). \tag{16.1.78}$$

If we assume $w_a^v = q w_l^v$, (16.1.78) can be written as

$$w_l^v (1-q) = A_1 k \left[I_0(kR) + \frac{I_1(kR)}{K_1(kR)} K_0(kR) \right] \exp(\sigma t + \mathrm{i}kz). \tag{16.1.79}$$

The continuity of the shear stress requires

$$\begin{aligned} &\frac{1}{\sqrt{J}} \left(\frac{\partial u_l^v}{\partial z} + \frac{\partial w_l^v}{\partial r} \right) - \frac{2}{\sqrt{J}} A_1 k^2 I_1(kR) \exp(\sigma t + \mathrm{i}kz) \\ &= \frac{m}{\sqrt{J}} \left(\frac{\partial u_a^v}{\partial z} + \frac{\partial w_a^v}{\partial r} \right) - 2 \frac{m}{\sqrt{J}} A_1 k^2 I_1(kR) \exp(\sigma t + \mathrm{i}kz). \end{aligned} \tag{16.1.80}$$

Since the potential flow solution satisfies the continuity of the normal velocity $u_l^i = u_a^i$, the viscous corrections to the normal velocity in the boundary layer should be very small. Thus $\partial u_l^v / \partial z$ and $\partial u_a^v / \partial z$ can be ignored and (16.1.80) becomes

$$\frac{\partial}{\partial r} \left(w_l^v - m w_a^v \right) = 2(1-m) A_1 k^2 I_1(kR) \exp(\sigma t + \mathrm{i}kz). \tag{16.1.81}$$

Assuming that the boundary layer thickness δ is small, we can write (16.1.81) approximately as

$$w_l^v \left(1 - mq\right) / \delta = 2(1-m) A_1 k^2 I_1(kR) \exp(\sigma t + \mathrm{i}kz). \tag{16.1.82}$$

Comparing (16.1.79) and (16.1.82), we obtain

$$\frac{1 - mq}{(1-q)(1-m)} \frac{1}{\delta} = \frac{2k I_1(kR)}{I_0(kR) + I_1(kR) \dfrac{K_0(kR)}{K_1(kR)}}. \tag{16.1.83}$$

Therefore, (16.1.83) needs to be satisfied if the continuities of the tangential velocity and stress are to be enforced. In other words, the assumptions on which VCVPF is based are valid only if (16.1.83) is satisfied. Since we do not solve the boundary layer problem, q and δ are unknown and we are not able to determine if (16.1.83) is satisfied. However, we may assume that δ is very small and estimate the possibility of satisfying (16.1.83) under different conditions, i.e. different values of m and k. We have the following observations regarding (16.1.83).

(1) Since δ is supposed to be small, (16.1.83) is easier to satisfy when the right hand side is larger. Calculation

shows that the right hand side of (16.1.83) is 5×10^{-7} when k =0.001 and is 1.36 when $k = 2$. Therefore, (16.1.83) can be satisfied for k close to k_c =2 but is very difficult to satisfy for small k. This observation could help to understand the results of the growth rate calculation, i.e., the agreement between VCVPF and the exact solution is good for k close to k_c but is poor when $k \ll 1$.

(2) The term on the left hand side of (16.1.83)

$$\frac{1-mq}{(1-q)(1-m)} \tag{16.1.84}$$

should be comparable to or even smaller than δ, so that (16.1.83) can be satisfied. We find that for certain values of q, (16.1.84) is small when m is much smaller than 1 and is large when m is close to 1. For example, if we fix q at 10, the value of (16.1.84) is 0.0125 when $m = 0.11$ and is 8.89 when $m = 0.9$. This observation may help to understand our growth rate calculation at low Reynolds numbers. In case 4, $m = 3.091 \times 10^{-4}$ and VCVPF is in good agreement with the exact solution in the region of maximum growth; in case 5, $m = 0.5455$ and VCVPF does not give the correct maximum growth rate σ_m and the associated wave-number k_m. The value of m does not seem to be important at high Reynolds numbers. In case 1 and 2, IPF, VPF, VCVPF all agree well with the exact solution in the region of maximum growth even when the value of m is relatively close to 1. This is because the boundary layer and the viscous correction are not important at high Reynolds numbers.

We have shown that the condition (16.1.83) can be satisfied in some cases (k close to $k_c = 2$ and $m \ll 1$), and is very difficult to satisfy in other cases ($k \ll 1$ or m close to 1). When (16.1.83) is satisfied, the assumption of continuous tangential velocity and stress is realized approximately and our calculation does show good agreement between VCVPF and VPF. When (16.1.83) is difficult to satisfy, VCVPF may not give a good approximation to the exact solution, especially at low Reynolds numbers. Thus, viscous potential flows with pressure corrections can be used to approximate viscous flows in problems involving the interface of two viscous fluids, but this approximation is not uniformly valid.

When the viscous corrections for the velocity and pressure are added to the irrotational flow, the complete form of the normal stress balance is

$$p_a^i + p_a^v - p_l^i - p_l^v + \frac{2}{\sqrt{J}}\left(\frac{\partial u_l^i}{\partial r} + \frac{\partial u_l^v}{\partial r}\right) - \frac{2m}{\sqrt{J}}\left(\frac{\partial u_a^i}{\partial r} + \frac{\partial u_a^v}{\partial r}\right) = \frac{\partial^2 \eta}{\partial z^2} + \frac{\eta}{R^2}. \tag{16.1.85}$$

The viscous corrections of the velocity satisfy the continuity equation

$$\frac{\partial u_l^v}{\partial r} + \frac{u_l^v}{r} + \frac{\partial w_l^v}{\partial z} = 0. \tag{16.1.86}$$

We may estimate the order of the terms in (16.1.86)

$$2\frac{u_l^v}{\delta} \sim \frac{w_l^v}{\lambda}. \tag{16.1.87}$$

Combining (16.1.82) and (16.1.87), we obtain

$$\frac{\partial u_l^v}{\partial r} \sim \frac{u_l^v}{\delta} \sim \frac{\delta}{\lambda}\frac{1-m}{1-mq}A_1 k^2 I_1(kR). \tag{16.1.88}$$

At the same time, we have

$$\frac{\partial u_l^i}{\partial r} \sim A_1 k^2 \left(I_0(kR) - \frac{I_1(kR)}{kR}\right). \tag{16.1.89}$$

If $(1-m)/(1-mq)$ is not a very big value, $\partial u_l^v/\partial r$ may be significantly smaller than $\partial u_l^i/\partial r$. A similar argument can show that $\partial u_a^v/\partial r$ could be significantly smaller than $\partial u_a^i/\partial r$. Therefore, $\partial u_l^v/\partial r$ and $\partial u_a^v/\partial r$ can be ignored in (16.1.85) and we obtain the normal stress balance equation (16.1.40) used in VCVPF calculation. Admittedly, omission of $\partial u_l^v/\partial r$ and $\partial u_a^v/\partial r$ is not justified for certain values of m and q, which may be partially responsible for the poor agreement between VCVPF and the exact solution in some cases.

Fluids	(1) Mercury-air	(2) Water-air	(3) SO100-air	(4) Glycerine-air	(5) SO10000-air
ρ_l (kg m^{-3})	1.35×10^4	1.00×10^3	9.69×10^2	1.26×10^3	9.69×10^2
μ_l (kg/m s)	1.56×10^{-3}	1.0×10^{-3}	0.1	0.782	10.0
γ (N/m)	0.482	7.28×10^{-2}	2.1×10^{-2}	6.34×10^{-2}	2.1×10^{-2}
$J = \rho_l \gamma D/\mu_l^2$	2.67×10^7	7.28×10^5	20.4	1.30	2.04×10^{-3}

Table 16.3. *The properties of five fluids surrounded by air used to study capillary instability and the Reynolds number $J = Oh^2$ where Oh is the Ohnesorge number.*

16.1.9 Capillary instability when one fluid is a dynamically inactive gas

There are two cases; (i) the exterior fluid is a gas or (ii) the interior fluid is a gas. The gas is dynamically inactive when $m = \ell = 0$. Dispersion relations for the cases in which one fluid is a dynamically inactive gas can be obtained by putting $m = \ell = 0$ in the fluid formulas

VPF	(eq16.1.16.2.24)
IPF	(eq16.1.16.2.25)
VCVPF	(eq16.1.16.2.50)
ES	(eq16.1.16.2.14)

where ES stands for the exact solution of Tomotika 1935.

(i) Exterior fluid is a gas

$$\text{VPF} : \sigma = -\frac{k^2\beta_l}{\sqrt{J}\alpha_l} \pm \sqrt{\left[\frac{k^2\beta_l}{\sqrt{J}\alpha_l}\right]^2 + \left(\frac{1}{R^2} - k^2\right)\frac{k}{\alpha_l}}; \tag{16.1.90}$$

$$\text{IPF} : \sigma = \pm\sqrt{\left(\frac{1}{R^2} - k^2\right)\frac{k}{\alpha_l}}; \tag{16.1.91}$$

$$\text{VCVPF} : \sigma = -\frac{k^2(\alpha_l + \beta_l)}{\sqrt{J}\alpha_l} \pm \sqrt{\left[\frac{k^2(\alpha_l + \beta_l)}{\sqrt{J}\alpha_l}\right]^2 + \left(\frac{1}{R^2} - k^2\right)\frac{k}{\alpha_l}}; \tag{16.1.92}$$

$$\text{ES} : \sigma \ \text{isthesolutionof}$$
$$\begin{vmatrix} 2k^2 I_1(kR) & (k^2 + k_l^2) I_1(k_l R) \\ F_1 & F_2 \end{vmatrix} = 0, \tag{16.1.93}$$

where F_1 and F_2 are defined in (16.1.15) and (16.1.16).

Calculations using these formulas were carried out for the five liquids listed in Table 16.3.

At high Reynolds numbers, the results using IPF, VPF, VCVPF and ES are essentially the same (all the theories give rise to essentially the same result in the case of water or mercury; refer readers to Funada & Joseph (2002)). At lower Reynolds numbers, IPF overestimates the growth rate considerably in the maximum growth region; the growth rate by VPF is in better agreement with the ES solution; the curves for VCVPF are almost indistinguishable from the ES curves (figure 16.7 and 16.8). The remarkably good agreement between VCVPF and ES seems universal; it is observed for $10^{-3} < J < 10^7$ and for any $k < k_c = 2$ (see table 16.4).

(ii) The interior fluid is a gas Next we consider cases in which the interior fluid is a gas with negligible viscosity and density; these are the inverse cases of those in § 5. We shall omit the details of the VCVPF calculation because they are similar to those presented in § 5. We directly present the growth rates computed

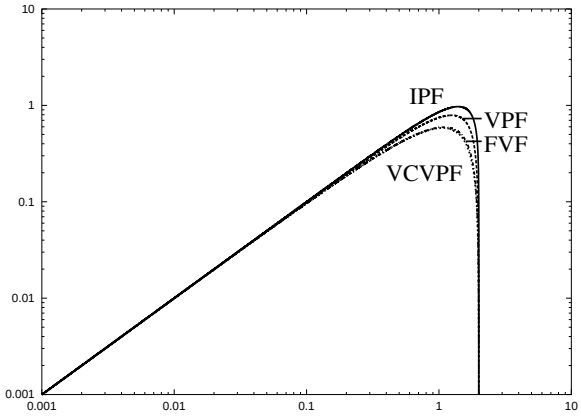

Fig. 16.7. The growth rate σ vs. k for case 3, SO100 in air. IPF and VPF slightly overestimate the growth rate in the region near the peak; the curve for the corrected solution (VCPVF) is almost indistinguishable from the exact solution (ES). FVF in the figure should be replaces by ES.

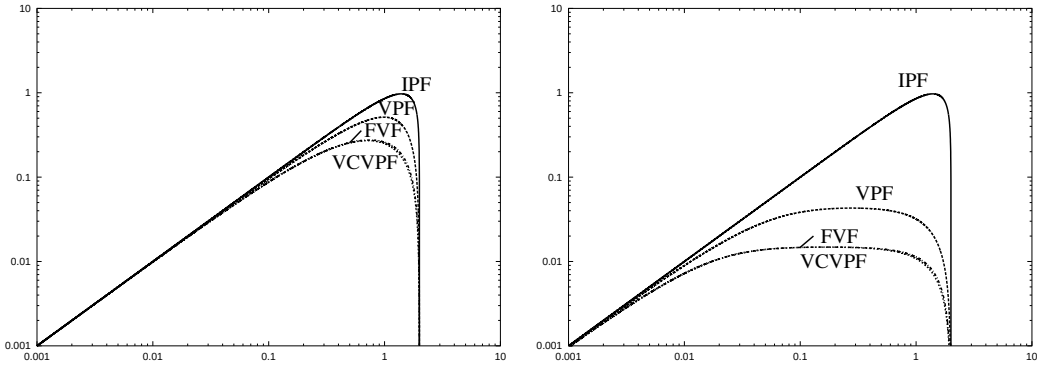

(a) (b)

Fig. 16.8. The growth rate σ vs. k for case 4, glycerine in air (a) and for case 5, SO10000 in air (b). The growth rates computed from IPF and VPF deviate considerably from the exact solution (ES), but the growth rates from the corrected solution (VCVPF) are nearly the same as the exact solution (see table 16.4). FVF in the figure should be replaces by ES.

by IPF, VPF, VCVPF and ES as following.

$$\text{IPF} : \sigma = \pm\sqrt{\left(\frac{1}{R^2} - k^2\right)\frac{k}{\alpha_a}}; \tag{16.1.94}$$

$$\text{VPF} : \sigma = -\frac{k^2\beta_a}{\sqrt{J'}\alpha_a} \pm \sqrt{\left[\frac{k^2\beta_a}{\sqrt{J'}\alpha_a}\right]^2 + \left(\frac{1}{R^2} - k^2\right)\frac{k}{\alpha_a}}; \tag{16.1.95}$$

$$\text{VCVPF} : \sigma = -\frac{k^2(\alpha_a+\beta_a)}{\sqrt{J'}\alpha_a} \pm \sqrt{\left[\frac{k^2(\alpha_a+\beta_a)}{\sqrt{J'}\alpha_a}\right]^2 + \left(\frac{1}{R^2} - k^2\right)\frac{k}{\alpha_a}}; \tag{16.1.96}$$

ES: σ is the solution of

$$\begin{vmatrix} 2k^2K_1(kR) & \left(k^2+k_a'^2\right)K_1(k_a'R) \\ F_5 & F_6 \end{vmatrix} = 0, \tag{16.1.97}$$

where α_a, β_a are defined in (4.5) and

$$F_5 = -\sigma K_0(kR) - \frac{2k^2}{\sqrt{J'}}\left(\frac{\mathrm{d}K_1(kR)}{\mathrm{d}(kR)}\right) + \left(\frac{1}{R^2} - k^2\right)\frac{k}{\sigma}K_1(kR), \tag{16.1.98}$$

$$F_6 = -\frac{2kk_a'}{\sqrt{J'}}\left(\frac{\mathrm{d}K_1(k_a'R)}{\mathrm{d}(k_a'R)}\right) + \left(\frac{1}{R^2} - k^2\right)\frac{k}{\sigma}K_1(k_a'R), \tag{16.1.99}$$

Case	VCVPF (A)		ES (A)		VCVPF (B)		ES (B)	
	k_m	σ_m	k_m	σ_m	k_m	σ_m	k_m	σ_m
1	1.39	0.97	1.39	0.97	0.97	2.32	0.97	2.31
2	1.39	0.97	1.39	0.97	0.96	2.31	0.96	2.31
3	1.06	0.58	1.09	0.59	0.53	1.58	0.60	1.61
4	0.72	0.27	0.74	0.28	0.21	0.84	0.28	0.86
5	0.17	0.015	0.17	0.015	0.0066	0.045	0.013	0.045

Table 16.4. *Maximum growth rate σ_m and the associated wavenumber k_m for VCVPF and ES in the 5 cases shown in table 16.1 (A) and in the 5 inverse cases (B) (see § 7), e.g. air-mercury.*

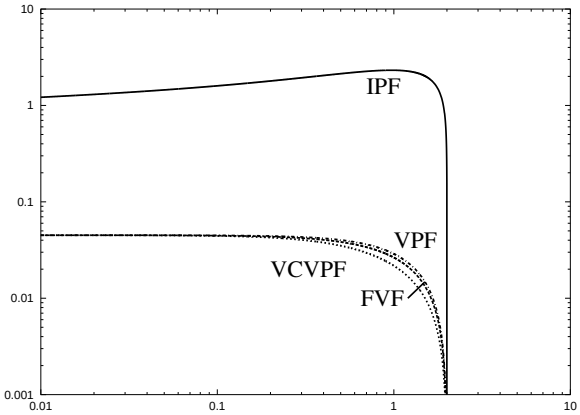

Fig. 16.9. The growth rate σ vs. k for case 5 (inverse), air in SO10000. The growth rate by IPF is significantly larger than that by ES; the results by VPF, VCVPF and ES are almost the same (see table 16.2). FVF in the figure should be replaces by ES.

with

$$k_a' = \sqrt{k^2 + \sqrt{J'}\sigma}, \quad J' = \frac{\rho_a D\gamma}{\mu_a^2}. \tag{16.1.100}$$

We calculate the growth rate curves for the inverse cases of those listed in table 16.1. Example curves are plotted in figure 16.9 for air in SO10000. At low Reynolds numbers (figure 16.9), the growth rate by IPF is significantly larger than that by ES for any $k < k_c = 2$; VPF and VCVPF both give good approximations to ES. At higher Reynolds numbers, the growth rate curves computed using IPF, VPF, VCVPF and ES are almost the same.

16.1.10 Conclusions

Purely irrotational theories of capillary instability of one viscous fluid cylinder in another viscous fluid were derived and compared with Tomotika's exact theory. In the case of two liquids the continuity condition, like no-slip and continuity of shear stresses, generate regions of vorticity which have an important effect on viscous decay. The exact solution, however, in surprisingly well approximated by VCVPF for waves near the peak value of the growth rate curve but is not well approximated by VCVPF for long waves.

The extra pressure derived for VCVPF is generally thought to arise in a vorticity layer at the gas liquid boundary. This idea still needs clarification, but in any case it is not used or needed in our purely irrotational theories.

In the cases in which one of the fluids is a dynamically passive gas (or vacuum), the purely irrotational theory of VCVPF with an extra pressure gives rise to a dispersion relation which is almost indistinguishable from the exact one, uniformly in the wave number. The same dispersion relation as given by VCVPF can be derived from the dissipation method. The approximation to the exact solution ES generated by VCVPF is much better than

VPF. As a rule of thumb, we can say that VPF gives a good approximation of the viscous effects in the case of short waves and VCVPF gives a good approximation for long waves. In the capillary instability problems studied here the short waves are stabilized by surface tension and do enter into the stability analysis.

16.2 Stability of a liquid jet into incompressible gases: temporal, convective and absolute instability

We carry out an analysis of the stability of a liquid jet into a gas or another liquid using viscous potential flow. The nstability may be driven by Kelvin-Helmholtz KH instability due to a velocity difference and a neckdown due to capillary instability. An explicit dispersion relation is derived and analyzed for temporal and convective/absolute (C/A) instability. We find that for all values of the relevant parameters, there are wavenumbers for which the liquid jet is temporally unstable. The cut-off wavenumber and wavenumber of maximum growth are most important; the variation of these quantities with the density and viscosity ratios, the Weber number and Reynolds is computed and displayed as graphs and asymptotic formulas. The instabilities of a liquid jet are due to capillary and KH instabilities. We show that KH instability cannot occur in a vacuum but capillary instability (and Rayleigh-Taylor instability) can occur in vacuum. We present comprehensive results, based on viscous potential flow, of the effects of the ambient.

Temporally unstable liquid jet flows can be analyzed for spatial instabilities by C/A theory; they are either convectively unstable or absolutely unstable depending on the sign of the temporal growth rate at a singularity of the dispersion relation. The study of such singularities is greatly simplified by the analysis here which leads to an explicit dispersion relation; an algebraic function of a complex frequency and complex wavenumber. Analysis of this function gives rise to an accurate Weber-Reynolds criterion for the border between absolute and convective instabilities. Some problems of the applicability to physics of C/A analysis of stability of spatially uniform and nearly uniform flows are discussed.

16.2.1 Introduction

This chapter is also allied to the analysis of temporal instability of the capillary jet given by Funada & Joseph (2002). Their analysis generalizes the inviscid analysis of Rayleigh (1878) in two ways: by accounting (i) for the viscosity of the jet and (ii) for the viscosity anddensity of the ambient media. The liquid jet is prey to capillary instability and Kelvin-Helmholtz instability due to the difference of the velocity of the jet and of the ambient media. The effects of discontinuous velocity can be obtained by a Galilean transformation to a fixed coordinate system relative to which the jet is moving with a velocity U. As a practical matter, the transformation $z \to z+Ut$ transforms disturbances of the form $\exp[\mathrm{i}(kz - \omega t)]$ to $\exp[\mathrm{i}(kz - \tilde{\omega} t)]$ where $\tilde{\omega} = \omega - kU$. A Kelvin-Helmholtz instability due to velocity discontinuity cannot occur when the no-slip condition is applied.

We compute in a coordinate system fixed on the ambient fluid relative to which the jet velocity is U. We consider temporal, convective and absolute instability. The analysis of these instabilities is greatly simplified by viscous potential flow which leads to an explicit dispersion relation $D(k, \omega) = 0$, in which the ambient media with viscosity μ_a and density ρ_a is fully represented. Moreover, the analysis applies equally to jets into liquid and jet into gas; ρ_a and μ_a stand for "air" for jets into air and for "ambient" for jets into liquid. This chapter is organized so as to emphasize the case of jets into air which can be compared to the prior literature, which is reviewed below. The case of jets of viscous liquids into viscous liquids can be analyzed because viscous potential flow is consistent with a discontinuous velocity across the jet boundary.

The liquid jet is subject to Kelvin-Helmholtz instability due to the discontinuous velocity and to capillary instability due to surface tension. We show that Kelvin-Helmholtz instabilities cannot occur in a vacuum. The only other paper to treat the case of combined KH and capillary instability is that of Lin & Lian (1989) who analyzed the viscous problem using the Navier-Stokes equations but neglecting the effects of shear from the viscous gas.

Other papers relevant to the stability of the liquid jet neglect viscosity altogether or neglect the effects of the ambient. Rayleigh's 1878 study of temporal instability, the study of spatial instability of Keller, Rubinow & Tu (1973), and Leib & Goldstein's 1986a study of C/A instability neglect viscosity and the effects of the ambient. Leib & Goldstein (1986b) and Le Dizès (1997) account for the jet viscosity but neglect the ambient. Many examples of transition from convective to absolute instability arising in the breakup of sheets and jets are presented in the monograph of S.P.Lin (2003). In particular, Lin has an interesting discussion of the relevance of this transition to the transition from dripping to jetting under gravity. The comparisons are suggestive but the agreement between C/A theory and experiments is not definitive.

16.2.2 Problem formulation

A long liquid cylinder of density ρ, viscosity μ and of mean radius a moves with a uniform axial velocity U relative to an ambient gas (air) of ρ_a, μ_a. With a cylindrical frame (r, θ, z) fixed on the gas, the liquid cylinder is put in the region of $0 \le r < a + \eta$ and $-\infty < z < \infty$, where $\eta = \eta(z, t)$ is the varicose interface displacement. The governing Navier-Stokes equations and interface conditions for disturbances of the cylinder and gas are made dimensionless with the following scales:

$$[\text{length, velocity, time, pressure}] = \left[2a,\ U,\ \frac{2a}{U},\ \rho U^2\right]. \tag{16.2.1}$$

In terms of this normalization, we may define Weber number W, Reynolds number R, density ratio ℓ and viscosity ratio m:

$$W = \frac{\gamma}{\rho 2aU^2}, \quad R = \frac{U2a}{\nu}, \quad \ell = \frac{\rho_a}{\rho}, \quad m = \frac{\mu_a}{\mu}, \tag{16.2.2}$$

where γ is the surface tension coefficient, $\nu = \mu/\rho$, $\nu_a = \mu_a/\rho_a$ and $m/\ell = \nu_a/\nu$.

This problem is a combination of capillary instability and Kelvin-Helmholtz instability. When $W = 0$ ($\gamma = 0$) the instability is generated by the velocity difference. An interesting feature of this instability is that even though the density and viscosity of the gas is much smaller than the liquid, the dynamical effects of the gas cannot be neglected. The relevant physical quantity is the kinematic viscosity $\nu = \mu/\rho$; Funada & Joseph (2001) found that the stability limit for viscous potential flow is nearly independent of the viscosity when $\nu_\ell > \nu_a$, with a sensible dependence when $\nu_\ell < \nu_a$, for small viscosities, the opposite of what intuition would suggest. Essentially the same result holds for Kelvin-Helmholtz of liquid jet, studied here. The other limit $W \to \infty$ or $U \to 0$ leads to capillary instability which was studied using viscous potential flow, by Funada & Joseph (2002). Our scaling fails when U tends to zero; in the case the scale velocity is γ/μ which is the characteristic velocity for capillary collapse and the relevant Reynolds number is $J = \rho\gamma 2a/\mu^2$. The basic flow in dimensionless coordinates is $(\partial\Phi/\partial z,\ \partial\Phi_a/\partial z) = (1, 0)$ in terms of the velocity potential Φ and Φ_a.

For the liquid cylinder in a disturbed state ($0 \le r < 1/2 + \eta$ and $-\infty < z < \infty$), the velocity potential $\phi \equiv \phi(r, z, t)$ of an axisymmetric disturbance satisfies the Laplace equation:

$$\left(\frac{\partial^2}{\partial r^2} + \frac{1}{r}\frac{\partial}{\partial r} + \frac{\partial^2}{\partial z^2}\right)\phi = 0, \tag{16.2.3}$$

and the Bernoulli equation:

$$\frac{\partial\phi}{\partial t} + \frac{\partial\phi}{\partial z} + \frac{1}{2}\left(\frac{\partial\phi}{\partial r}\right)^2 + \frac{1}{2}\left(\frac{\partial\phi}{\partial z}\right)^2 + p = f(t), \tag{16.2.4}$$

where $p \equiv p(r, z, t)$ is the pressure, and $f(t)$ is an arbitrary function of time t which may be put to zero. For the gas disturbance of infinite extent ($1/2 + \eta < r < \infty$ and $-\infty < z < \infty$), the velocity potential $\phi_a \equiv \phi_a(r, z, t)$ satisfies the equations:

$$\left(\frac{\partial^2}{\partial r^2} + \frac{1}{r}\frac{\partial}{\partial r} + \frac{\partial^2}{\partial z^2}\right)\phi_a = 0, \tag{16.2.5}$$

$$\ell\left[\frac{\partial\phi_a}{\partial t}+\frac{1}{2}\left(\frac{\partial\phi_a}{\partial r}\right)^2+\frac{1}{2}\left(\frac{\partial\phi_a}{\partial z}\right)^2\right]+p_a=f_a(t). \tag{16.2.6}$$

The kinematic condition at the interface $r=1/2+\eta$ is given for each fluid by

$$\frac{\partial\eta}{\partial t}+\frac{\partial\eta}{\partial z}+\frac{\partial\phi}{\partial z}\frac{\partial\eta}{\partial z}=\frac{\partial\phi}{\partial r},\quad \frac{\partial\eta}{\partial t}+\frac{\partial\phi_a}{\partial z}\frac{\partial\eta}{\partial z}=\frac{\partial\phi_a}{\partial r}, \tag{16.2.7}$$

and the normal stress balance at $r=1/2+\eta$ is given by

$$p-p_a-\frac{1}{R}\tau+\frac{m}{R}\tau_a=-W\left\{\frac{\partial^2\eta}{\partial z^2}\left[1+\left(\frac{\partial\eta}{\partial z}\right)^2\right]^{-3/2}-(1/2+\eta)^{-1}\left[1+\left(\frac{\partial\eta}{\partial z}\right)^2\right]^{-1/2}+2\right\}, \tag{16.2.8}$$

where the pressures at the interface are expressed by (16.2.4) and (16.2.6), and τ and τ_a denote the normal viscous stresses acting on the interface:

$$\tau=2\left[\frac{\partial^2\phi}{\partial r^2}-2\frac{\partial^2\phi}{\partial r\partial z}\frac{\partial\eta}{\partial z}+\frac{\partial^2\phi}{\partial z^2}\left(\frac{\partial\eta}{\partial z}\right)^2\right]\left[1+\left(\frac{\partial\eta}{\partial z}\right)^2\right]^{-1}, \tag{16.2.9}$$

$$\tau_a=2\left[\frac{\partial^2\phi_a}{\partial r^2}-2\frac{\partial^2\phi_a}{\partial r\partial z}\frac{\partial\eta}{\partial z}+\frac{\partial^2\phi_a}{\partial z^2}\left(\frac{\partial\eta}{\partial z}\right)^2\right]\left[1+\left(\frac{\partial\eta}{\partial z}\right)^2\right]^{-1}. \tag{16.2.10}$$

For a case of the interface displacement small compared with the mean radius, (16.2.7)-(16.2.10) may be expanded around $r=1/2$ to give a linear system of boundary conditions for small disturbances. We do not require the continuity of tangential velocity and shear stress. The other conditions are that the liquid velocity is finite at the center $r=0$, and the gas velocity should vanish as $r\to\infty$.

16.2.3 Dispersion relation

The potentials ϕ and ϕ_a are determined by (16.2.3) and (16.2.5). At the interface approximated by $r=1/2$, the kinematic conditions are given by

$$\frac{\partial\eta}{\partial t}+\frac{\partial\eta}{\partial z}=\frac{\partial\phi}{\partial r},\quad \frac{\partial\eta}{\partial t}=\frac{\partial\phi_a}{\partial r}, \tag{16.2.11}$$

and the normal stress balance is given by

$$-\left(\frac{\partial\phi}{\partial t}+\frac{\partial\phi}{\partial z}\right)+\ell\frac{\partial\phi_a}{\partial t}-\frac{2}{R}\frac{\partial^2\phi}{\partial r^2}+\frac{2m}{R}\frac{\partial^2\phi_a}{\partial r^2}=-W\left(\frac{\partial^2\eta}{\partial z^2}+4\eta\right). \tag{16.2.12}$$

Thus, we may have the solutions of the form

$$\eta=AE+c.c.,\quad \phi=A_1I_0(kr)E+c.c.,\quad \phi_a=A_2K_0(kr)E+c.c., \tag{16.2.13}$$

where A, A_1 and A_2 are the complex amplitudes, $E\equiv\exp(\mathrm{i}kz-\mathrm{i}\omega t)$, $\omega\equiv\omega_R+\mathrm{i}\omega_I$ denotes the complex angular frequency, $k\equiv k_R+\mathrm{i}k_I$ the complex wavenumber, $\mathrm{i}=\sqrt{-1}$ and *c.c.* stands for the complex conjugate of the preceding expression; $I_0(kr)$ and $K_0(kr)$ denote the zeroth order of modified Bessel functions of the first and second kind. Then ϕ gives the finite velocity at $r=0$ and ϕ_a gives the velocity which vanishes as $r\to\infty$.

Substitution of (16.2.13) into (16.2.11) and (16.2.12) gives the dispersion relation,

$$D(k,\omega)=(\omega-k)^2\alpha+\ell\omega^2\alpha_a+\mathrm{i}\frac{2k^2}{R}(\omega-k)b+\mathrm{i}\frac{2mk^2}{R}\omega b_a-W\left(k^3-4k\right)=0$$

which is a quadratic equation in ω

$$c_2\omega^2+2c_1\omega+c_0=0 \tag{16.2.14}$$

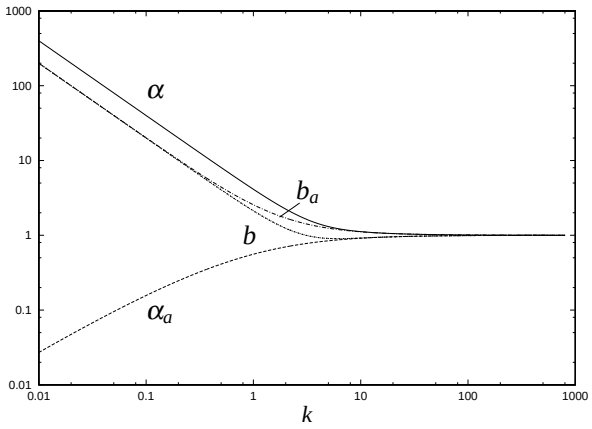

Fig. 16.10. Functions α, b_a, b and α_a versus real k; these functions tend to one for $k > 10$. The neutral curves of inviscid and viscous potential flow for $\ell = m$ are identical when $k > 10$; this will be seen in (16.2.33). The functions for $k > 10$ will lead to the asymptotic forms (16.2.23), (16.2.24) and (16.2.39)-(16.2.46).

with the coefficients $c_2 \equiv c_2(k)$, $c_1 \equiv c_1(k)$ and $c_0 \equiv c_0(k)$:

$$\left.\begin{aligned} c_2 = \alpha + \ell\alpha_a, \quad c_1 = -k\alpha + \mathrm{i}\frac{k^2}{R}\,(b + mb_a) = c_{1R} + \mathrm{i}c_{1I}, \\ c_0 = k^2\alpha - \mathrm{i}\frac{2k^3}{R}b - W\left(k^3 - 4k\right) = c_{0R} + \mathrm{i}c_{0I}, \end{aligned}\right\} \tag{16.2.15}$$

where α, α_a, b and b_a are defined as

$$\alpha = \frac{I_0(k/2)}{I_1(k/2)}, \quad \alpha_a = \frac{K_0(k/2)}{K_1(k/2)}, \quad b = \alpha - \frac{2}{k}, \quad b_a = \alpha_a + \frac{2}{k}. \tag{16.2.16}$$

It is noted for real k that $k\alpha \to 4$ and $\alpha_a \to 0$ as $k \to 0$, while $\alpha \to 1$ and $\alpha_a \to 1$ as $k \to \infty$; this will be shown in figure 16.10. Apart from the Bessel functions, (16.2.14) is a cubic equation in k; numerical calculations show that for each and every fixed set of parameters studied here, (16.2.14) gives rise to three complex roots.

16.2.4 Temporal instability

For this case k is real and $\omega = \omega_R + \mathrm{i}\omega_I$. Recalling that $W = \gamma/(\rho 2aU^2)$, we obtain pure KH instability with $W = 0$, and pure capillary instability with $W \to \infty$. A temporal growth rate curve is depicted as in figure 16.11, by which the maximum growth rate ω_{Im}, the associated wavenumber k_m and the cut-off wavenumber k_c are defined.

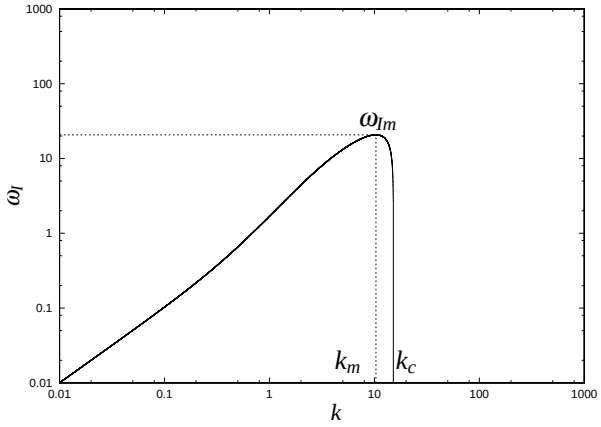

Fig. 16.11. Example of a growth rate curve defined in section 16.2.4, showing the main features: the shape, maximum ω_{Im}, k_m and the cut-off wavenumber k_c.

When the fluids are both inviscid as $R \to \infty$, (16.2.14)-(16.3.83) reduce to

$$(\alpha + \ell\alpha_a)\,\omega^2 - 2k\alpha\omega + k^2\alpha - W\left(k^3 - 4k\right) = 0. \tag{16.2.17}$$

The complex angular frequency $\omega = \omega_R + \mathrm{i}\omega_I$ is given by

$$\omega_R = \frac{k\alpha}{\alpha + \ell\alpha_a}, \qquad \omega_I = \pm\sqrt{\frac{k^2\ell\alpha\alpha_a}{(\alpha + \ell\alpha_a)^2} - \frac{W\left(k^3 - 4k\right)}{\alpha + \ell\alpha_a}} \tag{16.2.18}$$

in the unstable case, and

$$\omega_R = \frac{k\alpha}{\alpha + \ell\alpha_a} \pm \sqrt{-\frac{k^2\ell\alpha\alpha_a}{(\alpha + \ell\alpha_a)^2} + \frac{W\left(k^3 - 4k\right)}{\alpha + \ell\alpha_a}}, \qquad \omega_I = 0, \tag{16.2.19}$$

in the stable case. The neutral state is defined by $\omega_I = 0$; either $k = 0$ or $W = W_c$ where

$$W_c^{-1} = \left[\frac{\alpha + \ell\alpha_a}{\ell\alpha\alpha_a}\left(k - \frac{4}{k}\right)\right]_{k=k_c}. \tag{16.2.20}$$

Instability may arise in $0 < k < k_c$, where the cut-off wavenumber k_c ($k_c \geq 2$ for which $W_c^{-1} \geq 0$) is evaluated by (16.2.20) for given values of ℓ and W_c. For k large for which α and α_a approach 1 (see figure 16.10), (16.2.20) is approximated as $W_c^{-1} = \left(\ell^{-1} + 1\right)k_c$.

The effects of surface tension, leading to capillary instability are absent when $W = 0$; hence $W = 0$ is pure KH instability. Inspection of (16.2.18) shows that KH instability cannot occur when $\ell = 0$; the viscosity and density of the ambient vanish so the KH instability cannot occur in vacuum (no pressure can be generated in vacuum). Pure KH instability is Hadamard unstable† with growth rate proportional to k; the short waves grow exponentially with k at fixed t. The regularizing effect of surface tension is to stabilize short waves with $k > k_c$ given by (16.2.20). The maximum growth rate

$$\omega_{Im} = \overset{\max}{k}\ \omega_I(k) = \omega_I(k_m) \tag{16.2.21}$$

may be obtained from (16.2.18) at an interior maximum for which

$$\partial\omega_I/\partial k = 0. \tag{16.2.22}$$

This computation is slightly complicated by that $\alpha(k)$ and $\alpha_a(k)$ depend on k weakly. The values ω_{Im} and k_m depend on W and are plotted in figure 4.2. For large k, $\alpha(k) = \alpha_a(k) = 1$, and we find that

$$\omega_{Im} = \frac{2\ell\sqrt{\ell}}{3\sqrt{3}\,(1+\ell)^2\,W} \tag{16.2.23}$$

and

$$k_m = \frac{2\ell}{3\,(1+\ell)\,W}. \tag{16.2.24}$$

Equations (16.2.23) and (16.2.24) show that the maximum growth rate and the associated wavenumber tend to infinity for small W like $1/W$; the wavelength $\lambda_m = 2\pi/k_m$ tends to zero with W. Viscosity regularizes the growth rate but the wave length tends to zero with W as in the inviscid case (see figure 16.13).

For pure capillary instability with $W \to \infty$, the neutral boundaries are given by $k = 0$ and $k_c = 2$. In this limiting case, we may rescale as $\omega = \hat{\omega}\sqrt{W}$, by which (16.2.17) is expressed as

$$(\alpha + \ell\alpha_a)\,\omega^2 - W\left(k^3 - 4k\right) = 0 \quad \to \quad (\alpha + \ell\alpha_a)\,\hat{\omega}^2 - \left(k^3 - 4k\right) = 0, \tag{16.2.25}$$

† Hadamard instability is defined differently by different authors. For stability studies the growth rates $\sigma(k)$ goes to infinity with k, the growth rates are not bounded for short waves. Say, for example $\sigma = k$; the disturbance amplitude is proportional to $\exp(kt)$. This is a very bad instability; the amplitude tends to infinity with k for any fixed t no matter how small k; the more you refine the mesh the worse is the result; they are very unstable to short waves. See Joseph (1990) and Joseph & Saut (1990).

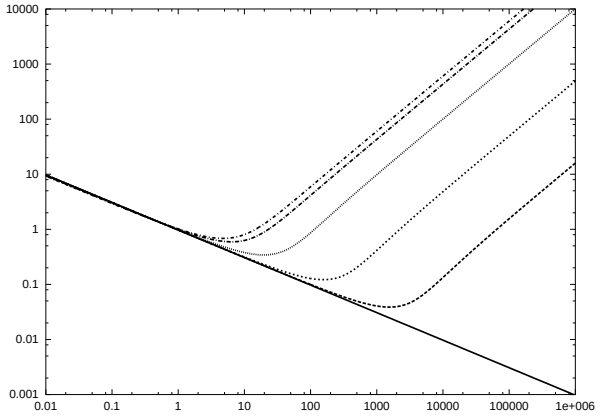

(a)

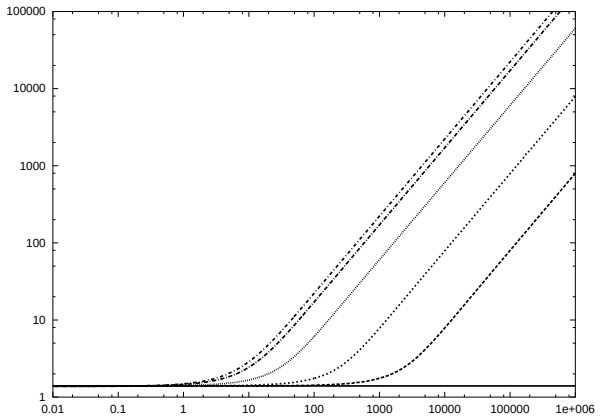

(b)

Fig. 16.12. (a) ω_{Im} versus W^{-1} and (b) k_m versus W^{-1}, for $\ell = 0$ (solid line), 0.0012 (broken line), 0.012 (dashed line), 0.1 (dotted line), 0.3455 (broken dotted line), 0.5 (dash dotted line). For large W^{-1} and $\ell \neq 0$, the curves approach the asymptotic form given respectively by (16.2.23) and (16.2.24).

so that the solution $\hat{\omega}$ is given by

$$\hat{\omega} = \hat{\omega}_R + \mathrm{i}\hat{\omega}_I = \pm\sqrt{\frac{k^3 - 4k}{\alpha + \ell\alpha_a}}; \tag{16.2.26}$$

hence instability ($\hat{\omega} = \mathrm{i}\hat{\omega}_I$) may arise in $0 < k < 2$. Disturbances with $k > 2$ are stable and have an angular frequency $\hat{\omega} = \hat{\omega}_R$. The single column with $\ell = 0$ is the case that Lord Rayleigh analyzed in 1878.

16.2.4.2 Viscous fluids

For $\omega = \omega_R + \mathrm{i}\omega_I$, the quadratic equation (16.2.14) is separated into the real and imaginary parts

$$c_2\left(\omega_R^2 - \omega_I^2\right) + 2\left(c_{1R}\omega_R - c_{1I}\omega_I\right) + c_{0R} = 0, \tag{16.2.27}$$

$$2c_2\omega_R\omega_I + 2\left(c_{1R}\omega_I + c_{1I}\omega_R\right) + c_{0I} = 0 \quad \rightarrow \quad \omega_R = -\frac{2c_{1R}\omega_I + c_{0I}}{2c_2\omega_I + 2c_{1I}}, \tag{16.2.28}$$

to give the quartic equation in ω_I alone:

$$a_4\omega_I^4 + a_3\omega_I^3 + a_2\omega_I^2 + a_1\omega_I + a_0 = 0, \tag{16.2.29}$$

with

$$\left.\begin{aligned} a_4 = c_2^3, \quad a_3 = 4c_2^2c_{1I}, \quad a_2 = c_2c_{1R}^2 + 5c_2c_{1I}^2 - c_2^2c_{0R}, \\ a_1 = 2c_{1R}^2c_{1I} + 2c_{1I}^3 - 2c_2c_{1I}c_{0R}, \quad a_0 = c_{1R}c_{1I}c_{0I} - c_{1I}^2c_{0R} - \frac{1}{4}c_2c_{0I}^2. \end{aligned}\right\} \tag{16.2.30}$$

Neutral curves Neutral curves, $\omega_I = 0$ in (16.2.29), are generated by the condition $a_0 = 0$:

$$a_0 = -\frac{k^6}{R^2}\left(m^2\alpha b_a^2 + \ell b^2\alpha_a\right) + \frac{k^4}{R^2}\left(b + mb_a\right)^2 W\left(k^3 - 4k\right) = 0. \tag{16.2.31}$$

One root of (16.2.31) is $k = 0$ and it is the only root when $W = 0$ (Kelvin-Helmholtz instability). The other roots are given by

$$W^{-1} = \frac{\left(b + mb_a\right)^2}{m^2\alpha b_a^2 + \ell b^2\alpha_a}\left(k - \frac{4}{k}\right), \tag{16.2.32}$$

which has the general form shown in figure 16.13. Equations (16.2.29) and (16.2.31) show that when $\ell = 0$, $m = 0$, the only instability is due to capillarity. KH instability is not possible in vacuum. An identical conclusion for KH instability of stratified gas-liquid flow in a horizontal rectangular channel follows from equation (3.4) in the paper by Funada & Joseph (2001). For large values of k, b, b_a, α and α_a tend to 1 and (16.2.32) reduces to

$$W^{-1} = \frac{\left(1 + m\right)^2}{m^2 + \ell}k. \tag{16.2.33}$$

When $\ell = m$ ($\nu = \nu_a$), this reduces to $(\ell + 1)\,k/\ell$ which is the same as the inviscid case given by (16.2.20).

A striking conclusion which follows from (16.2.31) and (16.2.32) is that the cut-off wavenumber $k = k_c$ satisfying (16.2.32) is independent of the Reynolds number R; when $k > k_c$, the liquid jet is stable.

A further comparison, (16.2.32) and (16.2.20), of inviscid and viscous potential flow shows that the neutral curves are identical under the condition that $m\alpha b_a = \ell b\alpha_a$. Figure 16.10 shows that $\alpha b_a = b\alpha_a$ for $k > 10$; in this case the neutral curves are identical when $\ell = m$ (or $\nu = \nu_a$). It is of interest that for jets of liquid into air $\ell \ll 1$ and $m \ll 1$. In this limit both (16.2.32) and (16.2.20) reduce to

$$W^{-1} = \frac{1}{\ell\alpha_a}\left(k - \frac{4}{k}\right). \tag{16.2.34}$$

This surprising and anti-intuitive result says that the neutral condition for a highly viscous liquid $m \to 0$ is the same as for two inviscid fluids provided that $\ell \ll 1$.

The ratio (16.2.32)/(16.2.20) may be written as

$$\frac{W_{VPF}^{-1}}{W_{IPF}^{-1}} = \frac{\left(b + mb_a\right)^2 \ell\alpha\alpha_a}{\left(m^2\alpha b_a^2 + \ell b^2\alpha_a\right)\left(\alpha + \ell\alpha_a\right)} \tag{16.2.35}$$

where VPF and IPF stand for viscous and inviscid potential flow. For large $k > 10$, this reduces to

$$\frac{W_{VPF}^{-1}}{W_{IPF}^{-1}} = \frac{\left(1 + m\right)^2 \ell}{\left(m^2 + \ell\right)\left(1 + \ell\right)}. \tag{16.2.36}$$

For $m = 0$ (the viscosity of the jet is much larger than the ambient)

$$\frac{W_{VPF}^{-1}}{W_{IPF}^{-1}} = \frac{1}{1 + \ell} \leq 1. \tag{16.2.37}$$

For $m \to \infty$ (the viscosity of the jet is much smaller than the ambient)

$$\frac{W_{VPF}^{-1}}{W_{IPF}^{-1}} = \frac{\ell}{1 + \ell} \leq 1. \tag{16.2.38}$$

In general, the neutral curve for viscous potential flow is below (or at least not above) that of inviscid potential flow.

For all values of ℓ, R and W, there are wave numbers for which $\omega_I > 0$; the liquid jet is always unstable to temporal disturbances in analysis based on viscous potential flow.

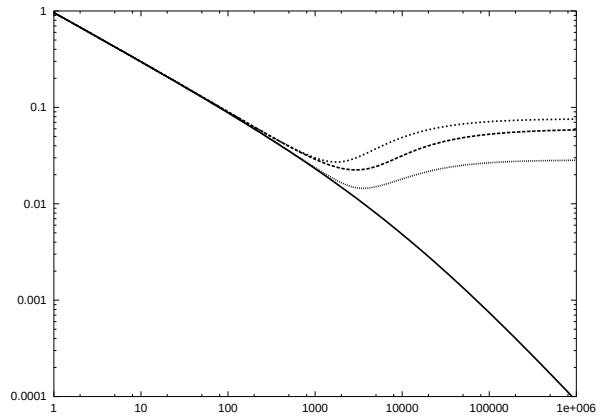

(a)

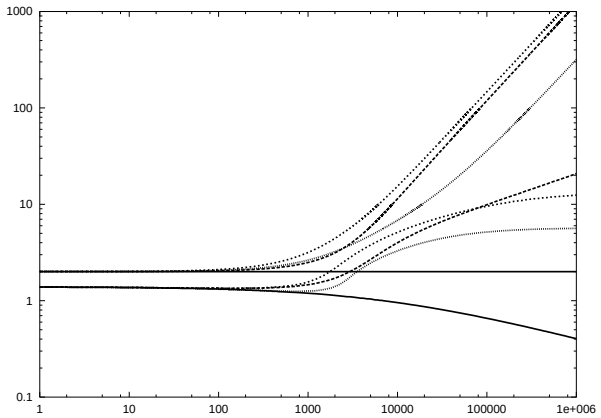

(b)

Fig. 16.13. (a) ω_{Im} versus W^{-1} ($= \rho 2aU^2/\gamma$) and (b) k_c (the upper curves) and k_m (the lower curves) versus W^{-1} for $R = 100$; the solid curve is for $\ell = 0$ and $m = 0$, the broken line for $\ell = 0.0012$ and $m = 0$, the dashed line for $\ell = 0.0012$ and $m = 0.018$, the dotted line for $\ell = 0$ and $m = 0.018$. Kelvin-Helmholtz (KH) instability for the liquid jet corresponds to $\gamma \to 0$ or $W^{-1} \to \infty$. The neutral curve is independent of the Reynolds number R. If surface tension and gravity are zero, KH flows are unstable for all k (see equation (2.27) in Funada & Joseph 2001). When $U \to 0$, we get capillary instability which is unstable to all waves with $0 < k < 2$. The interval of unstable wave $0 < k < k_c$ increases as the Weber number decreases (larger U, smaller γ). In general, the neutral curve for viscous potential flow lies above that for inviscid potential flow with equality for a given k when $m\alpha b_a = \ell b \alpha_a$ and for large $k > 10$, when $\ell = m$ ($\nu = \nu_a$) (see eqs(16.2.36)–(16.2.38)). The values $k_m(W^{-1})$ for which the growth is maximum depends on R. The maximum growth rates ω_{Im} are finite for $W \to 0$ but the associated wavenumbers are proportional to $1/W$ for small W.

Growth rate curves An example of a growth rate curve is shown as figure 16.11. All of the growth rate curves have this same form and may be characterized by three parameters: the maximum growth rate ω_{Im} and wavenumber k_m, $\omega_{Im} = \omega_I(k_m)$ and the cut-off wavenumber k_c, as shown in figure 16.11. ω_{Im} and k_m depend on R, but k_c is independent of R.

The variation of ω_{Im} and k_m with W^{-1} is shown in figure 4.3. The effect of viscosity is to regularize the Hadamard instability, ω_{Im} tends to a finite value as $W \to \infty$ (cf, figures 4.3 and 4.4). For large values of W^{-1}, KH instability dominates. The great difference between stability in vacuum $(\ell, m) = (0, 0)$ and inviscid gas $m = 0$, $\ell \neq 0$ is apparent for large values of W^{-1}.

For large k (> 10) for which $\alpha = \alpha_a = b = b_a = 1$, the imaginary part of the dispersion relation (16.2.28) gives ω_R:

$$\omega_R = \frac{k\omega_I + \dfrac{k^3}{R}}{(1+\ell)\,\omega_I + \dfrac{k^2}{R}\,(1+m)} = \frac{k}{(1+\ell)\,X}\left[X + \frac{k^2}{R}\,(\ell - m)\right], \tag{16.2.39}$$

where X is defined as

$$X = (1+\ell)\,\omega_I + \frac{k^2}{R}\,(1+m)\,. \tag{16.2.40}$$

The real part of the dispersion relation (16.2.27) leads to the quadratic equation of X^2:

$$\frac{k^2}{X^2}\frac{k^4}{R^2}\,(\ell-m)^2 - X^2 + 2Y = 0, \tag{16.2.41}$$

with

$$Y = \frac{1}{2}\left[\frac{k^4}{R^2}\,(1+m)^2 + \ell k^2 - (1+\ell)\,W\left(k^3 - 4k\right)\right], \tag{16.2.42}$$

whence the solution to (16.2.41) is expressed as

$$X = (1+\ell)\,\omega_I + \frac{k^2}{R}\,(1+m) = \left[Y + \sqrt{Y^2 + \frac{k^6}{R^2}\,(\ell-m)^2}\right]^{1/2}, \tag{16.2.43}$$

When $\ell = m$, the solution (16.2.43) reduces to

$$X = (1+\ell)\,\omega_I + \frac{k^2}{R}\,(1+m) = \sqrt{2Y}. \tag{16.2.44}$$

When $R \to \infty$, the solution (16.2.43) reduces to the inviscid case:

$$X = (1+\ell)\,\omega_I = \left[\ell k^2 - (1+\ell)\,W\left(k^3 - 4k\right)\right]^{1/2}. \tag{16.2.45}$$

The solution (16.2.43) is available to have the maximum growth rate and the cut-off wavenumber when those exist in large k under the condition that $\ell \neq 0$ or $m \neq 0$, for which W^{-1} is large.

The extremum value of ω_I is given by differentiating (16.2.43) and imposing $\partial\omega_I/\partial k = 0$ at $k = k_m$:

$$\omega_{Im} = -\frac{k_m^2}{R}\frac{(1+m)}{(1+\ell)} + \frac{R/\,(1+m)}{4k_m\,(1+\ell)}\left\{\frac{\partial Y}{\partial k} + \left[Y\frac{\partial Y}{\partial k} + \frac{3k^5}{R^2}\,(\ell-m)^2\right]\left[Y^2 + \frac{k^6}{R^2}\,(\ell-m)^2\right]^{-1/2}\right\}_{k=k_m} \tag{16.2.46}$$

The expression for k_m is rather cumbersome; it shows that $k_m \propto 1/W$ for small W even though $\omega_I(k_m)$ is bounded as $W \to 0$ (figures 4.3 and 4.4). It follows that the wave length $\lambda_m = 2\pi/k_m$ tends to zero with W. If this KH disturbance leads to breakup, we would find small liquid fragments even to fine mist.

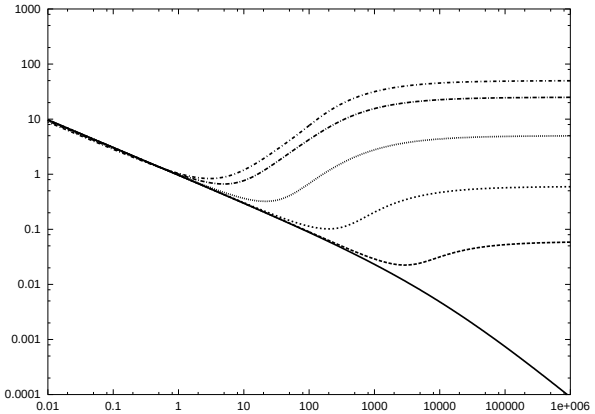

(a)

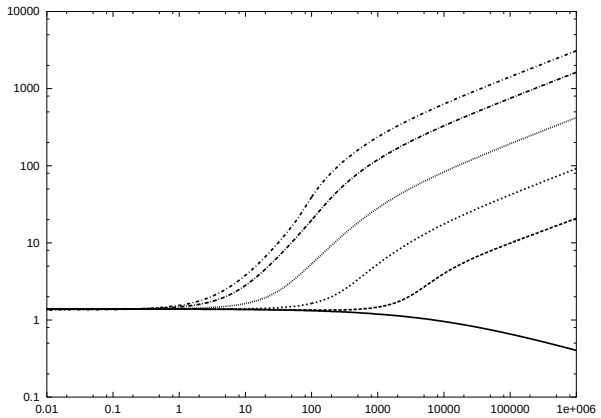

(b)

Fig. 16.14. (a) ω_{Im} versus W^{-1} and (b) k_m versus W^{-1} for $R = 100$, $m = 0$ and various ℓ; $\ell = 0$ (solid line), 0.0012 (broken line), 0.012 (dashed line), 0.1 (dotted line), 0.5 (broken dotted line), 1 (dash dotted line). For large W^{-1} and $\ell \neq 0$, the curves approach the asymptotic form given by (16.2.46).

16.2.4.3 Nonaxisymmetric disturbances

The authors of papers on spatial, temporal and C/A theory cited at the end of section 16.2.1 restrict their attention to axisymmetric disturbances. Yang (1992) studied the stability of an inviscid liquid jet to axisymmetric and non-axisymmetric temporal disturbances. He found wavenumber ranges for which the nonaxisymmetric disturbances grow faster, but the greatest peak values of $\omega_I(k_m)$ are for axisymmetric disturbances. A preliminary study of axisymmetric disturbances proportional to $\exp(\imath n\theta)$ with $n = 0$ and asymmetric disturbances with $n > 0$, especially with $n = 1$ yielded results similar to those found by Yang (1992) for the inviscid jet. The peak growth rates are always attained for $n = 0$ in flows with capillary numbers W larger than small value, say 1/10; for KH instability $W \to \infty$, the peak values for $n = 0$ and $n = 1$ are nearly identical (see figure 16.15).

Li & Kelly (1992) did an analysis of an inviscid liquid jet in a compressible high speed airstream. They found that $n = 1$ is the most dangerous mode when the Mach number is near to one. The case of nonaxisymmetric disturbances needs further study.

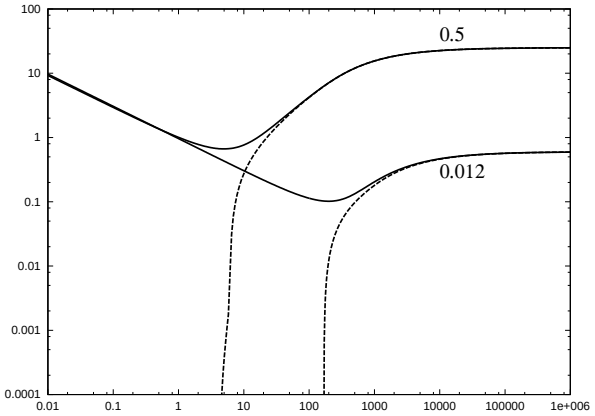

(a)

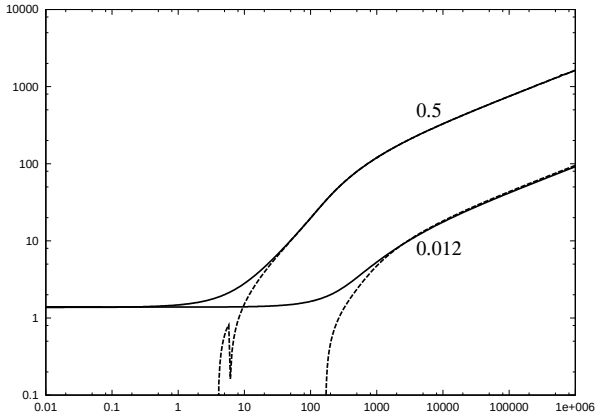

(b)

Fig. 16.15. (a) ω_{Im} versus W^{-1} and (b) k_m versus W^{-1} for $R = 100$, and $m = 0$; $\ell = 0.012$ and $n = 0$ (solid line), $\ell = 0.012$ and $n = 1$ (broken line), $\ell = 0.5$ and $n = 0$ (solid line), $\ell = 0.5$ and $n = 1$ (broken line).

16.2.5 Numerical results of temporal instability

Here we present neutral curves and growth rates for the stability of viscous liquids into air comparing viscous potential flow (VPF) with inviscid potential flow (IPF).

Using the data of Funada & Joseph (2002), various liquid-gas cases are shown in Table 16.5. The parameters of the growth rate curves for the 10 cases are defined in figure 16.11 and given in Table 16.6 for typical values of U. The neutral curves $W^{-1}(k)$ for all 10 cases start at $k = 2$. For large k (> 10), they may be computed exactly from (16.2.33) and compared with inviscid potential flow using (16.2.36). The differences between viscous and inviscid potential flow vanish for $k > 10$ when $m\alpha b_a = \ell b\alpha_a$ and for all k when $\rho_a \ll \rho$, $\mu_a \ll \mu$ when μ is very large, as shown previously.

Table 16.5. *Data of various liquid-gas cases.*

No.	liquid cylinder-gas	$\ell = \rho_a/\rho$	$m = \mu_a/\mu$	$m/\ell = \nu_a/\nu$	$\sqrt{\gamma/(\rho 2a)}$ m/sec
1	mercury-air	8.889E-05	1.154E-02	1.298E+02	5.976E-02
2	water-air	1.200E-03	1.800E-02	1.500E+01	8.532E-02
3	benzene-air	1.395E-03	2.769E-02	1.985E+01	5.793E-02
4	SO100-air	1.238E-03	1.800E-04	1.454E-01	4.655E-02
5	glycerine-air	9.547E-04	2.302E-05	2.411E-02	7.102E-02
6	oil-air	1.478E-03	3.830E-05	2.592E-02	5.984E-02
7	SO10000-air	1.238E-03	1.800E-06	1.454E-03	4.655E-02
8	SO10-air	1.238E-03	1.800E-03	1.454E+00	4.655E-02
9	silicon oil-nitrogen	1.345E-03	8.750E-04	6.508E-01	4.697E-02
10	silicon oil-nitrogen	1.326E-03	1.750E-03	1.319E+00	4.620E-02

Table 16.6. *Parameters of the growth rate curves identified in figure 16.11 for the 10 cases of liquid-gas flow in Table 16.5. Viscous (VPF) and (IPF) are compared.*

No	U m/sec	W	W^{-1}	R	ω_{Im}^{VPF}	k_m^{VPF}	k_c^{VPF}	ω_{Im}^{IPF}	k_m^{IPF}	k_c^{IPF}
	0.02	8.928	0.112	0.17308E+04	0.9709	1.394	2.000	0.9711	1.394	2.000
1	0.06	0.992	1.008	0.51923E+04	0.9709	1.394	2.000	0.9711	1.394	2.000
	0.10	0.357	2.800	0.86538E+04	0.9709	1.394	2.000	0.9712	1.394	2.000
	0.02	18.200	0.055	0.20000E+03	0.9698	1.393	2.000	0.9710	1.394	2.000
2	0.06	2.022	0.495	0.60000E+03	0.9699	1.393	2.000	0.9711	1.394	2.000
	0.10	0.728	1.374	0.10000E+04	0.9701	1.394	2.000	0.9713	1.394	2.000
	0.02	8.390	0.119	0.26462E+03	0.9696	1.393	2.000	0.9710	1.394	2.000
3	0.06	0.932	1.073	0.79385E+03	0.9699	1.394	2.000	0.9713	1.394	2.000
	0.10	0.336	2.980	0.13231E+04	0.9704	1.394	2.001	0.9718	1.395	2.001
	0.02	5.418	0.185	0.19380E+01	0.7890	1.244	2.000	0.9710	1.394	2.000
4	0.06	0.602	1.661	0.58140E+01	0.7893	1.244	2.000	0.9714	1.395	2.000
	0.10	0.217	4.614	0.96900E+01	0.7898	1.245	2.001	0.9722	1.396	2.001
	0.02	12.609	0.079	0.32148E+00	0.5138	0.988	2.000	0.9710	1.394	2.000
5	0.06	1.401	0.714	0.96445E+00	0.5139	0.988	2.000	0.9712	1.394	2.000
	0.10	0.504	1.983	0.16074E+01	0.5140	0.988	2.000	0.9714	1.395	2.000
	0.02	8.951	0.112	0.36431E+00	0.5028	0.977	2.000	0.9710	1.395	2.000
6	0.06	0.995	1.005	0.10929E+01	0.5029	0.977	2.000	0.9713	1.395	2.000
	0.10	0.358	2.793	0.18215E+01	0.5031	0.977	2.001	0.9718	1.396	2.001
	0.02	5.418	0.185	0.19380E-01	0.0430	0.278	2.000	0.9710	1.394	2.000
7	0.06	0.602	1.661	0.58140E-01	0.0430	0.279	2.000	0.9714	1.395	2.000
	0.10	0.217	4.614	0.96900E-01	0.0430	0.278	2.002	0.9722	1.396	2.001
	0.02	5.418	0.185	0.19380E+02	0.9488	1.376	2.000	0.9710	1.394	2.000
8	0.06	0.602	1.661	0.58140E+02	0.9492	1.377	2.000	0.9714	1.395	2.000
	0.10	0.217	4.614	0.96900E+02	0.9499	1.378	2.002	0.9722	1.396	2.001
	0.02	5.515	0.181	0.95200E+01	0.9273	1.359	2.000	0.9710	1.394	2.000
9	0.06	0.613	1.632	0.28560E+02	0.9277	1.359	2.000	0.9714	1.395	2.000
	0.10	0.221	4.533	0.47600E+02	0.9284	1.361	2.002	0.9722	1.396	2.002
	0.02	5.337	0.187	0.19300E+02	0.9485	1.376	2.000	0.9710	1.394	2.000
10	0.06	0.593	1.686	0.57900E+02	0.9489	1.377	2.000	0.9714	1.395	2.000
	0.10	0.213	4.684	0.96500E+02	0.9497	1.378	2.002	0.9723	1.396	2.002

16.2.6 Spatial, absolute and convective instability

The motivation for considering spatial instability of a liquid jet was very clearly expressed by Keller, Rubinow & Tu (1973) who noted that the disturbance initiating from the nozzle tip actually grows in space as it is swept downstream, where it is observed to break into drops, leaving a section of jet intact near the nozzle tip as would occur for a disturbance that is convectively unstable. Such disturbances proportional to $\exp(\mathrm{i}kz - \mathrm{i}\omega t)$ can be described by allowing k to be complex and ω real so that disturbances can grow in space but not in time. They found that Rayleigh's results are relevant only when the Weber number $W = \gamma/(\rho 2aU^2)$ is small and the spatial growth rate k_I is related to the temporal growth rate ω_I by the relation $k_I = \pm\omega_I + O(W)$, while the disturbance travels at the jet velocity. For large values of W, they found a new mode of faster growing disturbances whose wavelengths are perhaps too long to be observable.

Leib & Goldstein (1986b) showed that the new mode corresponds to an absolute instability which arises from a pinch point singularity in the dispersion relation. An absolutely unstable wave packet propagates upstream and downstream and hence such disturbances spread over the whole z domain of flow; the flow is unstable at any z, as t increases. This is not the picture advanced by Keller, Rubinow & Tu (1973) in which the region close to the discharge is never corrupted by growing disturbances.

One of the aims of the theory of absolute and convective instability is to provide a frame for the problem of spatial development of disturbances. The spatial development of controlled disturbances such as are generated by a vibrating ribbon at the start of a growing boundary layer or at the inlet of a plane Poiseuille flow calculated from spatial theory yielded good results with experiments in which disturbances were suppressed. However the spatial theory has no rigorous foundation; for example, a spatial mode, when it can be defined, is inadmissible when it is unbounded at infinity, though it may describe the spatial evolution of disturbances of a given frequency for a long time (see Drazin and Reid 1981, section 32 for experiments; section 47.1 for theoretical problems).

To deal with the problem of propagation of impulses, the concept of convective and absolutely unstable solutions (C/A for short) has been introduced. The definitions of instability in the C/A context is formulated in terms of the evolution of impulses at the origin in the (x, t) plane proportional initially to the product $\delta(x)\delta(t)$. A flow is called *linearly stable* if this disturbance decays to zero along all rays $x/t = \text{const}$. It is *linearly unstable* if the impulse tends to infinity along at least one ray $x/t = \text{const}$. An unstable flow is linearly *convectively unstable* if the impulse tends to zero along the ray $x/t = 0$ and is *absolutely unstable* if the impulse tends to infinity along the ray $x/t = 0$. Obviously an absolutely unstable impulse is linearly unstable.

A cartoon for wave packets propagating from the origin in these four cases is shown in figure 16.16.

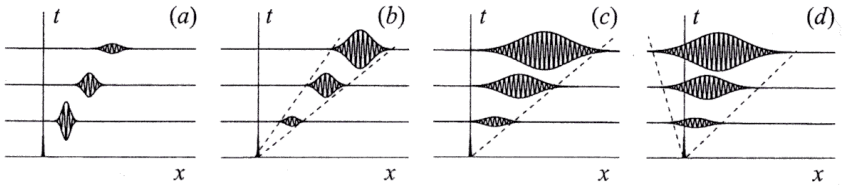

Fig. 16.16. Linear impulse response. (a) Linearly stable flow; (b) linearly convectively unstable flow; (c) marginally convectively/absolutely unstable flow; (d) absolutely unstable flow (after Huerre 2000, figure 8). The pictures here are for a response to a linear impulses; stability cannot be determined from the evolution of impulses alone. Convectively unstable flows in (b) are also temporally unstable; at any x, real wavenumbers exist for which disturbances outside the unstable wedge in (b) will grow.

The C/A concepts are not straightforward and need explanation. Huerre (2000) notes that

"A parallel shear flow of given velocity profile is said to be *convectively unstable* if the growing wavepacket produced in response to an impulsive source localized in space and time is advected away. It is *absolutely unstable* if the growing wavepacket expands around the source to contaminate the entire medium. In the case of parallel flows that are invariant under Galilean transformations, this distinction appears at first sight to be preposterous: a simple change of reference frame transforms a flow from convectively unstable to absolutely unstable and vice versa, and the 'laboratory frame'

is not properly defined. However, when Galilean invariance is broken, e.g. in spatially developing flows, in flows with a definite origin, or in flows forced at a specific streamwise station, the laboratory frame is singled out and it is precisely in these instances that the distinction between convective and absolute instability becomes of interest. It should be emphasized that, in order for these concepts to be relevant, one must enforce a *scale-separation* assumption: the flow under consideration must be slowly evolving along the stream over a typical instability wavelength. This strong hypothesis is made throughout the ensuing theoretical developments in order to recover the locally parallel flow instability properties as a leading-order approximation at each streamwise station."

Parallel flows which are temporally stable are also stable in the C/A theory. Temporally unstable flows can be absolutely or convectively unstable. Disturbances from a source, like a vibrating ribbon, can propagate without corrupting the source, only if the flow is convectively unstable and only if random disturbances at fixed points which are temporally unstable are suppressed.

In this paper we follow others in considering the open basic flow which has no spatial variation in the axial direction which is Galilean invariant. The point of novelty of our analyses is that the stability analysis is carried out using the equations of viscous potential flow which allow a discontinuous velocity at the jet surface but accommodates effects of viscosity, viscosity ratios, density ratios, etc. but still leads to an explicit dispersion relation.

Huerre & Monkewitz (1985) point out that the spatial stability theory is applicable when the flow is convectively unstable and not when the flow is absolutely unstable. They describe a methodology based on Bers (1975) criterion, to determine when a free shear layer is convectively unstable. Their problem is difficult and does not give rise to an explicit dispersion; numerical computations are required. The search for the border between absolute and convective instability is a function of prescribed parameters and requires knowledge of the dispersion relation for complex frequencies and wavenumbers. This search is greatly simplified in the case of the stability of the liquid jet based on viscous potential flow because the search for singularities of the dispersion relation is reduced to the study of algebraic equations of two complex variables.

We use the criterion of Bers (1975) which says that an unstable flow is convectively unstable if the modes proportional to $\exp(\mathrm{i}kz - \mathrm{i}\omega t)$ of complex frequency ω and k, which have a zero group velocity

$$G_V = \partial\omega_R/\partial k_R = 0, \tag{16.2.47}$$

are all temporally damped, $\omega_I < 0$. Otherwise the system is absolutely unstable. If ω_R does not change with k_R and $\omega_I < 0$, then a disturbance with excitation frequency ω_R will decay in time but can grow in space. On the other hand, we do not use the method of Briggs (1964) and Bers (1975). Instead, we implement an algebraic study of the dispersion relation.

Following Schmid & Henningson (2001), we may characterize the singularities of $D(k,\omega)$ at k_0, ω_0 by the equation

$$D(k_0,\omega_0) = 0, \quad \frac{\partial D}{\partial k}(k_0,\omega_0) = 0, \quad \frac{\partial^2 D}{\partial k^2}(k_0,\omega_0) \neq 0. \tag{16.2.48}$$

In the neighborhood of k_0, ω_0 a Taylor series expansion of $D(k,\omega)$ leads to

$$0 = \left.\frac{\partial D}{\partial \omega}\right|_0 (\omega - \omega_0) + \frac{1}{2}\left.\frac{\partial^2 D}{\partial k^2}\right|_0 (k - k_0)^2 + HO \tag{16.2.49}$$

where HO are terms that go to zero faster than the terms retained. This results in a square root singularity for the local map between the k and ω planes.

If we imagine $D(k,\omega) = 0$ to be solved for $\omega = \omega(k)$, then $D(k,\omega(k)) = 0$ is an identity in k and

$$0 = \frac{\mathrm{d}D}{\mathrm{d}k} = \frac{\partial D}{\partial k} + \frac{\partial \omega}{\partial k}\frac{\partial D}{\partial \omega} \tag{16.2.50}$$

and

$$\hat{c} \equiv \frac{\partial \omega}{\partial k} = -\frac{\partial D}{\partial k}\Big/\frac{\partial D}{\partial \omega} = \hat{c}_R + \mathrm{i}\hat{c}_I \tag{16.2.51}$$

can be said to be a complex-valued "generalized" group velocity which must be zero at the singularity. This is not the ordinary group velocity. If $\partial D/\partial\omega \neq 0$, and it is not equal to zero in this study, then

$$\hat{c} = \frac{\partial\omega}{\partial k} = 0 \quad \text{when } \frac{\partial D}{\partial k} = 0. \tag{16.2.52}$$

Moreover,

$$\frac{\partial\omega}{\partial k} = \frac{1}{2}\left(\frac{\partial\omega_R}{\partial k_R} + \frac{\partial\omega_I}{\partial k_I}\right) + \frac{\mathrm{i}}{2}\left(\frac{\partial\omega_I}{\partial k_R} - \frac{\partial\omega_R}{\partial k_I}\right) \tag{16.2.53}$$

and $\hat{c} = 0$ does not imply that the group velocity $G_V = \partial\omega_R/\partial k_R = 0$. However, since the Cauchy-Riemann condition for a function $\omega(k)$ holds, then $\partial\omega/\partial\bar{k} = 0$ and

$$\frac{\partial\omega_R}{\partial k_R} = \frac{\partial\omega_I}{\partial k_I}, \qquad \frac{\partial\omega_I}{\partial k_R} = -\frac{\partial\omega_R}{\partial k_I}. \tag{16.2.54}$$

Hence, if (16.2.52) holds, then (16.2.54) implies that

$$G_V = \frac{\partial\omega_R}{\partial k_R} = \frac{\partial\omega_I}{\partial k_I} = 0 \ \text{ and } \ \frac{\partial\omega_R}{\partial k_I} = -\frac{\partial\omega_I}{\partial k_R} = 0. \tag{16.2.55}$$

16.2.7 Algebraic equations at a singular point

A singular point satisfies (16.2.48); alternatively, $D = \hat{c} = 0$. These are complex equations, four real equations for k_R, k_I, ω_R and ω_I when the other parameters are prescribed. If $\omega_I < 0$ at a singular point the flow is convectively unstable. A critical singular point is a singular point such that $\omega_I = 0$.

For given values of the parameters (ℓ, W, R and $m = 0$), the solution $k = k_R + \mathrm{i}k_I$ ($\omega(k) = \omega_R + \mathrm{i}\omega_I$) of the dispersion relation (16.2.14) to (16.3.83) is obtained implicitly. Equation (16.2.14) is quadratic in ω and has two roots, ω_1 and ω_2:

$$\omega_1 = -\frac{c_1}{c_2} + \sqrt{\left(\frac{c_1}{c_2}\right)^2 - \frac{c_0}{c_2}}, \quad \omega_2 \equiv \omega = -\frac{c_1}{c_2} - \sqrt{\left(\frac{c_1}{c_2}\right)^2 - \frac{c_0}{c_2}}, \tag{16.2.56}$$

where c_0, c_1 and c_2 are defined in (16.2.15). The second root can be singular, thus here and henceforth, we drop the subscript $_2$ to simplify notation. A singular point $(k, \omega) = (k_0, \omega_0)$ can now be defined relative to ω

$$\omega_0 = \omega(k_0), \quad \omega(k) = \omega_0 + \left.\frac{\partial\omega}{\partial k}\right|_0 (k - k_0) + \frac{1}{2}\left.\frac{\partial^2\omega}{\partial k^2}\right|_0 (k - k_0)^2 + \cdots . \tag{16.2.57}$$

If

$$\left.\frac{\partial\omega}{\partial k}\right|_0 = 0 \quad \text{at} \quad k = k_0 \quad \text{and} \quad \left.\frac{\partial^2\omega}{\partial k^2}\right|_0 \neq 0 \quad \text{at} \quad k = k_0, \tag{16.2.58}$$

a pinch in the k plane is a square root branch point in the ω plane. We identify k_0 as the roots of

$$\frac{\partial\omega}{\partial k}(k_0) = 0, \quad (k - k_0)^2 = (\omega - \omega_0) \Big/ \left[\frac{1}{2}\left.\frac{\partial^2\omega}{\partial k^2}\right|_0\right]. \tag{16.2.59}$$

The critical singular point satisfies (16.2.58) and $\omega_I = 0$.

Our solution procedure is as follows: the root $\omega = \omega_R + \mathrm{i}\omega_I$, where $\omega_R \equiv \omega_R(k_R, k_I)$ and $\omega_I \equiv \omega_I(k_R, k_I)$, could be inverted implicitly for

$$k_R = k_R(\omega_R, \omega_I), \quad k_I = k_I(\omega_R, \omega_I). \tag{16.2.60}$$

The singular point is determined from the condition (16.2.58). The solutions must be implicit because of the Bessel function. The two real equations in (16.2.59) may be solved for k_R and k_I.

To seek a singular point k_0 at which $\hat{c} = \mathrm{d}\omega/\mathrm{d}k = 0$, the computation is made by means of Newton's method

$$\hat{c}(k) - \hat{c}(k_s) = \left(\frac{\mathrm{d}\hat{c}}{\mathrm{d}k}\right)_s (k - k_s)\,, \tag{16.2.61}$$

where k_s is a starting value which may be close to the singular point k_0. Since the solution k_0 is to satisfy $\hat{c}(k_0) = 0$, we may rewrite (16.2.61) as the following iteration algorithm:

$$k = k_s - \hat{c}(k_s) / \left(\frac{\mathrm{d}\hat{c}}{\mathrm{d}k} \right)_s . \tag{16.2.62}$$

For given k_s, the right-hand side of this is calculated to give a next approximate solution k. The iteration is repeated until $|k - k_s| < \epsilon$ ($\epsilon < 10^{-6}$) or until the iteration is made over 30 times. The solution k_0 also gives $\omega(k_0)$, then we can find the critical singular point when $\omega_I = 0$.

16.2.8 Subcritical, critical and supercritical singular points

The formation and properties of singular points is similar for all cases. Here we shall look at some typical cases for the formation of pinch points in the (k_R, k_I) plane and cusp points in the (ω_R, ω_I) plane. We use the Weber number parameter $\beta = \frac{\rho 2aU^2}{\gamma} = W^{-1}$ where W is the Weber number defined in (16.2.2).

First we fix the parameters $(\ell, R, m) = (0, 100, 0)$ and plot lines of constant ω_I and ω_R in the k_R, k_I plane in the subcritical ($\beta = 4.934$, figure 16.17), critical ($\beta = 5.134$, figure 16.18) and supercritical ($\beta = 5.334$, figure 16.19) case. The cusp singularity, with $\omega_I < 0$ at the cusp point is shown in figure 16.20. The pinch point in the subcritical case is in the region $\omega_I > 0$; this is in the region of absolute instability. The pinch point in the supercritical case is in the region $\omega_I < 0$; this is in the region of convective instability.

We draw the reader's attention to the fact the curves $k_I(k_R)$ on which $\omega_R =$ constant typically pass through regions in which ω_I is positive and negative. The only curves for which

$$\omega\left(k_R, k_I(k_R)\right) = \text{const} \tag{16.2.63}$$

that lie entirely in regions in which ω_I is of one sign pass through the pinch point. In the supercritical case shown in figure 16.19, $\omega_R = 1.743$ is the only frequency for $\omega_I < 0$ for all k_R. Of course, we may interpret ω_R as an excitation frequency.

Huerre & Monkewitz (1985) have described the evolution of a wave packet from an impulsive source in the convectively unstable case. They note that

...among all the wavenumbers contained in the impulsive source, the flow selects, along each ray $x/t =$ const. one particular complex wavenumber k^* given by

$$\frac{\mathrm{d}\omega}{\mathrm{d}k}(k^*) = \frac{x}{t}. \tag{16.2.64}$$

The group velocity then is real and the temporal amplification rate of the wave reduces to

$$\sigma = \omega_I(k^*) - k_I^*(\mathrm{d}\omega/\mathrm{d}k)(k^*). \tag{16.2.65}$$

The growth function then becomes

$$\exp\ (-k_I^* x + \omega_I t) = \exp\ (\omega_I - k_I^*(\mathrm{d}\omega/\mathrm{d}k))\, t. \tag{16.2.66}$$

Using (16.2.53) and (16.2.54), we find that the real part of the group velocity is

$$\frac{\partial\omega}{\partial k}(k^*) = \frac{\partial\omega_R}{\partial k_R}. \tag{16.2.67}$$

Focusing now on the lines $\omega_R(k_R, k_I(k_R)) =$ const in the k plane (figures 16.17-16.19) we find that

$$\frac{\mathrm{d}\omega_R}{\mathrm{d}k_R}\left(k_R, k_I(k_R)\right) = \frac{\partial\omega_R}{\partial k_R} + \frac{\partial\omega_R}{\partial k_I}\frac{\mathrm{d}k_I}{\mathrm{d}k_R} = \frac{\partial\omega_R}{\partial k_R} = 0. \tag{16.2.68}$$

The only curve $\omega_R =$ const which has $\omega_I \leq 0$ for all $k_R > 0$ is the one which passes through the pinch point. The harmonic content of the impulsive source produced by this frequency is not restricted. In general the harmonic content of impulsive sources that are convectively unstable depend on the frequency ω_R of the excitation.

In the sequel we will describe singular points as points at which the group velocity $G_V = \partial\omega_R/\partial k_R = 0$. This is a shorthand for the condition $D = 0$ and $\hat{c} = 0$ which is four equations for k_R, k_I, ω_R and ω_I. All of the graphs shown in the figures to follow satisfy the dispersion relation $D = 0$. We have shown in section 16.2.6 that the condition $\hat{c} = 0$ implies that $G_V = 0$. This leads to the condition of Bers (1975) a flow is convectively unstable when $\omega_I < 0$ and when $G_V = 0$.

The qualitative properties of singularities are the same in all cases. At a critical singular point $\omega_I = 0$. The values of parameters at critical singular points are given for $R = 100$, $R = 200$ and $R = 2000$ (Table 16.7) for 3 or 4 different values of m and $0 \leq \ell \leq 0.4$. We found that when $m = 0$, so that the ambient viscosity is zero,

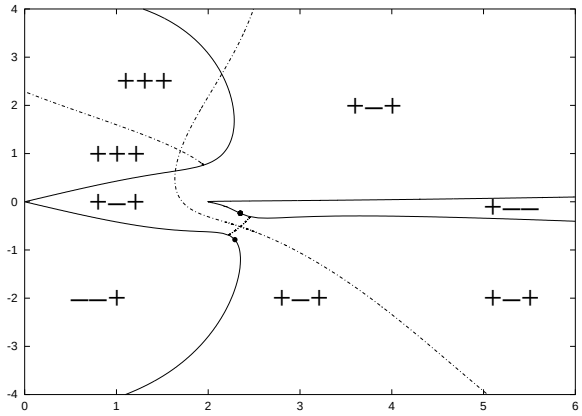

Fig. 16.17. k_I versus k_R for $\ell = 0$, $R = 100$, $\beta = 4.934$, and $m = 0$. Equation (16.2.14) gives rise to three complex roots k for each prescribed set of parameters; for each of the three k's there is one value of ω_I whose sign is marked on the figure. The value $\beta = 4.934 < \beta_c = 5.134$ is subcritical. The singular point $D = 0$ and $\hat{c} = 0$ (or $c = \partial\omega_R/\partial k_R = 0$) has $\omega_I > 0$ in the subcritical case and the flow is absolutely unstable; this point is not shown but the points • that will merge into a pinch point • in figure 8.2 are identified. The solid curves are given by $D = 0$ and $\omega_I = 0$. The dashed curves are for $D = 0$, $\omega_R = 1.7178$ and $\omega_I \geq 0$.

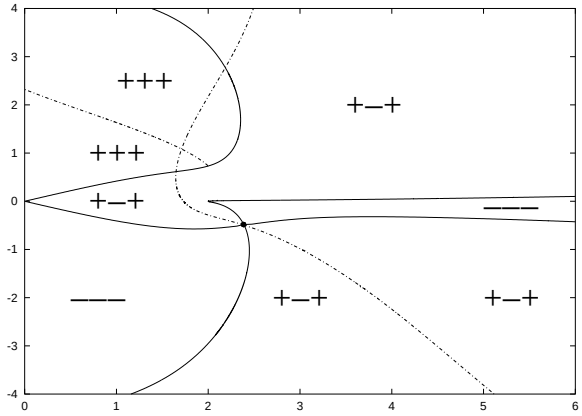

Fig. 16.18. k_I versus k_R for $\ell = 0$, $R = 100$, $m = 0$, and $\beta = \beta_c = 5.134$ is critical and identified by •. At this point $D = 0$, $\hat{c} = 0$, $(\omega_R, \omega_I) = (1.7304, 0)$ and $(k_R, k_I) = (2.392, -0.496)$. The dashed curve $D = 0$ and $\omega_R = 1.7304$ passes through the critical point and has $\omega_I \leq 0$.

one and only one critical β is found for given values of R and ℓ. When the ambient viscosity is finite ($m = 0.5$, 1) two critical values are found, but only one is spatially unstable $k_I < 0$.

The inviscid case $R \to \infty$ is degenerate and will be treated in section 16.2.9.

Figures 16.17 through 16.19 look at the (k_R, k_I) plane in the subcritical, critical and supercritical cases for $(\ell, R, m) = (0, 100, 0)$. In these figures we plot curves in the k_I versus k_R which arise from the real and imaginary part of the dispersion relation $D(k_R + \mathrm{i}k_I, \omega_R + \mathrm{i}\omega_I) = 0$ when ω_R or ω_I is fixed. The singular points are points on the curves which satisfy (16.2.52). The cusp point in (ω_R, ω_I) plane at criticality is shown in figure 16.20. These graphs are representative for all the non degenerate cases $R < \infty$. The explanations of the figures are given in the captions.

In figures 16.21 and 16.22 we have plotted β_c versus ℓ for $R = 2000$, 200 and 100 when $m = 0$ and $m = 0.5$, respectively.

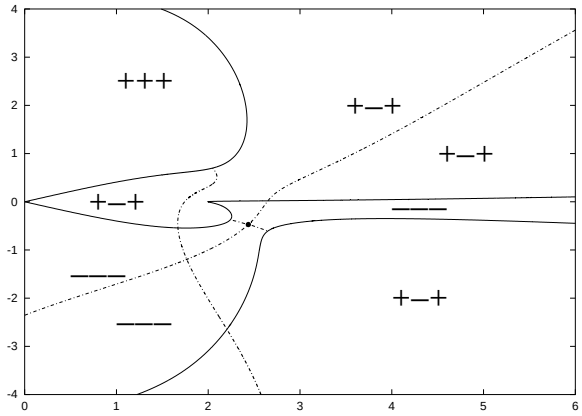

Fig. 16.19. k_I versus k_R for $\ell = 0$, $R = 100$, $m = 0$, and $\beta = 5.334 > \beta_c$ is supercritical. The singular point is shown as a dot $\bullet$ and $\omega_I < 0$ there. On dashed curves $\omega_R = 1.743$.

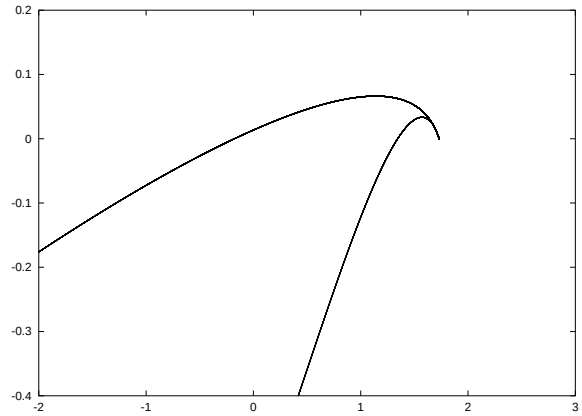

Fig. 16.20. Cusp point $(\omega_R, \omega_I) = (1.7304, 0)$. ω_I versus ω_R for $\ell = 0$, $\beta = 5.134$, $R = 100$ and $m = 0$; the solid curves are for $D = 0$ and $\hat{c} = 0$, which passes through the pinch point $(k_R, k_I) = (2.392, -0.496)$ in the (k_R, k_I) plane (see figure 16.18).

Figure 16.23 gives a summary of the behavior of singular points for inviscid $R \to \infty$ and viscous fluids $R = 100$, 200. A detailed explanation of this summary is given in the figure caption.

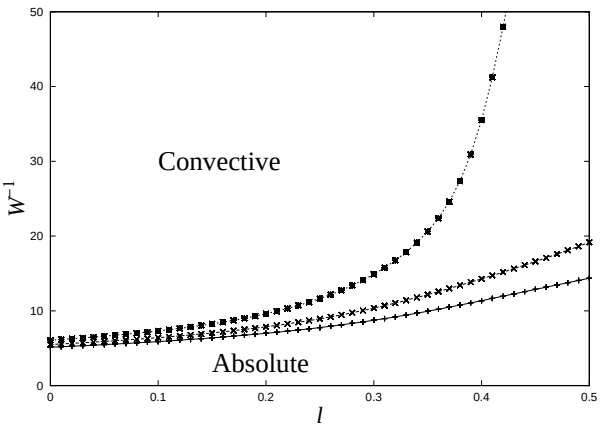

Fig. 16.21. β_c versus ℓ when $m = 0$; $R = 2000$ $(*)$, 200 $(\times)$, 100 $(+)$.

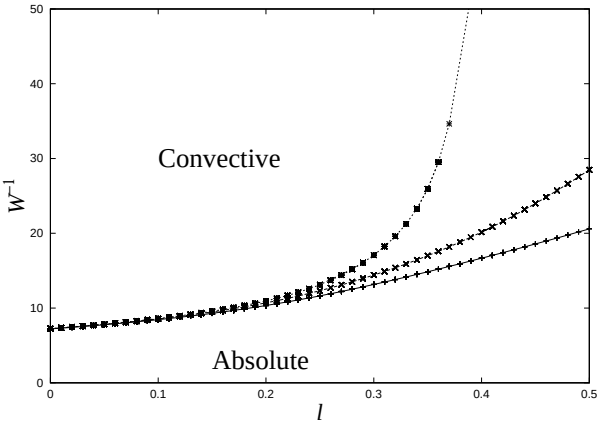

Fig. 16.22. β_c versus ℓ when $m = 0.5$; $R = 2000$ $(*)$, 200 $(\times)$, 100 $(+)$.

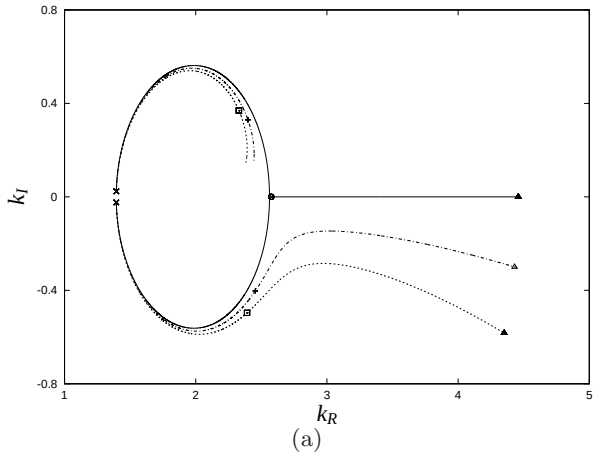

(a)

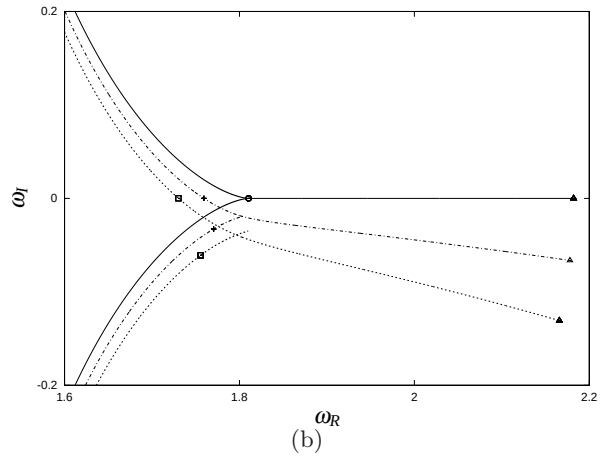

(b)

Table 16.7. *Critical values of $\beta = \beta_c(\ell, R, m)$ at a generic singular point ($D = 0$, $\hat{c} = 0$). At such a point the group velocity $\partial\omega_R/\partial k_R = 0$, (k_R, k_I) is a pinch point; (ω_R, ω_I) is a cusp point. A critical singular point also has $\omega_I = 0$. When $\beta < \beta_c$ the flow is subcritical (absolutely unstable) and disturbances with zero group velocity are amplified ($\omega_I > 0$, $k_I < 0$). When $\beta > \beta_c$ (convectively unstable) these disturbances decay temporally ($\omega_I < 0$, $k_I < 0$).*

R	m	ℓ	β_c	k_R	k_I	ω_R
		0.00	5.134	2.392	-0.496	1.730
		0.08	5.714	2.550	-0.565	1.823
	0	0.16	6.495	2.762	-0.668	1.945
		0.24	7.596	3.065	-0.834	2.116
		0.32	9.192	3.510	-1.127	2.360
		0.40	11.358	4.139	-1.643	2.689
		0.00	13.690	5.899	-1.024	2.585
		0.08	15.296	6.377	-1.340	2.832
100	1	0.16	17.452	7.004	-1.830	3.158
		0.24	20.396	7.837	-2.590	3.589
		0.32	24.320	8.889	-3.692	4.135
		0.40	29.182	10.044	-5.129	4.760
		0.00	7.206	3.225	-0.309	1.882
		0.08	8.158	3.478	-0.424	2.026
	0.5	0.16	9.484	3.840	-0.630	2.226
		0.24	11.352	4.374	-1.010	2.508
		0.32	13.814	5.129	-1.647	2.879
		0.40	16.664	6.058	-2.505	3.308
		0.00	5.493	2.454	-0.403	1.759
		0.08	6.198	2.646	-0.467	1.868
	0	0.16	7.193	2.920	-0.569	2.020
		0.24	8.696	3.350	-0.753	2.249
		0.32	11.042	4.074	-1.126	2.612
		0.40	14.276	5.203	-1.804	3.131
		0.00	13.638	6.046	-0.534	2.612
		0.08	15.306	6.606	-0.716	2.885
200	1	0.16	17.720	7.411	-1.036	3.279
		0.24	21.594	8.698	-1.679	3.906
		0.32	28.344	10.943	-3.081	4.975
		0.40	38.728	14.247	-5.688	6.539
		0.00	7.244	3.238	-0.162	1.891
		0.08	8.242	3.502	-0.230	2.044
	0.5	0.16	9.694	3.894	-0.374	2.266
		0.24	11.956	4.565	-0.706	2.616
		0.32	15.388	5.740	-1.368	3.161
		0.40	20.154	7.497	-2.412	3.943
		0.00	6.065	2.539	-0.192	1.799
		0.08	7.011	2.788	-0.229	1.937
	0	0.16	8.488	3.191	-0.296	2.151
		0.24	11.154	3.978	-0.447	2.542
		0.32	16.744	5.865	-0.865	3.417
		0.40	35.516	12.573	-2.650	6.620
		0.00	13.622	6.097	-0.054	2.621
		0.08	15.320	6.690	-0.073	2.905
2000	1	0.16	17.868	7.574	-0.109	3.333
		0.24	22.550	9.181	-0.201	4.120
		0.32	38.966	14.774	-0.847	6.873
		0.40	196.642	72.962	-21.449	33.075
		0.00	7.260	3.242	-0.016	1.894
		0.08	8.274	3.506	-0.024	2.050
	0.5	0.16	9.806	3.899	-0.042	2.285
		0.24	12.584	4.610	-0.132	2.713
		0.32	19.602	6.916	-0.665	3.830
		0.40	63.200	22.614	-4.872	11.276

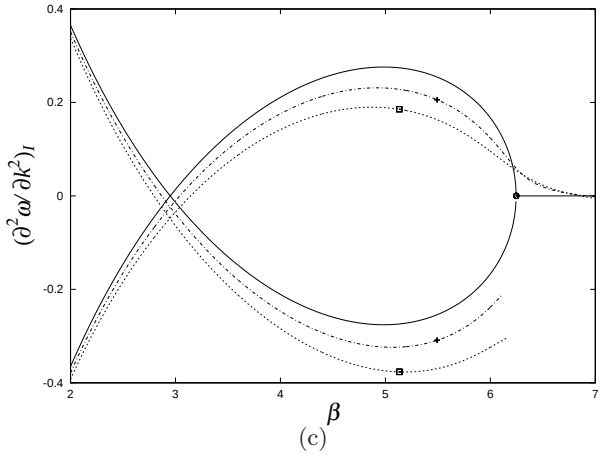

(c)

Fig. 16.23. Locus of singular points $D = 0$, $\hat{c} = 0$ for $m = 0$, $\ell = 0$, $R = 100$ (dashed line), $R = 200$ (dash dot line), $R \to \infty$ (solid line) for $10^{-3} \leq \beta \leq 10$. Critical singular points are those for which $\omega_I = 0$. $\beta = 10^{-3}$ $\times$, $\beta_c = 6.246$ $\circ$, $\beta_c = 5.134$ $\Box$, $\beta_c = 5.493$ $+$ and $\beta = 10$ $\triangle$. (a) k_I versus k_R, (b) ω_I versus ω_R, (c) $\left(\partial^2\omega/\partial k^2\right)_I$ versus β. $\beta < \beta_c$ is subcritical, $\beta > \beta_c > 0$ is supercritical. The supercritical inviscid branch $R \to \infty$, $\beta > 6.246$ is degenerate $\left(\partial^2\omega/\partial k^2\right)_I = \omega_I = k_I = 0$ there. Disturbances with zero group velocity are neutrally stable. The values of β on the upper branches $k_I > 0$ of the (k_R, k_I) plane are less than $\beta_c = 6.246$ and $\omega_I < 0$. These branches are subcritical and spatially and temporally damped. The lower branches $k_I < 0$ go from subcritical values $10^{-3} < \beta < \beta_c$ for $\omega_I > 0$ (for which the disturbances are spatially and temporally amplified) to supercritical values $\beta > \beta_c$: $\beta_c = 6.246$ for $R \to \infty$ and $\omega_I = 0$, $k_I = 0$ for $\beta > 6.246$, $\beta_c = 5.134$ for $R = 200$ and $\omega_I < 0$ there, $\beta_c = 5.493$ for $R = 100$ and $\omega_I < 0$ there. Disturbances with zero group velocity are temporally damped but spatially amplified ($\omega_I < 0$, $k_I < 0$) for supercritical values of β.

16.2.9 Inviscid jet in inviscid fluid ($R \to \infty$, $m = 0$)

This problem was studied for the case $\ell = 0$ by Keller, Rubinow & Tu (1973); they did not look at the problem of convective/absolute instability — treated later by Leib & Goldstein (1986a). Here we have looked at the inviscid problem for all density ratios and find the border, the critical $\beta = \beta_c$ at the singular point (16.2.48). We find that the singular point is degenerate, because the imaginary part of $\partial^2 D/\partial k^2$ at the pinch point vanishes for $0 < \ell < 0.3455$. The degeneracy appears in the collapse of the region in which $\omega_I < 0$ for large k_R into a line; this region of convective instability collapses onto a neutral region for which $\omega_I = 0$.

Table 16.8 lists values of parameter at the pinch point; figure 16.24 gives the critical curve $\beta_c = \beta(\ell)$ in the β versus ℓ plane. $\ell = 0.3455$ is an asymptote; when $\ell > 0.3455$, there is no pinch point and the flow is absolutely unstable.

Table 16.8. *Inviscid fluids ($R \to \infty$, $m = 0$). Values of (k_R, k_I) at pinch point singularity (see figure 16.24) indexed by the density ratio ℓ. The values of the frequency ω_R and the Weber number parameter β ($= W^{-1}$) are at the pinch point are also listed. Pinch point singularities do not exist when $\ell > 0.3455$; in this case all flows are absolutely unstable.*

No.	ℓ	β_c	k_R	k_I	ω_R	ω_I
1	0.00	6.246	2.576	0	1.810	0
2	0.04	6.710	2.696	0	1.877	0
3	0.08	7.280	2.840	0	1.958	0
4	0.12	8.004	3.025	0	2.060	0
5	0.16	8.962	3.290	0	2.196	0
6	0.20	10.298	3.681	0	2.387	0
7	0.24	12.282	4.274	0	2.677	0
8	0.28	15.496	5.317	0	3.162	0
9	0.32	22.038	7.514	0	4.199	0
10	0.3455	52.350	17.647	0	9.189	0
11	0.36	—	—	—	—	—
12	0.40	—	—	—	—	—

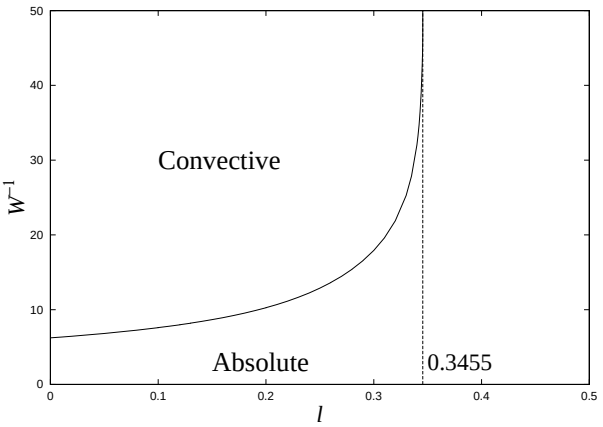

Fig. 16.24. Border between absolute and convective instability in the inviscid case $R \to \infty$, $m = 0$. The value of $\ell = 0.3455$ is asymptotic. The inviscid case is degenerate because the imaginary part of $\partial^2\omega/\partial k^2 = 0$ at the singular point. The consequence of this degeneracy is that at criticality $(\omega_I, k_I) = (0, 0)$ for all $\ell < 0.3455$. The condition $\omega_I < 0$ at the pinch point cannot be realized; ω_I at $\partial\omega_R/\partial k_R = 0$.

16.2.10 Exact solution; comparison with previous results

Using equations (2.17)-(2.21) in Funada & Joseph (2002) for capillary instability of both viscous fluids, we can modify the dispersion relation (2.17) so as to make the ambient fluid inviscid and the viscous column moving with uniform velocity. The resultant dispersion relation D for a viscous jet in an inviscid fluid is given by

$$D = \begin{vmatrix} I_1(k/2) & I_1(k_\ell/2) & K_1(k/2) \\ 2k^2 I_1(k/2) & \left(k^2 + k_\ell^2\right) I_1(k_\ell/2) & 0 \\ F_1 & F_2 & F_3 \end{vmatrix} = 0, \tag{16.2.69}$$

where

$$F_1 = (\omega - k)^2 I_0(k/2) + 2\mathrm{i}\,(\omega - k)\,\frac{k^2}{R}\left(\frac{\mathrm{d}I_1(k/2)}{\mathrm{d}(k/2)}\right) + W\left(4 - k^2\right) k I_1(k/2), \tag{16.2.70}$$

$$F_2 = 2\mathrm{i}\,(\omega - k)\,\frac{k k_\ell}{R}\left(\frac{\mathrm{d}I_1(k_\ell/2)}{\mathrm{d}(k_\ell/2)}\right) + W\left(4 - k^2\right) k I_1(k_\ell/2), \tag{16.2.71}$$

$$F_3 = -\ell\omega^2 K_0(k/2), \tag{16.2.72}$$

with k_ℓ defined as

$$k_\ell = \sqrt{k^2 - \mathrm{i}R\,(\omega - k)}. \tag{16.2.73}$$

The parameters ℓ, W and R are the ones defined in (16.2.2). The top row of (16.2.69) arises from the continuity of normal velocity, of the tangential stress and of the normal stress. Solving (16.2.69) implicitly using Newton's method for given values of (ω_R, ω_I) and the parameters, we have (k_R, k_I) and $\hat{c}$ numerically.

In figure 16.25 we have plotted the critical value β_c $(= W_c^{-1})$ versus R giving the border between absolute and convective instability for viscous jets in an inviscid fluid computed by Leib & Goldstein (1986b) for $\ell = 0$ and by Lin & Lian (1989) for $\ell = 0.0013$ and $\ell = 0.03$. The value $\beta_c = 6.3$ for an inviscid jet in an inviscid fluid was calculated by Leib & Goldstein (1986a). In figure 16.26 we compare the results from the theory of viscous potential flow given in section 16.2.3 with the results for viscous flow according to (16.2.69). The stability limits from the two theories are close.

The analysis for "fully viscous flow" neglects the dynamical effects of the viscous gas; these effects require the imposition of continuity of the tangential component of velocity and stress. The discontinuous velocity which induces Kelvin-Helmholtz instability is then inconsistent with the aforementioned continuity requirements. S.P.Lin (2003) attempted to address the effects of shear by a study of core-annular flow in a vertical pipe. This is a very different problem. He found a transition from convective to absolute instability but comparisons with experiments are not available.

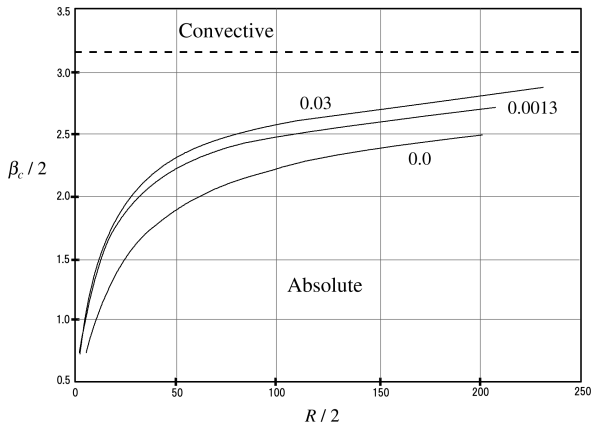

Fig. 16.25. Critical Weber number β_c $(= W_c^{-1})$ versus Reynolds number R from the literature: Leib & Goldstein (1986a) for inviscid jet in an inviscid fluid, $\beta_c = 6.3$ for $\ell = 0$, denoted by dashed line; solid lines are for viscous jets in an inviscid fluid $(m = 0)$ for $\ell = 0$ (Leib & Goldstein 1986b) and $\ell = 0.0013$ and $\ell = 0.03$ (Lin & Lian 1989).

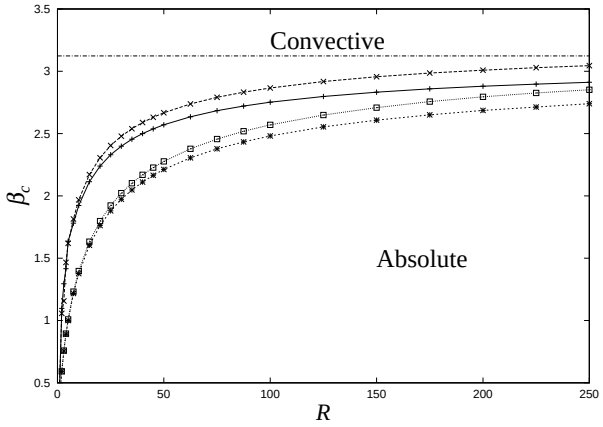

Fig. 16.26. β_c versus R comparing viscous flow (lower two curves) computed from the theory in section 16.2.10 for $m = 0$, $\ell = 0.0013$ $*$ and $\ell = 0.03$ $\Box$ with viscous potential flow (upper two curves) for the same values ($\ell = 0.0013$ $+$, $\ell = 0.03$ $\times$, $m = 0$).

16.2.11 Conclusions

(1) The computation of temporal and C/A instability of the liquid jet using viscous potential flow
(2) Extensive computation of the effects of the ambient density and viscosity and the viscosity of the liquid
(3) A demonstration that KH instability cannot occur in vacuum (but capillary instability and Rayleigh-Taylor instability can occur in vacuum)
(4) The derivation of a dispersion relation in the form of a polynomial in the complex frequency which can be used to study temporal, spatial and C/A instability
(5) A comprehensive analysis of temporal instability; for all values of the parameters there are wavenumbers for which the liquid jet is unstable
(6) An analysis of the relative importance of KH and capillary instability on the maximum growth, on the wave length of maximum growth and the cut-off wavenumber for inviscid and viscous liquids. KH instability is the dominant mechanism for small Weber numbers and capillary instability is dominant for large Weber numbers; the variation of the growth rates and wavenumbers in the two regimes is sharply different
(7) When viscosity and surface tension are zero, the liquid jet is Hadamard unstable to KH instability with growth rates proportional to k. Surface tension stabilizes the short waves. The maximum growth rate and the associated wavenumber are proportional to $1/W$ for small W when the fluid is inviscid. For viscous fluids the maximum growth rate is finite as $W \to 0$ (pure KH instability) but the wave length $\lambda_m = 2\pi/k_m$ tends to zero with W, as in the inviscid case. It can be said that the wave lengths for breakup due to KH instability are exceedingly short and that breakup due to KH instability leads to surpassingly small drops, essentially mist.
(8) The critical wavenumber k_c for marginal instability (stability for $k > k_c$) is independent of the Reynolds number of the liquid jet but the maximum growth rate and the wavenumber of maximum growth depend on the Reynolds number
(9) Under the realizable condition that $m\alpha b_a = \ell b \alpha_a$ the neutral curves for viscous potential flow are the same as for inviscid potential flow; this is a remarkable result. When $k > 10$ this criterion reduces to a statement that the neutral curves are the same when the kinematic viscosity of the liquid equals the kinematic viscosity of the gas; this result was proved for KH instability of a plane layer by Funada & Joseph (2001).
(10) A comprehensive study of the transition between convective and absolute stability of the combined KH stability and capillary instability of the liquid jet under a wide range of ambient condition for different liquid was carried out. Precise results were obtained for full ranges of the Weber and Reynolds number, density and viscosity ratios.
(11) The study of pinch point and cusp point singularities was greatly simplified by the fact that an explicit dispersion relation in the complex frequency and wavenumber planes could be studied by algebraic rather than geometric method of Bers (1975) and Briggs (1964)
(12) We show that the singular point for inviscid fluids when the density ratio ℓ is in $0 \leq \ell < 0.3455$, is degenerate; when $\ell > 0.3455$ the inviscid jet is absolutely unstable. The singular points for inviscid solutions in the supercritical case $\beta > \beta_c$ are degenerate since $\left(\partial^2\omega/\partial k^2\right)_I = 0$. In this case $k_I = 0$ and $\omega_I = 0$, so that the transition from absolute instability is to a neutral rather than to a convectively unstable state. All other cases are not degenerate and associate cusp points in the ω plane with pinch points in the k plane.
(13) The transition between convective and absolute stability computed by viscous potential flow is reasonably good agreement with the transition computed by fully viscous flow in which the flow is not assumed to be irrotational. It must be understood that KH instability cannot be studied exactly in the frame of the Navier-Stokes equations because the basic flow has a discontinuous velocity.

The liquid jet with no spatial development studied here is always unstable to temporal disturbances, convectively and absolutely unstable jets are temporally unstable; flows like Hagen-Poiseuille flow which are temporally stable would not admit C/A instability. Instability for jets with very slow spatial development should not be very different for jets with no spatial development. The predictions of temporal and C/A instability achieved

here have a somewhat tentative relation to actual experiments which emanate from nozzles in which the spatial development of the basic flow could have an important effect.

16.3 Viscous potential flow of the Kelvin-Helmholtz instability of a cylindrical jet of one fluid into the same fluid

Batchelor and Gill 1962 constructed a simple analysis of a cylindrical jet of one fluid into the same fluid. Their analysis is based on potential flow of an inviscid fluid. The interface in their problem is defined by a discontinuity of velocity. The fluid on either side of the discontinuity is the same. Here we show how to generalize the analysis to irrotational flow of a viscous fluid. Our analysis is a paradigm for generalizing problems of potential flow with discontinuous velocity profiles to include the effects of viscosity.

16.3.1 Mathematical formulation

Laplace equations are given by

$$\nabla^2\phi_0 = 0, \quad \nabla^2\phi_1 = 0, \tag{16.3.74}$$

and Bernoulli equations are

$$\frac{\partial\phi_0}{\partial t} + U\frac{\partial\phi_0}{\partial x} + \frac{p_0}{\rho} = f_0(t), \quad \frac{\partial\phi_1}{\partial t} + \frac{p_1}{\rho} = f_1(t). \tag{16.3.75}$$

The boundary conditions at the cylindrical surface $r = a + \eta \approx a$ are the kinematic conditions

$$\frac{\partial\eta}{\partial t} + U\frac{\partial\eta}{\partial x} = \frac{\partial\phi_0}{\partial r}, \quad \frac{\partial\eta}{\partial t} = \frac{\partial\phi_1}{\partial r}, \tag{16.3.76}$$

and the normal stress balance

$$p_0 - 2\mu\frac{\partial^2\phi_0}{\partial r^2} = p_1 - 2\mu\frac{\partial^2\phi_1}{\partial r^2}. \tag{16.3.77}$$

16.3.2 Normal modes; dispersion relation

The normal mode solution of the problem by (16.3.74)-(16.3.77) is in the form

$$\eta = A\mathrm{e}^{\mathrm{i}kx+\mathrm{i}n\theta-\mathrm{i}kct}, \quad \phi_0 = CI_n(kr)\mathrm{e}^{\mathrm{i}kx+\mathrm{i}n\theta-\mathrm{i}kct}, \quad \phi_1 = DK_n(kr)\mathrm{e}^{\mathrm{i}kx+\mathrm{i}n\theta-\mathrm{i}kct}. \tag{16.3.78}$$

The kinematic conditions give

$$\mathrm{i}k\,(U_0 - c)\,A = kCI_n'(ka), \quad -\mathrm{i}kcA = kDK_n'(ka) \tag{16.3.79}$$

The normal stress balance gives

$$\frac{\partial\phi_0}{\partial t} + U\frac{\partial\phi_0}{\partial x} + 2\nu\frac{\partial^2\phi_0}{\partial r^2} = \frac{\partial\phi_1}{\partial t} + 2\nu\frac{\partial^2\phi_1}{\partial r^2}, \tag{16.3.80}$$

which is then written as

$$\mathrm{i}k\,(U_0 - c)\,CI_n(ka) + 2\nu Ck^2I_n''(ka) = -\mathrm{i}kcDK_n(ka) + 2\nu Dk^2K_n''(ka) \tag{16.3.81}$$

where $\nu = \mu/\rho$.

For $n = 0$, α, α_a, b and b_a are defined as

$$\alpha = \frac{I_0(k/2)}{I_1(k/2)} = \frac{I_0(k/2)}{I_0'(k/2)}, \quad \alpha_a = \frac{K_0(k/2)}{K_1(k/2)} = -\frac{K_0(k/2)}{K_0'(k/2)}, \tag{16.3.82}$$

$$b = \alpha - \frac{2}{k} = \frac{I_0''(k/2)}{I_0'(k/2)}, \quad b_a = \alpha_a + \frac{2}{k} = -\frac{K_0''(k/2)}{K_0'(k/2)}. \tag{16.3.83}$$

It is noted for real k that $k\alpha \to 4$ and $\alpha_a \to 0$ as $k \to 0$, while $\alpha \to 1$ and $\alpha_a \to 1$ as $k \to \infty$, as shown in figure 16.10.

In the limit $ka \to \infty$,

$$\frac{I_n(ka)}{I_n'(ka)} \to 1, \quad \frac{I_n''(ka)}{I_n'(ka)} \to 1, \quad -\frac{K_n(ka)}{K_n'(ka)} \to 1, \quad -\frac{K_n''(ka)}{K_n'(ka)} \to 1, \tag{16.3.84}$$

For $n \geq 1$, the ratios of Bessel functions will be checked later.

If $\nu = 0$, then

$$(c - U_0)^2 \frac{I_n(ka)}{I_n'(ka)} = c^2 \frac{K_n(ka)}{K_n'(ka)} \tag{16.3.85}$$

$ka \to \infty$

$$(c - U_0)^2 \frac{I_n(ka)}{I_n'(ka)} = c^2 \frac{K_n(ka)}{K_n'(ka)} \;\to\; (c - U_0)^2 + c^2 = 0 \;\to\; c^2 - U_0 c + \frac{U_0^2}{2} = 0 \tag{16.3.86}$$

$$c = \frac{U_0}{2} \pm \sqrt{\frac{U_0^2}{4} - \frac{U_0^2}{2}} = \frac{U_0}{2}\left[1 \pm \mathrm{i}\right], \;\to\; \frac{c}{U_0} = \frac{1}{2}\left[1 \pm \mathrm{i}\right] \tag{16.3.87}$$

When $\nu \neq 0$ and $ka \to \infty$, we have

$$(c - U_0)^2 + 2\mathrm{i}\nu k\,(c - U_0) + c^2 + 2\mathrm{i}\nu k c = 0 \tag{16.3.88}$$

$$c = \frac{U_0 - 2\mathrm{i}\nu k}{2} \pm \sqrt{\left(\frac{U_0 - 2\mathrm{i}\nu k}{2}\right)^2 - \frac{U_0^2 - 2\mathrm{i}\nu k U_0}{2}} = \frac{U_0 - 2\mathrm{i}\nu k}{2} \pm \mathrm{i}\sqrt{\frac{U_0^2}{4} + \nu^2 k^2} \tag{16.3.89}$$

$$c_R = \frac{U_0}{2}, \quad c_I = -\nu k \pm \sqrt{\frac{U_0^2}{4} + \nu^2 k^2} = -\nu k + \sqrt{\frac{U_0^2}{4} + \nu^2 k^2} \tag{16.3.90}$$

When $c_I = 0$, the neutral state is given by

$$0 = -\nu k + \sqrt{\frac{U_0^2}{4} + \nu^2 k^2} \;\to\; \frac{U_0^2}{4} = 0 \tag{16.3.91}$$

The flow is unstable for all values of n, ka and all viscosities ν.

16.3.3 Growth rates and frequencies

The evolution of disturbances of the cylindrical jet is governed by the function

$$\mathrm{e}^{-\mathrm{i}kct}, \quad c = c_R + \mathrm{i}c_I. \tag{16.3.92}$$

Batchelor and Gill 1962 plotted c_R vs k and c_I vs k for an inviscid fluid. It is more revealing to compute the real and imaginary parts of the complex frequency $\omega = c/k$, with

$$\mathrm{e}^{-\mathrm{i}kct} = \mathrm{e}^{\omega_I(k,\nu)t}\mathrm{e}^{-\mathrm{i}\omega_R(k,\nu)t} \tag{16.3.93}$$

because the analytical character of the evolution is not disquised by the extraneous multiplicative factor k.

In figure 16.27 we present graphs of ω_I vs k and ω_R vs k for $\nu = 0$ and $\nu = 0.1$.

16.3.4 Hadamard instabilities for piecewise discontinuous profiles

The study of problems of irrotational flow of an inviscid fluid with a discontinuous velocity profile is widespread. There are two prototypical problems. In one problem, the velocity itself is discontinuous as in the jet problem considered here or in the problem of instability of the Rankine vortex with axial flow studied by Loiseleux, Chomaz and Huerre 1998 and related problems used to study absolute and convective instability. In another problem, the velocity is continuous but the slope of the profile is discontinuous. Such discontinuities are compatible with irrotational flows in which the effects of shear stresses are ignored but the effects of viscous normal stresses are not ignored. In fact, the effects of shear in any real fluid would quickly smooth discontinuities through the effects of a thin shear layer might persist for a time.

One of the troublesome difficulties which arises in the study of instability of vortex sheets defined by discontinuities of velocity of the type mentioned above, is Hadamard instability. In all these problems the growth rate increases without bound at any finite time as the wavelength $\lambda = 2\pi/k$ tends to zero. This kind of disaster cannot occur; as they say in medicine "the blooding always stops." The way in which short waves are regularized ought to describe the physical mechanisms at work.

The instability of the viscous jet described by **??**eq16.3.17) is given

$$\omega_I = -\nu k^2 + k\sqrt{\frac{U_0^2}{4} + \nu^2 k^2}. \tag{16.3.94}$$

When $\nu = 0$, $\omega_I = kU_0/2$ tends to infinity with k. If $\nu > 0$, then

$$\omega_I \to \frac{U_0^2}{8\nu} \tag{16.3.95}$$

and the small waves are unstable but Hadamard unstable. The growth rate for short waves increases as ν decreases and it is large when ν is small.

Hadamard instabilities may also be regularized by weakening the discontinuity as in the second problem in which the vorticity is discontinuous but the velocity is continuous. Shear layers may be modeled by such vorticity discontinuities as in figure 16.28.

The flow in figure 16.28 is not Hadamard unstable even when $\nu = 0$ (Joseph and Saut 1990, §7).

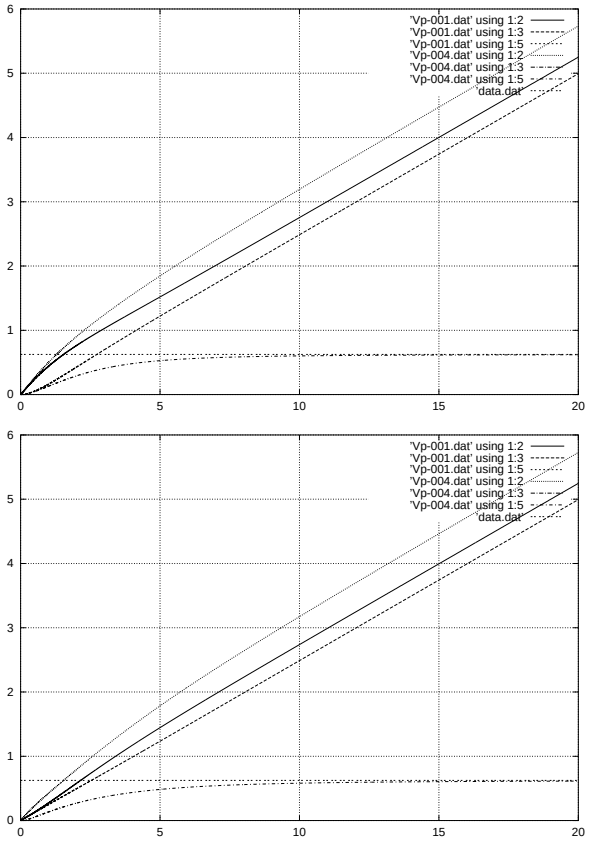

Fig. 16.27. ω_I vs k and ω_R vs k for $\nu = 0$ and $\nu = 0.1$. The problem considered by Batchelor and Gill 1962 is Hadamard unstable $e^{\omega_I t} \to \infty$ as $k \to \infty$, no matter how small is t. $n = 0$ above

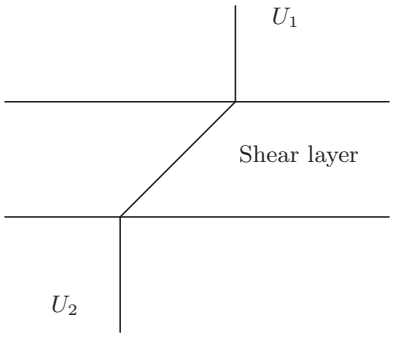

Fig. 16.28. Piecewise continuous velocity modeling a shear layer.

17
Stress induced cavitation

The usual criterion for cavitation is that cavities will form in a liquid when and where the pressure falls below a critical value. In the ideal case, the cavitation threshold is the vapor pressure. The pressure in an incompressible viscous liquid is not a thermodynamic or material property; it is the average stress (actually the negative of the average stress which is positive in tension). The viscous part of the stress is proportional to the rate of strain which has a zero average with positive and negative values on the leading diagonal in principal coordinates. It follows that in motion the the liquid will develop stresses which are both larger and smaller than the average value. The theory of stress induced cavitation seeks to relate the fracture or cavitation of a liquid to its state of stress rather than its average stress. This kind of theory requires that the state of stress be monitored in the evolving field of motion to determine when and where the liquid will fracture. The theory can thought to be an application area for Navier-Stokes fluid dynamics which can be studied by viscous potential flow when the flows are irrotational or nearly irrotational. The link between the theory of stress induced cavitation and viscous potential flow is the fact that viscous stresses can be computed on irrotational motions. In section 17.1 we give a comprehensive presentation of the physical foundations and mathematical formulation of the theory of stress induced cavitation. This presentation is taken from the 2006 paper of Padrino *et al.* ; it is new, comprehensive and otherwise unavailable. In section 17.2 we consider cavitation of a liquid in aperture flow by computing stresses on the well known potential flow solution for this problem in complex variables. This is a simple example of how the extension of potential flow solutions to viscous fluids leads to new results at small cost. Padrino *et al.* 2006 studied stress induced cavitation in streaming flow past a sphere. This solution is discussed in section 17.3; there are potential flow solutions there and they are compared with numerical solutions of the Navier-Stokes equation. In section 17.4 we construct a nonlinear model of capillary collapse and rupture of a liquid thread under the assumption that the collapse is symmetric with respect to a stagnation point at the throat. Stagnation point flow is irrotational. The cartoon for the model in figure 17.13 is defined by a periodic array of stagnation points between points of liquid depletion and liquid accumulation. The passage of liquid from points of depletion caused by capillary collapse to points of accumulation around which a liquid ball expands cannot be done without the generation of vorticity in an axisymmetric analogue to hyperbolic vortices xy=constant nested in the four quadrants at each stagnation point in vortex array described by 4.6.34. The analysis can be said to generate a Helmholz decomposition for rotational flows near points of stagnation. This model give rise a rupture criterion based on the generation of large viscous extensional stresses at the throat in the final stage of collapse.

17.1 Theory of stress induced cavitation

Winer & Bair (1987) and, independently, Joseph (1995, 1998) proposed the maximum tension criterion for cavitation which states that the flowing liquid will cavitate if the maximum tensile stress exceeds a critical value. Since this maximum stress is associated with a principal direction, this criterion is not isotropic. Winer & Bair (1987) introduced the idea that stress-induced cavitation may enter into the apparent shear thinning of liquid lubricants. They remarked that shear thinning may be the result of a yielding or cavitation event that takes place at a critical value of the liquid's tensile stress. They further note that 'for some high shear rate viscosity data at atmospheric pressure the principal normal stress may approach quite low values relative to

one atmosphere suggesting the possibility of cavitation or fracture of the material resulting in a reduced shear stress'. In a private communication, Prof. Bair noted that '...There was little interest from tribologists, so we dropped it until recently. In the original work we were able to see to the voids by eye using a clear plastic outer cylinder...'.

The maximum tension criterion is embedded as one possibility for liquid failure presented by analysis of the state of stress in Joseph's theory. A comparison of these two theories can be found in the study of cavitation in creeping shear flows by Kottke, Bair and Winer (2005). Numerous examples of cavitation in shear flow by other researchers are discussed by Kottke *et al.* (2005). Examples of stress-induced cavitation in extensional flow and shear flow were discussed by Joseph (1998). Pereira *et al.* (2001) did a theoretical study of cavitation in a journal bearing with axial throughput. They found that the inception of cavitation in a moving fluid is always stress induced. Funada *et al.* (2006) carried out an analysis of stress induced cavitation in a two-dimensional aperture flow modeling atomizers in which cavitation is well documented. The aperture flow was expressed using a complex potential and the stress calculated using viscous potential flow. They found that the viscous stress was huge near the tips of the aperture, thus cavitation could be induced. The region at risk to cavitation is larger, for a fixed cavitation number, when the Reynolds number is smaller.

17.1.1 Mathematical formulation

The stress in an incompressible Newtonian fluid is given by

$$\mathbf{T} = -p\mathbf{1} + 2\mu\mathbf{D}\left[\mathbf{u}\right], \tag{17.1.1}$$

where $\mathbf{D}\left[\mathbf{u}\right]$ is the symmetric part of the velocity gradient and $\mathrm{tr}\mathbf{D}\left[\mathbf{u}\right] = 0$, such that

$$\mathrm{tr}\mathbf{T} = T_{11} + T_{22} + T_{33} = -3p. \tag{17.1.2}$$

We define the stress at the cavitation threshold as p_{c}. It is positive when compressive and negative when tensile. Classically, the vapor pressure is taken as the threshold stress; however, in the next section, we discuss examples where different values, including tensile values, should be used for the cavitation threshold.

In the pressure criterion, the viscous part of the stress tensor is not considered and the liquid will cavitate when

$$-p + p_{\mathrm{c}} > 0. \tag{17.1.3}$$

The pressure criterion assumes that cavitation inception is determined by the average stress, called the pressure. The fluid cannot average its stresses; it sees only principal stresses and when the actual state of stress is considered there is at least one stress which is more compressive and another which is more tensile than the average stress. The most conservative criterion is the one which requires that the most compressive stress is larger than the cavitation threshold; suppose T_{22} is the most compressive and T_{11} is the most tensile (or least compressive) stress, then if

$$T_{22} + p_{\mathrm{c}} > 0 \tag{17.1.4}$$

for cavitation, it will surely be true that

$$-p + p_{\mathrm{c}} > 0 \quad \text{and} \quad T_{11} + p_{\mathrm{c}} > 0. \tag{17.1.5}$$

The maximum tension theory, which perhaps embodies the statement that liquids which are not specially prepared will cavitate when they are subject to tension, can be expressed by the condition that supposing T_{11} to be the maximum of the three principal stresses,

$$T_{11} + p_{\mathrm{c}} > 0. \tag{17.1.6}$$

The cavitation number K compares the cavitation threshold p_{c} with a typical pressure; here in our sphere problem, with the pressure p_∞ at infinity. We define

$$K = \frac{p_\infty - p_{\mathrm{c}}}{N_R} \tag{17.1.7}$$

where $N_R = \mu U/L$ for Stokes flow and $N_R = \rho U^2/2$ when inertia acts; L is a characteristic length scale. Later, the analysis will show that the stress difference between the free-stream pressure and the cavitation threshold $p_\infty - p_c$ is the critical value rather than the cavitation threshold by itself.

The maximum tension criterion (17.1.6) has recently been studied in a numerical simulation of bubble growth in Newtonian and viscoelastic filaments undergoing stretching by Foteinopoulou *et al.* (2004). They base their analysis on the Navier-Stokes equations for Newtonian fluids and the Phan-Thien/Tanner model for viscoelastic fluids. They compute the principal stresses and evaluate the cavitation threshold for the maximum tension criterion (17.1.6), the pressure theory (17.1.3) and the minimum principal theory (17.1.4). They find that the capillary number at inception is smallest for (17.1.6). As remarked by Kottke *et al.* (2005), the cavitation threshold p_c could be negative or positive. In the case of $p_c < 0$, the liquid shows tensile strength; for $p_c = 0$, a cavity will open if the maximum principal stress becomes positive (i.e., tensile), and, if $p_c > 0$, the cavitation threshold is given by a positive pressure (i.e., compressive stress). The latter case is typified by the pressure theory of cavitation determined by the local pressure dropping below the vapor pressure.

To each principal stress there corresponds a principal direction, which plays a role in the physics of cavity inception. Joseph (1998) asserts that 'if a cavitation bubble opens up, it will open in the direction of maximum tension. Since this tension is found in the particular coordinate system in which the stress is diagonal, the opening direction is in the direction of maximum extension, even if the motion is a pure shear. It may open initially as an ellipsoid before flow vorticity rotates the major axis of ellipsoid away from the principal tension axis of stress, or it may open abruptly into a 'slit' vacuum cavity perpendicular to the tension axis before vapour fills the cavity as in the experiments of Kuhl *et al.* (1994)'. These ideas are illustrated in cartoons showing the orientation of the principal directions on the surface of the sphere for each approach considered in this study.

Consider the expression for the stress tensor for a Newtonian fluid given in (17.1.1). Adding the diagonal tensor $p_c\mathbf{1}$ to both sides and decomposing $p = p_\infty + p^*$ yields

$$\mathbf{T} + p_c\mathbf{1} = -\left(p_\infty - p_c\right)\mathbf{1} - p^*\mathbf{1} + 2\mu\mathbf{D}. \tag{17.1.8}$$

Dividing through by the normalizing factor N_R, (17.1.8) becomes

$$\frac{\mathbf{T} + p_c\mathbf{1}}{N_R} = -\left(K + \frac{p^*}{N_R}\right)\mathbf{1} + \frac{2\mu}{N_R}\mathbf{D}. \tag{17.1.9}$$

The strain–rate tensor can be readily diagonalized. Thus the principal stresses and directions can be determined. Suppose now that $K = K_c$ at the marginal state separating cavitation from no cavitation. For shortness, let us call K_c the incipient cavitation number. This marginal state is defined by an equality in one of the three criteria (17.1.3), (17.1.4) or (17.1.6). For the maximum tension theory $K = K_c$ when $T_{11} + p_c = 0$. In particular, for the maximum principal stress T_{11}, (17.1.9) yields

$$\left(T_{11} + p_c\right)/N_R = -(K + p^*/N_R) + 2\mu D_{11}/N_R, \tag{17.1.10}$$

where D_{11} denotes the maximum principal rate of strain. Then, $K_c = \left(-p^* + 2\mu D_{11}\right)/N_R$ is, in general, a scalar function of the position in the fluid domain. For a positive cavitation number, consider $K = K_c + K^*$ such that $\left(T_{11} + p_c\right)/N_R = -K^*$. It is thus clear from (17.1.10) that

$$T_{11} + p_c < 0 \text{ when } K > K_c, \tag{17.1.11}$$

and

$$T_{11} + p_c > 0 \text{ when } K < K_c. \tag{17.1.12}$$

The latter condition implies that the liquid is at the most risk to cavitation in regions where $K < K_c$. For instance, for a fixed cavitation number K, no cavity will open if $K > K_{c,\max}$, the maximum value that K_c takes in the entire fluid domain. On the other hand, the cavitation number K based on the actual hydrodynamics, may vary in the fluid domain, since the cavitation threshold p_c may also change with position. For example, Singhal *et al.* (2002) included in their cavitation model the effect of the local turbulence pressure fluctuations in the phase-change threshold pressure.

17.1.2 Cavitation threshold

Cavitation can be defined as the formation, growth and collapse of a cavity in a liquid. In general, the 'formation' of a cavity implies both the appearance of a new void or the extension of a preexisting nucleus beyond a critical size large enough to be observed with the unaided eye (Young, 1989). The idea of the opening of a cavity in the liquid continuum brings into consideration the concept of liquid tensile strength, which is a material property. The pressure criterion for cavitation states that the liquid cavitates when the local pressure reaches the vapor pressure somewhere in the domain. Knapp, Daily & Hammit (1970) discusses that, although the inception of a cavity has been observed in experiments when local pressure is near the vapor pressure, deviations of various degrees have been reported for different liquids such that the results do not agree with the vapor pressure criterion. Knapp *et al.* define the vapor pressure as 'the equilibrium pressure, at a specified temperature, of the liquid's vapor which is in contact with an *existing* free surface.' They argue that the stress required to rupture the continuum in a homogeneous liquid is determined by the tensile strength, not by the vapour pressure. The literature on the tensile strength of liquids is vast and a good account of experimental results is given in the book by Knapp *et al.* (1970) for various liquids. In particular for water, values ranging from 13 to 200 atm are listed. Briggs (1950) reports inception of cavities in water induced by centrifugal force for pressures between vapor presssure and -300 atm (tension). Recently, Kottke, Bair & Winer (2003) measured the tensile strength of nine liquids, including water, lubricant and polymeric liquids. Theoretical estimates of the tensile strength of water render large negative values in the interval -500 atm to -10,000 atm, which, however, have never been reported from experiments (Strassberg, 1959). Both observed phenomena, the wide scatter of the experimental results and the inception of cavitation at pressures much higher than the theoretical tensile strength reported in the literature indicate the existence of weak spots in the fluid that allows breaking of the continuum. Plesset (1969) comments that bubbles can grow to macroscopic dimensions starting from voids of size already beyond the molecular level under tensile stresses much lower than the theoretical values predicted for pure liquids.

Fisher (1948) reasons that, in a similar manner as very greatly subcooled liquids (such as glass) may fail by the nucleation and growth of a crack, a fluid may fail under tension by the growth of a cavity starting from very small holes. By applying methods of nucleation theory, Fisher predicts fracture tensions for several liquids with values, however, one order of magnitude higher than the experimental evidence. Some mechanism is required to stabilize preexisting nuclei in the liquid. For a very small bubble suspended in the liquid, the pressure inside the bubble is much higher than the pressure in the surrounded liquid because of surface–tension forces. This pressure difference diffuses the gas out of the gas void until it vanishes. On the other hand, bubbles not so small will rise and escape through the surface. Harvey and collaborators (1944a) introduced the idea of stabilized gas pockets attached to submicroscopic and hydrophobic crevices in the surface of the liquid container or in solid impurities. The size of these nuclei can be of the order of microns. Harvey *et al.* (1944b) supported their theory with results from a series of experiments in which previously pressurized and unpressurized samples of water were boiled at atmospheric pressure such that the saturation pressure corresponding to the boiling temperature was taken as a rough measure of the effective tensile strength. Although quite broad scatter was observed in the results for the pressurized samples, they all boiled at temperatures much higher than the saturation temperature for atmospheric pressure, which was the boiling temperature showed by the unpressurized samples. Tensile strength of 16 atm were reported in some samples previously pressurized.

Harvey *et al.* (1947) performed a different type of experiments to investigate tensile strength of water by high-speed removal of a squared-ended glass rod from a narrow glass tube containing the liquid. Meticoulous cleaning of the glass surfaces and pressurization of the sample with the rod in position were done to remove hydrophobic spots and gas nuclei. In terms of the rod-withdrawal speed, they found that 'if the rod surface contained glass nuclei, or was hydrophobic and free of gas nuclei, cavitation ocurred at the rear end when the velocity was less than 3 m/s, but if completely hydrophilic and free of gas nuclei, the velocity could be 37 m/s (...) without cavitation.' Knapp (1958) confirmed Harvey's results performing experiments at a rather larger scale. Strasberg (1959) explored the onset of acoustically-induced cavitation in tap water finding that microscopic undissolved air cavities, which show a slow motion toward the surface, play an important role as nuclei. Apfel (1970) extended Harvey's theory to consider the condition required in a liquid for the inception of a vapor cavity from a solid impurity in the liquid. Crum (1970) examined the crevice model of Harvey *et al.* comparing its predictions with experimental evidence.

From the standpoint of hydrodynamic cavitation, stream nuclei carried by the moving liquid as particulates or microbubbles have a greater contribution as sites for onset of cavitation than the surface nuclei originated in crevices or cracks on the solid boundaries (Billet 1985 and references therein). Turbulence has been shown to influence cavitation inception and its effect has been accounted for in models through the phase-change threshold (Singhal *et al.* 2002).

The inception of a cavity can be an abrupt event, where the liquid must rupture, instead of a continuous one. Chen & Israelachvili (1991) and Kuhl *et al.* (1994) monitored the elastohydrodynamic deformations of two curve surfaces that move relative to each other separated by a thin–liquid film of nanoscopic dimensions. A low molecular weight polymer liquid of polybutadiene and bare mica smooth surfaces having strong adhesion to the liquid were utilized in the tests. When the surfaces move normally with a slow separation speed they bulge outward becoming pointed at the location of the shortest surface separation. This shape indicates the existence of a tensile stress acting on the surface. If the separation speed is increased beyond a critical value, a vapor cavity opens in the liquid at the position of the shortest separation, reducing the tensile stress, while the pointed surfaces suddenly recover their original shape. Chen & Israelachvili (1991) also used surfactant–coated mica surfaces, which have weak adhesion to the liquid, resulting in cavity formation at the liquid–solid interface. Kuhl *et al.* (1994) considered lateral sliding of a curved surface over a mostly plane surface with a thin liquid film in between. Describing the shape of the sliding element, they observed that 'the leading edge becomes more rounded and lifts off while the trailing edge becomes more pointed.' For a sliding speed larger than some critical value, the pointed trailing edge snaps back, while a small cavity opens in the wake.

Cavitation inception has been observed in liquids undergoing shearing, suddenly changing the rhelogical response of the samples. Bair and Winer (1990) inferred cavitation inception by detecting yielding of a synthetic oil during rheological tests using a rotating concentric cylinder rheometer for a shear stress near the hydrostatic pressure (1.73 MPa). A similar phenomenon was noticed by Bair and Winer (1992) for polybutene in simple shear at low pressures (0.1 to 1 MPa) for a shear stress of 0.075 MPa in excess of the internal absolute pressure. This magnitude may represent the amount of tension that this liquid can resist without the opening of a cavity. Archer, Ternet & Larson (1997) visualized the opening of bubbles within a sample of low–molecular–weight polysterene subjected to start-up of steady shearing flow. They noticed that bubbles seemed to appear near dust particles. As a consequence of cavitation, the shear stress abruptly drops after it reaches a maximum of 0.1 MPa. Kottke *et al.* (2005) observed the inception of cavities in polybutene undergoing shearing tests using a Couette viscometer. Cavities become visible when the measured shear stress matches the ambient pressure. According to their principal normal stress cavitation criterion (PNSCC), this result implies that the sample liquid is not able to withstand tension. They suggest that cavitation grows from preexisting nuclei stabilized in some cracks or crevices on the solid boundaries.

The previous survey has shown that the idea of minute gas and vapor pockets in the liquid acting as nucleation sites is plausible and generally accepted. Nevertheless, a precise definition of the cavitation threshold and a clear description of the wide gamut of factors that influence this critical value is yet to be accomplished. We use the words 'cavitation threshold' and 'breaking strength' as synonymous with the threshold at which the liquid continuum will fracture. This threshold can vary from place to place in a sample. The threshold need not be a material parameter. In the case of heterogeneous nucleation, the cavitation threshold depends on the sample preparation, the density and nature of nucleation sites. In the case of homogeneous nucleation, the threshold may be taken as the vapor pressure. The vapor pressure is a thermodynamic quantity which is defined for uniform isotropic samples for which the stress tensor is isotropic; for static samples, bubble nucleation is a function of pressure and nothing else. In this paper, the cavitation threshold, p_c, is not necessarily the vapor pressure; this value is regarded as given and is not a subject for study here. For liquid which cannot withstand tension, $p_c = 0$.

17.2 Viscous potential flow analysis of stress induced cavitation in an aperture flow

It is well known that cavitation may be induced at sharp edges of the inlet of nozzles such as those used in atomizers. It is at just such edges that the pressure of an inviscid fluid into a nozzle is minimum. At higher

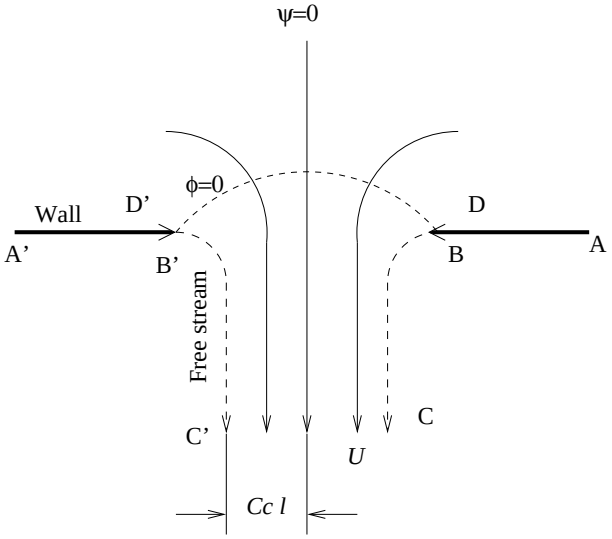

Fig. 17.1. Flow through an aperture in a flat plate.

pressure drops (larger cavitation number) the liquid in the nozzle may break away from the nozzle wall; the flow then attaches to the sharp edge of the nozzle and is surrounded by atmospheric gas. The term incipient cavitation is used to define the situation where cavitation first appears. The term supercavitation describes the situation where there is a strong cavitation flow near the nozzle exit, which is very beneficial to atomization. Total hydraulic flip describes the situation where the liquid jet completely separates from the nozzle wall. Hydraulic flip occurs in a variety of nozzles of different cross sections provided that the edge at inlet is sharp and not round. The aperture flow in a flat plate considered here (figure 17.1) is a nearly perfect two dimensional model of total hydraulic flip. Experiments documenting the transition to hydraulic flip from cavitating have been presented by Bergwerk (1959), Soteriou *et al.* (1995), Chaves *et al.* (1995), Laoonual *et al.* (2001) and a few others.

The outstanding property of the hydraulic flip is the disappearance of any sign of the cavitation that was there before the flow detached. To our knowledge, reports of the observations of the disappearance of cavitation are for very low viscosity liquids, such as water and diesel oil. In the analysis of aperture flow which follows, we find cavitation at the sharp edge for all fluids with viscosity larger than zero, but for low viscosity liquids it would be very hard to observe.

Our analysis is based on the theory of stress induced cavitation; the flow will cavitate at places where the principal tensile stress $T_{11} > -p_v$ where p_v is the vapor pressure. The theory of viscous potential flow allows us to compute these stresses directly and easily from the classical potential flow solution for aperture flow. Liquid samples which are not specially prepared ordinarily do not cavitate at the vapor pressure; various impurities can reduce the cavitation threshold and degassing followed by massive pressurization can increase the cavitation threshold. It is more realistic to think of p_v as the breaking strength of the liquid which depends on the history of the liquid sample. Readers may find it convenient to consider the case $p_v = 0$; in this case the sample will fail under tension.

17.2.1 Analysis of stress induced cavitation

The aperture flow in a flat plate is shown in figure 17.1. The magnitude in the resulting jet will reach some uniform value U downstream of the edges. The half-width of the jet is $C_c\ell$, where C_c is the contraction coefficient and ℓ is the half-width of the aperture. The complex potential for this flow is given implicitly by (Currie 1974, p.129)

$$f(z) = \phi + \imath\psi = -\frac{2C_c\ell U}{\pi} \ln\left\{\cosh\left[\ln\left(U\frac{\mathrm{d}z}{\mathrm{d}f}\right)\right]\right\} - \imath C_c\ell U. \tag{17.2.1}$$

The stress is calculated by

$$\mathbf{T} = -p\mathbf{1} + 2\mu\nabla \otimes \nabla\phi. \tag{17.2.2}$$

The pressure can be calculated using Bernoulli's equation

$$p + \frac{\rho}{2}(u^2 + v^2) = p_d + \frac{\rho}{2}U^2 = p_u, \tag{17.2.3}$$

where p_u is the upstream pressure and p_d is the downstream pressure at a position where the velocity reaches the uniform velocity U. The velocities are evaluated using from the potential

$$u = \frac{1}{2}\left(\frac{\mathrm{d}f}{\mathrm{d}z} + \frac{\mathrm{d}\bar{f}}{\mathrm{d}\bar{z}}\right), \qquad v = \frac{\imath}{2}\left(\frac{\mathrm{d}f}{\mathrm{d}z} - \frac{\mathrm{d}\bar{f}}{\mathrm{d}\bar{z}}\right). \tag{17.2.4}$$

It follows that the rate of strain tensor is

$$2\mathbf{D} = \begin{pmatrix} \left(\dfrac{\mathrm{d}^2 f}{\mathrm{d}z^2} + \dfrac{\mathrm{d}^2 \bar{f}}{\mathrm{d}\bar{z}^2}\right) & \imath\left(\dfrac{\mathrm{d}^2 f}{\mathrm{d}z^2} - \dfrac{\mathrm{d}^2 \bar{f}}{\mathrm{d}\bar{z}^2}\right) \\ \imath\left(\dfrac{\mathrm{d}^2 f}{\mathrm{d}z^2} - \dfrac{\mathrm{d}^2 \bar{f}}{\mathrm{d}\bar{z}^2}\right) & -\left(\dfrac{\mathrm{d}^2 f}{\mathrm{d}z^2} + \dfrac{\mathrm{d}^2 \bar{f}}{\mathrm{d}\bar{z}^2}\right) \end{pmatrix}. \tag{17.2.5}$$

To use the maximum tension criterion for cavitation, the principal axes coordinates in which $2\mathbf{D}$ is diagonalized need to be found. In the two-dimensional case under consideration here, the diagonalized rate of strain tensor is

$$2\mathbf{D} = \begin{pmatrix} \lambda & 0 \\ 0 & -\lambda \end{pmatrix}, \quad \text{where} \quad \lambda = 2\left|\frac{\mathrm{d}^2 f}{\mathrm{d}z^2}\right|. \tag{17.2.6}$$

Thus the maximum tension T_{11} is given by

$$T_{11} = -p + \mu\lambda = -p_u + \frac{\rho}{2}(u^2 + v^2) + \mu\lambda, \tag{17.2.7}$$

and the cavitation threshold is given by

$$T_{11} = -p_v. \tag{17.2.8}$$

Combining (17.2.7) and (17.2.8), we obtain

$$T_{11} + p_v = -p_u + p_v + \frac{\rho}{2}(u^2 + v^2) + \mu\lambda = 0. \tag{17.2.9}$$

We use $\frac{\rho}{2}U^2$ to render (17.2.9) dimensionless

$$\begin{aligned} \frac{T_{11} + p_v}{\frac{\rho}{2}U^2} &= \frac{-p_u + p_v}{p_u - p_d} + \frac{u^2 + v^2}{U^2} + \frac{\mu\lambda}{\frac{\rho}{2}U^2} \\ &= -\frac{1+K}{K} + \left|\alpha(\frac{\phi}{\ell U}, \frac{\psi}{\ell U})\right|^2 + \frac{1}{R_e}\frac{2\pi}{C_c}\left|\beta(\frac{\phi}{\ell U}, \frac{\psi}{\ell U})\right| = 0, \end{aligned} \tag{17.2.10}$$

where the dimensionless parameters are defined as

$$\text{Cavitation} \quad \text{number} \quad K = \frac{p_u - p_d}{p_d - p_v}, \tag{17.2.11}$$

$$\text{Reynolds} \quad \text{number} \quad R_e = \frac{\rho\ell U}{\mu}, \tag{17.2.12}$$

and the complex functions α and β are given by

$$\alpha = \left[e^{\gamma} \pm \sqrt{e^{2\gamma} - 1}\right]^{-1}, \quad \beta = \left[e^{\gamma} \pm \frac{e^{2\gamma}}{\sqrt{e^{2\gamma} - 1}}\right]\alpha^3, \tag{17.2.13}$$

with

$$\gamma = -\frac{f + \imath C_c \ell U}{2C_c \ell U}\pi = -\frac{\pi}{2C_c}\frac{\phi}{\ell U} - \frac{\imath\pi}{2C_c}\frac{\psi}{\ell U} - \frac{\imath\pi}{2}. \tag{17.2.14}$$

The definition (17.2.11) for the cavitation number follows Bergwerk (1959) and Soteriou *et al.* (1995) and is somewhat different from the definition by Brennen in which the denominator is the dynamic stagnation pressure.

For a flow with given cavitation number K and Reynolds number, equation (17.2.10) gives the positions where cavitation inception occurs in terms of $\phi/\ell U$ and $\psi/\ell U$. The dimensionless description (17.2.10) is independent of the vapor pressure or any dimensional parameters entering into the definition of K and R_e.

17.2.2 Stream function, potential function and velocity

The complex potential of the flow (17.2.1) is implicit and not convenient to use. Therefore we invert the potential to obtain a function in the form $z = z(f)$. First we transform the variables as

$$z' = \frac{\pi z}{2C_c\ell}$$

which gives

$$U\frac{\mathrm{d}z}{\mathrm{d}f} = U\frac{\mathrm{d}z}{\mathrm{d}z'}\frac{\mathrm{d}z'}{\mathrm{d}\gamma}\frac{\mathrm{d}\gamma}{\mathrm{d}f} = -\frac{\mathrm{d}z'}{\mathrm{d}\gamma}. \tag{17.2.15}$$

By virtue of (17.2.14) and (17.2.15), we have

$$\gamma = \ln\left\{\cosh\left[\ln\left(-\frac{\mathrm{d}z'}{\mathrm{d}\gamma}\right)\right]\right\}$$

which can be written as

$$e^{\gamma} = -\frac{1}{2}\left[\frac{\mathrm{d}z'}{\mathrm{d}\gamma} + \left(\frac{\mathrm{d}z'}{\mathrm{d}\gamma}\right)^{-1}\right].$$

Thus we obtain

$$\frac{\mathrm{d}z'}{\mathrm{d}\gamma} = -e^{\gamma} - \sqrt{e^{2\gamma}-1}. \tag{17.2.16}$$

Integration of (17.2.16) gives

$$z' = -e^{\gamma} - \sqrt{e^{2\gamma}-1} + \frac{1}{2\imath}\ln\left(\frac{1+\imath\sqrt{e^{2\gamma}-1}}{1-\imath\sqrt{e^{2\gamma}-1}}\right) - \pi/2. \tag{17.2.17}$$

We prescribe the value of the complex potential and compute the corresponding position z by (17.2.17). The computational results are shown in figure 17.2(a) where the stream and potential functions are plotted in the z plane. The velocity is then obtained using (17.2.4) and shown as a vector plot in figure 17.2(b).

Nearly all the flow through the aperture emanates from regions of irrotationality; vorticity generated by no-slip at the wall of the aperture is confined to a boundary layer and its effects are neglected here. Stress-induced cavitation can arise where the irrotational stresses are very large, but the maximum stress, hence the point of inception, is probably at the edge of the aperture where the vorticity is greatest. We will show in the next section that viscous potential flow predicts cavitation at the tip whenever the viscosity is larger than zero. Therefore the effects of vorticity could be important only if they were such as to suppress cavitation at the tip. Even in this case, the fluid could cavitate in the irrotational region outside the boundary layer. We note that the boundary layer is shrinking near the tip of the aperture due to favorable pressure gradient; the aperture flow is analogous to the flow with suctions on the wall which suppress the boundary layer thickness. Therefore the boundary layer could be very thin near the tip of the aperture and our theory can be applied to the region near the tip but outside the boundary layer. Our results indicate that cavitation may occur in such regions. The main unsolved question is the extend to which vorticity generated at the boundary of the aperture corrupts the main flow when the Reynolds number is not large.

17.2.3 Cavitation threshold

We use water as an example to illustrate the stress induced cavitation. The vapor pressure of water at 20°C is 2339 Pa and we assume that the downstream pressure is the atmospheric pressure: $p_d = p_a = 10^5$Pa. First we

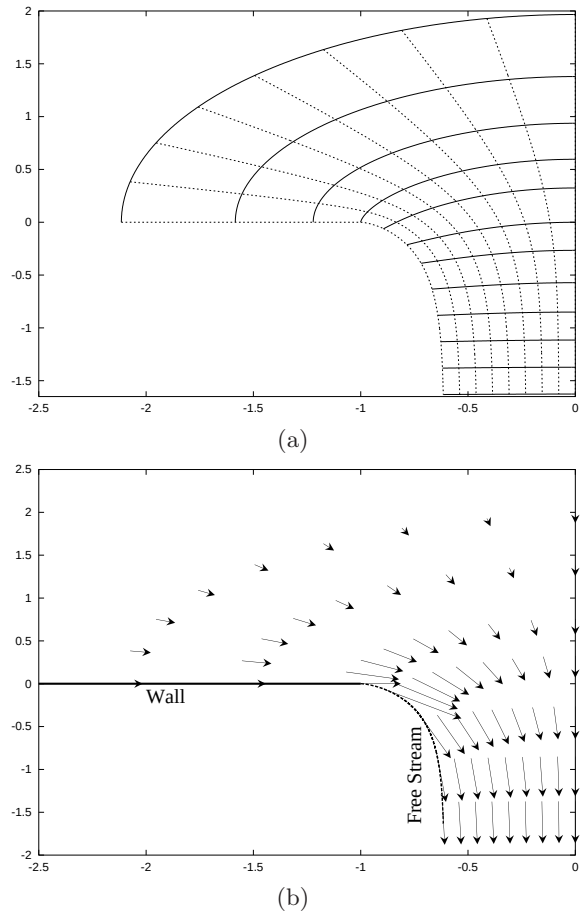

Fig. 17.2. (**a**). The stream and potential functions in the z plane. The x and y coordinates are normalized as $(x/\ell, y/\ell)$. The stream and potential functions are in the range $-C_c < \psi/(\ell U) < 0$ and $-0.375 < \phi/(\ell U) < 1.75$, respectively. The contraction coefficient $C_c = \pi/(2+\pi) = 0.611$ and the edge of the nozzle is at $(x/\ell, y/\ell) = (-1, 0)$. (**b**) The velocity in the z plane. Only half of the flow field is shown due to the symmetry.

calculate the pressure using the Bernoulli's equation (17.2.3). The pressure does not depend on the Reynolds number and we show the pressure distribution for different cavitation numbers in Fig. 17.3.

The pressure criterion for cavitation is that cavitation occurs when the pressure is lower than the vapor pressure. The minimum pressure in the aperture flow is the downstream pressure and $p_d = 10^5\text{Pa} > p_v = 2339\text{Pa}$. Thus the pressure criterion predicts no cavitation for the case under consideration. However, we will show that cavitation occurs in the aperture flow according to the tensile stress criterion (Joseph 1995, 1998).

Next we include the viscous part of the stress and consider the maximum tension T_{11}. The cavitation criterion is that cavitation occurs when $T_{11} + p_v \geq 0$. T_{11} depends on both the Reynolds number and the cavitation number. We show the contour plot for $(T_{11}+p_v)/(\rho U^2/2)$ with different R_e and K in Fig. 17.4. More graphs, with different values of R_e and K can be found in Funada *et al.* 2006 (see http://www.aem.umn.edu/people/faculty/joseph/ViscousPo

Although the velocity is continuous everywhere in the aperture flow, its derivative, and therefore the viscous stress, are singular at the sharp edge. Thus at the sharp edge for all fluids with viscosity larger than zero, $T_{11} + p_v$ is always larger than zero and cavitation occurs. In our analysis here, we shall avoid the singular points and calculate the stresses at points very close to the edges. This is partially justified by the fact that in reality the edges are not perfectly sharp. As Chaves *et al.* (1995) noted "... Microscopic pictures of the nozzle inlet still show however small indentations of the corner, i.e. less than 5 micrometers." (The diameter of the nozzle in their experiments was 0.2 mm or 0.4 mm).

In figure 17.4, the curves on which $T_{11} + p_v = 0$ are the thresholds for cavitation. On the side of a $T_{11} + p_v = 0$

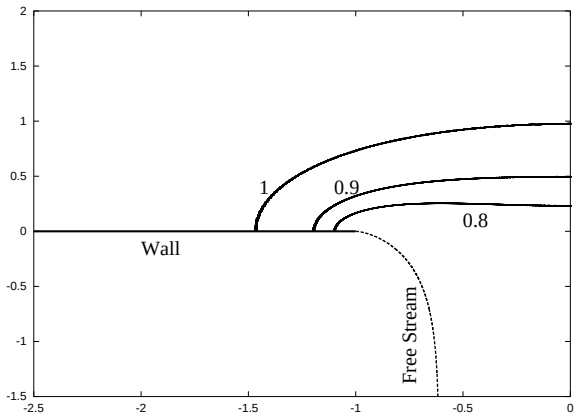

(a)

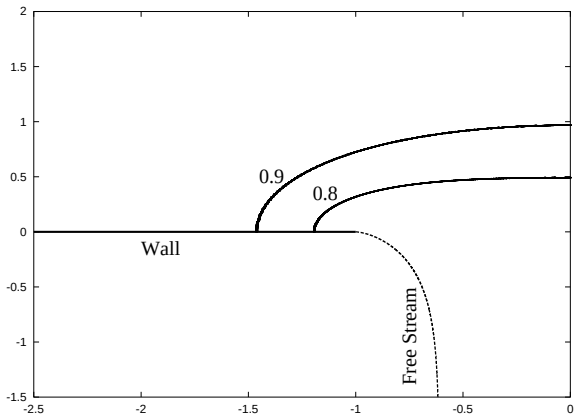

(b)

Fig. 17.3. Contour plot for $(p - p_v)/(\rho U^2/2)$ in the $(x/\ell, y/\ell)$ plane, (a) $K = 10$; (b) $K = 1000$. In the flow field, $p - p_v > 0$ everywhere. Thus there is no cavitation according to the pressure criterion.

curve which is closer to the sharp edge, $T_{11} + p_v > 0$ and cavitation appears; on the other side of the $T_{11} + p_v = 0$ curve, $T_{11} + p_v < 0$ and there is no cavitation.

In figure 17.5, we single out the threshold curves on which $T_{11} + p_v = 0$ and plot these curves corresponding to different R_e at $K = 1$ and $K = 100$. The cavitation region is larger when R_e is smaller; when R_e is larger, cavitation is confined to a very small region near the edge of the aperture. The cavitation region is larger and is stretched to far downstream when K is larger. This shows that supercavitation, i.e. cavitation extending to the nozzle exit, can be achieved when K is large. This predicted supercavitation occurs under hydraulic flip condition, and is not the same as the supercavitation observed in experiments.

Now we focus on the point $(x/\ell = -1.01,\ y/\ell = 0)$, which is upstream to the left sharp edge and very close to it. We can identify values of R_e and K which give rise to $T_{11} + p_v = 0$ at this point. These values can be plotted on the R_e and K plane as shown in figure 17.6. On one side of the plotted curve, $T_{11} + p_v > 0$ and cavitation occurs at this point; on the other side, there is no cavitation at this point. Figure 17.6 shows that small R_e and large K favor cavitation. This can be understood readily because small R_e leads to large viscous stress and large K leads to small pressure. Both of these effects contribute to a large value of $T_{11} = -p + \mu\lambda$.

17.2.4 Conclusions

We use the potential flow through an aperture as a 2D model to study the hydraulic flip observed in injection flows at a nozzle. The pressure in the flow field is computed using Bernoulli's equation and the viscous stress is evaluated on the potential. The stress tensor is transformed to the principal axes coordinates and the principal

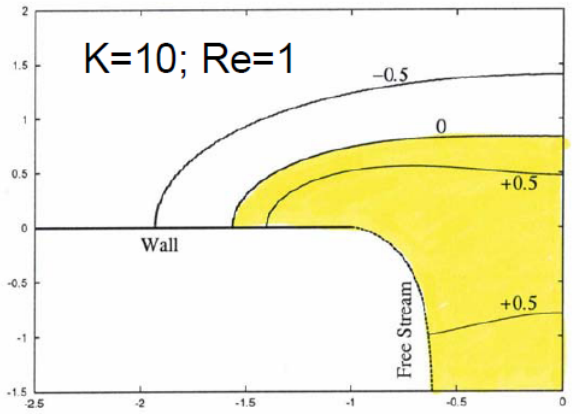

(a)

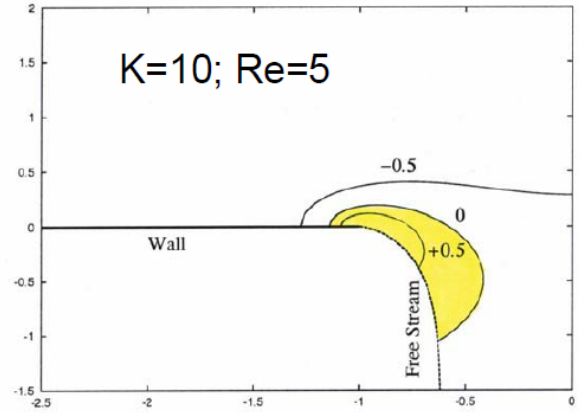

(b)

Fig. 17.4. Contour plot for $(T_{11} + p_v)/(\rho U^2/2)$ in the $(x/\ell, y/\ell)$ plane, (a) $K = 10$ and $R_e = 1$; (b) $K = 10$ and $R_e = 5$. Cavitation occurs inside the curve on which $T_{11} + p_v = 0$. Figure 17.3(a) and 17.4(a) can be compared to show the effect of the viscous stress cavitation.

stress T_{11} is obtained. If T_{11} is larger than the negative value of the vapor pressure p_v, the flow will cavitate. We find that cavitation occurs for all fluids with viscosity larger than zero at the sharp edges of the aperture. The region in which cavitation occurs depends on the Reynolds number R_e and the cavitation number K. The cavitation region is larger if R_e is smaller and K is larger. The cavitation is confined to very small regions near the edges of the aperture when R_e is larger and K is smaller.

Researchers do not observe cavitation in hydraulic flip. The reason may be that the Reynolds numbers in nozzle flows are usually very high (in the order of thousands and tens of thousand). Thus even if cavitation occurred at the edge of the nozzle, the cavities would collapse quickly outside the small cavitation region (the time for cavities to collapse is in the order of microseconds according to Chaves *et al.* 1995) and would be very difficult to observe. The effects of liquid viscosity on cavitation are apparently not known; we could not find an evaluation of these effects in the literature. The results obtained here and in Joseph (1998) suggest that an increase in viscosity lowers the threshold to stress induced cavitation.

17.2.5 Navier-Stokes simulation

A full Navier-Stokes simulation of stress-induced cavitation in aperture flow was carried out by Dabiri, Sirignano and Joseph 2006 to evaluate the conclusions stated in 17.2.4. The computations were done using the finite volume package SIMPLER. The free surface was generated using level sets. The effects of surface tension were not computed. To secure convergence using this numerical package it is necessary to have an active ambient. In these calculations the gas-liquid density ratio is 10^{-4} and the viscosity ratio is 1.5×10^{-4}. The computations

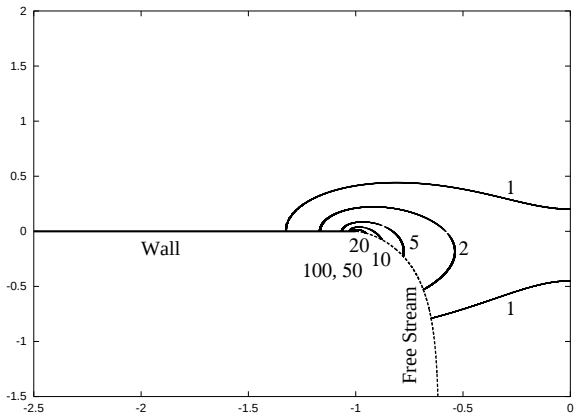

(a)

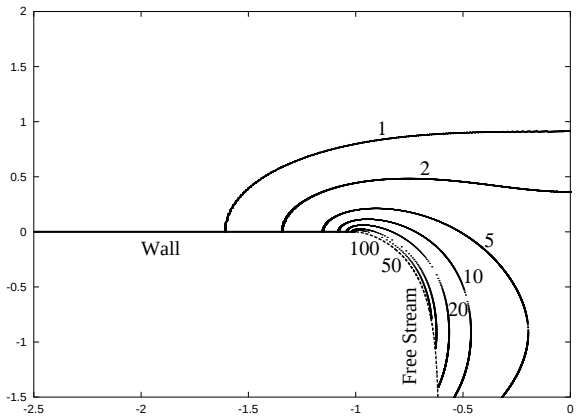

(b)

Fig. 17.5. The cavitation threshold curves on which $T_{11} + p_v = 0$ in different flows with $R_e = 1$, 2, 5, 10, 20, 50 and 100. The cavitation number is fixed at $K = 1$ in (a) and $K = 100$ in (b). Cavitation occurs inside the curve on which $T_{11} + p_v = 0$.

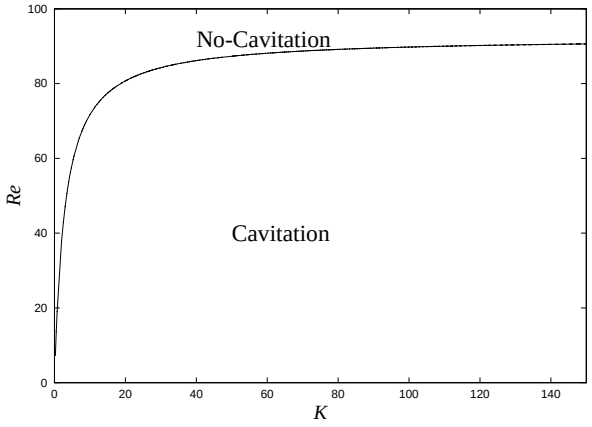

Fig. 17.6. The curve on which $T_{11} + p_v = 0$ at the point $(x/\ell = -1.01,\ y/\ell = 0)$ in the R_e vs K plane. Below the curve, $T_{11} + p_v > 0$ and cavitation occurs at the point; above the curve, $T_{11} + p_v < 0$ and there is no cavitation at the point.

are not sensitive to changes of these ratios for small ratios. The Reynolds number in these calculations is based on the Bernoulli's velocity of the jet, which is larger than the average velocity of jet for low Reynolds number. For example, for flow with $Re = 1$ the jet velocity is about 20% of Bernoulli velocity and this causes the strain rates and therefore the stresses to be scaled down with the same ratio. This could be the reason that the regions with large stresses are smaller in the NS solution.

The results of the computations are exhibited in figures 17.7 and 17.8. Isolines for tensile stresses are marked

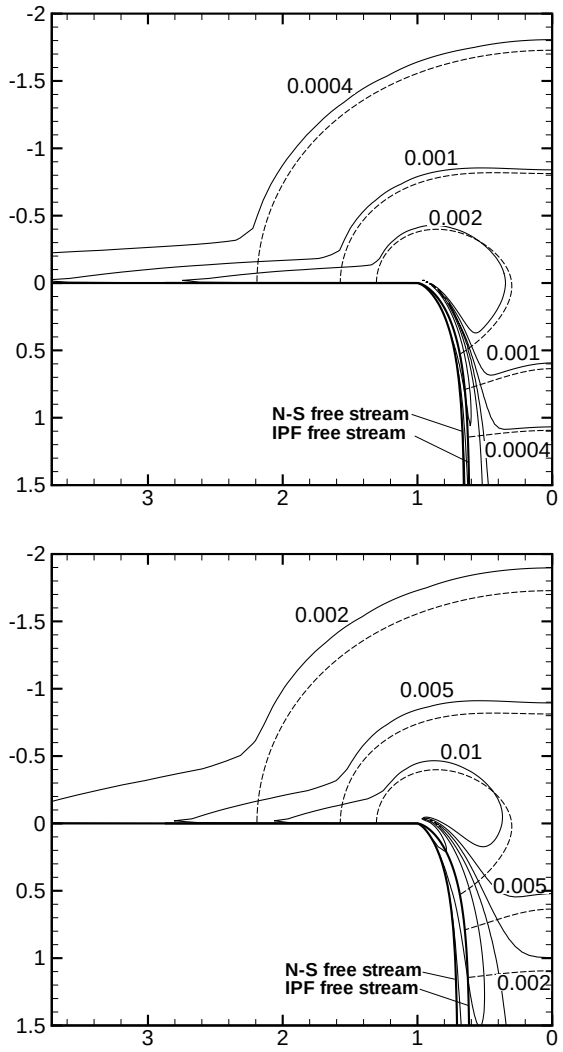

Fig. 17.7. Viscous stress contours for Navier-Stokes solution (solid lines) compared to viscous potential flow solution (dashed lines) for ρ-ratio=1e^{-4} and μ-ratio=1.5e^{-4} (Top): Re =500, (Bottom): Re =100.

on the figures; high numbers identify high stresses. The liquid is most at risk to stress induced cavitation when the stress level is positive and high. The regions of high stress are near the corner in the NS and VPF calculations. We could say that the computations of regions vulnerable to stress induced cavitation are given with reasonable accuracy by VPF, even for low Reynolds numbers.

It is of interest that the free surface in the hybrid VPF calculation done here is a free surface streamline associated with potential flow of an inviscid fluid. The pressure is constant on the free streamline, so that the speed there is constant as shown by the Bernoulli equation. For a true VPF, the normal stress balance contains a viscous term and the pressure is not constant in the liquid on the free surface. The free streamline theory does not apply to VPF. Probably, the free surface computed with VPF would be closer to the free surface given by the NS solution. It is of interest to create VPF theory to update the free streamline theory of IPF.

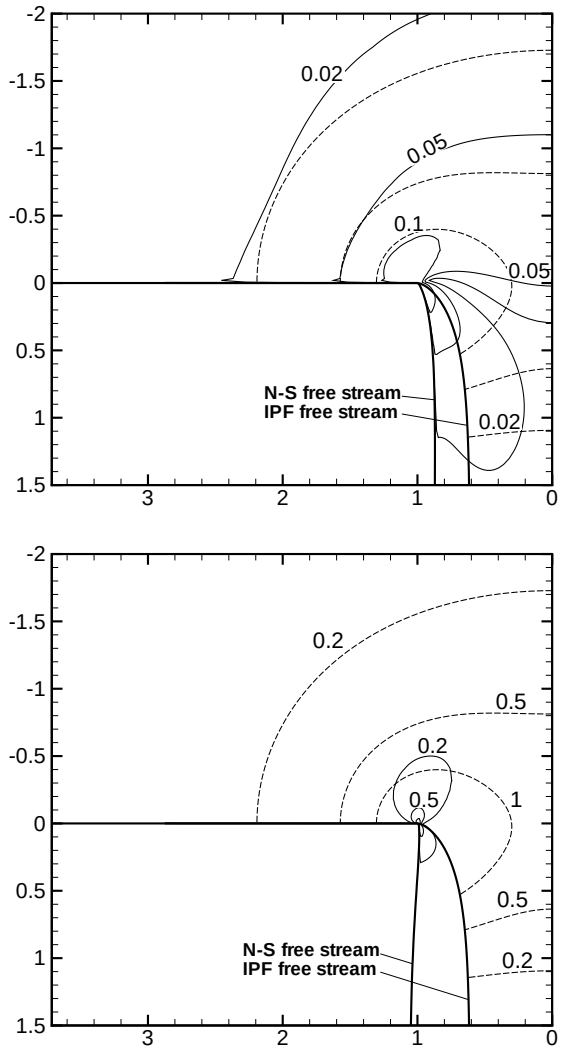

Fig. 17.8. Viscous stress contours for Navier-Stokes solution (solid lines) compared to viscous potential flow solution (dashed lines) for ρ-ratio=1e^{-4} and μ-ratio=1.5e^{-4} (Top): Re =10, (Bottom): Re =1.

17.3 Streaming motion past a sphere

Padrino *et al.* 2006 solved the problem of stress induced cavitation in the axisymmetric streaming flow past a sphere. This is a canonical problem for cavitation behind blunt bodies; the application of the maximum tension theory to this problem is new. Padrino *et al.* derived explicit analytic formulas for this theory in the Stokes flow limit and for the irrotational flow of a viscous fluid. The cavitation thresholds for these analytic approaches were compared with exact results from a direct numerical simulation. The direct simulation allows us to compare cavitation thresholds between the stress induced maximum tension theory with pressure alone theory. (This is different than the the calculation in aperture flow where the flow is irrotational and the fluid viscous. In the irrotational flow of a viscoius fluid the pressure is given by Bernoulli's equation and does not depend on viscosity.) Both theories computed with the same Navier Stokes package depend on the Reynolds number. The liquid is always at greater risk to cavitation to viscous stresses than to the pressure alone theory. The difference between the approaches of the two theories increases as the Reynolds number decreases and is greatest at the boundary of the sphere where the motion is pure shear and if the shear stress is large enough the liquid will fracture even when the pressure is much higher than the critical pressure. Readers with an interest in the theory of stress induced cavitaion will profit from reading the paper of Padrino *et al.* . For our purpose here we can show how the the cavitation threshold formula is formed from the irrotational theory.

17.3.1 Irrotational flow of a viscous fluid

Kuhn de Chizelle, Ceccio & Brennen (1995) studied the interactions between a travelling cavity and the potential flow exterior to the thin boundary layer around an axisymmetric headform. Liu & Brennen (1998) presented a mechanistic model for hydrodynamic cavitation event rate for flow over a headform that utilizes the pressure distribution given by potential flow modified to accomodate boundary layer effects. There is no literature other than the paper of Funada *et al.* (2006) on analysis of stress-induced cavitation using potential flow. The analysis of this problem, given below, is completely transparent; the effects of vorticity on cavitation on a solid sphere are mainly associated with the formation of wakes and the displacement of the region of irrotational flow. Considering the irrotational flow of a viscous fluid, the principal strain-rates and stresses and their corresponding principal directions can be determined. Then, the maximum tension criterion is applied to evaluate the cavitation threshold. The theory of viscous potential flow considered here includes the viscous components in the definition of the state of stress in the flowing liquid.

Irrotational flows of incompressible viscous fluids satisfy the Navier-Stokes equations and give rise to the usual Bernoulli equation because

$$\mu\nabla^2\mathbf{u} = \mu\nabla\nabla^2\phi = 0, \tag{17.3.1}$$

no matter what the value of μ. The stresses are given by

$$\mathbf{T} = -p\mathbf{1} + 2\mu\nabla\otimes\nabla\phi = \frac{1}{3}\mathrm{Tr}\,(\mathbf{T})\,\mathbf{1} + 2\mu\nabla\otimes\nabla\phi, \tag{17.3.2}$$

where p is the average stress given by (17.1.2).

The flow is axisymmetric and steady and the potential $\phi(r,\theta)$ satisfies $\nabla^2\phi = 0$. In this analysis, spherical-polar coordinates are utilized.

The potential for this flow is

$$\phi = U\left(r + \frac{1}{2}\frac{a^3}{r^2}\right)\cos\theta. \tag{17.3.3}$$

The velocity $\mathbf{u} = \mathbf{e}_r u_r + \mathbf{e}_\theta u_\theta$ is given by

$$u_r = \frac{\partial\phi}{\partial r} = U\left(1 - \frac{a^3}{r^3}\right)\cos\theta, \tag{17.3.4}$$

$$u_\theta = \frac{1}{r}\frac{\partial\phi}{\partial\theta} = -U\left(1 + \frac{1}{2}\frac{a^3}{r^3}\right)\sin\theta. \tag{17.3.5}$$

Note that the no-slip condition must be relaxed for viscous potential flow. So, the boundary layer is not resolved. The pressure is given by

$$\begin{aligned} p &= p_\infty + \rho\frac{U^2}{2} - \frac{\rho}{2}\left(u_r^2 + u_\theta^2\right) \\ &= p_\infty + \rho\frac{U^2}{2}\left[1 - \left(1 - \frac{a^3}{r^3}\right)^2 \cos^2\theta - \left(1 + \frac{1}{2}\frac{a^3}{r^3}\right)^2 \sin^2\theta\right], \end{aligned} \tag{17.3.6}$$

where p_∞ is the constant value of the pressure at infinity. The non-zero components of the viscous stress

$$2\mu\mathbf{D}\left[\nabla\phi\right] \tag{17.3.7}$$

are

$$2\mu D_{rr} = 2\mu\frac{\partial u_r}{\partial r} = 6\mu U\frac{a^3}{r^4}\cos\theta, \tag{17.3.8}$$

$$2\mu D_{\theta\theta} = 2\mu\left(\frac{1}{r}\frac{\partial u_\theta}{\partial\theta} + \frac{u_r}{r}\right) = -3\mu U\frac{a^3}{r^4}\cos\theta, \tag{17.3.9}$$

$$2\mu D_{\varphi\varphi} = 2\mu\left(\frac{u_r}{r} + \frac{u_\theta}{r}\cot\theta\right) = -3\mu U\frac{a^3}{r^4}\cos\theta, \tag{17.3.10}$$

$$2\mu D_{r\theta} = \mu\left[r\frac{\partial}{\partial r}\left(\frac{u_\theta}{r}\right) + \frac{1}{r}\frac{\partial u_r}{\partial\theta}\right] = 3\mu U\frac{a^3}{r^4}\sin\theta. \tag{17.3.11}$$

The matrix of components

$$2\mu\begin{bmatrix} D_{rr} & D_{r\theta} & 0 \\ D_{r\theta} & D_{\theta\theta} & 0 \\ 0 & 0 & D_{\varphi\varphi} \end{bmatrix} = 3\mu U\frac{a^3}{r^4}\begin{bmatrix} 2\cos\theta & \sin\theta & 0 \\ \sin\theta & -\cos\theta & 0 \\ 0 & 0 & -\cos\theta \end{bmatrix} \tag{17.3.12}$$

can be rotated into diagonal form through an angle α satisfying

$$\tan 2\alpha = \frac{2}{3}\tan\theta. \tag{17.3.13}$$

From (17.3.13) we look for the angle α that puts by rotation with axis $\mathbf{e}_\varphi$ the direction given by the unit vector $\mathbf{e}_\mathrm{r}$ into the principal direction corresponding to the most tensile (or the least compressive) principal stress in the plane of the motion. Without lack of generality, we consider this angle α to be in the interval $-0.5 \le \alpha/\pi \le 0.5$.

The diagonal form of $2\mu\nabla\otimes\nabla\phi$ is given by

$$3\mu U\frac{a^3}{r^4}\begin{bmatrix} \frac{1}{2}\cos\theta + \frac{\sin\theta}{\sin 2\alpha} & 0 & 0 \\ 0 & \frac{1}{2}\cos\theta - \frac{\sin\theta}{\sin 2\alpha} & 0 \\ 0 & 0 & -\cos\theta \end{bmatrix}. \tag{17.3.14}$$

At $\theta = \pi/2$, where the pressure is smallest, $\alpha = \pi/4$ and the diagonal form is

$$3\mu U\frac{a^3}{r^4}\begin{bmatrix} 1 & 0 & 0 \\ 0 & -1 & 0 \\ 0 & 0 & 0 \end{bmatrix}, \tag{17.3.15}$$

giving rise to tension and compression.

We next consider the whole stress using (17.3.2), which may be written as

$$\mathbf{T} + p_\mathrm{c}\mathbf{1} = \left(-p + p_\mathrm{c}\right)\mathbf{1} + 2\mu\nabla\otimes\nabla\phi \tag{17.3.16}$$

with the addition of the cavitation threshold p_c. After arranging, expression (17.3.16) becomes

$$\begin{aligned} \frac{\mathbf{T} + p_\mathrm{c}\mathbf{1}}{\frac{1}{2}\rho U^2} &= -\left[K + 1 - \left(1 - \frac{a^3}{r^3}\right)^2\cos^2\theta - \left(1 + \frac{a^3}{2r^3}\right)^2\sin^2\theta\right]\begin{bmatrix} 1 & 0 & 0 \\ 0 & 1 & 0 \\ 0 & 0 & 1 \end{bmatrix} + \\ &\quad + \frac{3}{Re}\left(\frac{a}{r}\right)^4\begin{bmatrix} \cos\theta + \frac{2\sin\theta}{\sin 2\alpha} & 0 & 0 \\ 0 & \cos\theta - \frac{2\sin\theta}{\sin 2\alpha} & 0 \\ 0 & 0 & -2\cos\theta \end{bmatrix} \end{aligned} \tag{17.3.17}$$

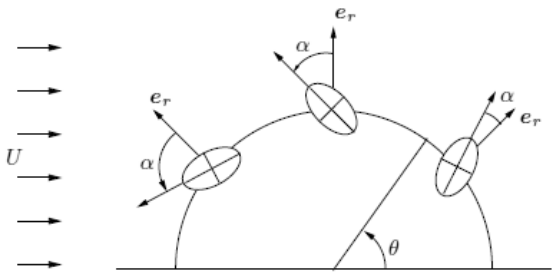

Fig. 17.9. Schematic view of the orientation of the principal directions in the plane of motion for irrotational flow of a viscous fluid according to (17.3.13) on the surface of the sphere. The major axis in the ellipse represents the maximum tensile stress. The angle α puts the direction defined by the unit outward normal vector $\boldsymbol{e}_r$ into the principal direction of the maximum tensile stress.

where

$$K = \frac{p_\infty - p_\mathrm{c}}{\frac{1}{2}\rho U^2} \tag{17.3.18}$$

is the cavitation number and

$$Re = \frac{\rho U a}{\mu} \tag{17.3.19}$$

is the Reynolds number.

For the viscous potential flow solution (17.3.17), one can show that at any point the most tensile (least compressive) and most compressive (least tensile) principal stresses lie in the plane of motion (i.e., the plane where the velocity vector is contained). Suppose now that T_{11} is the largest of the three principal values of stress. Then, according to the maximum tension theory, the locus of the cavitation threshold is given by

$$T_{11} + p_\mathrm{c} = 0, \tag{17.3.20}$$

giving rise to isolines $(a/r, \theta) = f(K_\mathrm{c}, Re)$ for the cavitation threshold. The largest values of the viscous irrotational stress are at the boundary $r = a$ where the neglected vorticity is largest. In §17.3.2, it is shown that $\theta = 0$ for very low Re and $\theta = \pi/2$ for very high Re are the points most vulnerable for cavitation under the respective conditions.

Equation (17.3.17) gives the form of the diagonalized stress tensor at each point (r, θ) in the axially symmetric flow. T_{11}, T_{22} and $T_{33} = T_{\varphi\varphi}$ are principal stresses in the principal axes coordinates with bases $\mathbf{e}_1$,$\mathbf{e}_2$, $\mathbf{e}_\varphi$. In the present case, the angle α changes with θ, $\tan 2\alpha = \frac{2}{3}\tan\theta$. A representation of the orientation of the principal axes in the plane of motion at the surface of the sphere $r = a$ as predicted by (17.3.13) is presented in Figure 17.9.

It is apparent from (17.3.17) that the largest stresses are at the boundary of the sphere where $r = a$. Certainly the liquid will cavitate when $K = (p_\infty - p_\mathrm{c}) / \left(\frac{\rho}{2}U^2\right) < 0$; only $K > 0$ is of interest. Using now the maximum tension criterion, we see that cavitation occurs for $0 < K < K_\mathrm{c}$ and the fluid is most at risk to cavitation for θ at which $K_\mathrm{c}(\theta)$ is greatest. For viscous potential flow, this most dangerous θ is at $\theta = 0$ when Re is small and at $\theta = \pi/2$ when Re is large. It follows that the place most at risk to cavitation runs from the rear stagnation point at $\theta = 0$ when Re is small to $\theta = \pi/2$ when Re is large.

Next contour plots with lines of constant K representing the cavitation threshold from (17.3.17) for various Re are presented and compared with the results from the numerical simulation and the Stokes solution for the lowest Re (see Figures 17.10, 17.11 and 17.12).

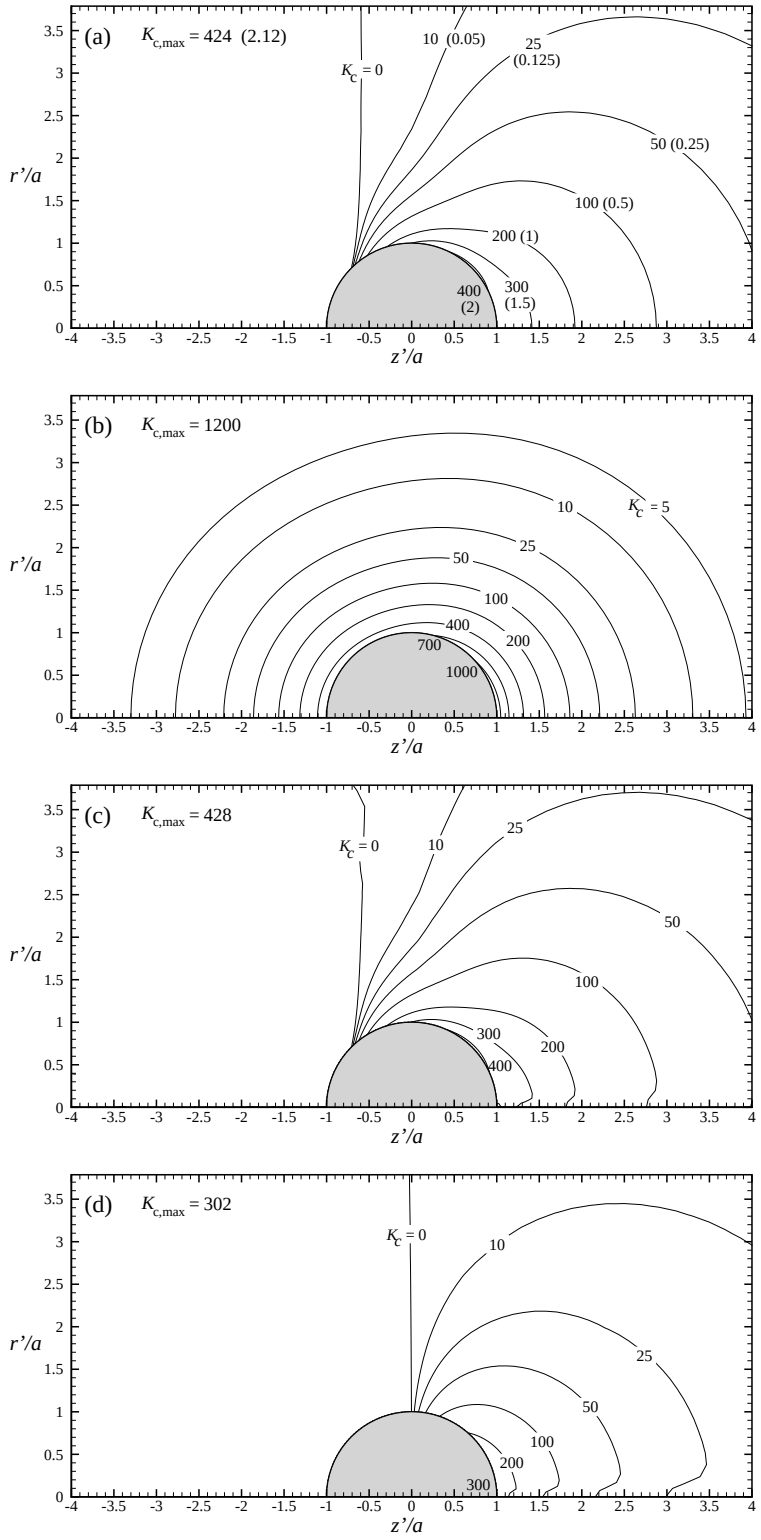

Fig. 17.10. Contours of critical cavitation number K_c given by the condition $T_{11} + p_c = 0$ according to the maximum tension criterion for a Reynolds number $Re = 0.01$ from (a) Stokes flow; (b) the irrotational flow of a viscous fluid (17.3.17), and (c) numerical solution; the pressure criterion given by $K_c = -c_p$ is shown in (d) using the numerical pressure field. The cavitation number K is defined in terms of the dynamic pressure $\rho U^2/2$. For a given cavitation number K, cavitation occurs in the region where $K < K_c$. A different normalization of the cavitation number and of the critical cavitation number is used for Stokes flow rather than the normalization used for the other cases (17.3.18). The contour lines for the normalization of $p_\infty - p_c$ with the viscous-stress scale $\mu U/a$ are presented in parenthesis in (a). The ratio of the normalization factors is $Re/2$.

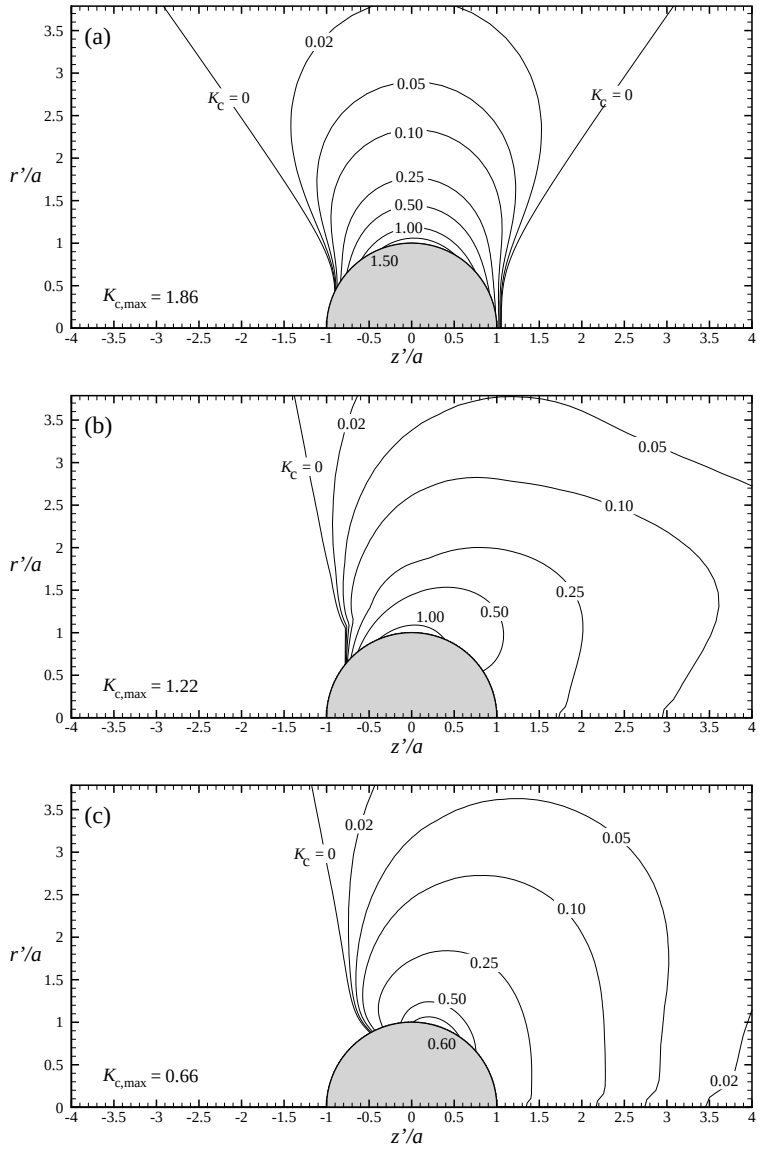

Fig. 17.11. Contours of critical cavitation number K_c given by the condition $T_{11} + p_c = 0$ according to the maximum tension criterion for a Reynolds number $Re = 10$ from (a) the irrotational flow of a viscous fluid (17.3.17), and (b) numerical solution; the pressure criterion given by $K_c = -c_p$ is shown in (c) using the numerical pressure field. The cavitation number K is defined in terms of the dynamic pressure $\rho U^2/2$. For a given cavitation number K, cavitation occurs in the region where $K < K_c$.

17.3.2 An analysis for maximum K

Here we look for the angular position on the surface of the sphere at which the maximum value of the cavitation number K occurs. This position is the most vulnerable to cavitation.

For the potential flow solution, the stress tensor is given in (17.3.17). Suppose that T_{11} is the maximum tensile stress such that $T_{11} \geq T_{33} \geq T_{22}$. If we consider the surface of the sphere $r = a$ and use the cavitation criterion $T_{11} + p_c = 0$, we obtain from (17.3.17)

$$K = \frac{9}{4}\sin^2\theta - 1 + \frac{3}{Re}\left(\cos\theta + \frac{2\sin\theta}{\sin 2\alpha}\right), \tag{17.3.21}$$

Considering the expression for α given in (17.3.13)

$$\tan 2\alpha = \frac{2}{3}\tan\theta, \tag{17.3.22}$$

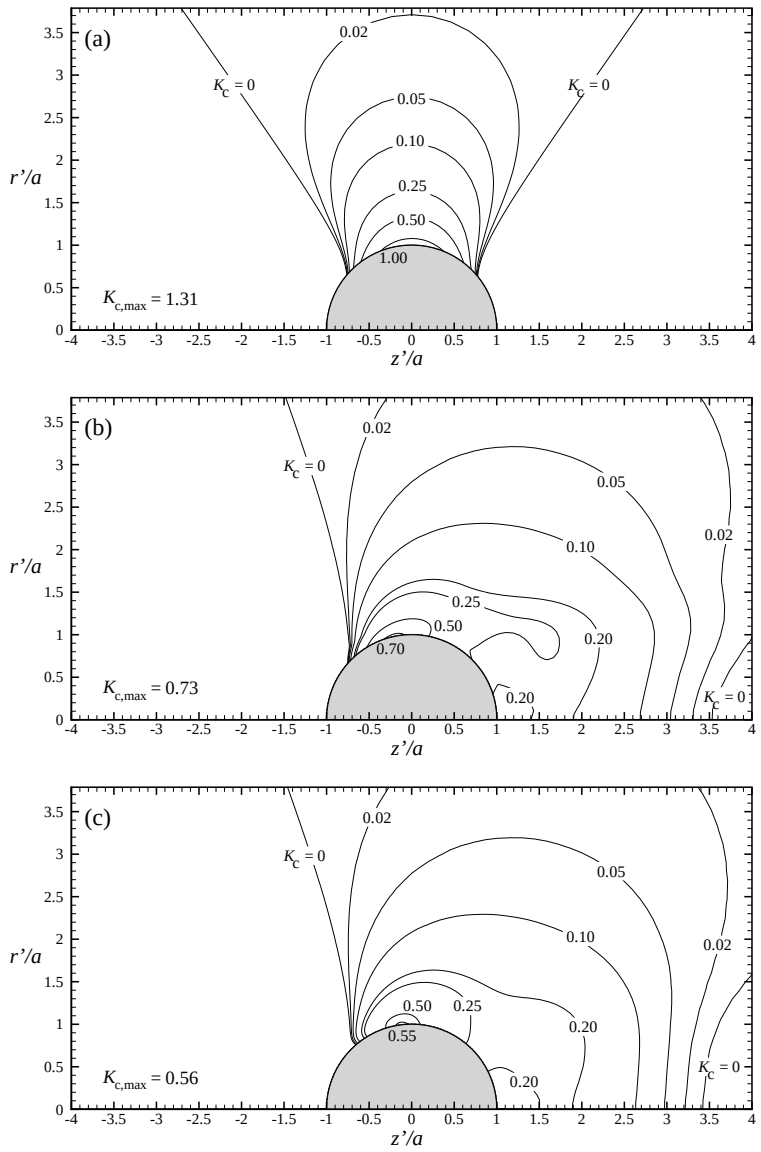

Fig. 17.12. Contours of critical cavitation number K_c given by the condition $T_{11} + p_c = 0$ according to the maximum tension criterion for a Reynolds number $Re = 100$ from (a) the irrotational flow of a viscous fluid (17.3.17), and (b) numerical solution; the pressure criterion given by $K_c = -c_p$ is shown in (c) using the numerical pressure field. The cavitation number K is defined in terms of the dynamic pressure $\rho U^2/2$. For a given cavitation number K, cavitation occurs in the region where $K < K_c$.

we can write (17.3.21) as

$$K = \frac{9}{4}\sin^2\theta - 1 + \frac{3}{Re}\left[\cos\theta + 3\cos\theta\sqrt{1 + \frac{4}{9}\tan^2\theta}\right], \tag{17.3.23}$$

for $0 \le \theta \le \pi/2$, whereas

$$K = \frac{9}{4}\sin^2\theta - 1 + \frac{3}{Re}\left[\cos\theta - 3\cos\theta\sqrt{1 + \frac{4}{9}\tan^2\theta}\right], \tag{17.3.24}$$

for $\pi/2 < \theta \le \pi$. Taking the derivative of K in (17.3.23), we find

$$\frac{\partial K}{\partial \theta} = \frac{9}{2}\sin\theta\cos\theta - \frac{3}{Re}\sin\theta\left[1 + \frac{5}{\sqrt{9 + 4\tan^2\theta}}\right]. \tag{17.3.25}$$

It is obvious that $\theta = 0$ is a solution of $\partial K/\partial\theta = 0$ at any Reynolds number. We compute $\partial^2 K/\partial\theta^2$ to

determine whether K at $\theta = 0$ is a local maximum or minimum. From (17.3.25), the second derivative of K is

$$\frac{\partial^2 K}{\partial \theta^2} = \frac{9}{2}\cos 2\theta + \frac{60\sec\theta\tan^2\theta}{Re\left(9+4\tan^2\theta\right)^{3/2}} - \frac{\cos\theta}{Re}\left(3 + \frac{15}{\sqrt{9+4\tan^2\theta}}\right). \tag{17.3.26}$$

When $\theta = 0$, we have

$$\frac{\partial^2 K}{\partial \theta^2}(\theta = 0) = \frac{9}{2} - \frac{8}{Re}. \tag{17.3.27}$$

Thus $\partial^2 K/\partial\theta^2$ at $\theta = 0$ is negative when $Re < 16/9$ and positive when $Re > 16/9$. This result indicates that K at $\theta = 0$ is a local maximum when $Re < 16/9$ and is a local minimum when $Re > 16/9$. Substitution of $\theta = 0$ in (17.3.23) yields

$$K(\theta = 0) = \frac{12}{Re} - 1, \tag{17.3.28}$$

which is a local maximum of K for $Re < 16/9$ in the interval $0 \le \theta \le \pi/2$.

Besides $\theta = 0$, there is a second solution for $\partial K/\partial\theta = 0$ which depends on Re and has a very complicated expression. If the value of Re is very high, then $\partial K/\partial\theta \approx 9\sin(2\theta)/4$. The second solution is close to $\theta = \pi/2$. We also notice that $\partial^2 K/\partial\theta^2 < 0$ at $\theta = \pi/2$ when Re is high. Therefore, the maximum value of K occurs near $\theta = \pi/2$ when Re is high in the interval $0 \le \theta \le \pi/2$.

Similarly, from (17.3.24), K has a local maximum at $\theta = \pi$ when $Re < 4/9$ and has a local minimum at this position when $Re > 4/9$ in the interval $\pi/2 < \theta \le \pi$. Substitution of $\theta = \pi$ into (17.3.24) gives this local maximum for $Re < 4/9$ in the interval $\pi/2 < \theta \le \pi$,

$$K(\theta = \pi) = \frac{6}{Re} - 1. \tag{17.3.29}$$

A second solution, as a complicated function of Re, can be written for $\partial K/\partial\theta = 0$. For high Re, this solution gives that K goes to a maximum when θ approaches $\pi/2$.

A comparison of (17.3.28) and (17.3.29) allows us to discard the position $\theta = \pi$. Summarizing our findings for viscous potential flow, K reaches a maximum at $\theta = 0$ when $Re < 16/9$ in the interval of interest $0 \le \theta \le \pi$. In addition, in the limit of high Re, K is maximum at $\theta = \pi/2$ in this interval. These results are verified in Figures 17.10 (b) for low Re and Figures 17.12 (a) for high Re.

17.4 Symmetric model of capillary collapse and rupture

† The breakup of a liquid capillary filament is analyzed as a viscous potential flow near a stagnation point on the centerline of the filament towards which the surface collapses under the action of surface tension forces. The analysis given here is restricted to cases in which the neckdown is symmetric around the stagnation point. The cartoon for the model in figure 17.13 is defined by a periodic array of stagnation points between points of liquid depletion and liquid accumulation. The passage of liquid from points of depletion caused by capillary collapse to points of accumulation around which a liquid ball expands cannot be done without the generation of vorticity in an axisymmetric analogue to to the hyperbolic vortices xy =constant nested in the four quadrants at each stagnation point in the vortex array described by (4.6.31). The analysis can be said to generate a Helmholtz decomposition for rotational flow near a point of stagnation. We find that the neck is of parabolic shape and its radius collapses to zero in a finite time; the curvature at the throat tends to zero much faster than the radius, leading ultimately to a microthread of nearly uniform radius. During the collapse the tensile stress due to viscosity increases in value until at a certain finite radius, (which may be estimated as $2\gamma/p_a$ where γ is surface tension and p_a is atmospheric pressure, about 1.5 microns for water in air) the stress in the throat passes into tension, presumably inducing cavitation there. The Reynolds number at which the stress passes into tension decreases as $1/\nu^2$ where ν is the kinematic viscosity. Viscous threads rupture at very low Reynolds numbers. Numrical studies and experiments show that low viscosity liquids generate satellite drops, but highly viscous liquids appear to follow the dynamics of the breakup model presented here.

† T.S. Lundgren & D.D. Joseph 2006, unpublished.

17.4.1 Introduction

The breakup of liquid jets is generally framed in terms of the capillary pressure $\gamma/R(z,t)$ due to surface tension γ acting at the neck of radius $R(z,t)$. The capillary pressure is greatest at the position z where R is smallest, an unstable situation in which liquid is squeezed out of the neck further reducing R and increasing the capillary pressure there. This picture leads to an inevitable collapse of the radius to zero. The conventional view is that the capillary instability just described leads to "pinchoff" but the physics required to actually rupture the thread is not revealed. Here we are promoting the idea that the filament ruptures by cavitation due to tensile stresses induced by the motion out of the neck. The idea that liquids can cavitate by tensile stresses associated with motions, rather than by lowering the pressure was introduced by Joseph 1995. One of the interesting implications of this idea (Joseph 1998) is that cavitation in a pure shear flow may be induced by a tensile stress at 45° from the direction of shearing in a pure shear flow.

Capillary collapse is the final stage of dynamics which may be framed as starting from the capillary instability of a liquid cylinder. The initial instability of the liquid cylinder was studied by Funada and Joseph 2002 and Wang, Joseph and Funada 2005a. Funada and Joseph 2002 assumed that the motion of the viscous cylinder is irrotational; the velocity is given by $\boldsymbol{u} = \nabla\phi$, $\nabla^2\phi = 0$ and the viscous terms in the normal stress balances are evaluated from the potential. They derived a dispersion relation, σ vs. k, where σ is the growth rate and k the wave number. They compared growth rate curves for potential flows of inviscid and viscous fluids in which the conditions on the tangential components of the velocity and stress are neglected with the growth rates from the normal mode reduction of the Navier-Stokes equations (called exact) in which the vorticity and continuity of the tangential velocity and stress are not neglected. Many liquids with viscosities differing by many orders of magnitude were studied. In all cases there is a strict separation of the growth rate curves computed by three theories. The growth rates for inviscid potential flow are largest and those for the Navier-Stokes theory are smallest with viscous potential flow between. The curves are crowded when the viscosity is small and are widely separated when the viscosity is large. The potential flow solution for viscous fluids is in a modest agreement with the exact results, but the result for inviscid fluids are well off the mark.

Wang, Joseph and Funada 2005a implemented method proposed by Joseph and Wang 2004 for computing a viscous correction of the irrotational pressure induced by the discrepancy between the non-zero irrotational shear stress and the zero shear stress boundary condition at a free surface. The theory with an additional viscous pressure correction added to the irrotational pressure is called the viscous correction viscous potential flow (VCVPF). The corrected theory leads to a connection formula between the irrotational shear stress and the added viscous pressure which arises in a very thin boundary layer which is not analyzed and not needed. The linearized equations in this layer are used to show that the added pressure is harmonic and the additional contributions of the viscosity to the normal stress are small compared to the viscous irrotational contribution.

The analysis of capillary instability using the added pressure is in remarkable agreement with the results of exact analysis for in all cases. The growth rate curves for VCVPF are nearly identical to those computed from the exact theory, uniformly in k. The two theories differ at most by a few percent whereas, for the case of highly viscous liquids, the analysis for inviscid liquids give large unrealistic growth rates. The popular idea that viscous potential flow should be a small perturbation of inviscid potential flow is wrong.

The reader may think that the calculation of an added viscous pressure correction takes the theory away from purely irrotational flow, even though the velocities are obtained from the potential. However, exactly the same results that arise from VCVPF also arise from the dissipation method in which the pressure never enters; all the quantities needed are obtained from solutions of Laplace equation for the potential. The dissipation method used for the calculation of capillary instability is the strict analog of the dissipation method used by Lamb 1932 to determine the effects of viscosity on the decay of irrotational water and by Levich 1949 to determine the drag on a spherical gas bubble.

The problem of capillary collapse considered here is rather different than the problem of capillary instability of a liquid cylinder. One obvious difference is that the instability problem is linear but the collapse problem is very nonlinear. Less obvious is the role of the pressure correction which arises in the linear problem from the need to compensate the unbalanced irrotational shear stress. In the problem considered here the shear stress is

continuous at the throat and the normal stresses are balanced there. A harmonic correction p_v of the irrotational pressure p_i is required to balance the normal stress away from the throat. This additional contribution to the pressure generates a vortical contribution to the velocity away from the throat.

17.4.2 Analysis

In this paper we study the collapse of a capillary filament under surface tension forces which squeeze liquid symmetrically from the throat at $z = 0$ in figure 17.13. The analysis is local; terms of order z^4 are neglected but the local stagnation flow can be thought to be embedded in a global periodic structure of stagnation points with depletion at throats and accumulation at crests, as is shown in figure 17.13.

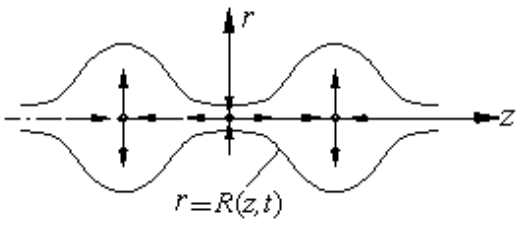

Fig. 17.13. Periodic structure of stagnation points as a cartoon of the dynamics of capillary collapse. The collapse will give rise to a periodic string of liquid drops. The analysis here is local focusing on dynamics of collapse at $z = 0$.

We assume that the flow in the neighborhood of the throat is an axially symmetric straining flow, or stagnation point flow, with velocity components

$$u_z = a\,(t)\,z, \tag{17.4.1}$$

$$u_r = -\frac{1}{2}a\,(t)\,r, \tag{17.4.2}$$

and determine the strain rate $a(t)$ and the capillary shape, $r = R(z, t)$, by satisfying the appropriate boundary conditions at the capillary surface. The velocity field described by equations (17.4.1) and (17.4.2) is incompressible and irrotational, therefore despite being a viscous flow, it may be described by a velocity potential $\left(u_z = \dfrac{\partial\phi}{\partial z},\ u_r = \dfrac{\partial\phi}{\partial r}\right)$ of form

$$\phi = \frac{1}{2}az^2 - \frac{1}{4}ar^2. \tag{17.4.3}$$

The pressure p_i in the flow is determined from the unsteady version of the Bernoulli equation

$$\frac{\partial\phi}{\partial t} + \frac{1}{2}\left(u_r^2 + u_z^2\right) + \frac{p_i}{\rho} = \frac{p_0}{\rho} \tag{17.4.4}$$

in the form

$$\frac{p - p_0}{\rho} = -\left(\frac{1}{2}\dot{a} + \frac{1}{2}a^2\right)z^2 + \left(\frac{1}{4}\dot{a} - \frac{1}{8}a^2\right)r^2. \tag{17.4.5}$$

The stagnation pressure p_0 may be related to a distant state of rest at the center of the inflating balloon into which liquid is driven from the collapsing throat see figure 17.13); p_0 is a global reference in an otherwise local solution. The overdot denotes a time derivative.

In this flow the state of stress is given by two principal stresses;

$$T_{zz} = -p + 2\mu \frac{\partial u_z}{\partial z} = -p + 2\mu a, \tag{17.4.6}$$

$$T_{rr} = -p + 2\mu \frac{\partial u_r}{\partial r} = -p_i - \mu a. \tag{17.4.7}$$

The normal traction at a point on the free surface, the force per unit area which the surface exerts on the fluid, is

$$T_{nn} = n_r^2 T_{rr} + n_z^2 T_{zz}, \tag{17.4.8}$$

where n_r and n_z are components of the unit outward normal. A force balance at the free surface gives the boundary condition

$$-T_{nn} - p_a = \gamma\kappa, \tag{17.4.9}$$

where p_a is atmospheric pressure, p_0 is the surface tension force per unit length and p_0 is the mean curvature, given by

$$\kappa = -\frac{\dfrac{\partial^2 R}{\partial z^2}}{\left(1 + \left(\dfrac{\partial R}{\partial z}\right)^2\right)^{3/2}} + \frac{1}{R\left(1 + \left(\dfrac{\partial R}{\partial z}\right)^2\right)^{1/2}}. \tag{17.4.10}$$

Equation (17.4.9) is the condition which drives the capillary collapse. It should be pointed out that the condition of zero shear stress at the boundary is satisfied exactly at the throat because u_z is independent of r.

Since the free surface must move with the fluid, we also have the kinematic condition

$$u_r = \frac{\partial R}{\partial t} + u_z \frac{\partial R}{\partial z} \tag{17.4.11}$$

at $r = R(z,t)$. This may be written

$$-\frac{1}{2} aR = \frac{\partial R}{\partial t} + az \frac{\partial R}{\partial z}. \tag{17.4.12}$$

The mathematical problem is to find a function $R(z,t)$ which satisfies the conditions expressed by equations (17.4.9) and (17.4.12). We will show that a function of form

$$R(z,t) = R_0(t) + R_2(t) z^2 + O\left(z^4\right) \tag{17.4.13}$$

is suitable and determine $R_0(t)$, $R_2(t)$ and the strain rate $a(t)$ by expanding these conditions for small z. To the lowest order in z^2

$$\begin{aligned} \frac{T_{nn}}{\rho} &= \frac{T_{rr}}{\rho} = -\frac{p_i}{\rho} - va \\ &= -\frac{p_0}{\rho} - va + \frac{1}{2}\left(\dot{a} + a^2\right) z^2 - \left(\frac{1}{4}\dot{a} - \frac{1}{8}a^2\right) R^2 \\ &= -\frac{p_0}{\rho} - va + \frac{1}{2}\left(\dot{a} + a^2\right) z^2 - \frac{1}{4}\left(\dot{a} - \frac{a^2}{2}\right)\left(R_0^2 + 2R_2 z^2\right) \end{aligned} \tag{17.4.14}$$

and to the same order

$$\kappa = \frac{1}{R_0} - 2R_2. \tag{17.4.15}$$

Equation (17.4.12) gives the two equations

$$-\frac{1}{2} aR_0 = \dot{R}_0, \tag{17.4.16}$$

$$-\frac{5}{2} aR_2 = \dot{R}_2. \tag{17.4.17}$$

From these, we see that $R_2 = CR_0^5$, where C is a constant depending on starting conditions. This result implies

that R_2 tends to zero faster than R_0 which means that the parabola flatters out during collapse. It follows then that the R_2 term in (17.4.14) is of lower order and the term proportional to z^2 can not be balanced.

To balance the terms proportional to z^2 in (17.4.14), we introduce a pressure correction p_v where $p = p_i + p_v$. We find this correction among harmonic functions $\nabla^2 p_v = 0$ so that

$$\nabla^2 p = \nabla^2 p_i = -\rho \mathrm{div}\left(\boldsymbol{u} \cdot \nabla \boldsymbol{u}\right),$$

where $\boldsymbol{u} = \nabla\phi$ and p_i is given by (17.4.5). The required harmonic function is found in the form

$$p_v = C\left(-\frac{r^2}{2} + z^2\right), \tag{17.4.18}$$

and, after adding p_v to (17.4.5) we get

$$\frac{p - p_0}{\rho} = -\left(\frac{1}{2}\dot{a} + \frac{1}{2}a^2 - \frac{C}{\rho}\right) z^2 + \left(\frac{1}{4}\dot{a} - \frac{1}{8}a^2 - \frac{C}{2\rho}\right) r^2.$$

To balance the terms proportional to z^2 in (17.4.14), we choose

$$C = \frac{\rho}{2}\left(\dot{a} + a^2\right).$$

Then

$$\frac{p - p_0}{\rho} = -\frac{3}{8}a^2 r^2. \tag{17.4.19}$$

This pressure difference is negative and is most negative at the boundary $r = R$.

The pressure correction induces a vortical velocity $\mathbf{v}$ which vanishes at the throat. The velocity $\boldsymbol{u} = \boldsymbol{u}_i + \mathbf{v}$, where the components of $\boldsymbol{u}_i = \nabla\phi$ are given by (17.4.1), and

$$\frac{\partial \mathbf{v}}{\partial t} + \mathbf{v} \cdot \nabla \mathbf{v} + \boldsymbol{u}_i \cdot \nabla \mathbf{v} + \mathbf{v} \cdot \nabla \boldsymbol{u}_i = -\nabla \frac{p_v}{\rho} + \nu \nabla^2 \mathbf{v}. (20) \tag{17.4.20}$$

We shall show that the left side of (20) is of lower order and may be neglected near the stagnation point. Writing $(v_r,\ v_z) = (u,\ w)$, and using (17.4.18), we have

$$\begin{aligned} 2Cz &= \mu\left[\frac{\partial^2 w}{\partial z^2} + \frac{1}{r}\frac{\partial}{\partial r}\left(r\frac{\partial w}{\partial r}\right)\right], \\ -Cr &= \mu\left[\frac{\partial^2 u}{\partial r^2} + \frac{1}{r}\frac{\partial}{\partial r}\left(r\frac{\partial u}{\partial r}\right) - \frac{u}{r^2}\right], \\ \frac{\partial w}{\partial z} &+ \frac{1}{r}\frac{\partial}{\partial r}\left(ru\right) = 0. \end{aligned} \tag{17.4.21}$$

The solution of (17.4.21) which vanishes at the origin is

$$\begin{aligned} w &= \frac{C}{3\mu} z^3, \\ u &= -\frac{C}{2\mu} r z^2. \end{aligned} \tag{17.4.22}$$

The vorticity for this axisymmetric solution is given by

$$\frac{\partial u}{\partial z} - \frac{\partial w}{\partial r} = -\frac{C}{\mu} r z. \tag{17.4.23}$$

The largest terms on the right side of (20) for values of r and z are $O\left(z^3\right)$ and $O\left(rz^2\right)$. The vortical velocity $\mathbf{v}$ does not enter into any leading balance discussed below.

To leading order, $T_{nn} = T_{rr} = -p + \mu a$ and $-T_{rr} - p_a = \dfrac{\gamma}{R_0}$, which is in the form

$$-\frac{3\rho}{8} R_0^2 - \mu a + p_0 - p_a = \frac{\gamma}{R_0}. \tag{17.4.24}$$

Since we are most interested in small R_0, we can pick out the dominant terms in (17.4.24) as R_0 tends to zero. These are

$$-2\mu\frac{\dot{R}_0}{R_0} = \frac{\gamma}{R_0} \tag{17.4.25}$$

which is a balance between the *viscous* part of the normal force (which resists the collapse) and the surface tension force (which drives it). The large R_0^{-1} term cancels from each side giving

$$\dot{R}_0 = -\frac{1}{2}\frac{\gamma}{\mu} \tag{17.4.26}$$

with solution

$$R_0 = \frac{\gamma}{2\mu}(t_* - t) \tag{17.4.27}$$

where t_* is a constant of integration. Therefore we have a solution in which R_0 tends to zero in a finite time. It is easy to see that the neglected terms in equation (17.4.24) give a correction to R_0 of order $(t_* - t)^2$. With the additional term the solution becomes

$$R_0 = \frac{\gamma}{2\mu}(t_* - t) - \frac{\gamma}{2\mu}\frac{p_0 - p_a}{4\mu}(t_* - t)^2 + \ldots \quad . \tag{17.4.28}$$

The strain rate is,

$$a = -2\frac{\dot{R}_0}{R_0} = \frac{2}{t_* - t} - \frac{p_0 - p_a}{2\mu} + \ldots, \tag{17.4.29}$$

The axial stress at leading order is given by

$$\begin{aligned} T_{zz} &= -p + 2\mu a = -p_0 + \frac{3}{8}\rho a^2 r^2 + 2\mu a \\ &= -p_0 + \frac{3}{2}\dot{R}_0^2\left(\frac{r}{R_0}\right)^2 + 2\mu a \\ &= \frac{3}{8}\frac{\rho\gamma^2}{\mu^2}\left(\frac{r}{R_0}\right)^2 + \frac{4\mu}{t - t_*} - (2p_0 - p_a) \end{aligned} \tag{17.4.30}$$

where $\dot{R}^2 = \gamma^2/4\mu^2$, from (17.4.26). The stress induced cavitation will occur when and where the axial stress passes into tension. This will always occur first at the boundary of the capillary where $r/R_0 = 1$.

Consider next the axial stress at the stagnation point

$$T_{zz} = -(2p_0 - p_0) + \frac{2\gamma}{R_0(t)}. \tag{17.4.31}$$

The thread will pass into tension over the whole cross section at $z = 0$ when T_{zz} given by (17.4.31) becomes positive and passes into tension.

We see that when R_0 is sufficiently small T_{zz} can become positive. This means that the axial stress becomes tension instead of compression. Liquids can not support much tension without rupturing. This would occur here when R_0 is somewhat less than the critical value

$$R_{0cr} = \frac{2\gamma}{(2p_0 - p_a)} \tag{17.4.32}$$

which, it should be noted, is independent of the viscosity. This value is fairly large; for water with $\gamma =$ 75 dynes/cm and estimating $p_0 - p_a$ in the static balloon to be approximately $2\gamma/B$ which is nearly zero for a large radius B, we get $p_0 = p_a = 10^6$ dynes/cm^2 and $R_{0cr} = 1.5$ μm.

A Reynolds number for the collapsing capillary may be defined by

$$R_e = \frac{R_0\dot{R}_0}{\nu} \tag{17.4.33}$$

based on the throat radius and the velocity of collapse, using equation (17.4.26) for the latter quantity gives

$$R_e = \frac{R_0\gamma}{2\rho\nu^2} \tag{17.4.34}$$

which is the ratio of R_0 to a viscous length (Peregrine *et al.* 1990) $2\rho\nu^2/\gamma$ which is very small for water, about .027 μm. Therefore using R_{0cr} (=1.5 micron) for R_0, the Reynolds number at collapse is about 55 for water (the collapse velocity is about 37 m/s). For more viscous liquids the Reynolds number at collapse could be very small. For the solution presented here there is no restriction on the magnitude of the Reynolds number.

17.4.3 Conclusions and discussion

Neckdown of a liquid capillary thread was studied in a local analysis based on viscous potential flow. One objective of this study was to show that during collapse the thread will enter into tension due to viscosity and can be expected to fracture, or cavitate, at a finite radius.

The flow in the throat of the collapsing capillary is locally a uniaxial extensional flow, linear in z and r, with a time dependent strain rate $a(t)$. This viscous potential flow satisfies the Navier-Stokes equation and all the relevant interfacial conditions, including continuity of the shear stress.

The principal dynamic balance is between the surface tension forces, which are trying to collapse the capillary, and the radial viscous stress which is resisting the collapse. Since mass must be conserved a large axial flow results from squeezing liquid out of the neck and this results in a large viscous extensional stress. The extensional stress passes into tension at $R_0 = 1.5$ μm (for water and air) long before R_0 actually collapses to zero.

The solution is symmetric about $z = 0$, the position of the smallest radius; the axial velocity is odd and the radial velocity, pressure and interface shape

$$R(z,t) = R_0(t) + R_2(t)z^2 + O\left(z^4\right)$$

are even in z. At lowest order the interface is a parabola in which $R_2(t)$ is proportional to R_0^5, hence in the limit of collapsing radius $R_2 \to 0$ much more rapidly then R_0 and the shape approaches that of a straight cylinder. The radius tends to zero linearly, like $(t_* - t)$, collapsing to zero in a finite time. At the same time the strain rate $a(t)$ tends to infinity like $(t_* - t)^{-1}$.

An authorative review of the capillary breakup literature prior to 1997 was given by Eggers 1997. A part of this literature review describes theoretical studies of inviscid potential flow. These studies can be easily extended to accommodate the irrotational effects of viscosity which are in fact hugely important in the extensional flows under consideration here. Eggers notes that the most extensive numerical study of breakup prior to 1997 is due to Ashgriz and Mashayek 1995. They used periodic boundary conditions in the axial direction and considered initial sinusoidal disturbances of different wave lengths of wave number k. Their computations lead to the symmetric configurations shown in figure 17.14. They note that "The linear theory predicts that the breakup point is always at the neck (trough) of the initial disturbance. However, figure 17.14 clearly shows that the breakup point is closer to the swell points." When $Re > 0.1$, the breakup point moves to the swell and the center stagnation point is a points of fluid accumulation leading to satellite drops. When $Re = 0.1$ (and perhaps when $Re < 0.1$) the breakup is at the neck which is a stagnation point of fluid depletion which is modeled by the theory given here. A symmetric form of breakup of a liquid bridge at a low Reynolds number (3.7×10^{-3}) is shown in figure 17.15, taken from the paper of Spiegelberg, Gaudet, and McKinley 1994. The outer fluid eliminates buoyancy and has a viscosity 1000 times smaller than the inner fluid. Brenner *et al.* 1997 discuss the breakdown of the similarity solution of Eggers at high Reynolds number. In their figure 1(c) they show the shape of a pure glycerol interface just before rupture which appears to be symmetric.

In the literature on capillary collapse and rupture the focus is on collapse which is universally framed as a pinch-off and the fundamental physics governing the rupture of the thread is not considered. A pinch-off is a squeezing flow; the radius of the jet at the pinch point collapses, squeezing fluid out as the filament collapses. Here one finds a stagnation point; stagnation point flow is a potential flow and the effects of viscosity in such a flow may be huge. Certainly, potential flow of an inviscid fluid is not the right tool here. We can get results in which viscosity acts strongly using viscous potential flow. The question is not whether viscosity is important, which it is, but whether vorticity is important.

Pinch-off at swell points (figure 17.16) is greatly different than the pinch-off at a neck (figure 17.15). It is generally believed the break-up at swell points in long, skinny threads is very well described by Eggers' 1993 one dimensional universal solution. The final stage of breakup at the neck in the Lundgren-Joseph model developed here leads also to a long skinny thread but the dynamics of the breakup of the long skinny threads at the final stage are greatly different (the details are given in the appendix to this section). It is of interest that the low Reynolds number similarity solution of Papageriou which falls into the Eggers class of similarity solutions is symmetric. Rothbert *et al.* 2001 discuss the transition from a symmetric to asymmetric scaling function before pinch-off; symmetric forms are shown in their figure 2.

Chen *et al.* 2002 have studied pinch-off and scaling during drop formation using high-accuracy computation and ultra-fast high-resolution imaging. They discuss dynamic transition from potential flow with a 2/3 scaling due to Keller and Miksis 1983 to an inertial-viscous regime described by Eggers' 1993 universal solution. They find overturn before breakup in experiments in water (1 cp) well before the dynamic transition from the potential flow to the inertial-viscous regime. On the other hand, an 85 cp glycerol-water solution is said to exhibit this transition. The potential flow solutions discussed by Chen *et al.* 2002 are for inviscid solutions. Of course, water and glycerol are not inviscid. The scaling of Keller and Miksis 1983 which gives rise to the 2/3 power collapse law does not work for viscous potential flow. The spoiler is their equation (3.3) expressing the normal stress balance. To this equation we must add the viscous component $2\mu\partial U_n/\partial n$. The term $(\nabla\phi)^2$ in (3.3) scales like ϕ^2/L^2 whereas the viscous component scales like ϕ/L^2, so that the similarity transformation does not factor through. Analogies have been put forward between capillary pinch-off of a viscous fluid thread and van der Waals driven ruptures of a free thin viscous sheet Vaynblat *et al.* 2001. The observation that a filament under capillary collapse ruptures in a "pinch-off" does not come to grips with the physics which leads to a loss of the continuum. One idea is that thread breaks under the action of disjoining pressures. Unfortunately, a mathematical theory for disjoining pressures for thin threads is not available.

The recent literature on capillary collapse is presently dominated by the discovery of self-similar, finite time singularity formation. These solutions are discussed in the recent papers Chang *et al.* 1999, McKinley and Tripathi 2000, and in the paper of Chen *et al.* 2002. This literature does not treat the physics of rupture or breakup by cavitation and does not compute stresses. All of the above mentioned authors find that capillary radius decreases to zero linearly in time, but the rate of collapse differs from author to author. McKinley and Tripathi 2000 write the formula

$$R_{\text{mid}}^{(t)} = R_1 - \frac{2X-1}{6}\frac{\gamma}{\mu}t$$

for the neck radius of the collapsing capillary in the stage of final decay as t increases to t^* when $R_{\text{mid}}^{(t^*)} = 0$. They give the X obtained by different authors in their Table 1, but without the value $X = 2$ obtained here for viscous potential flow, giving the fastest decay. Eggers (1997, 1993) obtained $X = 0.5912$ and Papageoriou 1995 obtained $X = 0.7127$. The solutions of the two authors last named have vorticity; Papageriou's solution has no inertia. McKinley and Tripathi 2000 note that very close to breakup the solution of Papageriou crosses over to Egger's similarity solution. The transitions between different similarity solutions are less well understood than the similarity solutions themselves. These transitions can be regarded as a form of instability. It is possible that the solution in this paper can be described as a transition to rupture.

The solution of Eggers 1993 gives rise to a universal scaling law which has been observed for viscous liquids but not in water (see Chen *et al.* 2002). The long wave approximation used to derive universal scalings may prevent it from resolving the dynamics of rupture. The similarity solution of Eggers does not lead to a cavitation threshold; in his solution the tension due to extension increases but not fast enough to overcome the compression due to the capillary pressure of the thinning filament.

The criterion for the termination of the continuum is probably not a finite time singularity; the thread radius does not go to zero. It comes apart before then.

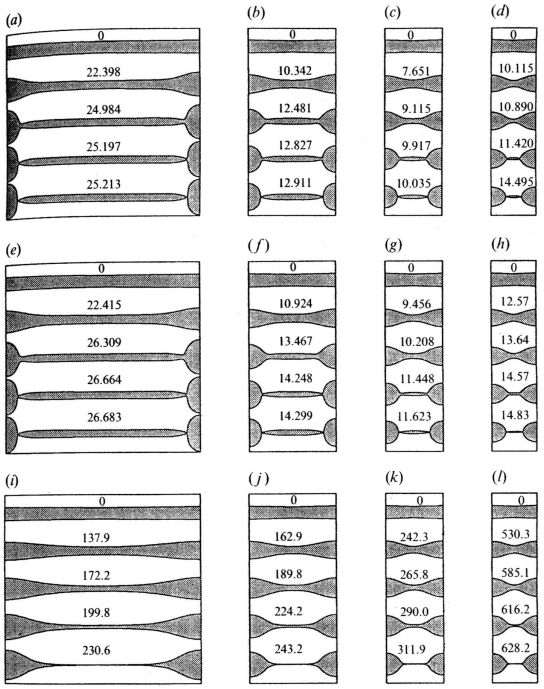

Fig. 17.14. (Ashgritz and Mashayek, 1995) Time evolution of the instability of a capillary liquid jet, $\epsilon_0 = 0.05$: (a) $k = 0.2$, $Re = 200$, (b) $k = 0.45$, $Re = 200$, (c) $k = 0.7$, $Re = 200$, (d) $k = 0.9$, $Re = 200$, (e) $k = 0.2$, $Re = 10$, (f) $k = 0.45$, $Re = 10$, (g) $k = 0.7$, $Re = 10$, (h) $k = 0.9$, $Re = 10$, (i) $k = 0.2$, $Re = 0.1$, (j) $k = 0.45$, $Re = 0.1$, (k) $k = 0.7$, $Re = 0.1$, (l) $k = 0.9$, $Re = 0.1$. The numbers on the figures indicate the corresponding times.

17.4.4 Appendix

Comparison of the symmetric solution of Lundgren and Joseph 2006 (called LJ) with the similarity solution of Eggers 1993 (called E)

We refer to equations (1) through (6) in the 1993 paper of Eggers. The variables used by E are here designated with cavot overbar

$$\begin{aligned}
\hat{\boldsymbol{v}} &= (\hat{v}_z, \hat{v}_r)\,, \\
\frac{\partial \hat{v}_r}{\partial r} + \frac{\partial \hat{v}_z}{\partial z} + \frac{\hat{v}_r}{r} &= 0, \\
\hat{v}_z &= \hat{v}_0(z,t) + \hat{v}_z(z,t) r^2, \\
\hat{v}_r(z,r,t) &= -\hat{v}_0'(z,t)\frac{r}{2} - \hat{v}_z'(z,t)\frac{r^3}{4}, \\
\hat{p}(z,r,t) &= \hat{p}_0(z,t) + \hat{p}_z(z,t) r^2.
\end{aligned}$$

Using these expressions, E reduces the normal stress balance (17.4.4) to a pressure equation

$$p = \hat{p}_0(z,t) = \gamma\left(\frac{1}{R_1} + \frac{1}{R_2}\right) - \mu \hat{v}_0'(z,t)$$

at leading order.

In Eggers analysis, the lowest order balance is for the r independent part of the foregoing representations.

$$\begin{aligned}
\hat{v}_r &= 0, \\
\hat{v}_z &= \hat{v}_0(z,t), \\
p = \hat{p}_0(z,t) &= \gamma\left(\frac{1}{R_1} + \frac{1}{R_2}\right) - \mu \hat{v}_0'.
\end{aligned}$$

The expressions for $\hat{v}_r = -\hat{v}_0'(z,t)\dfrac{r}{2}$ are needed to compute $\hat{v}_r$. The radial component of momentum at lowest

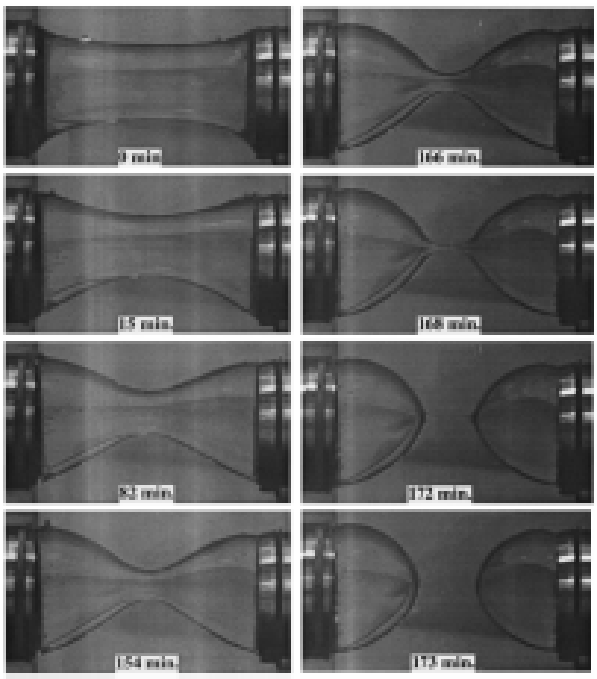

Fig. 17.15. Liquid-bridge evolution starting from an unstable configuration. The disk diameter is 3.8 cm, the Reynolds number is 3.7×10^{-3}. The outer fluid, which eliminates buoyancy forces, has a viscosity approximately 1000 times smaller than the inner fluid. (Spiegelberg, Gaudet, and McKinley, 1994).

order has no r independent terms and, therefore is dropped as lower order and does not enter into the analysis leading to his similarity solution. According to (E), the radial momentum is not relevant at leading order.

E neglects the radial momentum equation [(1) in E's paper]. LJ solve this problem at $O(r)$; it is not neglected.

Recalling now the analysis of LJ just given, we have the velocity decomposed in Helmholtz form, where $\phi = \frac{1}{2}az^2 - \frac{1}{4}ar^2$, $\boldsymbol{v} = \nabla\phi + \boldsymbol{u}$, where $\nabla\phi$ is the irrotational velocity and $\boldsymbol{u}$ is rotational velocity.

$$\begin{aligned}
\boldsymbol{u} = (u_z,\ u_r) &= (w, u)\,, \\
\boldsymbol{v} = (v_z,\ v_r) &= \left(\frac{\partial\phi}{\partial z} + w,\ \frac{\partial\phi}{\partial r} + u\right), \\
w &= \frac{c}{3\mu}z^3, \\
u &= -\frac{c}{2\mu}rz^2, \\
c &= \frac{\rho}{2}\left(\dot{a} + a^2\right).
\end{aligned}$$

The value of c is what it takes to balance the normal stress at order z^2. We get

$$\begin{aligned}
v_z &= az + \frac{c}{3\mu}z^3, \\
v_r &= -\frac{a}{2}r - \frac{c}{2\mu}z^2 r, \\
\frac{p - p_0}{\rho} &= -\frac{3}{8}a^2r^2.
\end{aligned}$$

Now we verify that the equation (1) of radial momentum E is satisfied at leading order. The left side of (1) in E, is evaluated using the expansion of LJ just given.

$$\frac{\partial\hat{v}_r}{\partial t} + \hat{v}_r\frac{\partial\hat{v}_r}{\partial r} + \hat{v}_z\frac{\partial\hat{v}_z}{\partial z} \ \rightarrow\ -\frac{\dot{a}}{2} + \frac{a^2}{4}.$$

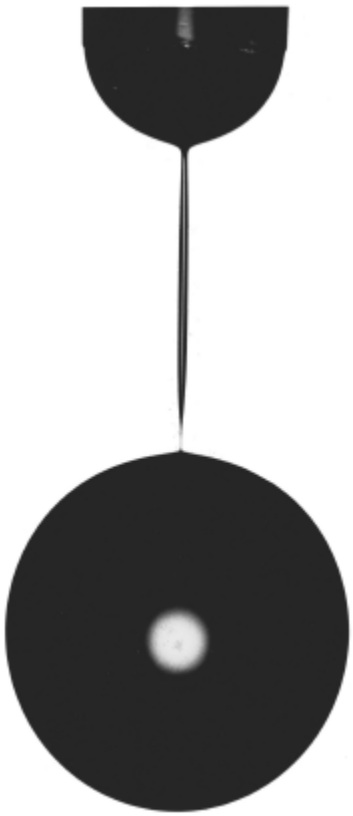

Fig. 17.16. A drop of a glycerol and water mixture, 100 times as viscous as water, falling from a nozzle 1.5 mm in diameter. As opposed to the case of water, a long neck is produced (Shi, Brenner, and Nagel, 1994).

The right side reduces as follow

$$-\frac{1}{\rho}\frac{\partial \hat{p}}{\partial r}+\nu\left[\frac{\partial^2 \hat{v}_r}{\partial r^2}+\frac{\partial^2 \hat{v}_r}{\partial z^2}+\frac{1}{r}\frac{\partial \hat{v}_r}{\partial r}-\frac{\hat{v}_r}{r^2}\right],$$
$$\rightarrow\ -\frac{3}{4}a^2-\frac{\nu c}{\mu}=\frac{3}{4}a^2-\frac{1}{2}\left(\dot{a}+a^2\right).$$

The two sides are in balance.

A summary of the comparison just derived follow

p_0

$$\mathrm{LJ}\begin{cases} v_z=az, \\ v_r=-\dfrac{a}{2}r, \\ \dfrac{p-p_0}{\rho}=-\dfrac{3}{8}a^2r, \end{cases}$$

p_0 is a reference pressure equal to pressure at the stagnation point in the expanding ball (figure 17.13).

$$\mathrm{E}\begin{cases} v_z=\hat{v}_0(z,t), \\ \hat{v}_r=0, \\ \hat{p}=\gamma\left(\dfrac{1}{R_1}+\dfrac{1}{R_2}\right)+\mu\hat{v}_0' \end{cases}$$

The normal stress balance for E is the expansion for $\hat{p}$. The normal stress balance for LJ is their (24)

$$-\frac{3}{8}\rho R_0^2 - \mu a + p_0 - p_a = \bar{R}_0.$$

The pressure in the two solutions is radically different. The pressure does not enter into the leading balance of LJ; their analysis balances the capillarity against the viscous part of the normal stress.